Engineered models of the lymphatic stroma to study cell and fluid transport

Jennifer H. Hammel

Dissertation submitted to the faculty of the Virginia Polytechnic Institute and State University in partial fulfillment of the requirements for the degree of

Doctor of Philosophy
In
Biomedical Engineering

Jennifer M. Munson, Chair
LaDeidra Monet Roberts
Rebecca R. Pompano
Margarita Gutova
Elaheh Rahbar

September 12th, 2024
Blacksburg, VA

Keywords: lymphatics, lymph node, interstitial fluid flow, tissue engineering, transport

© 2024 Jennifer H. Hammel

Engineered models of the lymphatic stroma to study cell and fluid transport

Jennifer H. Hammel

ABSTRACT

The lymphatic system plays essential roles in regulating fluid balance and immunosurveillance. Across the body, local lymphatic vessels collect waste in the form of lymph and deliver it to nearby lymph nodes (LNs) to be filtered and screened for pathogens. With broad implications in adaptive immunity, cancer metastasis, and cancer treatment, developing novel in vitro models will provide new platforms to explore lymphatic function in health and disease. This dissertation sought to develop tissue-specific engineered models of the LN stroma and the meningeal lymphatics to examine the transport of cells and fluid. Within the LN, fibroblastic reticular cells (FRCs) maintain a network of extracellular matrix conduits that guide varying rates of interstitial fluid flow (IFF) based on inflammatory state. Eventually, that flow exits the LN through the afferent lymphatics, consisting of lymphatic endothelial cells (LECs). We first developed a spatially organized model of the LN stroma consisting of a monolayer of LECs on the underside of a tissue culture insert and an FRC-laden hydrogel within. We demonstrate that high magnitude IFF (3.0 μm/s) had positive impacts on FRCs but disrupted the integrity of the LEC barrier, and these effects were accompanied by increased secretion of a variety of inflammatory chemokines. We also show that IFF of any magnitude decreased T cell egress from the model. Next, we sought to apply the LN stroma model toward understanding metastasis. LN metastasis is the most important prognostic factor in breast cancer, with size of metastasis informing treatment plan. Metastasis greatly alters the structure of the LN, which in turn alters transport. However, the impact of altered transport on cancer progression is not well understood. We added different numbers of breast cancer cells to our LN stroma model to examine tumor burden. We found that tumor cells invaded the LEC barrier at similar numbers regardless of initial burden. Additionally, at the highest tumor burden, diffusivity in the stroma was significantly decreased. Most excitingly, flow velocity was positively correlated with FRC spread in the hydrogel, demonstrating the contributions of FRCs to transport. Finally, we looked to the central nervous system (CNS). The meningeal lymphatics are responsible for draining cerebrospinal fluid to the cervical lymph nodes for CNS immunosurveillance. We developed a simple model of a meningeal lymphatic vessel lumen consisting of a monolayer of LECs on the underside of a tissue culture insert and a monolayer of meningeal fibroblasts within. This is, to our knowledge, the very first in vitro model of the meningeal lymphatics. We demonstrate that our model has barrier function and is capable of immune cell transmigration and egress. We examined how systemic chemotherapy for breast cancer could cause off-target disruption of the meningeal lymphatics and found that docetaxel was significantly deleterious. We further began to explore leukemia cell behavior in our LN stroma and meningeal lymphatics model. Throughout this dissertation, we emphasize the importance of incorporating fluid and cell transport into engineered models of immunity. These models represent a step toward building up the complexity of in vitro lymphatic models to improve pre-clinical screening and understand pathophysiology.

Engineered models of the lymphatic stroma to study cell and fluid transport

Jennifer H. Hammel

GENERAL AUDIENCE ABSTRACT

The lymphatic system plays essential roles in regulating fluid balance and immune system surveillance. Across the body, local lymphatic vessels collect waste in the form of lymph and deliver it to nearby lymph nodes (LNs) to be filtered and screened for pathogens like viruses or bacteria. With broad implications in immunity, cancer metastasis, and cancer treatment, developing novel models in the lab using human cells and 3-dimensional biomaterials will provide new platforms to explore lymphatic function in health and disease. This dissertation sought to develop engineered models that were specific to the lymph node stroma and the meningeal lymphatics to examine the transport of cells and fluid. Within the LN, fibroblastic reticular cells (FRCs) maintain a network of channels that guide varying rates of interstitial fluid flow (IFF) based on how inflamed the LN is. Eventually, that flow exits the LN through the afferent lymphatics, consisting of lymphatic endothelial cells (LECs). We first developed a spatially organized model of the LN stroma consisting of LECs on the underside of a porous membrane and an FRC-laden hydrogel above the membrane and demonstrated that high magnitude IFF altered morphology, immune cell behavior, and inflammatory protein secretion in the model. Next, we sought to apply the LN stroma model toward understanding cancer metastasis. LN metastasis is the most important prognostic factor in breast cancer, with size of metastasis informing treatment plan. Metastasis greatly alters the structure of the LN, which in turn alters the transport of lymph and immune cells. However, the impact of altered transport on cancer progression is not well understood. We added different numbers of breast cancer cells to our LN stroma model to examine tumor burden and found that tumor cells invaded the LECs at similar rates regardless of initial density, but that diffusion, a transport parameter, was significantly changed by high tumor cell density. Finally, we looked to the central nervous system (CNS). The meningeal lymphatics are responsible for draining cerebrospinal fluid to the cervical lymph nodes to screen for pathogens in the CNS. We developed a simple model of a meningeal lymphatic vessel lumen consisting of LECs and meningeal fibroblasts on either side of a porous membrane. This is, to our knowledge, the very first in vitro model of the meningeal lymphatics. We examined how systemic chemotherapy for breast cancer could cause off-target disruption of the meningeal lymphatics and found that docetaxel was significantly damaging to the model. Throughout this dissertation, we emphasize the importance of incorporating fluid and cell transport into engineered models of lymphatics. These models represent a step toward building up complexity to improve the toolset for pre-clinical screening and studying disease progression.

ACKNOWLEDGEMENTS

This work would not have been possible without the extensive support of my family and friends. Science happens through connection and community. The past four years have been full of challenges, but also full of inspiration, friendship, and love. I couldn't have done it without all of you.

First, I would like to thank my mentor, Jenny, for encouraging me to constantly explore new ideas and learn new things. Thank you for always having my back and advocating for me. Your ideas are always exciting and inspiring and have helped me find new ways to look at my data. You've taught me new ways to ask scientific questions and provided me with opportunities I never could've imagined. I leave the lab having learned so much about the skills I have and their limitless applications.

I have been fortunate enough to have the additional mentorship of Leah Bellas, Monet Roberts, and Rebecca Pompano. Leah, thank you for taking a chance on an inexperienced undergrad and being the first to teach me how to be a scientist. I would not be here without your invaluable guidance and support. It has made all the difference. Monet, you have been an endless source of support, kindness, and insight throughout this process. Working hands-on with you and watching you start your own lab has been an incredible experience. You have taught me so much about the scientific process and mentorship. Rebecca, thank you for always having a helpful tip and a thoughtful question. Your perspective has helped me develop new ways of looking at in vitro modeling. Additionally, I would like to acknowledge my committee members Elaheh Rahbar and Margarita Gutova for giving me new ideas, feedback, and guidance throughout this process.

Thank you to all the current, former, and honorary Munson Lab members who have provided so much support to me over the years. Kinsley, thank you for being the best virtual cell-culture trainer anyone could ask for and getting me up and running in the lab. During our overlap in the Munson Lab, you were an incredible source of mentorship and kindness. Caleb, thank you for being a source of calm in the lab, for your excellent on-the-spot problem solving, and for always lending a hand. In organizing social outings for the lab, you helped me settle into a new place. Lincoln, thank you for always being a friendly face and listening about our lab woes. Cora, Savieay, and Gabi, thank you for always listening and being a support during stressful times. Sophia, thank you for being the absolute best mentee anyone could ask for. It's been a pleasure watching you grow and learn and I can't wait to see what you do next. Sharon, thank you for being a consistent source of help and reality checks. I've learned so much about how to effectively do science from talking to you. Your knowledge is invaluable. Katie and Jessica, thank you for all the pep talks and encouragement. You were both there with support and motivation when I needed it.

When I began this process, I did so with two others: Yami and Aileen. You have both been such an incredible source of support and love.

Yami, thank you for being the best movie-going, thrift shopping, swimming, and winery-touring buddy I could've asked for. I'll never forget how much support you gave me as I worked through my prelims. You were always there to listen and to get me through whatever source of stress or challenge there was. The Munson Lab is not the same without you.

Aileen, thank you for being an unwavering source of support through this process. I have learned so much from you about friendship and community. Your perspective on everything under the sun has been so valuable to me. Thank you for always being willing to lend an ear and let me vent. Thank you for keeping me grounded. You helped me get through all of it – classes, quals, prelims, and writing this dissertation – while encouraging me to try new hobbies and stay connected with the world. You are an incredible scientist and friend and I can't wait to see what amazing things you do next.

Finally, I'd like to acknowledge my soon-to-be husband and my parents.

Ben, my love. I am so grateful for you. You have been my lifeline through the second half of this degree. You have kept me company through late nights of experiments and writing. You have listened and helped talk through every challenge, uncertainty, and decision. You have taken so much weight off my shoulders. Thank you for being a constant source of joy and light. You have kept me fed, hydrated, and happy. Your love and warmth have gotten me through this. I am so grateful to have such an amazing partner. Thank you for always championing me and my work. I can't wait to marry you and start our next chapter. It's you and I, always.

Dad, you always told me that I would do something great. I have such fond memories of watching science documentaries, playing chess, and going out to see the local fish and fauna. I started research for you. I wanted to understand what happened to you and how I could help prevent it. I know you would be so proud of me and so interested in my work. I've often wished I could pick up the phone and call you during this process. I miss you. I wish you could see this.

Finally, none of this would have been possible without the endless support of my mom. Mom, thank you for being my biggest supporter. You've always told me that I could do anything I put my mind to and encouraged me to keep striving for more. I know how much effort you put into getting me to college. You didn't know how any of it worked, but you figured it out. You always figure it out, because you are an incredible problem solver, and you don't give up. These are the qualities you've instilled in me that have made it possible for me to get the first PhD in our family. Thank you for never doubting me for a second.

This dissertation is dedicated to

My mom, Ginny, for always believing in me.

The love of my life, Ben, for getting me through.

And my dad, John E. Hammel, who I know would've loved to see this.

CONTENTS

ACKNOWLEDGEMENTS iv
CONTENTS vii
LIST OF TABLES ix
LIST OF FIGURES x
CHAPTER 1. Modeling the lymphatic system in health and disease xiii
1.1 Importance and physiology of the lymphatic system 1
1.2 In vitro modeling of the lymphatics 8
1.3 Key considerations for lymph node engineering principles 12
1.4 Existing models of the lymph node 18
1.5 Applications of a lymph node stroma model in basic science and pathophysiology 21
1.6 Looking to distant lymphatic vessels in the central nervous system 23
1.7 Novel lymphatic stroma models for fluid and cell transport 26
CHAPTER 2. Engineered lymph node stroma model for examining interstitial fluid flow 27
2.1 Summary 28
2.2 Introduction 28
2.3 Methods 30
2.4 Results and Discussion 38
2.5 Conclusion 58
CHAPTER 3. Examining tumor burden-related changes to transport in engineered lymph node stroma 59
3.1 Summary 60
3.2 Introduction 61
3.3 Methods 62
3.4 Results 67
3.5 Discussion 83
CHAPTER 4. Modeling the meningeal lymphatics lumen for applications in off-target chemotherapeutics and central nervous system metastasis 88
4.1 Summary 89
4.2 Docetaxel-mediated disruption to meningeal lymphatics integrity in vitro 90
4.2.1 Introduction 90

4.2.2 Methods 91
4.2.3 Results 94
4.2.4 Discussion 105
4.3 Applications in CNS Leukemia 109
4.3.1 Introduction 109
4.3.2 Methods 110
4.3.3 Results 112
4.3.4 Discussion 118
4.4 Applications of the meningeal lymphatics model 120
CHAPTER 5. Discussion 122
5.1 Discussion 123
5.2 Future Directions 139
5.3 Final remarks 146
Appendix A 148
Appendix B. Sex differences and transport in engineered adipose tissue toward studying lipedema 149
B.1 Introduction 149
B.2 Materials and Methods 153
B.3. Results 156
B.4 Discussion 162
References 167

LIST OF TABLES

Table 1.1 Physical properties of the lymph node..... 13

Table 2.1. Gene expression targets and assay IDs. 37

Table 2.2. The LN stroma model is responsive to high magnitude interstitial fluid flow. 57

Table 2.3. LN stroma model flow response in the presence of T cells is altered. 57

Table 3.1. Demographics of control and metastatic human lymph node samples…….....…..63

LIST OF FIGURES

Figure 1.1. The lymphatic system runs through the body and drains to lymph nodes. 2

Figure 1.2. Lymph node structure.. 6

Figure 2.1. Custom apparatuses for pressure heads and flow rate analysis.. 32

Figure 2.2. Activated T cell egress is decreased with interstitial fluid flow..... 39

Figure 2.3. Lymph node stroma model development. 41

Figure 2.4. Flow magnitude and diffusion are unchanged in the presence of LN stroma.. 42

Figure 2.5. Fibroblastic reticular cells have enhanced proliferation and coverage. 43

Figure 2.6. LEC proliferation is unchanged with interstitial fluid flow.. 44

Figure 2.7. T cell egress through the LEC monolayer is decreased. 45

Figure 2.8. LEC monolayers are disrupted with flow and CD4+ T cell presence. 47

Figure 2.9. FRCs invade the LEC monolayer.. 48

Figure 2.10. T cells mitigate flow-mediated FRC spread and are retained in the gel. 49

Figure 2.11. Representative images of FRC networks (green) in the presence of T cells. 50

Figure 2.12. CCL2 gene expression is upregulated by 0.8 µm/s interstitial flow.. 52

Figure 2.13. Collagen structure is not changed by interstitial fluid flow.. 53

Figure 2.14. Cytokine secretion of LN stroma is altered under high interstitial flow. 54

Figure 2.15. Chemokine secretion is significantly increased under high flow magnitude. 55

Figure 3.1. Enhanced collagen deposition in metastatic lymph nodes.. 67

Figure 3.2.The area of collagen is increased in metastatic lymph nodes. 68

Figure 3.3. No significant differences in collagen metrics observed between sexes..... 69

Figure 3.4. No significant differences in collagen metrics in metastatic lymph nodes. 69

Figure 3.5. There are potential differences in coherency and orientation of collagen..... 70

Figure 3.6 Collagen capsule thickness is unchanged between control and metastatic 71

Figure 3.7. There are no significant correlations between collagen and other metrics.. 72

Figure 3.8. Pan-cytokeratin staining in metastatic lymph nodes demonstrates high tumor. 73

Figure 3.9. Tumor burden negatively correlates with %area collagen. 74

Figure 3.10. Experimental schematic of varying tumor burden.. 74

Figure 3.11. A portion of tumor cells are retained at the top of the LN stroma.. 75

Figure 3.12 Tumor cells invade into the bulk hydrogel in the LN stroma model..... 76

Figure 3.13. Tumor cells invade to the membrane of the LN stroma model.. 77

Figure 3.14. Tumor cells traverse the membrane and are found associated with LECs. 78

Figure 3.15. Fluid pathways in the LN stroma models are similar across groups. 79

Figure 3.16. Flow magnitude and divergence are unchanged by tumor cell presence.. 80

Figure 3.17. Diffusivity decreases with increasing tumor cell burden in vitro..... 81

Figure 3.18. There are strong correlations between transport and model morphology.. 82

Figure 3.19. Second harmonic generation imaging of lymph node stroma models. 83

Figure 4.1. In vitro meningeal lymphatic model development.. 94

Figure 4.2. Docetaxel disrupts LEC and MC coverage and alters proliferation.. 96

Figure 4.3. Monoculture controls are treated with 1 µM carboplatin, 1 µM docetaxel..... 97

Figure 4.4 LEC junctions and morphology are impacted by chemotherapy treatment 99

Figure 4.5. Proliferation in the ML model is altered by chemotherapy.. 100

Figure 4.6. Proliferation in monoculture controls.. 101

Figure 4.7. Combination treatment does not demonstrate more disruption than docetaxel. 102

Figure 4.8. Blocking VEGFR3 does not ameliorate chemotherapy-induced changes. 103

Figure 4.9. T cell transmigration is unchanged after treatment.. 104

Figure 4.10. Meningeal cells are not disrupted by MTX or Ara-C..... 112

Figure 4.11. Methotrexate disrupts LEC monolayer integrity.. 113

Figure 4.12. Leukemia cell egress is decreased by ML model compared to either. 115

Figure 4.13. Conditioned media from flow conditioned lymph node stroma models. 116

Figure 4.14. Jurkat leukemia cells have increased invasion in the presence of. 117

Figure 4.15. Jurkats egress from the LN stroma model.. 117

Figure 4.16. Overview of applications and features of the meningeal lymphatics model. 120

Figure 5.1. LN stroma model morphology after 5 days of culture.. 141

Figure 5.2. Gene expression of LN stroma under flow conditions for 5 days.. 142

Figure 5.3. Transport metrics in LN stroma after 5 days of flow conditioning.. 143

Figure 5.4. Representative images of breast cancer cells in flow conditioned LN stroma. 144

Figure A.1. Vasculife is the optimal media for LECs in the in vitro model. 148

Figure B.1. Lipedema is the excess accumulation of adipose tissue in the lower extremities. .. 150

Figure B.2. Workflow for engineered adipose tissue.. 153

Figure B.3. Metrics for adipocyte maturity.. 155

Figure B.4. Male adipocytes are larger and more responsive to hypoxia.. 156

Figure B.5. Fatty acid transport in engineered AT.. 157

Figure B.6. Estradiol treatment pilot study suggests changes in adipocyte maturity.. 158

Figure B.7. Flow mapping of engineered adipose tissue.. 159

Figure B.8. Ex vivo flow mapping of adipose tissue.. 160

Figure B.9. Flow metrics are more consistent in ex vivo tissue.. 161

Figure B.10. Adipocyte response to IFF is variable.. 162

List of Symbols and Abbreviations

ALL	Acute lymphoblastic leukemia
ANOVA	Analysis of variance
Ara-C	Cytarabine
ASC	Adipose-derived stem cell
AT	Adipose tissue
BBB	Blood brain barrier
BSA	Bovine serum albumin
CNS	Central nervous system
CSF	Cerebrospinal fluid
DC	Dendritic cell
DCE	Dynamic contrast enhanced
dCLN	Deep cervical lymph node
DMSO	Dimethyl sulfoxide
ECM	Extracellular matrix
ER	Estrogen receptor
FFPE	Formalin fixed paraffin embedded
FRC	Fibroblastic reticular cell
HBSS	Hank's balanced salt solution
HER2	Human epidermal growth factor receptor 2
HuALN	Human artificial lymph node
IFF	Interstitial fluid flow
IFNγ	Interferon-gamma
IL-6	Interleukin 6
LD	Lipid droplet
LEC	Lymphatic endothelial cell
LN	Lymph node
LRA	Lymphatic ring assay
MC	Meningeal cell
MLV	Meningeal lymphatic vessel
MRI	Magnetic resonance imaging
MTX	Methotrexate
PBS	Phosphate buffered saline
PDMS	Polydimethylsiloxane
PDPN	Podoplanin
PhotoHA	Methacrylated hyaluronic acid
PR	Progesterone receptor
PSR	Picrosirius red
RT	Room temperature
SCS	Subcapsular sinus
VEGF-C	Vascular endothelial growth factor C
VEGFR-3	Vascular endothelial growth factor receptor 3

Chapter 1. Modeling the lymphatic system in health and disease

1.1 Importance and physiology of the lymphatic system

**portions of this section are the author's original writing directly taken from: Hammel et al 2021, "Modeling Immunity In Vitro: Slices, Chips, and Engineered Tissues"*(1)*

1.1.1 Overview of the lymphatic system

Throughout the body, an inter-connected network of lymphatic vessels and lymph nodes provide waste clearance, maintain fluid balance, and perform constant immunosurveillance (**Figure 1.1**). Lymphatic vessels are found in nearly every tissue in the body, tracking with blood vasculature and delivering fluid to over 500 lymph nodes. Within tissues, initial lymphatic vessels (that lack a basement membrane and have loose 'button' junctions) collect interstitial fluid. This fluid, 'lymph' then travels to the collecting lymphatic vessels that transport the fluid to the lymph nodes. Lymph nodes act as a filter, allowing the lymph fluid to be screened by immune cells in the node for any potential threats. If a threat is identified, an immune response is mobilized, and immune cells exit by the efferent lymphatics. From start to end, the lymphatic system is essential to well-being. However, this same system that protects the body can also serve to disseminate cancer and facilitate progression.

Lymphatic vessels were traditionally viewed as maintaining a passive role in the immune response or were even excluded as a formal part of the immune system. Therefore, models of the lymphatics so far have focused primarily on fluid flow and biomechanics, as reviewed previously by Nipper & Dixon (2). However, new studies are highlighting the important roles that lymphatic endothelial cells play in presenting antigen to the immune system and regulating cell entry to the lymphatic network (3,4). Due to the lack of basement membrane, initial lymphatic vessels are highly responsive to interstitial fluid flow—a benefit that allows for easy immune cell trafficking (5). Lymphatics have now been implicated in antitumor immune responses, autoimmune diseases, and the regulation of inflammation (5). Indeed, lymphatics have been added to

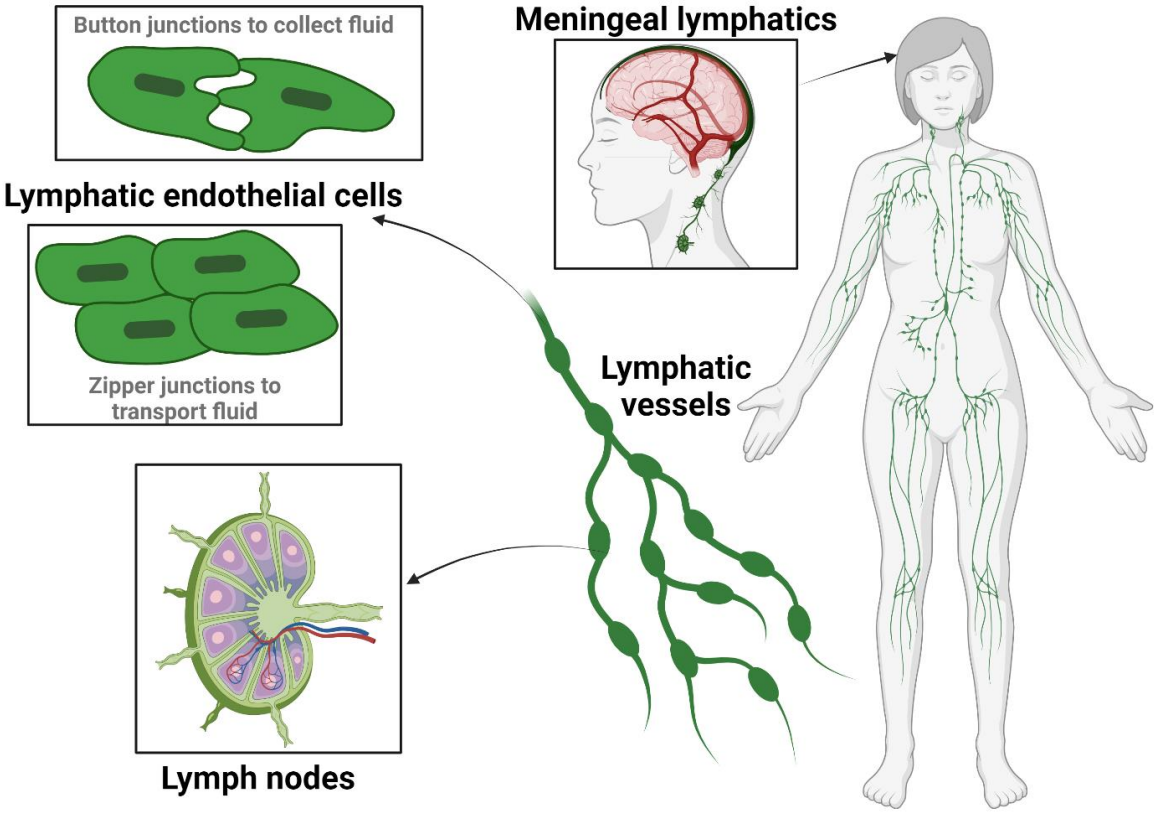

Figure 1.1. The lymphatic system runs through the body and drains to lymph nodes for immunosurveillance. *Created with biorender.com.*

cultures of breast cancer cells and mammary fibroblasts to recreate initial lymphatic–tumor cell interactions during metastatic spread, showing that lymphatic endothelial cells (LECs) reduce therapeutic efficacy (6). An emphasis on lymphatic-immune interactions is an essential step toward recapitulating immunity in vitro, with the eventual goal of modeling immunity during cancer growth. Within, we aim to develop lymphatic models to understand immune cell trafficking, tumor progression and dissemination, and off-target impacts of chemotherapeutics.

1.1.2 Fluid regulation

Lymphatic vessels are essential for maintaining fluid balance in the body. Within tissues, interstitial fluid is slowly moving in between cells, containing proteins and waste. Primarily sourced from leaky blood vasculature, multiple liters per day seep into the interstitium. Excess of this fluid is collected by lymphatic capillaries, becoming 'lymph'. Lymphatic capillaries, or

initial lymphatics, have a discontinuous basement membrane and have loose 'button' junctions, providing gaps of several microns to permit cell and fluid collection. Baluk et al demonstrated alternating VE-cadherin and CD31 staining along the borders of LEC-LEC contacts (7). Beyond VE-cadherin, tight junction proteins, such as claudin-5, demonstrate discontinuous expression at LEC-LEC interfaces (7). These gaps are utilized by antigen presenting cells, e.g. dendritic cells and macrophages, to travel to local lymph nodes. These dendritic cells travel for as long as one hour to reach the lymphatic capillaries (8), and are further stimulated by inflammation-induced increases in interstitial fluid flow (9) and CCL21 secretion from the lymphatics (10). In rat initial lymphatics, flow rates of approximately 14 μL/hour were measured (11). In human skin, flow rate was approximately 10 μm/s (12).

Next, fluid and cells travel through the collecting lymphatic vessels. Here, flow is pulsatile. Collecting lymphatic vessels are surrounded by smooth muscle cells that allow contraction and have periodic unidirectional valves with intrinsic pumping (13). Measurements of flow in collecting lymphatic vessels vary greatly from 50 μm/s to 1500 μm/s, depending on the location and size of the lymphatics as well as the measurement strategy (11,14,15). The collecting lymphatic vessels have continuous junctions, called zipper junctions, to retain lymph within the vessel for transport. Collecting vessels transport an estimated 8 liters a day (16).

Finally, lymph is drained to the lymph node. Within the lymph node, some fluid is reabsorbed by the blood vasculature (17). The rest, now screened and filtered, exits the lymph node via the efferent lymphatics and eventually returns to the blood circulation at the subclavian veins (18). It is estimated that about 8 liters become afferent lymph each day, and half of that is reabsorbed by the blood vasculature of the lymph node. Thus, approximately 4 liters per day are returned to the circulatory system by the efferent lymphatics (16).

1.1.3 Immunity and inflammation

Beyond fluid transport, immune cell trafficking is a key function of the lymphatic system. Immune cells must maintain migration between peripheral tissues and lymph nodes for immunosurveillance. Immune cells such as T and B cells begin in the circulatory system, explore peripheral tissues, and are drained by the lymphatics to the lymph node, where they search for antigens, exit, and begin the cycle again. Antigen presenting cells, such as the dendritic cells mentioned above, reach the 'end of the line' in the lymph node, but require the lymphatics to traffic there. Dendritic cells comprise only 10-15% of cells within the lymph. The vast majority are T cells (19). The function of T cells and B cells and the dynamics of their recirculation are further explored in section 1.1.4.

The function of the lymphatic system is intricately connected with inflammation. Characterized by redness, heat, swelling, and pain, inflammation is a key defensive response to threat by pathogens. Inflammation leads to enhanced drainage by the lymphatic vessels, partially due to increased interstitial fluid, and partially due to inflammatory chemokines that enhance lymphatic permeability (20). In an in vitro model, TNF-a, IL-6, IL-1B, IFN-y, and LPS all led to decreased barrier function in LECs (21). However, inflammatory mediators can also reduce lymphangiogenesis and lymphatic pumping frequency (22–24), proving the complexity of inflammation in regulating physiological functions. Indeed, lymphatic vessels respond to inflammation by altering chemokine secretion as well. CCL21 and CX3CL1 are secreted basolaterally, or into the tissue, by the lymphatics in response to inflammation, enhancing dendritic cell transmigration and trafficking to the lymph node (25–27). CXCL12 is also secreted by LECs in response to inflammation, enhancing lymphangiogenesis (28) and supporting dendritic cell trafficking via the CXCR4/CXCL12 axis (29). However, LECs secrete a multitude

of chemokines to direct immune cell trafficking, among which CCL1, CCL2, CCL5, CCL20, and CCL27 are listed (30,31). Beyond CXCL12, vascular endothelial growth factor C (VEGF-C), can also modulate inflammatory lymphangiogenesis to expand the lymphatic network and drainage (32).

Finally, the lymphatics are essential toward clearing up acute inflammation and returning to steady-state. Without adequate drainage, fluid buildup overtime can lead to edema, causing tissue dysfunction. An expanded lymphatic network has been shown to reduce inflammation-induced edema (33). Additionally, in a mouse model of chronic cutaneous inflammation, lymphatic activation via VEGF-C and VEGF-D significantly reduced chronic inflammation (34). Thus, the lymphatic system has been identified as a potential therapeutic target in diseases of chronic inflammation (35).

Lymphatic vessels themselves play a plethora of roles in inflammation and immune cell trafficking. However, a complete understanding of the lymphatic system and the immune response requires discussion of the lymph node, the crux of immunity.

1.1.4 Lymph node structure and function

All afferent lymphatic vessels lead to the lymph node. The human body has around 500 of them, each playing essential roles in immunosurveillance and adaptive immunity. Modeling the lymph node has been a major goal in the field of immunoengineering. However, the complexity of lymph node spatial organization and cell populations is challenging to recapitulate in vitro. As noted above, lymphatic vessels throughout the body collect excess fluid and waste from tissues. This lymph is then delivered via afferent lymphatic vessels directly into the lymph node for screening. Lymph is delivered to the subcapsular sinus, followed by the cortex, the paracortex, and the medulla, where it exits via efferent lymphatics (**Figure 1.2**). Each of these

zones is home to specific immune cells and specialized fibroblasts that siphon and guide lymph fluid throughout the node to be screened. Here, we will define the important physiology of each region.

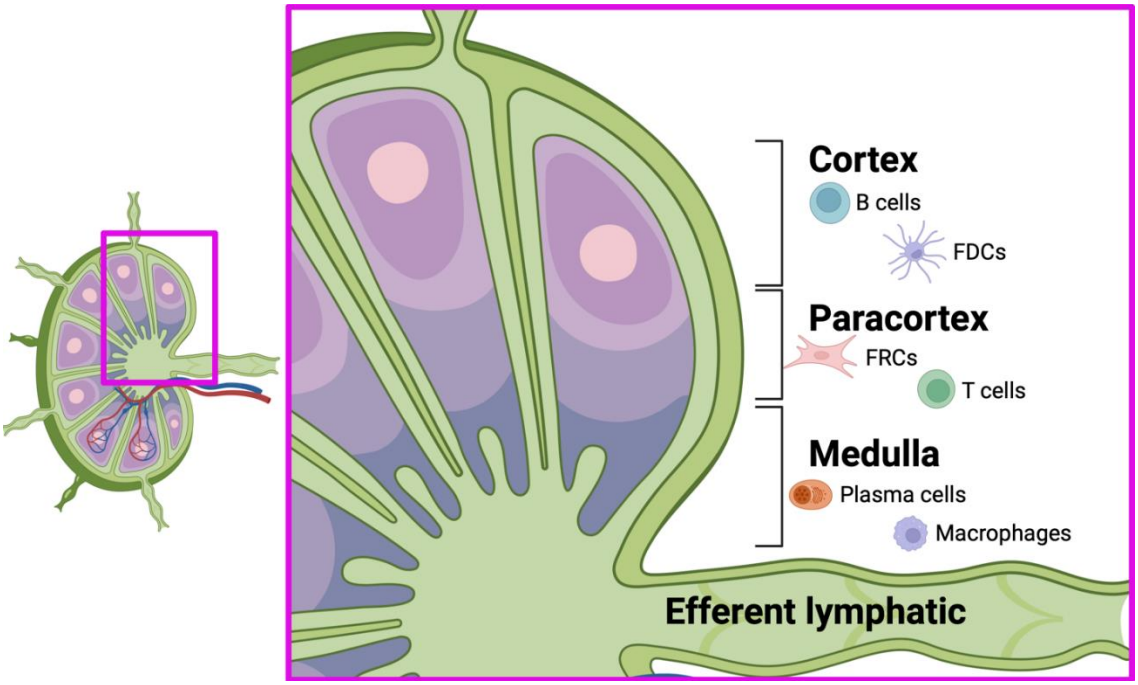

Figure 1.2. Lymph node structure. *The lymph node (LN) is divided into three main regions. The cortex consists mainly of B cells and follicular dendritic cells (DCs). The paracortex has fibroblastic reticular cells (FRCs) and T cells. The medulla contains plasma cells and macrophages. The LN drains out of efferent lymphatic vessels. Created with Biorender.com.*

The lymph node is encapsulated by dense collagen matrix, called the capsule. The subcapsular sinus (SCS), which receives lymph from outside of the node, is found between the capsule and the cortex. The SCS is lined with lymphatic endothelial cells and surrounds the entire LN, connecting to other sinuses in the node. Within the SCS, there are macrophages and dendritic cells (DCs) that capture antigens or pathogens and communicate with B cells in the cortex to initiate an effective immune response (36).

After reaching the SCS, the next region that lymph reaches is the cortex. The cortex is home to B cell follicles and is the seat of adaptive immunity. Antigens that are not captured by

SCS macrophages or DCs are transported in lymph to the cortex, where follicular DCs can step in. Follicular DCs capture and present antigens to B cells. Naïve B cells circulate throughout the body, traveling from LN to LN, spending about 24 hours in each in search of antigen (37,38). Within the LN, they home to the follicles and screen FDCs for antigens. Upon finding an antigen, B cells become activated, forming a germinal center and recruiting CD4+ helper T cells from the paracortex. After activation, B cells undergo final differentiation into one of three lineages. B cells can become short-lived plasmablasts that produce antigen-specific antibodies and are part of the immediate immune response. For lasting immunity, B cells can become antigen-specific plasma cells or memory B cells, which are both considered quiescent and long-lived. Antigen-specific plasma cells home to the bone marrow, where they reside and consistently secrete antibodies in preparation for another encounter with the same antigen (39). Memory B cells are found in the LN and in circulation, remaining quiescent until the antigen is confronted again (40). However, these B cell responses, and lasting adaptive immunity, are not possible without the contributions of T cells from the paracortex.

The paracortex is mainly defined by T cells and fibroblastic reticular cells (FRCs). FRCs form conduits out of extracellular matrix that guide ~10% of lymph into the paracortex (41). These conduits are made of various fibrillar and non-fibrillar collagens, as well as decorin, fibronectin, perlecan, laminins, vitronectin, and more (42). Though most dense within the T cell zone, the conduit network connects through the SCS and cortex as well (43). Flow rate from the cortex to the paracortex through conduits has been estimated at about 35 microns per minute (44), allowing inflammatory markers to reach throughout the LN and promote immune response.

T cell migration within the paracortex is modulated by FRCs via direct contact and chemokine secretion. FRCs maintain T cell survival via IL-7 (45) and control the proliferation of

T cells via the iNOS/IFNgamma pathway (46). The main T cell subsets found in the LN are CD4+ helper T cells and CD8+ cytotoxic T cells. T cells also circulate the body and LNs in search of antigen, spending between 12 and 24 hours in each LN (38,47,48). Upon reaching the paracortex, T cells migrate randomly, screening DCs for antigen. CD4+ helper T cells are estimated to screen 5000 dendritic cells per hour, migrating upwards of 10 microns per minute (49). CD8+ cytotoxic T cells are estimated to screen 500 DCs per hour, migrating between 10 and 30 microns per minute (50). After finding an antigen and becoming activated, CD4+ helper T cells proliferate rapidly and migrate to the germinal centers, where they assist in B cell activation and differentiation. Initial activation of CD8+ cytotoxic T cells also occurs via antigen presentation by DC, followed by interaction with activated CD4+ helper T cells to drive memory CD8 T cell development.

Finally, the medulla contains a large amount of plasma cells that secrete antibodies, macrophages, blood vessels, and the efferent lymphatics (51). Both naïve and activated T cells egress from the lymph node through this pathway, either to continue searching for antigens or to mount an antigen-specific attack.

The lymph node begins and ends with lymphatic vessels, with specialized regions in between that are organized and connected by specialized fibroblasts, such as the aforementioned FRCs. Yet, current lymph node models tend to focus entirely on immune cell interaction. In developing tissue engineered models of the lymph node, it is essential to consider not only the biological contributions, but the physical properties of the tissue as well.

1.2 In vitro modeling of the lymphatics

portions of this section are the author's original writing directly taken from: Suarez, Hammel*, and Munson, 2023, "Modeling lymphangiogenesis: pairing in vitro and in vivo metrics"* (52)

There are many important elements to creating an in vitro model that adequately recapitulates a tissue, including physical, chemical, and biological cues (53). Though in vitro

models may lack the full complexity of the in vivo environment, they allow for more precise control over the microenvironment and can reduce potential confounding factors. The process by which lymphatics expand and form new vessels is called lymphangiogenesis. This ability is a cornerstone of lymphatic models.

1.2.1 Cell sourcing

The first step toward developing in vitro models is sourcing the relevant cell types. Though lymphatics are found throughout the body, a few key primary sources are typically utilized for cell culture. Dermal LECs, isolated from human neonatal foreskin or adult skin, and lymph node LECs are commercially available. LECs can also be isolated from primary tissues using specific cell surface markers such as lymphatic endothelial hyaluronan receptor-1 (LYVE-1) (54), podoplanin/D2-40 (55), and VEGFR-3/Flt-4 (56,57). Nuclear prospero-related homeobox 1 (PROX-1) protein can also identify LECs (58,59). Other tissue sources for commercial LECs include human lung (60,61), rat mesentery (62), and mouse mesentery (63). Culturing primary LECs in vitro comes with a set of limitations. Like many primary cell types, primary LECs are limited in passage number, require specific cell seeding densities, may grow slowly, and require plate coatings of fibronectin or collagen which could alter cellular behaviors (64). Additionally, the shear stresses that may occur during standard passaging procedures can activate LECs (65,66). There is further evidence that LECs may dedifferentiate or have changes in transcriptional profiles in vitro due to a lack of important microenvironmental cues (67). Optionally, LECs can be immortalized for more stable and long-lasting cultures (68,69).

1.2.2 Metrics of in vitro lymphatic models

In vitro models of lymphatics can vary greatly in complexity from monolayers to explants. In 2D culture, simple metrics such as migration can easily be quantified using scratch

assays and tissue culture insert migration assays. A scratch assay is performed by growing a confluent monolayer of cells and then physically creating a “scratch” with a pipet tip and tracking cell migration into the empty space over time, as described by Liang et al (70). This technique is simple, inexpensive, and can be performed with any adherent cell type. Simple 2D cultures can also be used to quantify proliferation via bromodeoxyuridine (BrdU) and MTT (chemical name 3-(4,5-dimethylthiazol-2-yl)-2,5-diphenyltetrazolium bromide) assays (71). A tissue culture insert assay allows the quantification of cellular transmigration. Originally called the Boyden chamber assay, tissue culture insert assays are now a common methodology whereby cells are seeded as a monolayer or atop a layer of basement membrane on a porous membrane, with a chemoattractant placed in the media beneath (72). After a set amount of time, the number of cells that have migrated to the underside of the tissue culture insert can be quantified with a simple nuclear stain (73). The transmigration assay can also be adapted to examine 3D behaviors with hydrogel systems, interstitial fluid flow, and tumor microenvironment interactions (6,74–76). These models provide straightforward methodology for examining migration and proliferation, two outcomes involved in lymphangiogenesis.

A step up in complexity for in vitro models incorporates hydrogels or spheroids to observe lymphangiogenesis as the formation of vessel-like structures. First performed in 1998 by Kubota et al. (77), the tube formation assay involves plating endothelial cells on top of basement membrane extract (i.e., Matrigel) and has become ubiquitous for observing angiogenesis in vitro (78). The cells can readily adhere to the matrix and form tubular structures that resemble networks within 24 h. Additionally, LEC spheroids can be embedded within a hydrogel to observe how the cells invade the surrounding microenvironment, called the spheroid sprouting assay. This assay recapitulates lymphangiogenesis by allowing new sprouts to form from pre-

existing structures (79). Nascent work using self-assembled lymphatic networks in hydrogels is also underway (80,81), with a focus on microfluidic devices (69,82–89). Recent microfluidic models use hydrogel (often collagen)-laden polydimethylsiloxane (PDMS) with hollow channels for seeding lymphatic endothelial cells, called gravitational lumen patterning, and allow for flow through the lumen, which can be pressure-head induced or provided by pumps (69,84,87,90). In these devices, there is precise control of the microenvironment and mechanical forces experienced by cells in vitro. They are often paired with in silico models to examine chemokine diffusion and fluid transport (90–92). These devices are often the most physiologically relevant in vitro models but are not commonly paired with in vivo work.

Lymphangiogenesis can be modeled ex vivo using the lymphatic ring assay (LRA), where mouse lymphatic thoracic ducts are dissected and embedded into hydrogels for time-lapse imaging (93). This assay allows for bona fide lymphangiogenesis as the explant provides a mature lymphatic vessel from which new vasculature can sprout. An alternative ex vivo assay uses rat mesentery tissue with live imaging of lymphatic vascular development for 5 days (94). However, the inability to perform these assays with human lymphatics is a limitation of the current ex vivo systems. Mouse and human endothelial cells respond differently to inflammation (22) and anti-angiogenic drugs are more effective in mouse models than in human patients (95). Additionally, though many subsets of LECs have similar gene expression between mice and humans, there are some differences, such as the high expression of IL-6, MMP-2, and lysyl oxidase in humans but not mice, pointing to differences in basal inflammatory states and matrix remodeling mechanisms (96). Beyond migration and proliferation, the crux of many lymphangiogenesis-specific studies revolves around VEGF-C and -D and their receptors, VEGFR-2 and VEGFR-3. VEGF-C and -D can be quantified at the protein level with ELISA or

Western blot. The receptors can be visualized via immunocytochemistry or flow cytometry. These techniques are compatible with most in vitro assays. Further, LECs can be visualized using antibodies for LYVE-1, PROX-1, podoplanin, and CD31/PECAM-1, allowing the quantification of LEC morphology and junctions. It is important to note that CD31 is a better marker for LECs in vitro, as in vivo, CD31 expression is higher in blood vasculature than in lymphatic vasculature (97,98). Outside of lymphangiogenesis, functional LEC assays can include characterization of permeability, immune cell trafficking, and fluid transport, as discussed in recent reviews (99–101).

A critical gap in the literature is a lack of in vitro models of the lymph node that allow for the study of lymphangiogenesis. Tumor crosstalk and chemotherapeutics are known to cause lymphangiogenesis in the lymph node (6,102,103). As many tumors metastasize to the lymph node and evade the immune system, it is essential to develop physiologically relevant models. Many studies utilize animal models to recapitulate the complexity of immune response. However, mouse and humans show notable differences in their immune system and lymph nodes (104). An in-depth discussion of existing in vitro lymph node models can be found below in section 1.4.

1.3 Key considerations for lymph node engineering principles

This section is the author's original writing directly adapted from: Hammel et al 2022, "Engineering in vitro immune-competent tissue models for testing and evaluation of therapeutics" (53)

Models of immune tissues may provide superior insight into drug efficacy prior to in vivo testing, but creating such models is not trivial. The complexities of the immune system are difficult to recreate in entirety in vitro, and special care should be paid to parameters that can affect immune system function and outcomes. Most engineered systems consist of cells

embedded in some sort of biomaterial, either natural or synthetic, with the goal of recapitulating a physiological state. The specific components that exist within these systems vary significantly from application to application, but the design parameters are common when selecting specific elements for a model. In particular, appropriate biological, physical and chemical cues must be incorporated, as cell behavior can be impacted, for example, by chemical makeup of a matrix, the stiffness, porosity, and biodegradability (105). Thus, the selection of the biomaterial backbone is a major element of an engineered model, with most of these systems consisting of hydrogels. The hydrogel material also impacts immunomodulation, with the ability to enhance or reduce immune cell activation (106,107). Many reviews exist to summarize critical hydrogel properties (105,108–111). Here, we will summarize important design aspects of engineered models for drug screening in the context of immunity.

Table 1.1 Physical properties of the lymph node. *Adapted from Hammel et al 2022 (53).*

Tissue	***Stiffness (kPA)***	***Interstitial flow (µm/s)***	***Pore size (µm)***	***Refs***
Lymph node	0.12-9.5	0.02-0.2 (T cell zone; from computational model)	5-30	(41,112–116)

1.3.1 Matrix mechanics

Physical tissue properties such as the extracellular matrix (ECM) stiffness, permeability, and interstitial flow depend strongly on physiological state and have significant impacts on immune cell activation, proliferation, and function (117,118). Stiffness can be tested via shear rheometry or dynamic mechanical analysis and is typically reported in measures of Pascals (110). Within the lymph node, stiffness has been estimated from 0.12-9.5 kPa (115,116,119).

Many studies have demonstrated the effects of stiffness and other mechanical cues on immune cells. For example, Hickey et al engineered an artificial T-cell stimulating matrix that preserved T cell phenotype and function ex vivo with stiffnesses ranging from 0.2 kPa to 3 kPa. Tuning the stiffness of the engineered matrix had effects on T cells, with higher proliferation and stimulation in softer gels (120). Saitakis et al tested stiffnesses of 0.5, 6.4, and 100 kPa and found that altering stiffness modulated T lymphocyte migration, morphology, and cytokine secretion. Only the highest stiffness caused changes to T cell metabolic activity and cell cycle. T cell migration velocity and distance as well as cell spreading increased with increasing stiffness (121). Therefore, T cells recognize a wide range of stiffnesses in the body and alter their behavior accordingly; we refer the interested reader to a recent review on T cell mechanobiology (122). We note that stiffness can be both a chemical and physical cue, translating to the presentation of binding sites on matrices.

1.3.2 Fluid flow and immune cell function

Similarly, fluid flow also has impacts on immune cells, inducing proliferation, migration with or against the direction of flow, and immune cell polarization (1). In the lymph node, computational modeling has estimated interstitial flow to range from 0.02-0.2 μm/s (41). In vitro, antigen specific binding of T cells and dendritic cells is increasingly disrupted as shear stress is increased (0.01 to 12.0 Dyn cm^2), and significantly disrupted at high shear stress typically found in the arteries (120 Dyn cm^2) (123). Low levels of fluid flow (0.1–1 mm/sec) also increase lymphatic permeability and enhance dendritic cell migration through lymphatics (124). In vivo, it seems that much of the biological response to flow depends on linear velocity (length/time) and/or shear rate (1/s). While experimental fluid flow through hydrogels is often reported in

volumetric flow rates (volume per time), consideration of the linear flow rates may be important for cellular function.

1.3.3 Porosity modulates immune cell migration

Flow through a matrix is directly related to porosity. Hydrogels used for 3D culture are typically highly porous, which facilitates transport of oxygen, nutrients, and waste by flow and diffusion. Porosity is defined as the amount of pore space relative to the scaffold. Porosity can be measured through a multitude of methods, some of which include gravimetric methods, mercury porosimetry, liquid displacement, and scanning electron microscopy (109). Typically, pore size is measured via imaging, such as SEM or microcomputed tomography. In the lymph node, pore size varies widely by region, but has been reported between 5 and 30 microns (112–114). Porosity and pore size can affect cell proliferation, differentiation, and angiogenesis (109).

The ability of immune cells to deform and migrate through small pores is also dependent on porosity. Non-adherent immune cells typically utilize amoeboid migration, characterized by fast migration speeds, rounded cell shapes, and no adherence. Rather than relying on degrading the extracellular matrix, T-lymphocytes migrate along the matrix and squeeze through any existing gaps (125). Therefore, the porosity of a designed system must allow for immune cell migration or provide additional cell types to aid immune cells in highly dense networks.

1.3.4 Diffusion in engineered models

In an in vitro model, just as in vivo, mass transport of applied drugs, nutrients, and secreted signals has a significant impact on the observed efficacy. Diffusion and flow through a 3D matrix are directly related to porosity, as discussed above. In addition to these physical parameters, diffusion is also controlled by concentration gradients. In immune-competent models in particular, diffusion of cytokines is a critical aspect to consider. Indeed, a local cytokine niche

may form around cytokine producing cells, whose niche size is controlled by the competition between the rates of secretion, diffusion, and consumption of the cytokine (126). Understanding the mechanisms of cytokine diffusion are essential toward immune outcomes, where cytokines can guide migration, control inflammation, and regulate differentiation and apoptosis. The physicochemical properties of a 3D matrix can be tailored to match in vivo tissues for maximum physiological relevance.

1.3.5 Cell sourcing and experimental design

Fundamental to developing an immunocompetent model is choosing the required cell types and desired outcomes. As it is neither possible nor desirable to include every single cell type that is present in vivo, the cell types should be selected based on the desired functional output of the model. To screen innate immune functions, tissue-resident cells such as macrophages, natural killer cells, neutrophils, or dendritic cells may be required. For adaptive immunity, T cells and/or B cells are needed, as well as dendritic cells if antigen presentation is required.

Once the cellular components are chosen, it is necessary to identify a cell culture medium that supports the viability and function of all the cells in combination. Known as the ‘‘common media” problem, this is an ongoing challenge for any co-culture model. Like media choice, the sourcing of immune cells has great implications on in vitro models and can present unique challenges and opportunities. Donated human blood proves a readily available source of circulating white blood cells. Large quantities of these cells can also be obtained from leuko-reduction collars, which are discard products after platelet donation via apheresis (127). Donated white blood cells contain a mixture of cell types (e.g. T cells, B cells, granulocytes, monocytes) in a mixture of activation states (e.g. naive, effector, and memory T cells) (128,129), a limitation

that must be acknowledged or else accounted for by purification of the cells prior to use in the model system. Furthermore, unlike cell lines or even primary fibroblasts, naive lymphocytes, and many other immune cells, do not proliferate in culture. Thus, they must be obtained fresh every few days or must be treated with a mitogen to induce proliferation and activation. When working with primary human cells, it is not uncommon to observe large (e.g. 10-fold) variations in response to stimulation from donor to donor, which means that each experiment must be conducted with internal (same-donor) controls or else powered with a large number of replicates to detect differences between treatment conditions. Beyond immune cells, when screening potential therapeutics, the type and source of other cell types, such as tumor cells or stromal cells, also impacts results.

Finally, sex-matching is an interesting variable to consider, whose effects on 3D models of immunity are not yet well understood. The potential for sex-matching in vitro models is a growing aspiration in the field. As reviewed by Klein and Flanagan, sex differences in immune system function have been observed pre- and post- puberty, including differences in autoimmune disorder occurrence, infectious disease susceptibility, and responses to vaccination (130). Sex hormones regulate innate immune cells and affect susceptibility to viral infection among other impacts. Human females have higher antigen-presenting cell efficiency, higher macrophage activation, higher T cell proliferation, greater numbers of B cells, and higher antibody production. Human males have higher pro-inflammatory cytokine production, larger thymuses, and greater numbers of natural killer cells (130). Thus, it may be possible to detect sex differences in the immune response of 3D models if all cells are sourced from donors of the same sex.

1.4 Existing models of the lymph node

portions of this section are directly taken from Hammel et al 2021, "Modeling Immunity In Vitro: Slices, Chips, and Engineered Tissues" in the Annual Review of Biomedical Engineering

1.4.1 Organoid technology

Interestingly, engineered tissues for the study of immunity have largely focused on replicating specific functions, as compared with other engineered systems that focus on tissue structure (131). As such, lymph node organoids are designed after organic development from precursor cell types and aim to mimic specific functions, such as antibody production. These organoids provide a platform to control the cell and matrix elements of the microenvironment around cultured immune cells and to better replicate in vivo conditions, although they usually do not incorporate fluid flow. A 2017 study by Purwada & Singh (132) produced ex vivo immune organoids, consisting of B cells from mouse spleen, that replicated the germinal center reaction of secondary lymphoid organs. The ECM was designed to mimic in vivo conditions by using cross-linked, RGD-presenting gelatin. In this immune organoid platform, the naive B cells were successfully differentiated into the germinal center phenotype and were capable of antibody class switching. Further, they were more proliferative and viable compared with 2D systems, providing a successful platform to study B cell development in secondary lymphoid organs (132). This study demonstrates the advantages of organoid technology: allowing precise control of ECM and cell–cell contacts to replicate in vivo immune organs.

1.4.2 Bioreactors

Adding another layer of complexity to immune organoids, bioreactors introduce the element of flow. The HuALN (human artificial lymph node) bioreactor, developed by Giese et al (133), is used extensively as an in vitro model of the lymph node. The HuALN incorporates several cell types (T cells, B cells, DCs), a hydrogel matrix, and micro-organoid structures. It has

enabled reproduction of functions such as antigen-specific antibody production and proinflammatory and anti-inflammatory cytokine secretion (133). Another bioreactor system—designed for bone marrow cultures—was adapted to culture immune cells isolated from tonsils. Immune cells including monocytes, DCs, B cells, and T cells were viable over several weeks without the addition of specific growth factors, produced antigen-specific antibodies, and self-organized into cell-specific aggregates (134). These results demonstrate the importance of fluid flow to immune function.

1.4.3 Hydrogel systems

Despite being a quintessential tissue engineering approach, cells in hydrogels have been limited in their use as models of the lymph node. Interestingly, 3D hydrogels have been mainly applied to modeling fibroblastic reticular cells in the T zone of the lymph node. In vivo, T zone FRCs deposit and remodel ECM to guide lymphocyte migration and secrete CCL19 and CCL21 to direct immune cell interaction. Tomei et al. (135) encapsulated FRCs in type I collagen and Matrigel on macroporous polyurethane scaffolds and applied interstitial flow (1–23 μL/min). This 3D in vitro system recapitulated the morphology of FRCs in vivo and confirmed the importance of flow for lymph node function, showing that flow enhanced FRC organization, and in its absence, the FRCs did not produce CCL21 (135). Since that study, more work using 3D hydrogels to model the T zone and stromal cells of the lymph node has been published (136,137), validating the benefits of a 3D matrix format that is less dense than organoid cultures. In a patient-specific model developed by Votanopoulos et al. (138), matched lymph node and melanoma cells were aggregated together into immune-enhanced patient tumor organoids (iPTOs) for testing cancer drug efficacy. The iPTOs were able to replicate 85% (six out of seven)

of patient immune responses. The iPTOs were then used to activate naive T cells before transfer to melanoma-only tumor organoids, where they were able to promote tumor cell death.

1.4.4 Pre-clinical models

Apart from bioreactors and 3D hydrogels, the modular immune in vitro construct (MIMIC®) system provides a sophisticated way to recapitulate patient-specific immune response (139). The MIMIC system has four components: a leukocyte module, a peripheral tissue equivalent (PTE) module to simulate innate immune responses, a lymphoid tissue equivalent (LTE) module to simulate adaptive immune responses, and a functional assay module. In the first module, leukocytes are collected from donors and cryopreserved. In the PTE module, human umbilical vein endothelial cells are cultured to confluence above a layer of collagen, after which donor peripheral blood mononuclear cells are applied and differentiated into DCs, APCs, and macrophage-like cells. In the LTE module, DCs, follicular DCs, T cells, and B cells are applied sequentially. Finally, the functional assay module is customized for each study to confirm how effective the immune responses from the PTE and LTE modules are against the antigen (139). Typically used in vaccine development, MIMIC incorporates multiple elements of immunity, is highly patient-specific, and serves as a useful in vitro clinical trial system.

1.4.5 Toward a spatially organized lymph node model

So far, engineered lymph node models have focused on recapitulating immune function and have proven successful. Recently, great strides have been taken toward developing spatially organized lymph node models. Mazzaglia et al developed a murine lymph node on chip, designated “eLN” with FRCs, LEC-lined channels, and distinct positioning of T and B cells. The eLN demonstrated naïve immune cell activation upon stimulation with phorbol 12-myristate 13-acetate (PMA) and ionomycin. With immune cells that recognize ovalbumin, the eLN was able

to mount an antigen-specific response (140). Emphasizing structure in future human models will enable the investigation of lingering biological questions about lymph node structure and function.

The models discussed above, such as organoids consisting of B cells and fibroblasts, 3D scaffolds with FRCs and T cells, and bioreactors consisting of B cells, T cells, and DCs are important and useful models. However, limited work has been done examining how the stromal cells, namely the FRCs and LECs, contribute to immune response. No human model has incorporated both FRCs and LECs, much less added immune cells and interstitial fluid flow. To answer questions of crosstalk, an ideal model of the lymph node stroma will include: spatial separation of cell types, sustained IFF, fibroblastic reticular cell networks, an intact lymphatic endothelial cell barrier, and demonstrate immune cell migration and egress capabilities.

1.5 Applications of a lymph node stroma model in basic science and pathophysiology

1.5.1 Modulating fluid flow

A spatially organized model of the lymph node stroma will have extensive applications in basic science and normal immune function. The importance of interstitial flow to lymph node function is well understood, however, experimental manipulation of IF in vivo is not trivial. As mentioned, a plethora of computational models have been developed to study flow in the lymph node (41,141). Outside of this, advanced imaging techniques such as dynamic contrast enhanced magnetic resonance imaging, computed tomography, Doppler optical coherence tomography, near-infrared, chronic lymph node windows, and non-invasive fluorescence imaging have been used to track flow in lymph nodes (14,142–147). To actually manipulate fluid flow in vivo, afferent lymphatics are cannulated to control perfusion (148,149). However, the small scale of

fluid movement through the conduit system in the LN parenchyma makes it challenging to visualize and quantify using these methodologies (150,151). Tomei et al established the impact of IF on FRCs in an engineered model (135). However, many questions remain about how fluid dynamics in the LN parenchyma impact the efficacy of the immune response. Developing an in vitro platform where magnitude and duration of IF can be easily tuned would be of great importance to understanding this relationship. Further, precise control of included cell types allows for the examination of cell-cell crosstalk in cases such as immune cell trafficking. Understanding how T cells interact with and migrate on the LN stroma under differential flow rates will provide extensive insight into how flow alters immunity.

1.5.2 Modeling cancer metastasis and progression

Further, this model will have applications in pathophysiology. In almost every disease state, the immune system and the lymph nodes respond. The lymphatics are implicated in primary and secondary lymphedema, rejection of transplanted organs (152), and cancer progression (6), and are suspected to be involved in Crohn's disease, obesity, atherosclerosis, and cardiovascular disease (153). Previous work in the Munson Lab has established that lymphangiogenesis can support breast cancer growth and spread (6).

During breast cancer progression, the first regions of metastasis are generally the regional lymph nodes that drain the tumor. In 1889, Stephen Paget advanced the seed and soil hypothesis – that cancer cells may spread throughout the body, like seeds, but will only grow in suitable "soil" e.g., tissues (154). The question of why the lymph node is suitable "soil" has been of great interest. Lymph node metastasis is the strongest prognostic factor in breast cancer survival rates (155,156) and can precede distant metastasis to other organs. Regional lymph nodes receive waste, in the form of lymph from local tumors, that contains proteins that modulate the lymph

node microenvironment (157). Tumor cells can use this route of drainage for a direct path to the lymph node. Further, LNs secrete ligands, such as CXCL12, that enhance the metastasis of CXCR4+ or CCR7+ tumor cells (158–160), though there are a multitude of alternate mechanisms in the LN to promote metastasis (157). Though one would expect the lymph node, a linchpin of immune response, to be a harsh environment for cancer cells, the pre-metastatic lymph node exhibits immunosuppression. Tumors are also adept at hijacking the immune system to support its growth. Therefore, tumor cells are able to condition the lymph node and utilize the node's secreted factors to migrate toward it, where a hospitable environment for growth and dissemination is found.

Further, increased interstitial flow is associated with cancer spread (161,162). Tumors have elevated interstitial pressure, driving outward flow and enhancing lymph transport. Breast cancer specifically has been shown to have increased invasion with interstitial fluid flow in vitro (163–166). Therefore, this enhanced IFF may support tumor migration to the lymph node. Further, the lymph node exhibits increased flow during inflammation. However, the dynamics of breast cancer metastasis and interstitial flow within the lymph node are not yet understood, particularly in the context of other stromal cell types, such as FRCs.

1.6 Looking to distant lymphatic vessels in the central nervous system

1.6.1. Overview of the meningeal lymphatics

Beyond the lymph node, models of the distant lymphatics will also prove useful, as cancer metastasis can occur in distant parts of the body, and many disease states cause systemic dysfunction. One key lymphatic system is the meningeal lymphatics, a field of intense study since their rediscovery in 2015 (167,168).

The meninges are fluid filled layers of tissue in the central nervous system (CNS) that protect the brain and play many roles in homeostasis. There are three meningeal layers – going from outermost to innermost, they are the dura mater, the arachnoid mater, and the pia mater. Meningeal lymphatic vessels (MLVs) are primarily found in the dura, where they track along the transverse and superior sagittal sinuses. Vascular smooth muscle cells on the sinuses provide VEGF-C to maintain the MLVs (169). The meningeal lymphatics drain cerebrospinal fluid from the meninges, delivering it to the cervical lymph nodes in the neck for CNS immunosurveillance. MLVs demonstrate similar physiology to initial lymphatic vessels elsewhere in the body. The meninges are a reservoir for immune cells and the meningeal lymphatics are implicated in the trafficking of these cells. If this pathway is commonly utilized for cell trafficking, it stands to reason that it could be commandeered by cancer cells.

1.6.1. Differences between meningeal and peripheral lymphatic vessels

Interestingly, though peripheral lymphatics systems develop in the embryo from venous vasculature, the MLVs arise post-natally (169). Additionally, MLVs respond to VEGF-C, but not VEGF-D, differing from the peripheral lymphatics (169). However, MLVs do express the ubiquitous lymphatic markers Prox1, VEGFR3, LYVE-1, and CD31 (167,168). Indeed, MLVs are most similar to initial lymphatics, with button junctions, a discontinuous basement membrane, and a lack of surrounding smooth muscle cells (168,169). The meningeal lymphatics are also considered less extensive than other similar surveilling lymphatic systems. Many questions still remain about how the meningeal lymphatics regulate transport in the brain, both in steady state and during CNS disease.

1.6.2. Existing models of the meningeal lymphatics

Since their discovery, studies of the meningeal lymphatics have been mostly mouse model-based (170–172). These studies have implicated the meningeal lymphatics in diseases such as Alzheimer's (170), traumatic brain injury (171), and brain cancer (172,173). Interestingly, studies have begun examining how meningeal lymphatics are involved in cancer treatment response and how they can be augmented to improve anti-tumor immunity. Disruption of meningeal lymphatic vessels in mice impaired the efficacy of radiotherapy, while VEGF-C overexpression enhanced efficacy (174). Enhancement of meningeal lymphatic drainage has been proposed as a treatment mechanism for all of the aforementioned diseases. However, the study of meningeal lymphatics is still in its infancy. The field as a whole is making rapid progress in mouse models, but studying this system in humans is not trivial. Thus, sourcing human cells and developing physiologically relevant in vitro models will provide an additional tool in this burgeoning field.

The benefits of in vitro models are endless, including high throughput, high potential for experimental manipulation, and speed of study. An ideal model of the meningeal lymphatics would include both identified cell types, the LECs and the meningeal fibroblasts, and would be able to transport fluid and immune cells. This model could then be applied toward CNS metastasis. Breast cancer specifically is known to metastasize to the brain, frequently the parenchyma (175) but at times, the leptomeninges (176). With the known fact that breast cancer cells travel through the lymphatics, this could be a path for breast cancer to metastasize to the CNS. Therefore, this model could be a testing ground for understanding breast cancer CNS metastasis. Further, systemic chemotherapy is not confined to the impacted area, and healthy tissues are exposed to the toxic chemotherapy as well. Patients undergoing systemic

chemotherapy often report cognitive issues, called “chemo brain.” Understanding how systemic chemotherapy impacts distant lymphatic systems may contribute to the knowledge and understanding of side effects and development of chemoresistant metastases elsewhere in the body.

1.7 Novel lymphatic stroma models for fluid and cell transport

Within, we present two novel models of the lymphatic stroma. First, a model of the lymph node stroma, consisting of an FRC-laden hydrogel atop a LEC monolayer. In Chapter 2, we will explore how interstitial fluid flow alters the LN stroma and T cell retention and egress. In Chapter 3, we will apply the model toward examining breast cancer metastasis and tumor burden in the lymph node, taking a look at how tumor presence alters transport. Second, we present the first in vitro model of the meningeal lymphatics. In Chapter 4, we will utilize this model to examine off-target effects of systemic chemotherapy, immune cell transmigration, and CNS leukemia. Together, these models provide a springboard for furthering the understanding of lymphatic stroma in health and disease.

CHAPTER 2

ENGINEERED LYMPH NODE STROMA MODEL FOR EXAMINING INTERSTITIAL FLUID FLOW

2.1 Summary

The lymph node is the seat of adaptive immunity, filtering lymph and providing constant immunosurveillance. Lymph flows through the lymph node via extracellular matrix conduits that are maintained by fibroblastic reticular cells (FRCs) and exits the lymph node via efferent lymphatics. Within the lymph node parenchyma, dense populations of T cells are constantly migrating and recirculating to search for antigens. The flow rate in the lymph node can change drastically with inflammation. However, the effect of interstitial flow on the lymph node stroma and T cells is not well understood. Herein, we sought to develop a spatially distinct model of the lymph node stroma. Our model consists of a monolayer of lymphatic endothelial cells on the underside of a tissue culture insert to represent the efferent lymphatics, and an FRC-laden hydrogel within the tissue culture insert to represent the parenchyma. We examined static conditions and two flow rates, 0.8 µm/s and 3.0 µm/s, to represent normal flow and pathological flow, respectively. Within, we demonstrate that the LN stroma model responds to 3.0 µm/s interstitial flow by enhanced proliferation and networking by FRCs and disruption of LEC barrier integrity. Interestingly, these effects were largely mitigated in the presence of T cells, which showed decreased egress with interstitial flow. However, flow-induced increases in cytokine secretion were consistent with and without T cells. We further demonstrated that activated T cells secrete more interferon-gamma in response to 3.0 µm/s interstitial flow. Overall, our work has established a LN stroma model that is responsive to interstitial flow and can be tailored to experimental questions around T cell crosstalk and migration.

2.2 Introduction

Developing human immunocompetent engineered models is a crucial next step toward understanding disease progression and enhancing pre-clinical drug screening (53). Lymph nodes

(LNs) are an essential part of the immune system, providing immunosurveillance of the lymph and mounting antigen-specific responses. Thus, immunocompetent models of the LN have broad applicability in areas such as anti-tumor immunity, viral infections and vaccinations, and autoimmune disorders. Within the LN, a network of fibroblastic reticular cells (FRCs) guides T cell migration and enwraps conduits made of extracellular matrix to guide lymph fluid through the node for screening. The LN further contains densely packed immune cells, including helper CD4+ T cells and cytotoxic CD8+ T cells. To provide immunosurveillance, T cells consistently recirculate from the blood to LN and back to blood on the scale of approximately 12 to 24 hours (38,47,177). Within the LN, T cell migration is guided by FRCs via direct contact and chemokine secretion. If a naïve T cell does not encounter an antigen, it will leave the LN through the efferent lymphatics and continue to circulate. This constant turnover allows for rapid detection of antigens. However, the contribution of physical forces, such as interstitial fluid flow, on the dynamics of T cell recirculation is not well understood.

The LN is organized to receive and sample lymph fluid, resulting in constant interstitial fluid flow (IFF) that bathes both the stroma and T cells. After filtering through the FRC-mediated conduit system, fluid subsequently leaves the lymph node through transmural flow to the efferent lymphatics. The rate of IFF drastically increases during inflammation, where the inflammatory state also reduces T cell egress. The impact of IFF on fibroblasts outside the lymph node is well established, with increased alignment (178–180), proliferation (181,182), motility (183,184), and upregulation of matrix related genes and matrix remodeling (182,185,186) all widely reported. However, only one study has observed FRC response to IFF, demonstrating enhanced networking and gene expression for chemokines (135). Additionally, lymphatic endothelial cell monolayers show enhanced permeability in response to transmural flow (187),

mediated via the loosening of “button” junctions. Though the impact of IFF on lymphocytes is understudied, shear stress has been shown to induce migration in the opposite direction of flow (188) and altered proliferation in T cells (189). Thus, enhanced IFF could modify the behavior of the stroma and T cells to promote the adaptive immune response. Understanding how biophysical cues (e.g. flow, stiffness, matrix density) impact immune cell migration upon arrival to the LN is key toward developing immunocompetent models. Development of lymph node stroma models that could answer these questions is underway, with spatially organized murine models (140) or human models focused on LECs (190) or FRCs (135–137,191). However, no human model has been developed that incorporates both of these stromal components and interstitial fluid flow.

Herein, we sought to develop a spatially organized model of the LN stroma to understand IFF-mediated stromal changes and T cell retention vs egress. Our model consists of FRC-laden hydrogel, representing the T cell zone, above a monolayer of LECs on the underside of a tissue culture insert, representing an efferent lymphatic. By combining collagen and hyaluronic acid, this hydrogel model is capable pressure head-driven IFF. CD4+ and CD8+ T cells can migrate through the FRC region and egress across the LEC monolayer, providing a vital tool toward understanding recirculating T cell dynamics.

2.3 Methods

Cell culture

Human lymph node lymphatic endothelial cells (LECs) (Sciencell) were cultured on fibronectin coated flasks in VascuLife® VEGF-Mv Endothelial Complete media, containing 5% fetal bovine serum and additional supplements as provided by the supplier (Lifeline Cell Technology). Human lymph node fibroblasts (FRCs) were cultured on poly-L-lysine coated

flasks in fibroblast medium with 10% fetal bovine serum and 5% fibroblast growth supplement (Sciencell). All cells were maintained at 5% CO^2 and 37°C.

T cells were isolated from leukocyte reduction system cones (STEMCELL Technologies) using a density gradient separation followed by immunomagnetic negative selection for target populations (STEMCELL Technologies). Donor age and sex are provided by the vendor. T cells were maintained in Immunocult T Cell Expansion Medium supplemented with 10 ng/mL interleukin-7 (R&D), interleukin-2 (Gibco), or with Immunocult Human CD3/CD28 T cell activator (STEMCELL Technologies).

PhotoHA/collagen hydrogels

Methacrylated hyaluronic acid (PhotoHA) (Advanced Biomatrix) was reconstituted at 10 mg/mL in sterile 1X phosphate buffered saline (PBS) and stored at 4°C for up to one month. The photoinitiator, lithium phenyl-2,4,6-trimethylbenzoylphosphinate (LAP), was reconstituted at 17 mg/mL in sterile 1X PBS and stored at 4°C for up to two weeks. A 0.5% collagen solution was made on ice using high concentration collagen I from rat tail (Corning), 1N NaOH, water, and 10x PBS. LAP was added to PhotoHA at 0.02 times the volume of PhotoHA. Collagen solution, PhotoHA solution, and cell culture media was combined to give a final concentration of 0.4% PhotoHA and 0.2% Collagen. The hydrogel solution was first photocrosslinked at 50 mW/cm^2 for 45 seconds with 385 nm light (Thorlabs Collimated LED 1700 mA controlled by Thorlabs DC2200 High-Power 1-Channel LED Driver) and then placed in a 37°C incubator for 30 minutes for thermal crosslinking of collagen.

Pressure head driven interstitial flow

Darcy's Law was used to calculate pressure head height vs interstitial flow. To create interstitial fluid flow, media was applied atop the hydrogel to generate a pressure head as

previously described (192,193). For static conditions, 700 μL of media was placed in the lower chamber of a 12 well plate, and 100 μL was placed atop the gel. For 0.8 μm/s flow, 100 μL of media was placed in the lower chamber of a 12 well plate, and 700 μL was placed atop the gel. For the high flow condition, 12mm fluorinated ethylene propylene clear tubing was cut and secured onto the tissue culture insert (**Figure 2.1A)** and 2.7 mL is placed atop the hydrogel. To accommodate tubing and maintain sterility, lid raisers in the dimensions of a 12-well plate were 3D printed and sterilized with ethanol (**Figure 2.1.B-C**).

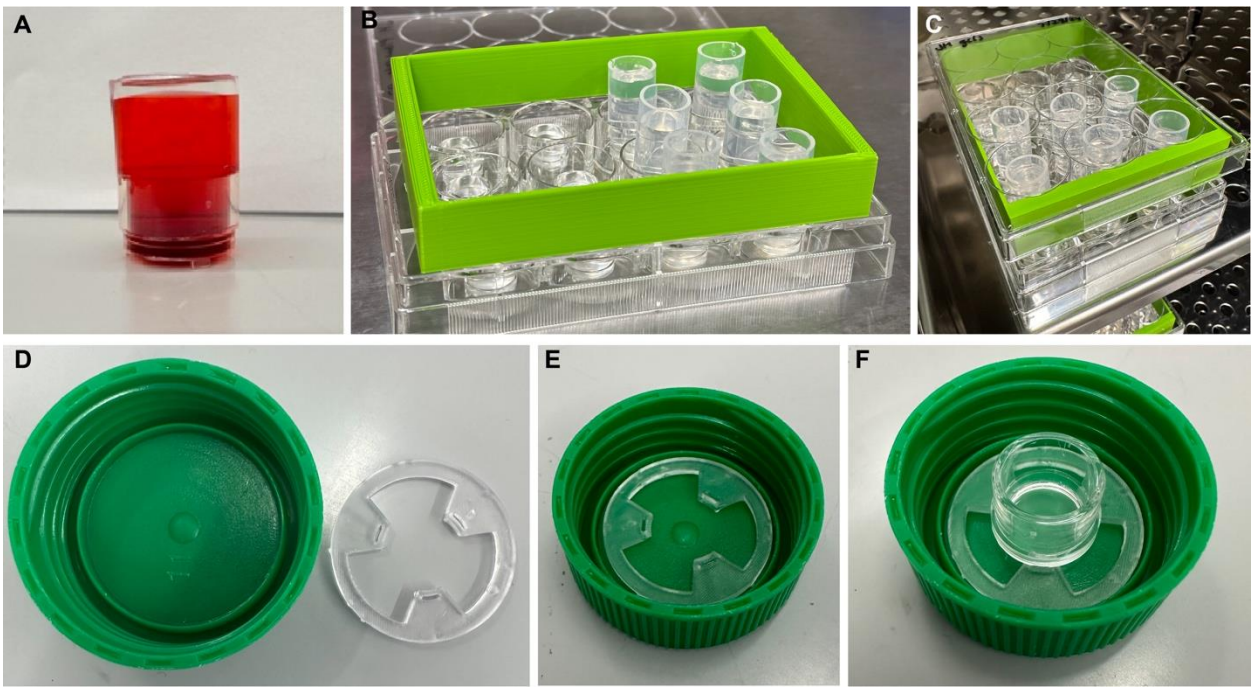

Figure 2.1. Custom apparatuses for pressure heads and flow rate analysis. *PE50 tubing secures onto the tissue culture insert with no leaks (A). 3D printed lid raisers to the specifications of a 12 well plate (B-C) maintain sterility in the incubator. A 3D printed insert with slots for tissue culture insert legs is created to the specifications of a 50 mL conical tube lid (D-F).*

Flow-mediated egress assays

CD4+ and CD8+ T cells were labeled with CellTrace™ CFSE (Invitrogen) and embedded in PhotoHA/collagen gels as described above at 500,000 per mL of hydrogel. AIM-V universal media was used to create pressure heads, supplemented with IL-7 or IL-2 for naïve T

cells and CD3/CD28 immunocult activator for activated T cells. After 24 hours, flow through media was collected and analyzed via flow cytometry.

LN stroma model

At confluence, LECs were passaged with Accutase and seeded in Vasculife complete on the bottom of 12-mm tissue culture inserts with 8 µm pore size (Corning) at 50,000 per insert for 2 hours (6,165,194). Vasculife was added and the LECs were cultured for 48 hours to reach confluency. Next, FRCs were resuspended in PhotoHA-collagen solution formulated as described above and photo- and thermally crosslinked in the LEC-coated tissue culture inserts. The LN stroma model was cultured for 24 hours prior to experimental manipulation. For flow studies, pressure heads were applied as described above and LN models were cultured for 24 hours prior to fixation with 4% paraformaldehyde. For T cell studies, CD4+ and CD8+ T cells were labeled with 1 µm CFSE and 50,000 were added to each LN model in the media above the hydrogel under designated flow conditions. After 24 hours, flow-through media was collected for flow cytometry and models fixed for staining and imaging.

Flow cytometry

Flow through media was spun down at 0.3 rcf for 10 minutes. Then, cell pellets were resuspended in PBS and transferred to 96 well plates. For viability staining, LIVE/DEAD™ Fixable near IR reactive dye (Invitrogen) was diluted 1:1000. Cells were spun down at 2000 rcf for 1 minute and resuspended with viability dye for 15 minutes on ice. Cells were spun down again and washed with flow cytometry buffer consisting of Hank's balanced salt solution (HBSS) + 3% bovine serum albumin (BSA) twice before flow cytometry is performed on a Guava Cytometer. Analysis is performed via GuavaSoft. Singlets were gated using forward

scatter height and area. T cells were identified via viability and CFSE staining. The concentration of T cells was then extrapolated to an estimated total count to report percent egress.

MRI flow analysis

Tissue culture inserts with tissue engineered systems are secured in a 50 mL conical tube cap (**Figure 2.1D-F**). To allow interstitial flow, 100 μL of PBS is added beneath the tissue culture insert membrane. Tissue culture inserts are then stabilized and positioned in the MRI scanner. PE50 tubing was secured on the top of the tissue culture insert to infuse Gadolinium-DTPA via a syringe pump (Harvard Apparatus, Pump 11 Elite) later. Pre-contrast T1 images were taken as a baseline using a FLASH sequence with the following parameters: TE 3.0 ms, TR 150 ms, flip angle 30°, FOV 19.2 × 22.0 mm, matrix 192×220, slice number 9, slice thickness 0.8 mm, number of average 7, total scan time 3 mins. Then, 1:100 Gadolinium-DTPA (BioPal) was injected above the hydrogel at 1.0 ml/min flow rate. After 30 seconds, T1-weighted images were taken using the same parameters as baseline T1 images for 4 total post-contrast images. Spatial and temporal resolution were recorded for each imaging session. This dynamic series of contrast enhanced MRI images (DCE-MRI) captures the movement of the Gd-based contrast agent through the hydrogel over time. Pixel brightness corresponds to contrast agent concentration, allowing analysis of fluid movement within the substrate. We employ a physics-based method by solving the inverse problem of the diffusion-advection equation to estimate advection and diffusion parameters from observed pixel intensity changes, resulting in a vector fluid flow field of the hydrogel. To do this, we used "Lymph4D," a previously published and openly available tool (195). This approach enables analysis of fluid flow properties such as divergence, where lower divergence indicates more uniform flow and less spreading or expansion of the measured fluid.

Proliferation assay

After 18 hours, 10 μM EdU was added to culture media for the final 6 hours. Gels were fixed in 4% formaldehyde in 1x PBS for 1 hour. Detection was performed using Click-iT™ EdU Alexa Fluor™ 488 dye as specified by the manufacturer (Invitrogen). The number of EdU+ nuclei and the total number of nuclei, as detected by DAPI, were hand quantified in FIJI to report % proliferation.

Cytokine analysis

Media was flash frozen in liquid nitrogen and stored at -80°C until assays were performed. Hydrogels were removed from the tissue culture insert with forceps and degraded with collagenase and dispase for 30 minutes at 37C while shaking. Degraded hydrogel solution is then stored at -80°C until use. Interferon gamma was detected using an enzyme-linked immunosorbent assay as specified by the manufacturer (Biolegend). A four parameter logistical curve was used to determine IFNgamma concentration in samples (myassays.com). IL-6, CCL2, CXCL8, and CXCL12 were detected using a ProCartaPlex Multiplex Immunoassay (ThermoFisher). Quantification was performed on a Luminex xMAP. A five parameter logistical curve was generated via ThermoFisher ProcartaPlex Analysis App to determine concentrations.

Immunofluorescence

To visualize cell organization, we performed immunocytochemistry on fixed LN stroma models for F-actin and CD31. LN stroma models were fixed in 4% formaldehyde for 1 hour. Blocking with donkey serum in 0.01% triton x-100 was performed for 6 hours at room temperature (RT) on a rocker. LN stroma models are then incubated with 4 μg/mL sheep anti-human CD31 (R&D) in blocking solution overnight at 4°C on a rocker. LN stroma models were rinsed with PBS three times for 20 minutes on a rocker at RT. Next, gels were incubated with 5

µg/mL donkey anti-sheep AlexaFluor 647 in blocking solution overnight at 4°C on a rocker, followed by a rinse as previously described. Finally, gels were stained with 1:400 Alexa Fluor™ 488 Phalloidin and DAPI for 6 hours at RT on a rocker. LN stroma models were rinsed and stored in PBS until imaging.

Imaging

Immunostained LN stroma models were placed on a glass coverslip to allow imaging of the intact model. For whole-gel imaging, Z-stacks with a 10 µm step size were taken on a Nikon Spinning Disk with a 10X objective. For LEC monolayers, a 20X objective was used. Three regions of interest were captured for each technical replicate. For second harmonic generation, an LSM 880 confocal microscope and 20X objective were used as previously described (196).

Image quantification

Image analysis was performed in FIJI (197). Total f-actin+ area was used to determine the FRC distribution throughout the model. CD31+ area was used to determine LEC coverage of the tissue culture insert. CD31+ junctions were analyzed for disruption by counting LECs with discontinuous cell-cell contact. Portions of the monolayer where LECs were missing due to death were not considered to be disrupted junctions. For T cell counts, FIJI's analyze particle function was used.

Gene expression

LN stroma constructs were removed from tissue culture inserts with forceps and placed into Trizol. RNA was isolated via phase separation and purified via Quick-RNA MicroPrep Kit including the optional DNase treatment (Zymo Research). Fifty ng of RNA was converted to cDNA using the QuantiTect Reverse Transcription Kit (Qiagen). Gene-specific TaqMan assays (ThermoFisher Scientific) were used to quantify expression (**Table 1**) using 2 µL of cDNA

template and TaqMan Universal Master Mix (ThermoFisher Scientific) and cycled following the manufacturer's instructions. PCR reactions were run in triplicate on a QuantStudio 3 (ThermoFisher Scientific). No template controls were included in each PCR run.

A standard curve of pooled samples was run for each gene to allow quantitative analysis. The quantity of each gene was determined from the standard curve, and normalized with the housekeeping gene, GAPDH, to provide relative expression for each sample.

Table 2.1. Gene expression targets and assay IDs.

Target	**TaqMan Assay ID**
CCL2	Hs00234140_m1
CXCL8	Hs00174103_m1
TGFbeta	Hs00998133_m1
COL1A1	Hs00164004_m1
FN1	Hs01549976_m1
MMP2	Hs01548727_m1

Tissue staining

Formalin-fixed paraffin embedded (FFPE) normal human lymph nodes (AMSBIO) were sectioned at 5 μm and adhered to glass slides. Multi-plex staining was performed according to the manufacturer's specifications (Akoya Biosciences). Slides were imaged on an Akoya Phenocycler.

Statistics

One-way or two-way analysis of variances (ANOVA), followed by Tukey's multiple comparison t-tests were performed using GraphPad Prism version 10.0.0 for Windows

(GraphPad Software, Boston, Massachusetts USA) with significance at $p<0.05$. All p-values are reported on the graphs.

2.4 Results and Discussion

Activated immune cells demonstrate decreased egress under interstitial flow

Interstitial fluid flow is an ever-present force within the body, yet the study of its influence on cell behavior in the immune system is still nascent. Herein, we sought to understand the impact of interstitial fluid flow on T cell behavior. In the LN microenvironment, there are an abundance of CD4+ and CD8+ T cells (**Figure 2.2.A**) that experience drastic changes in interstitial fluid flow based on the level of inflammation. However, T cells are found in a range of microenvironments throughout the body. Thus, we first sought to understand how T cells alone would respond to IFF. To model T cell response to interstitial flow, T cells were encapsulated in PhotoHA/collagen gels and subjected to 0, 0.8 (physiological) or 3.0 µm/s (pathological) flow for 24 hours (**Figure 2.2.B).** Overall, we saw significantly less egress in naïve cells compared to their activated counterparts (**Figure 2.2.C**). Egress trended downward with interstitial fluid flow in activated CD4+ T cells and was significantly decreased in activated CD8+ T cells (**Figure 2.2.C**). IFNγ was not detected in media from naïve CD4+ or CD8+ T cells (**Figure 2.2.D**). In activated CD4+ T cells, IFNγ secretion into the supernatant trended upward under 3.0 µm/s flow, though this effect was not significant (**Figure 2.2.D**). Interestingly, IFNγ secretion by activated CD8+ T cells was significantly increased by interstitial flow, both between the static control and between flow rates, demonstrating the potential importance of flow magnitude in this effect (**Figure 2.2.F**). Notably, IFNγ can bind to hyaluronic acid (198), and thus, exploration of IFNγ within the hydrogel could be of interest.

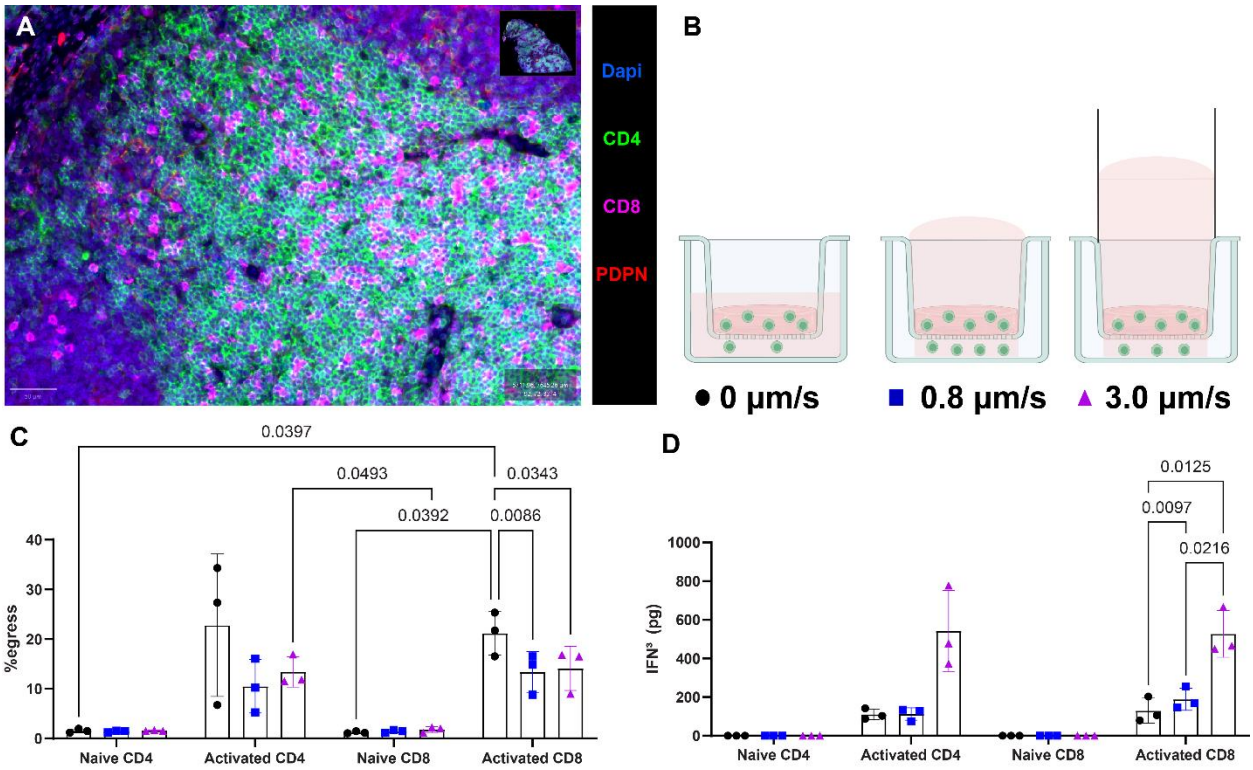

Figure 2.2. Activated T cell egress is decreased with interstitial fluid flow. *A human lymph node section demonstrates high density of CD4 and CD8 T cells (A). Scale bar is 50 µm. Schematic of T cells under varying pressure heads for IFF (B). Percent egress of naïve and activated CD4 and CD8 T cells is quantified and reported (C). Interferon-gamma secretion as determined by ELISA is quantified and reported (D). Each data point represents a biological replicate (n=3). Significance was determined by two-way ANOVA followed by Tukey's t-test, with significant p values (<0.05) reported on each graph.*

It is important to note that photocrosslinking produces reactive oxygen species (ROS) that interfere with T cell migration (199), and thus, naïve T cells may be more susceptible to ROS than activated T cells. In the lymph node, T cells exhibit random motion as they scan for an antigen, and alternate between slow and fast migration (200). Naïve T cells and activated T cells have similar speeds, but activated T cells undergo more directed and environmentally guided motion, at times forming 'swarms' of stationary cells (200–202). T cell migration is a highly complex phenomenon, mostly regulated by other cell types in the microenvironment. Generally, changes to cell migration under flow in monoculture are often attributed to self-propelled chemotaxis via autologous gradients (203), or cells moving toward nutrients. As T cells rely on

signals from other cell types, the decrease in T cell egress could potentially be caused by T cells moving toward the pressure head of media, where a larger amount of nutrients would be found. However, in the body, there are a plethora of external signals for T cells experiencing flow that may alter their behavior. Therefore, we sought to develop a spatially organized model of the lymph node stroma.

Lymph node stroma model development

In the lymph node, organized fibroblastic reticular cells orchestrate T cell migration. T cells circulate through the lymphatic system and travel through LNs, where FRCs siphon lymph and dendritic cells present antigens to naïve T cells. Once an antigen is detected, T cells become activated and the entire LN mounts an immune response, with antigen-specific immune cells egressing from efferent lymphatics. However, if that antigen is not found, the T cells will remain naïve and eventually egress through the same pathway. We sought to develop a model that would have the spatial organization of an FRC network and an efferent lymphatic seen in human samples (**Figure 2.3.A,B**). We utilized commercially available primary human cells derived from lymph nodes to enhance physiological relevance and adaptability. Using a tissue culture insert, intact LEC monolayers are formed on the underside (**Figure 2.3.C**), oriented so that their basal side is in contact with the tissue culture insert and thus the FRC-laden hydrogel, while the apical side opens into the well. This orientation allows the monolayer to serve as an efferent lymphatic. Within the insert, FRC-laden hydrogel is photo- and thermally crosslinked above the LEC monolayer, creating a spatially distinct LN stroma model (**Figure 2.3.D).** Within, the FRCs can form inter-connected networks in the model (**Figure 2.3.E**) and LECs maintain a confluent monolayer (**Figure 2.3.F**). Thus, we can recapitulate parts of the architecture of the T cell zone in a facile and simplified way.

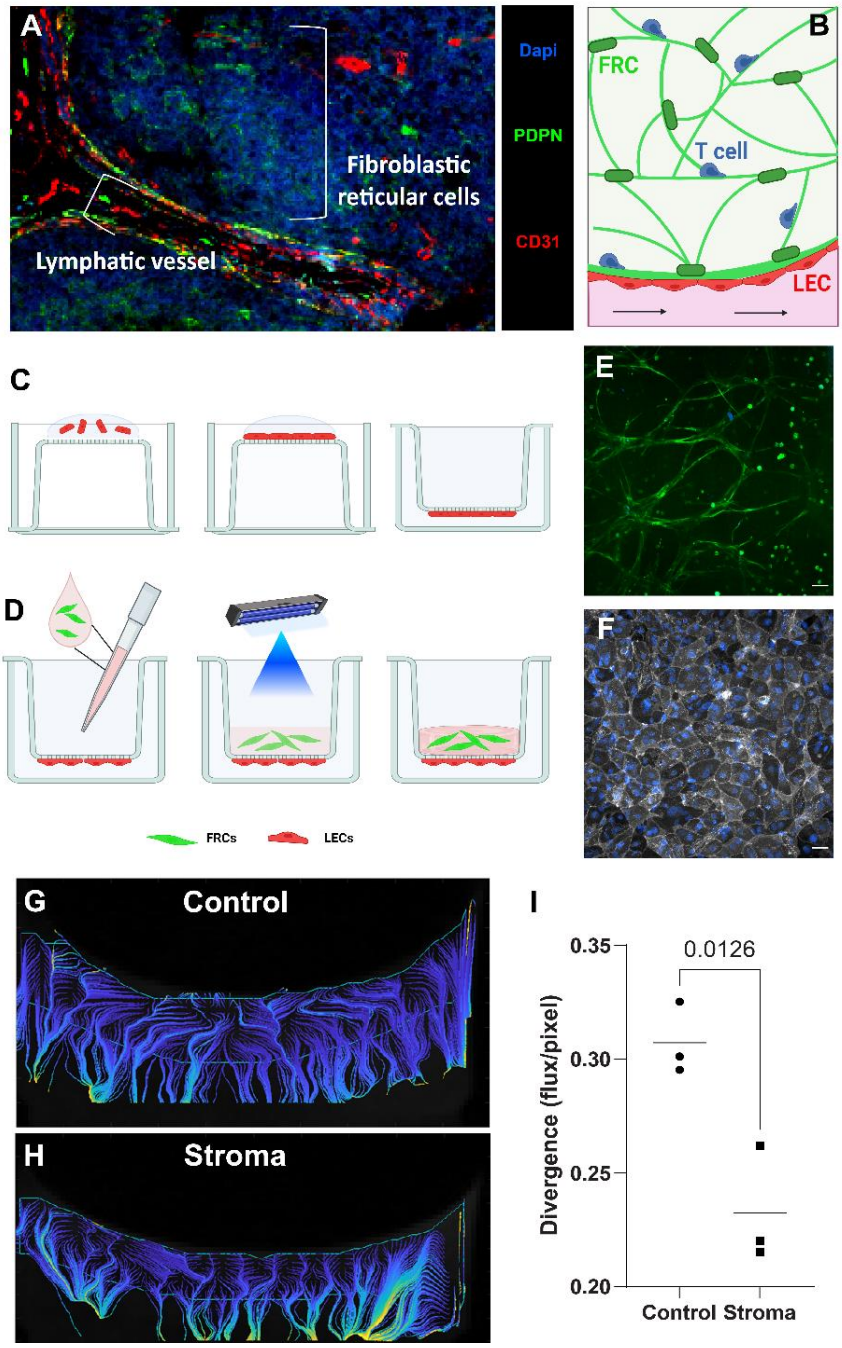

Figure 2.3. Lymph node stroma model development. *In human lymph nodes, lymphatics (PDPN+,CD31+) and fibroblastic reticular cells (PDPN+) form the structure of the T cell zone (A). Schematic of intended structure of T cell zone model (B). LECs were seeded on the underside of a tissue culture insert (C). PhotoHA-collagen gels laden with FRCs are crosslinked above the LECs (D). With this methodology, FRCs formed networks (E) and LECs formed an intact monolayer (F). The presence of LN stroma alters fluid transport in the hydrogel (G-H). Divergence of fluid is significantly decreased in the presence of LN stroma (I). Each data point represents a biological replicate (n=3). Significance was determined by one-way ANOVA followed by Tukey's t-test, with significant p values (<0.05) reported on the graph.*

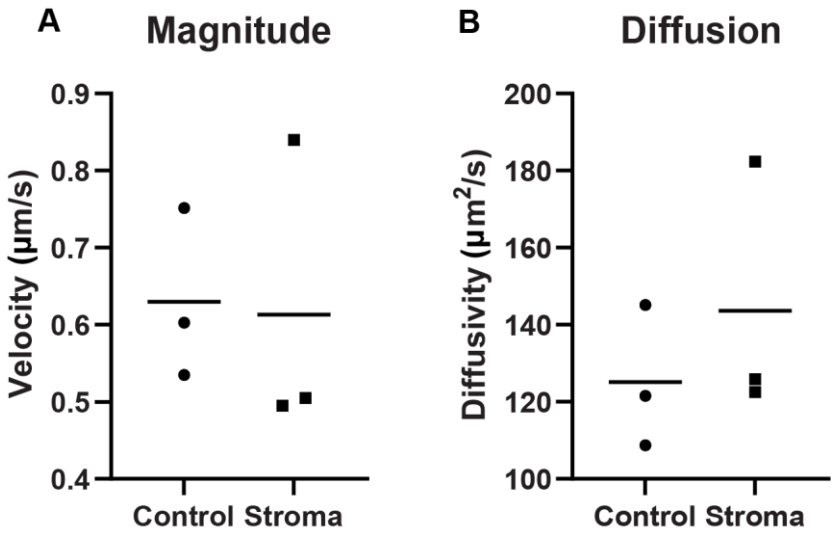

Figure 2.4. Flow magnitude and diffusion are unchanged in the presence of LN stroma. *Each data point represents a biological replicate (n=3).*

This methodology is further compatible with magnetic resonance imaging (MRI), allowing the examination of flow paths through the model. We utilized dynamic contrast enhanced MRI to determine the changes to diffusive and convective flows. In an empty PhotoHA-collagen gel, streamlines show that flow is well distributed throughout the hydrogel (**Figure 2.3.G**). When LN stroma is present, the streamlines gather and converge, with fewer locations for flow to exit the hydrogel (**Figure 2.3.H**). The flow velocity (**Figure 2.4.A**) and diffusion (**Figure 2.4.B**) were unchanged in the presence of stroma. Significantly, the divergence of velocity vectors was decreased, indicating more convergence of streamlines and development of pathways through the construct (**Figure 2.3.I)**. Thus, we know that the LN stroma, outside of chemokine secretion, does alter fluid flow through the hydrogel via physical changes.

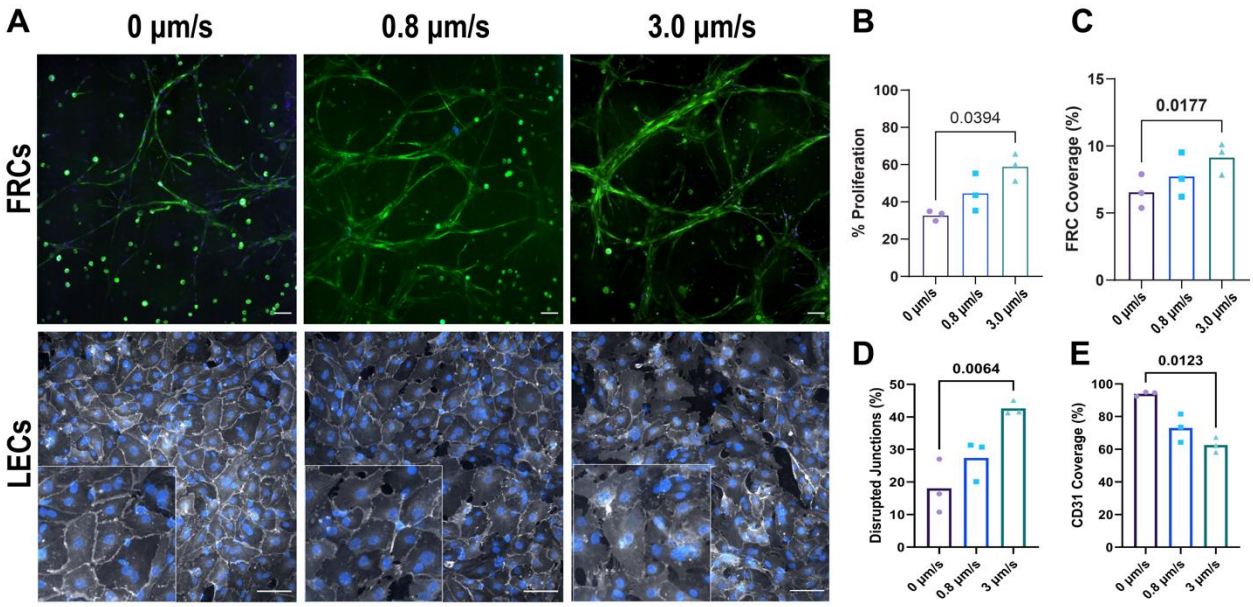

Figure 2.5. Fibroblastic reticular cells have enhanced proliferation and coverage in response to IFF. *LECs show disrupted barrier integrity. Representative images of FRCs under 0, 0.8, and 3.0 µm/s flow rates, visualized with F-actin (green). LECs are visualized with CD31 (gray). Nuclei are stained with DAPI (blue). Scale bars are 100 µm. FRC proliferation (B) and coverage (C) are quantified. LEC disrupted junctions (D) and coverage (E) are quantified. Each point represents a biological replicate, for n=3. Each data point represents a biological replicate (n=3). Significance was determined by two-way ANOVA followed by Tukey's t-test, with significant p values (<0.05) reported on each graph.*

Lymph node stroma have differential responses to interstitial fluid flow

Beyond the gaps in knowledge of T cell response to IFF, IFF in the lymph node itself is not well understood. As we saw differences in transport, we wished to examine the structures of the stromal model that developed with the presence of the cellular components, and secondarily, to determine how interstitial velocities could alter these cellular components. Thus, the LN stroma model was subjected to 0, 0.8, or 3.0 µm/s flow to probe IFF response. Representative images demonstrated FRC networks visualized with a phalloidin stain for F-actin (**Figure 2.5.A**). FRC proliferation was significantly increased under 3.0 µm/s flow (**Figure 2.5.B**). Similarly, FRC network area was only significantly increased by 3.0 µm/s flow (**Figure 2.5.C**).

LEC monolayers demonstrated intact monolayers under static conditions and disruption under flow. Visually, LEC-LEC junctions show loose, spindly connections, with small gaps in

between under flow conditions (**Figure 2.5.A**). Quantification demonstrated that LEC junctions were significantly disrupted by 3.0 µm/s flow (**Figure 2.5.D**). In addition, LEC coverage was significantly decreased under 3.0 µm/s flow (**Figure 2.5.E**). LEC proliferation was unchanged by IFF (**Figure 2.6**).

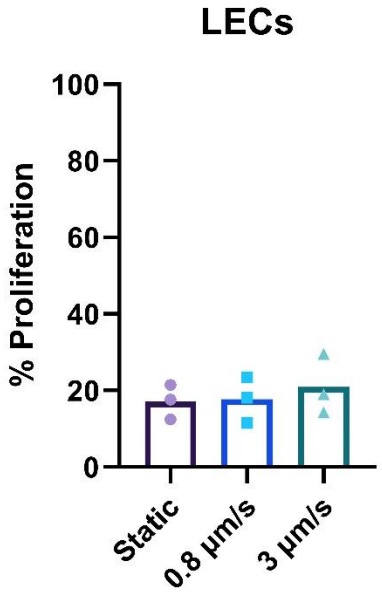

Figure 2.6. LEC proliferation is unchanged with interstitial fluid flow. *Each data point represents a biological replicate (n=3).*

We have demonstrated that IFF was disruptive to LEC coverage and junctions. Efferent lymphatics are known to loosen their junctions to collect interstitial fluid. Decreased LEC coverage could be explained by FRC invasion into the monolayer. It remains unknown whether LEC disruption precedes FRC invasion, or if FRC invasion under flow causes the disruption. However, representative images suggest that LECs can remain intact, even with FRCs present on the layer. We further demonstrated that IFF, particularly at higher flow rates, was beneficial to FRC proliferation and coverage, tracking with prior studies (135). Thus, this model allows the examination of IFF response of both cell types.

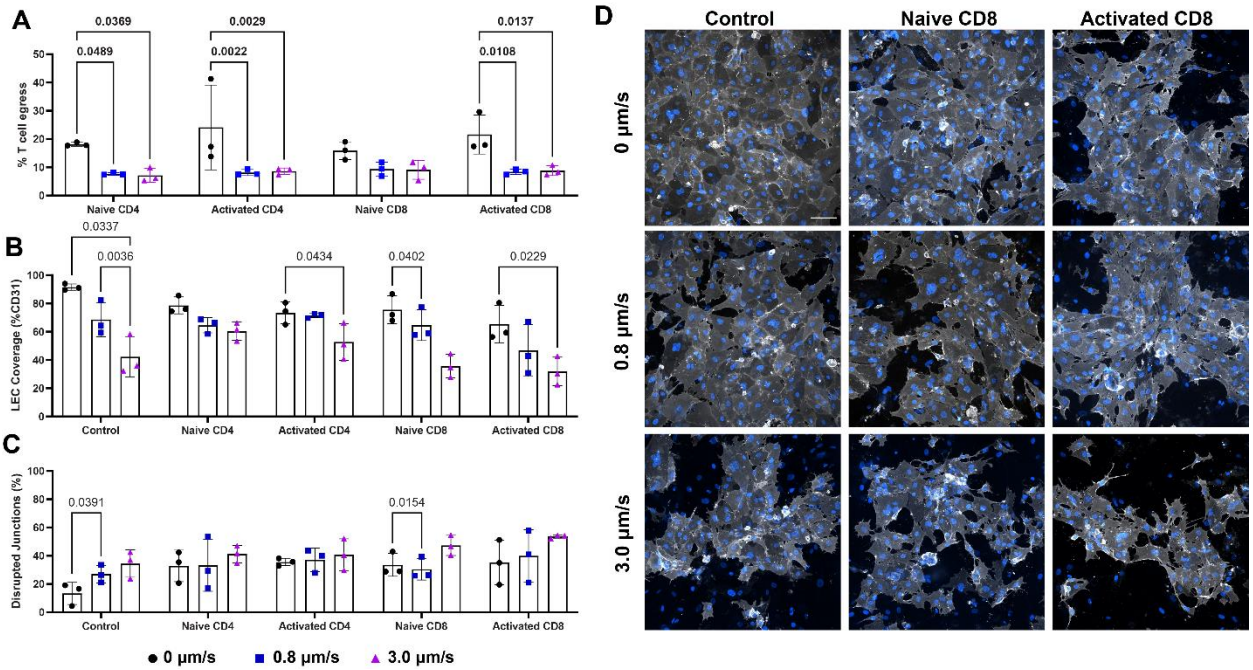

Figure 2.7. T cell egress through the LEC monolayer is decreased with interstitial fluid flow, despite decreased barrier integrity. *Naïve and activated CD4+ and CD8+ T cell egress from LN stroma varies by condition (A). Quantification of LEC monolayer coverage (B) and disrupted junctions (C). Representative images demonstrate disrupted CD31+ LEC monolayers under flow and in the presence of CD8+ T cells (D). CD31 is visualized in gray and nuclei are visualized in blue. Each data point represents a biological replicate (n=3). Significance was determined by two-way ANOVA followed by Tukey's t-test, with significant p values (<0.05) reported on each graph. Scale bar is 100 µm.*

Naïve and activated T cells egress from the LN stroma, decreased under flow

Next, we sought to understand T cell egress under IFF in the LN stroma. In the lymph node, there are a large variety of T cell populations. As a first pass, we examined naïve and activated CD4+ and CD8+ T cells. After establishing the LN stroma model, T cells were added above the FRC-laden hydrogel under static or flow conditions to simulate T cell recirculation. All T cell populations were able to migrate through and egress from the LN stroma model. Naïve and activated CD4+ T cells demonstrated similar % egress from the LN stroma model (**Figure 2.7.A**). For both naïve and activated CD4+ T cells, egress was significantly decreased between static and flow conditions, but not between flow magnitudes. CD8+ T cells also exhibited similar levels of egress between naïve and activated (**Figure 2.7.A**). For naïve CD8+ T cells, there were

no significant differences in egress under flow. For activated CD8+ T cells, egress was decreased between static and flow conditions, but not between flow magnitudes (**Figure 2.7.A**).

In this system, the changes in egress could still be due to nutrients. However, interstitial fluid flow increases with inflammation, which could suggest an antigen and the need for T cell response. Thus, this physical signal could encourage T cells to move toward the direction of flow in search of antigen. Overall, these results demonstrate that T cells are responsive to IFF in the LN stroma.

T cells exacerbate flow-mediated disruption of LEC junctions

As the LN is a holistic system with continuous communications between cell types, we sought to examine how the presence of T cells and IFF would impact LEC barrier integrity. The presence of IFF significantly decreased LEC coverage in the control (**Figure 2.7.B**). Interestingly, the presence of naïve CD4+ T cells seemed to mitigate LEC disruption. For activated CD4+ and naïve and activated CD8+, flow-mediated disruption was still present (**Figure 2.7.B**). LEC junction disruption was significantly increased by flow conditions in the control, but not in the presence of naïve or activated CD4+ T cells or activated CD8+ T cells (**Figure 2.7.C**). Representative images of the LEC monolayers demonstrate disruption in the presence of CD4+ (**Figure 2.8**) and CD8+ T cells (**Figure 2.7.D**). Overall, the presence of T cells erased the impacts of IFF in LEC junction disruption, but not overall coverage. Many T cell-secreted cytokines, including IFNγ, have anti-lymphangiogenic effects (20,204). Additionally, T cells are likely egressing between the junctions of LECs, increasing their disruption outside of flow magnitude.

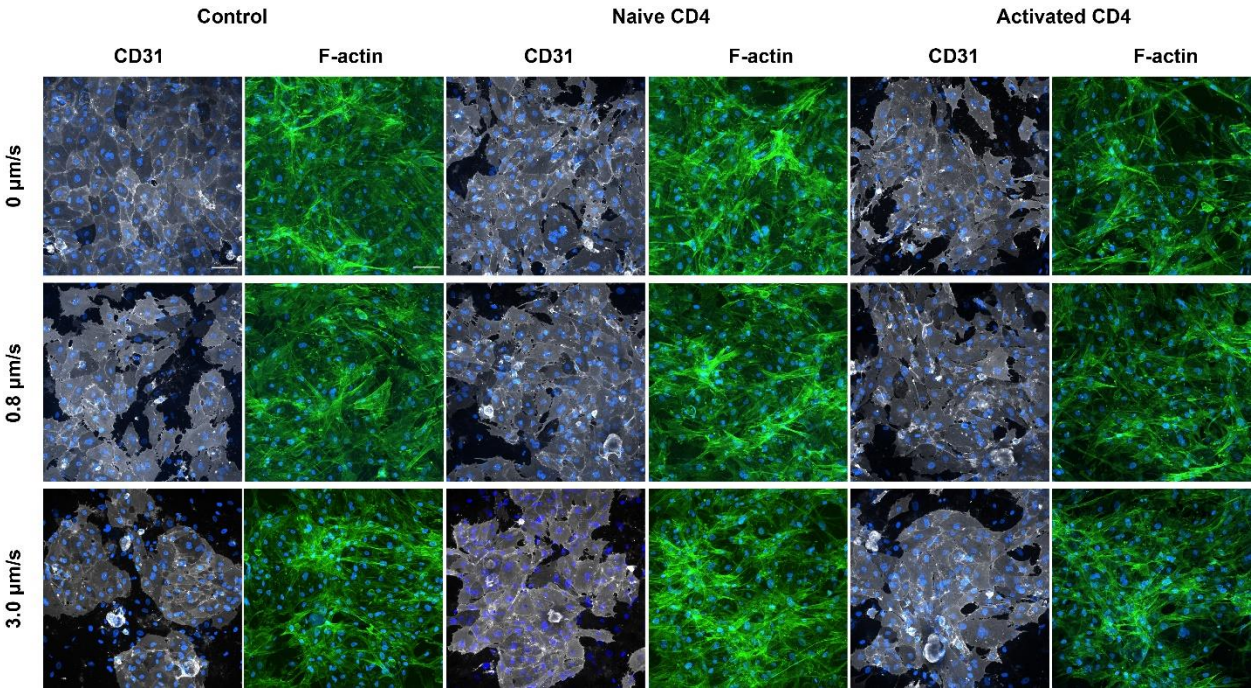

Figure 2.8. LEC monolayers are disrupted with flow and CD4+ T cell presence. *LECs are stained for CD31 (gray). Both LECs and FRCs are positive for F-actin (green). Scale bars are 100 µm.*

FRCs invasion into the LEC monolayer is decreased with T cell co-culture

As fibroblasts are known to be more migratory under flow, we sought to determine whether disruption of the LEC monolayer could be due to FRC invasion and whether T cells mitigated this effect. To do this, f-actin staining was quantified and compared to CD31 staining (**Figure S5**). The percent area of F-actin was not significantly altered by interstitial flow in the control or CD4+ T cell groups (**Figure 2.9.A**). Interestingly, F-actin area was significantly decreased by flow in the presence of CD8+ T cells (**Figure 2.9.A**). To determine how much of the f-actin staining was coming from FRCs vs LECs, the ratio of F-actin to CD31 is reported. As the ratio increases, there is purported to be a higher number of FRCs compared to LECs, as FRCs are only F-actin+ and LECs are double positive. The ratio of F-actin to CD31 was significantly increased in the control under 3.0 µm/s flow. Amongst all CD4+ and CD8+ T cells,

the ratio was unchanged (**Figure 2.9.B**), suggesting that FRCs are not displacing LECs as an effect of T cell co-culture. Representative images show fibroblastic morphology of F-actin stains on the LEC monolayer, demonstrating that there is some level of FRC invasion into the LEC monolayer (**Figure 2.9.C**). Overall, we have shown that T cell presence mitigated flow-induced FRC invasion.

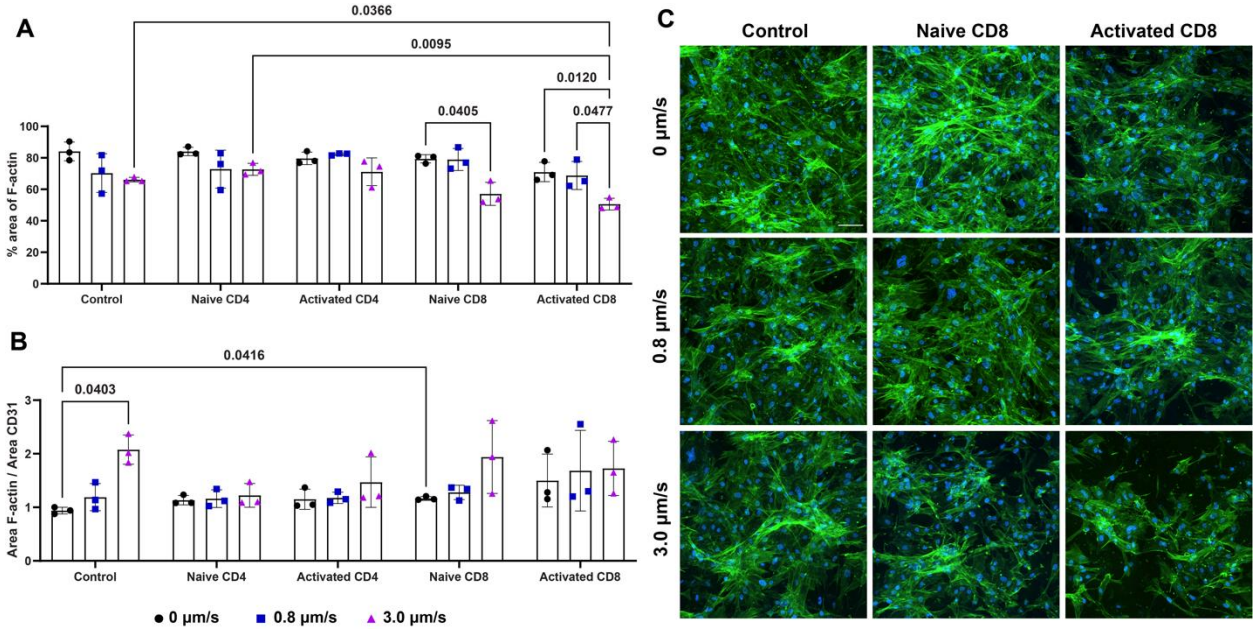

Figure 2.9. FRCs invade the LEC monolayer. *The area of F-actin (green) on the monolayer (A) and the ratio of F-actin to CD31 (B) are reported. Representative images of LEC monolayers demonstrated fibroblast invasion (C). Scale bar is 100 µm. Each data point represents a biological replicate (n=3). Significance was determined by two-way ANOVA followed by Tukey's t-test, with significant p values (<0.05) reported on each graph.*

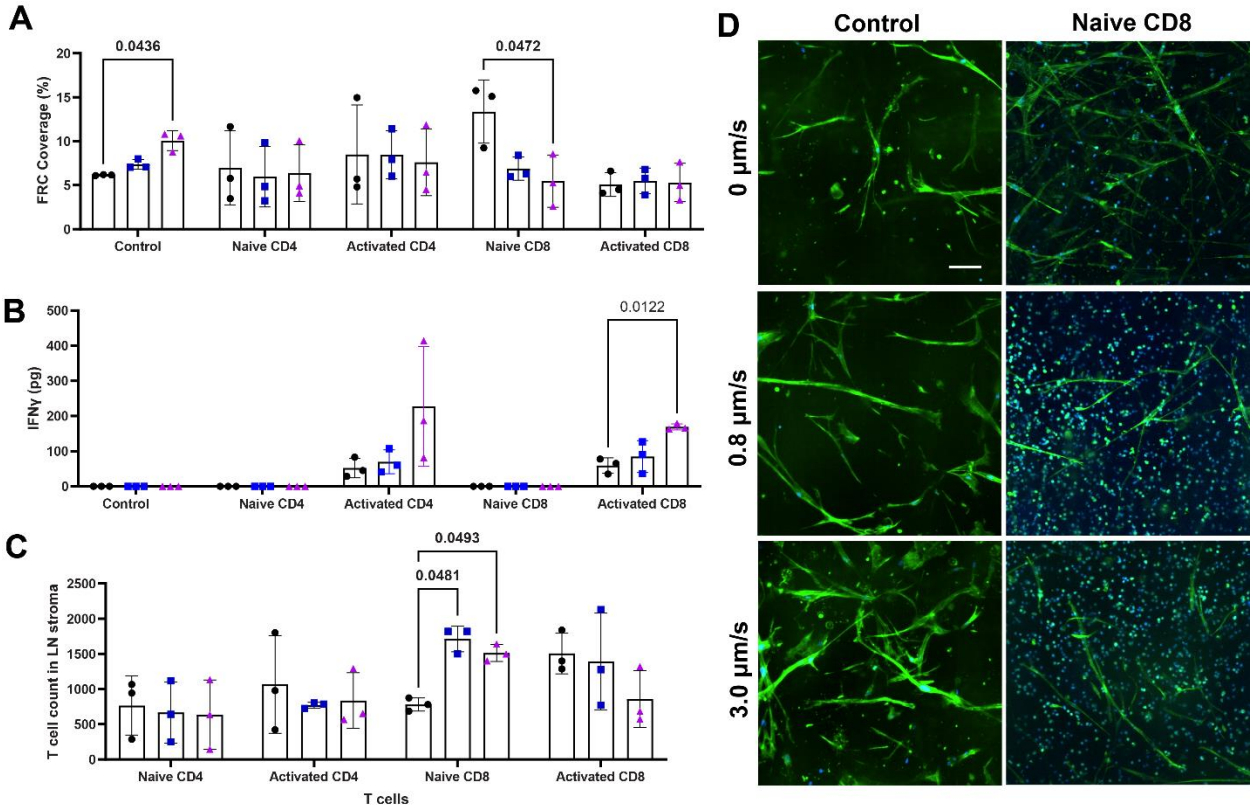

Figure 2.10. T cells mitigate flow-mediated FRC spread and are retained in the gel regardless of flow rate. *Number of T cells within the hydrogel (A). Interferon gamma secretion by T cells in the LN stroma (B). FRC coverage in the presence of T cells and interstitial flow (C). Representative images of FRCs (green) and CD8 T cells (blue). Scale bar is 50 µm. Each data point represents a biological replicate (n=3). Significance was determined by two-way ANOVA followed by Tukey's t-test, with significant p values (<0.05) reported on each graph.*

Flow response of FRCs is mitigated by T cell presence

Next, we sought to examine how T cell presence would impact the FRC network. FRC coverage was significantly increased under 3.0 µm/s flow in the control (**Figure 2.10.A**). Interestingly, FRC coverage was unchanged by flow in the presence of naïve and activated CD4+ T cells as well as activated CD8+ T cells. When in the presence of naïve CD8+ T cells, FRC coverage was significantly decreased by 3.0 µm/s flow. Representative images show CD4+ and CD8+ T cells with FRCs in the model (**Figure 2.10.D, Figure 2.11**). Thus, these results demonstrate that T cells in turn may be secreting factors that alter LN stroma response to flow.

For example, lymphotoxin beta secretion by T cells has been shown to support FRCs (205). In addition, a hallmark of activated T cells is the secretion of IFNγ that initiates a feedback loop with FRCs meant to maintain LN function (206). We have shown that T cells mitigate the flow response of FRCs, suggesting an important crosstalk pathway.

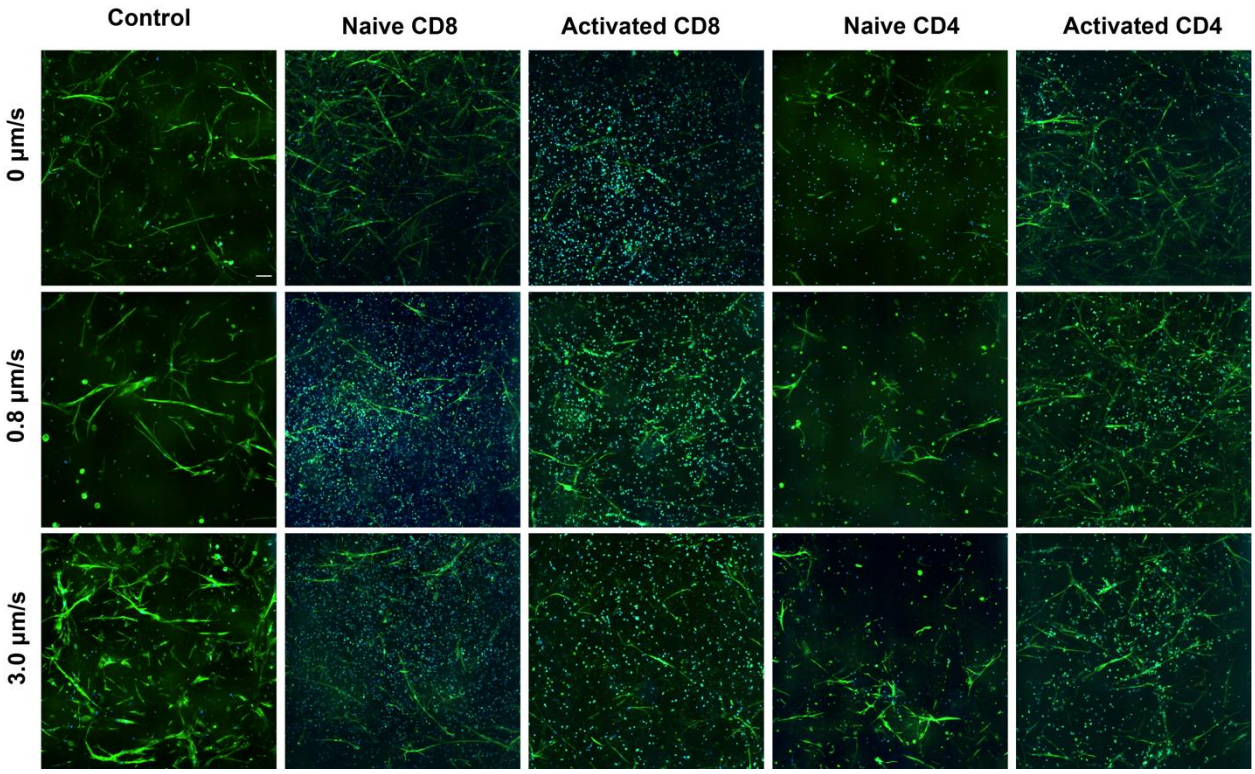

Figure 2.11. Representative images of FRC networks (green) in the presence of T cells (blue). *Scale bar is 100 µm.*

IFNγ secretion by activated CD8+ T cells is enhanced by high magnitude flow

As noted, T cells produce IFNγ as a function of activation, and this cytokine has known impacts on the stroma. IFNγ is anti-lymphangiogenic (20,204) and FRCs respond to IFNγ by suppressing T cell proliferation (206,207). We detected IFNγ in the supernatant to determine how IFF would alter T cell cytokine secretion in the LN stroma and if that correlated with

changes to the stroma. In the presence of LN stroma, naïve CD4+ and CD8+ T cells do not produce detectable levels of IFNγ. Activated CD4+ T cells trend toward higher IFNγ secretion under flow. Activated CD8+ T cells secrete significantly more IFNγ under 3.0 μm/s flow (**Figure 2.10.B**). Comparing to activated CD8+ T cells alone in the PhotoHA/collagen gel, as performed in Figure 1, these results demonstrate that higher flow rates are required to alter IFNγ secretion in the presence of LN stroma. However, as naïve T cells do not secrete IFNγ, other cytokines are likely involved in the observed changes to the stroma.

T cell count in LN stroma varies by donor

In addition to egress, we sought to understand the T cells that were retained within the LN stroma. The number of T cells retained in the FRC region of the hydrogel varied widely amongst donors in naïve and activated CD4+ T cells. Interestingly, naïve CD8+ T cell retention was significantly increased under flow conditions and activated CD8+ T cell retention trended downward under flow (**Figure 2.10.C**). Differences in T cell retention could translate to varying levels of proliferation among T cell donors. Taken together, our results demonstrate that there are extensive changes to morphology and behavior of all cell types in the LN stroma model. We next sought to determine whether these changes could be due to physical remodeling of the microenvironment or changes in chemokine profiles.

Matrix remodeling genes are not significantly altered by FRCs in response to flow

To understand why T cell egress is altered by the presence of LN stroma and IFF, we sought to determine the changes occurring in the microenvironment by measuring gene expression of LN stroma under flow (**Figure 2.12.A**). Dense matrix is known to decrease T cell infiltration and motility (208–210). FRCs are known to secrete major structural collagens, such as type I collagen, basement membrane proteins, such as fibronectin, and proteolytic enzymes,

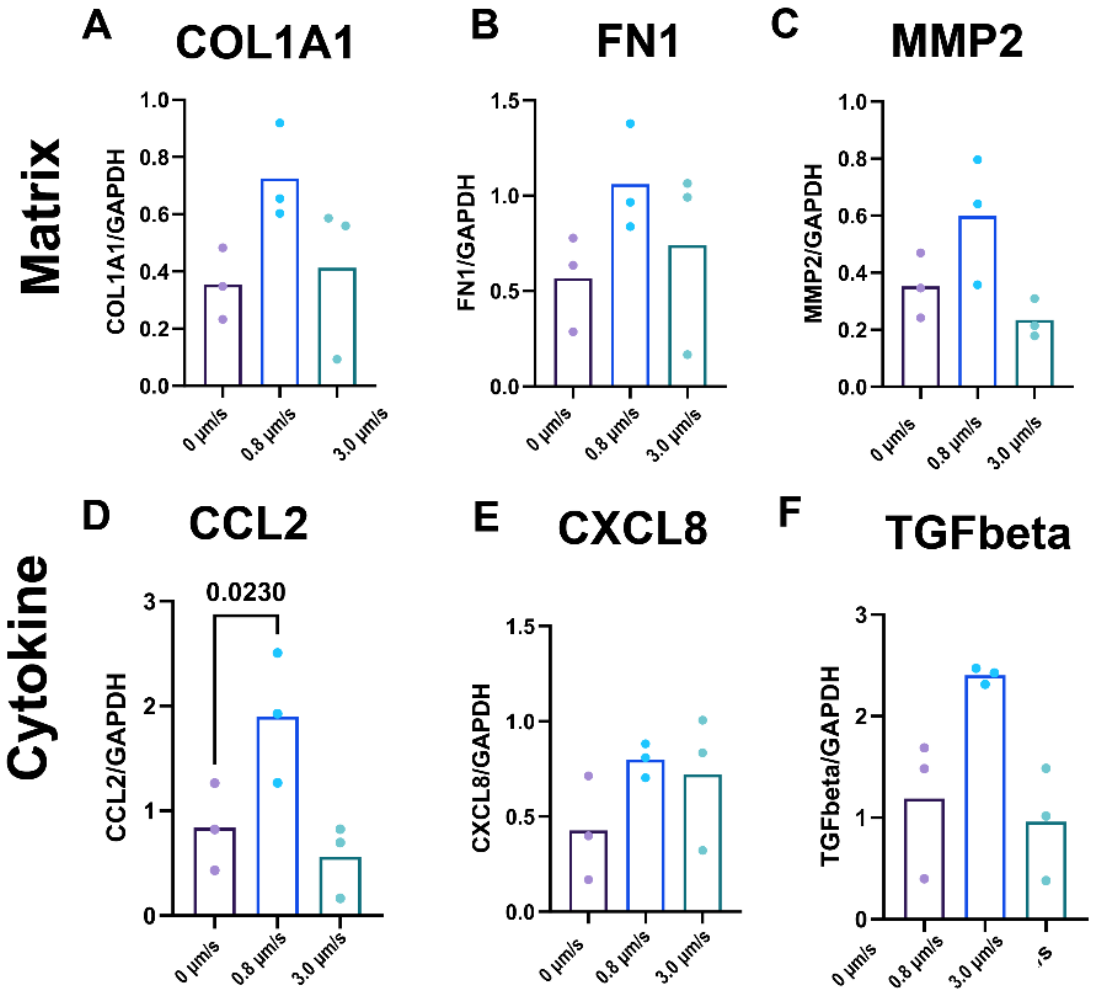

Figure 2.12. CCL2 gene expression is upregulated by 0.8 µm/s interstitial flow. *Gene expression was analyzed in LN stroma models without T cells. For matrix remodeling, COL1A1 (B), FN1 (C), and MMP2 (D) are reported. For cytokines, CCL2 (E), CXCL8 (F), and TGFbeta (G) are reported. Each data point represents a biological replicate (n=3). Significance was determined by one-way ANOVA followed by Tukey's t-test, with significant p values (<0.05) reported on each graph.*

such as matrix metalloproteinases (42,211). For matrix remodeling related genes, COL1A1 (**Figure 2.12.B**), FN1 (**Figure 2.12.C**), and MMP2 (**Figure 2.12.D**) were not significantly altered under 0.8 µm/s flow. Additionally, second harmonic generation imaging demonstrated no distinct visual differences in collagen structure between static and flow conditions (**Figure 2.13**). However, the alignment (212,213) and type of matrix deposited further alters T cell migration (214,215). Future work could involve matrix-specific staining to determine whether FRCs are

depositing high levels of ECM such as fibronectin. Additionally, extending the time of culture may be necessary to sufficiently observe deposition.

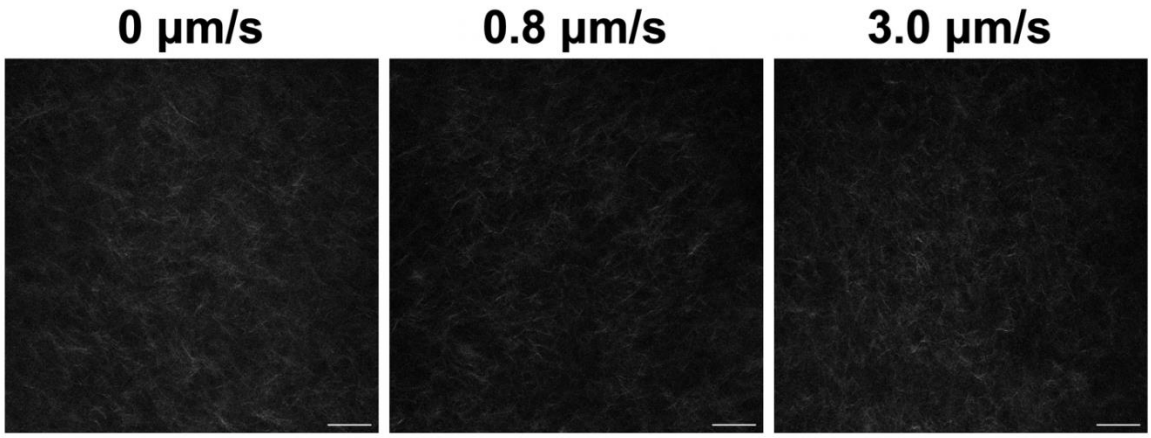

Figure 2.13. Collagen structure is not changed by interstitial fluid flow. *Second harmonic generation imaging of collagen in the LN stroma models. Scale bar is 100 μm.*

Inflammatory chemokine secretion is enhanced under high magnitude flow

Next, we sought to analyze whether altered FRC chemokine secretion could be responsible for changes in T cell egress, with the thought that more chemoattractants in the media could cause T cell retention. We selected chemokines that are known to be involved in T cell migration and secreted by the primary fibroblastic reticular cells in the model (191). We first examined the gene expression of chemokines. While most were unchanged, CCL2 stood out as significantly upregulated by 0.8 μm/s flow, but not 3.0 μm/s flow (**Figure 2.12.E**). CCL2 is an inflammatory marker, known to be expressed by lymph node stromal cells in the T cell zone, with FRCs producing higher levels than LECs (216,217). In vitro, addition of CCL2 caused concentration-dependent enhanced chemotaxis (218,219). However, contrasting studies demonstrate impaired response to chemokines and homing to lymph nodes at low doses of CCL2 (220), but increased CD4 and CD8 T cell accumulation in LNs with higher CCL2 expression (221).

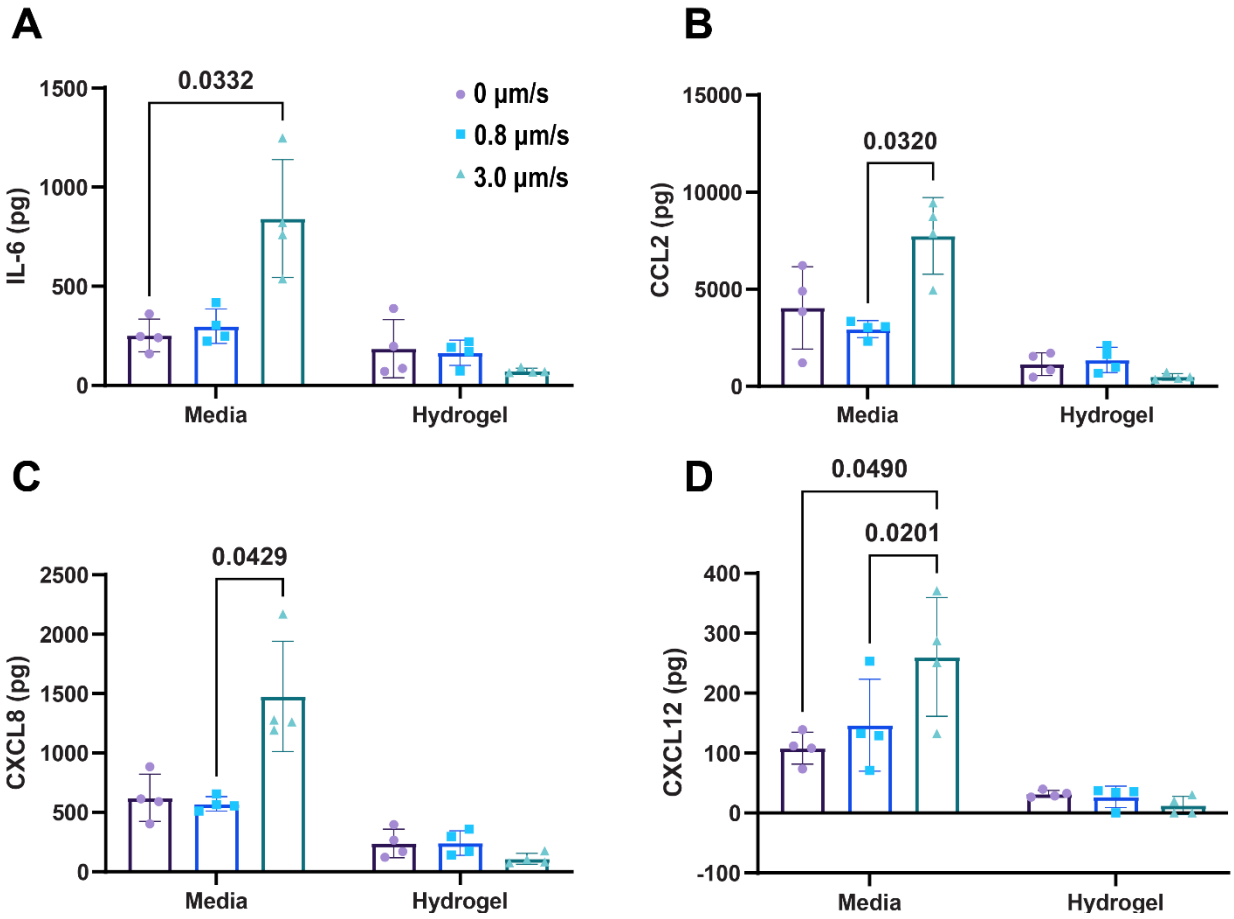

Figure 2.14. Cytokine secretion of LN stroma is altered under high interstitial flow. *Protein quantification of IL-6 (A), CCL2 (B), CXCL8 (C), and CXCL12 (D) was performed via Luminex in LN stroma models with and without T cells. Each data point represents a biological replicate (n=3). Significance was determined by one-way ANOVA followed by Tukey's t-test, with significant p values (<0.05) reported on each graph.*

Interestingly, though chemokines were not significantly upregulated at the gene level by 3.0 µm/s flow, there was significance at the protein level. IL-6 secretion was significantly increased in media from the LN stroma by 3.0 µm/s flow compared to the static control (**Figure 2.14.A**).

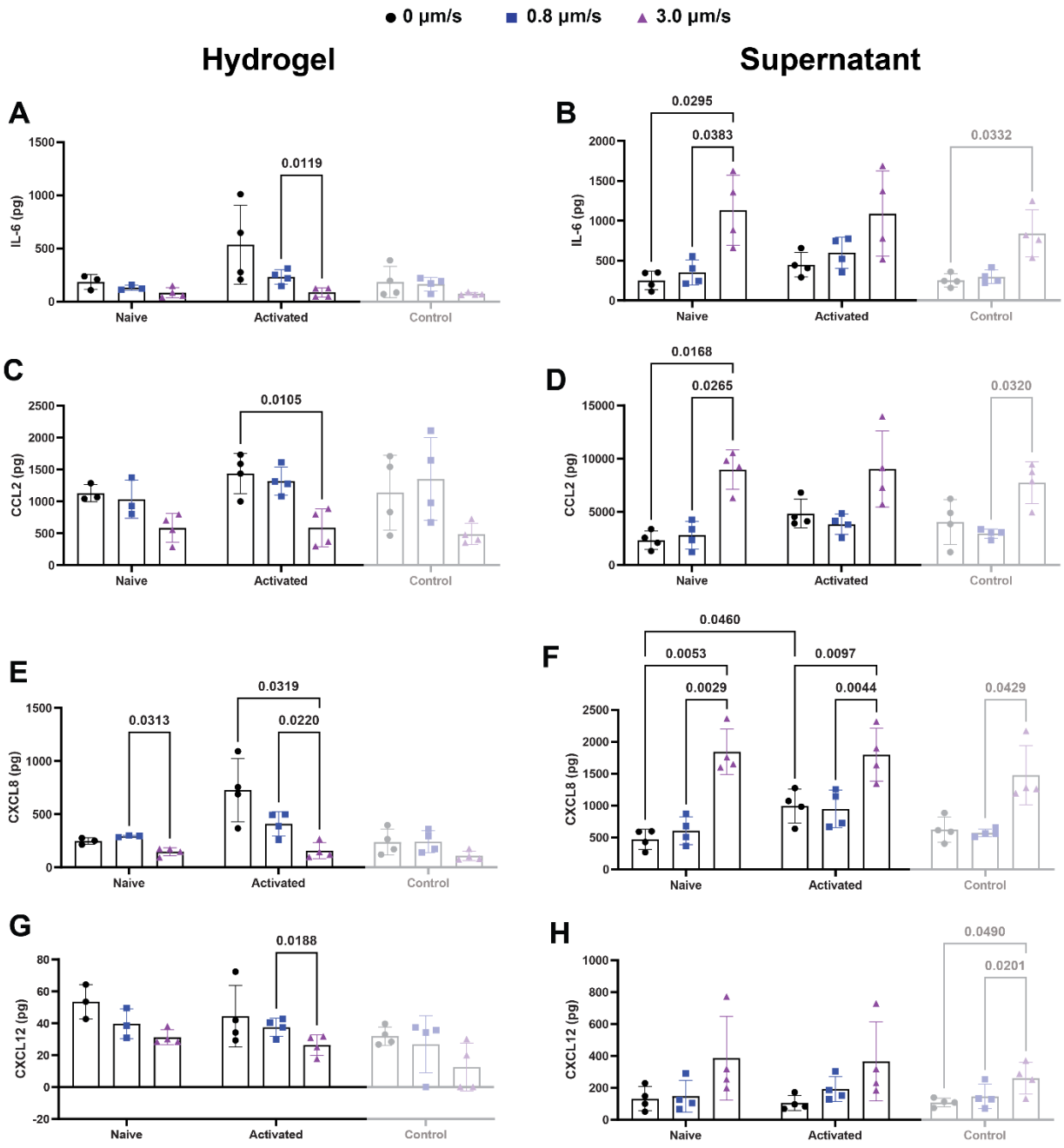

Figure 2.15. Chemokine secretion is significantly increased under high flow magnitude in the presence of T cells. *Protein quantification of IL-6 (A,B), CCL2 (C,D), CXCL8 (E,F), and CXCL12 (G,H) was performed via Luminex in LN stroma models with and without T cells. Each data point represents a biological replicate (n=3). Significance was determined by one-way ANOVA followed by Tukey's t-test, with significant p values (<0.05) reported on each graph.*

CCL2 and CXCL8 secretion were upregulated under 3.0 µm/s compared to 0.8 µm/s flow, but not the static control, due to high variability in the static condition (**Figure 2.14.B,C**). Finally, CXCL12 secretion was significantly upregulated in the 3.0 µm/s condition compared to both static and 0.8 µm/s flow (**Figure 2.14.D**). Within the hydrogel, there were no significant differences in the secretion of any chemokine within the LN stroma under flow (**Figure 2.14.A-D**). Additionally, there was less detected chemokine in the hydrogel compared to the supernatants.

We also examined whether the presence of naïve and activated CD4 T cells would alter the secretion of these chemokines (**Figure 2.15**). Overall, there were no significant differences between LN stroma alone and LN stroma with CD4+ T cells. Interestingly, in the presence of CD4+ T cells, the secretion of chemokines was generally decreased in the hydrogel under 3.0 µm/s flow (**Figure 2.15.A, C, E, G**). In contrast, the secretion of chemokines was generally increased in the supernatant under 3.0 µm/s flow (**Figure 2.15.B, D, F, H**), though this varied by chemokine and T cell activation state. Among these chemokines, IL-6 is known to enhance T cell motility (222), IFN-γ production (223), and cause decreased egress from the lymph node (224). The roles of CXCL8 and CXCL12 are less clear, but both are known enhance T cell migration under certain conditions (225–229). However, the lack of increased secretion at 0.8 µm/s flow suggests that chemokines alone do not determine T cell egress in this LN stroma model.

Flow magnitude alters response in the lymph node stroma model

Ultimately, we have built a model of the lymph node stroma and examined response to interstitial fluid flow under varying conditions. We demonstrated that varying interstitial fluid flow can drastically alter the morphology and protein secretion of the model. At 0.8 µm/s flow,

Table 2.2. The LN stroma model is responsive to high magnitude interstitial fluid flow.

Metric	***+ 0.8 µm/s flow***	***+ 3.0 µm/s flow***
FRC proliferation	–	↑
FRC coverage	–	↑
LEC proliferation	–	–
LEC disrupted junctions	–	↑
LEC coverage	–	↓
Matrix remodeling genes	–	–
IL-6 secretion	–	↑
CCL2 secretion	–	↑
CXCL8 secretion	–	↑
CXCL12 secretion	–	↑

Table 2.3. LN stroma model flow response in the presence of T cells is altered.

Metric	***+ 0.8 µm/s flow***	***+ 3.0 µm/s flow***
FRC coverage	–	–
LEC disrupted junctions	–	–
LEC coverage	↓	↓↓
T cell egress	↓	↓
T cells in LN stroma	–	–
IFNg secretion	–	↑
IL-6 secretion	–	↑
CCL2 secretion	–	↑
CXCL8 secretion	–	↑
CXCL12 secretion	–	–

changes to the LN stroma were less pronounced (**Table 2**). However, we still saw differences in T cell egress. Therefore, this flow rate may be utilized to answer questions about T cell migration in response to flow without the confounding factors of varying chemokines in the microenvironment. In contrast, we present the 3.0 µm/s flow rate as a model of inflammation in the lymph node stroma without any exogenous factors. We saw changes to FRC remodeling, LEC disruption, T cell behavior, and inflammatory chemokines (**Table 2, Table 3**). This model is ideal for answering questions around crosstalk in the lymph node during inflammatory states.

Additionally, the presence of T cells mitigated many flow-induced changes to LN stroma morphology (**Table 3**). Thus, this work emphasizes the importance of crosstalk between cell types in response to interstitial fluid flow.

2.5 Conclusion

Overall, we have successfully established a spatially organized lymph node stroma model that is easily modified toward experimental questions around interstitial fluid flow and T cell retention and egress. This work has helped establish the relevance of physical cues, such as interstitial fluid flow, within engineered models of the immune system. Future work will aim to identify a mechanism and how crosstalk between T cells and the stroma under flow alters response to antigens. Eventually, more immune cells could be included in the model to replicate adaptive immunity.

CHAPTER 3

EXAMINING TUMOR BURDEN-RELATED CHANGES TO TRANSPORT IN ENGINEERED LYMPH NODE STROMA

3.1 Summary

Lymph node metastasis is one of the most significant indicators of prognosis in breast cancer patients. Upon arrival in the lymph node, tumor cells are altered by their new surroundings and in turn alter the lymph node microenvironment. Metastatic lymph nodes are enlarged and immunosuppressed. Though these tumor cells are suspected to exit the lymph node and create more metastases, this process is not well understood. The lymph node parenchyma is bathed in constant interstitial fluid flow that is altered with inflammation. This flow is delivered through extracellular matrix conduits maintained by fibroblastic reticular cells in the node that may be recruited by invading tumor cells to alter the matrix, and thus, fluid flow. Though fluid flow has been implicated in tumor cell invasion across the body, the impact of flow on tumor cells within the lymph node has not yet been elucidated. As the tumor cells remodel the microenvironment, they may influence changes in transport that in turn impact their ability to exit the lymph node and continue metastatic spread. Within, we first sought to characterize alterations in matrix structure in human tissue samples. We demonstrate enhanced collagen area in metastatic lymph nodes. We then correlated collagen area with tumor burden and unexpectedly found that increasing tumor area correlated with decreased collagen. Next, we sought to adapt our pre-established lymph node stroma model, consisting of a monolayer of lymphatic endothelial cells underneath of a fibroblastic reticular cell laden hydrogel, into a metastatic model. We recapitulated varying tumor burden by adding different numbers of tumor cells into the model. We found that tumor cells were able to migrate all the way through the LN stroma model, regardless of initial tumor cell burden. We examined transport and found no significant changes in flow velocity or divergence in metastatic LN stroma models. However, diffusivity was decreased in the highest tumor burden group. Finally, we correlated the

morphology of the LN stroma models with transport metrics and found that the degree of fibroblastic reticular cell spread within the bulk hydrogel positively correlated with flow magnitude. Overall, we have established a metastatic LN stroma model that demonstrates tumor cell invasion throughout. Most excitingly, we have established a direct connection between fibroblastic reticular cell morphology and flow magnitude.

3.2 Introduction

Metastasis to the lymph node (LN) is the most significant prognostic factor in breast cancer. Within the LN, tumor deposits can be stratified by size into micro- and macro-metastases. Though there is a binary impact of less favorable prognosis with lymph node metastasis, the impact of size of metastasis is still debated among contradicting studies (230–232). Regardless, size of metastasis is still clinically relevant in deciding treatment course, as macro-metastases indicate the need for further axillary treatment, and micro-metastases can be treated as 'node negative' (233,234).

The healthy LN is highly organized to allow for efficient screening of lymph for antigens and mount an immune response if necessitated. Fluid flow in the LN is essential for function and provides key signals to the cells that orchestrate immunity. However, this flow also encourages tumor cell invasion, as increased pressure in the tumor results in enhanced drainage, driving tumor cells to the sentinel LNs (157,235–237).

Tumor positive LNs are enlarged and immunosuppressed, further demonstrating increased proteolytic activity (238) and increased matrix (239). The density and porosity of the matrix are directly related to transport. In the LN, the primary arbitrators of matrix remodeling are the fibroblastic reticular cells (FRCs) (240,241). In metastatic lymph nodes, cancer-

associated fibroblasts (CAFs) support the growth and treatment resistance of metastases (242–244). However, the role of FRCs, or their conversion to CAFs, is not well understood.

Additionally, the ability of tumor cells to exit the lymph node through the efferent lymphatics and create distant metastases, known as sequential spread, has been widely debated, with Naxerova et al demonstrating sequential progression from the lymph node in only one-third of patients with metastatic colorectal cancer (245). However, it is established that breast cancer cells within the LN can undergo genetic changes compared to breast cancer cells from the primary tumor at varying rates (246–249). Nonetheless, lymphatic vessels are known to serve as a route for breast cancer dissemination, through a variety of mechanisms (250). Altered transport within the lymph node itself would indeed impact the efferent lymphatics, and thus, the ability of tumor cells to egress from the node, causing further metastatic spread.

Herein, we sought to characterize structural changes to human metastatic lymph nodes with increasing tumor burden, followed by developing an in vitro model of tumor burden. In Chapter 2, we established a spatially organized model of the LN stroma with interstitial fluid flow, consisting of FRC-laden hydrogel atop a monolayer of lymphatic endothelial cells (LECs). In this chapter, we added varying numbers of breast cancer cells to the LN stroma model to create a metastatic LN stroma model and examine how tumor burden impacts invasion and transport properties.

3.3 Methods

Picrosirius red staining

Formalin-fixed paraffin embedded (FFPE) control (AMSBIO) and metastatic (National Disease Research Interchange) human lymph nodes (**Table 3.1**) were sectioned at 5 µm and adhered to glass slides. Slides were baked at 60°C overnight before staining. Picrosirius red

staining was performed as specified by the manufacturer (NovaUltra). Slides are mounted with VectaMount Express Mounting Medium (Vector Labs). Tissues are imaged on an Olympus VS200 Slide Scanner at 20X using polarized light.

Table 3.1. Demographics of control (left) and metastatic (right) human lymph node samples.

Age	***Sex***	***Race***
30	Female	L
32	Female	L
60	Female	L
68	Female	L
63	Female	L
38	Female	L
42	Female	L
46	Female	L
35	Female	L
39	Female	L
30	Male	L
32	Male	L
66	Male	L
34	Male	L
67	Male	L
51	Male	L
55	Male	L
59	Male	L
61	Male	L
48	Male	L

Age	***Sex***	***Race***	***Hormone Receptors***
52	Female	W	Triple Negative
69	Female	B	Triple Negative
45	Female	W	Triple Negative
33	Female	W	Triple Negative
81	Female	W	Triple Negative
62	Female	W	Triple Negative
49	Female	W	ER+PR+HER2-
51	Female	W	ER+PR+HER2-
67	Female	W	ER+PR+HER2-
61	Female	W	ER+PR+HER2-
46	Female	W	ER+PR+HER2-
69	Female	W	ER+PR+HER2-
44	Female	W	ER+PR+HER2-
63	Female	W	ER+PR+HER2-
56	Female	W	Triple Negative
70	Female	W	Triple Negative
44	Female	W	Triple Negative
39	Female	W	Triple Negative
70	Female	W	Triple Negative
58	Female	C	Triple Negative

Picrosirius red analysis

For analysis of picrosirius red, a custom Matlab code developed by K. Degen is utilized. Polarized light images are thresholded and green and red pixels are measured. For coherency, a fourier transform is utilized to assign a value from 0 to 1 for coherency of fibers. Additionally, OrientationJ (251,252) in FIJI (197) was utilized to examine alignment. Finally, QuPath was used to take measurements of the collagen capsule.

Multi-plex immunofluorescent staining via Akoya Phenocycler

Multi-plex staining is performed as specified by Akoya Biosciences on a select group of control and cancer lymph nodes. Briefly, slides are baked overnight at 60°C, deparaffinized in xylene, and rehydrated in ethanol and water. Antigen retrieval is performed at pH 9 for 20 minutes at high pressure. Primary antibodies conjugated with DNA barcodes are added to the tissue and fixed with 1.6% paraformaldehyde and methanol. Flow cells are sealed onto each slide and DAPI and secondary staining and detection is performed on the Akoya Phenocycler.

Cell culture

Lymphatic endothelial cells (LECs) and fibroblastic reticular cells (FRCs) are cultured as described in Chapter 2. MCF-7 cells are cultured in Eagle's Minimum Essential Medium with 0.01 mg/ml insulin and 10% fetal bovine serum, as described by the manufacturer (ATCC). All cells were maintained at 5% CO^2 and 37°C.

Metastatic LN stroma model

The LN stroma model is established as described in Chapter 2. Briefly, LECs are seeded on the underside of a 12-mm tissue culture insert. After 2 days, FRC-laden hydrogel consisting of methacrylated hyaluronic acid (PhotoHA) and type I collagen is polymerized with 385 nm light for 45 seconds, followed by thermal crosslinking for 30 minutes at 37°C. LN stroma models are then incubated for 24 hours prior to experimental manipulation with tumor cells. MCF7 cells are resuspended in Vasculife complete and 100, 1000, or 10,000 cells are added to each LN model. Models are then maintained in Vasculife for 5 days at 37°C.

Immunofluorescence

After 5 days, LN stroma models are fixed in 4% paraformaldehyde. The hydrogels are gently removed from the tissue culture insert using a paint brush and transferred to 24 well

plates. The membrane from the tissue culture insert is cut out using a scalpel and placed on charged glass slides.

Membranes are incubated in 0.01% triton x-100 with donkey serum for 45 minutes. Then, membranes are stained with 1:50 sheep anti-human CD31 (R&D) and 1:100 mouse anti-human pan-cytokeratin (Invitrogen) in 0.01% Triton-X + donkey serum for 2 hours at room temperature (RT). Membranes are rinsed with PBS and incubated with 1:400 donkey anti sheep 647 (Invitrogen) and 1:400 donkey anti mouse 555 (Invitrogen) for 1 hour. Finally, membranes are stained with 1:5000 DAPI for 15 minutes. Membranes are mounted with Fluoromount-G (SouthernBiotech) and the coverslip is sealed with nail polish.

LN stroma model hydrogels undergo blocking as described in Chapter 2 with 0.01% triton x-100 and donkey serum for 6 hours. All staining is performed on a rocker. Then, 1:100 mouse anti-human pan-cytokeratin (Invitrogen) in 0.01% triton x-100 and donkey serum is added to the hydrogels at 4C on a rocker overnight. Hydrogels are rinsed with PBS three times at RT. Next, hydrogels are incubated with 1:400 donkey anti mouse 555 (Invitrogen) in blocking solution for 6 hours at RT. Hydrogels are rinsed in PBS overnight at 4C. Finally, hydrogels are incubated with 1:400 AlexaFluor 488 Phalloidin and Dapi for 6 hours at RT. Hydrogels are stored in PBS until imaging.

Metastatic LN stroma model imaging

Membranes from the LN stroma model on slides are imaged at 20X on a Zeiss AxioObserver. Hydrogels are carefully transferred to a glass coverslip and another coverslip is placed above. Then, hydrogels are imaged on a Nikon Spinning Disk at 10X. Z-stacks of the entire gel were taken with a 10-micron step size. Three regions of interest were imaged in each technical replicate.

Image quantification

For LEC monolayers on the membranes, CD31 coverage was analyzed via thresholding and measurement of CD31+ area in FIJI. Pan-cytokeratin+ tumor cells were manually counted. Within the hydrogel, three regions were analyzed. First, the top of the hydrogel, where tumor cells were added. Here, F-actin and pan-cytokeratin were thresholded and area was measured. As tumor cells are double positive, the panCK area was subtracted from the F-actin area to ensure only FRCs were captured in the measurement. The next region analyzed was the middle of the gel. Z-projections of the gel, excluding the top and bottom, were thresholded for F-actin. Tumor cells were manually counted. Finally, the bottom of the hydrogel was quantified as described for the top of the hydrogel.

Magnetic resonance imaging

Dynamic contrast enhanced (DCE)-MRI was utilized to obtain transport metrics in the LN stroma models as described in Chapter 2 and by Kingsmore et al (195). Briefly, LN stroma models were secured in a Bruker 9.4T MRI scanner and 300 µL of gadolinium (BioPal) was injected onto the model. Images were taken every 3 minutes for a total of 4 post-contrast images. Analysis is performed using Lymph4D (195).

Statistics

One-way analysis of variances (ANOVA), followed by Tukey's t-tests with multiple hypothesis correction were performed using GraphPad Prism version 10.0.0 for Windows (GraphPad Software, Boston, Massachusetts USA) with significance at $p<0.05$. All p-values are reported on the graphs.

3.4 Results

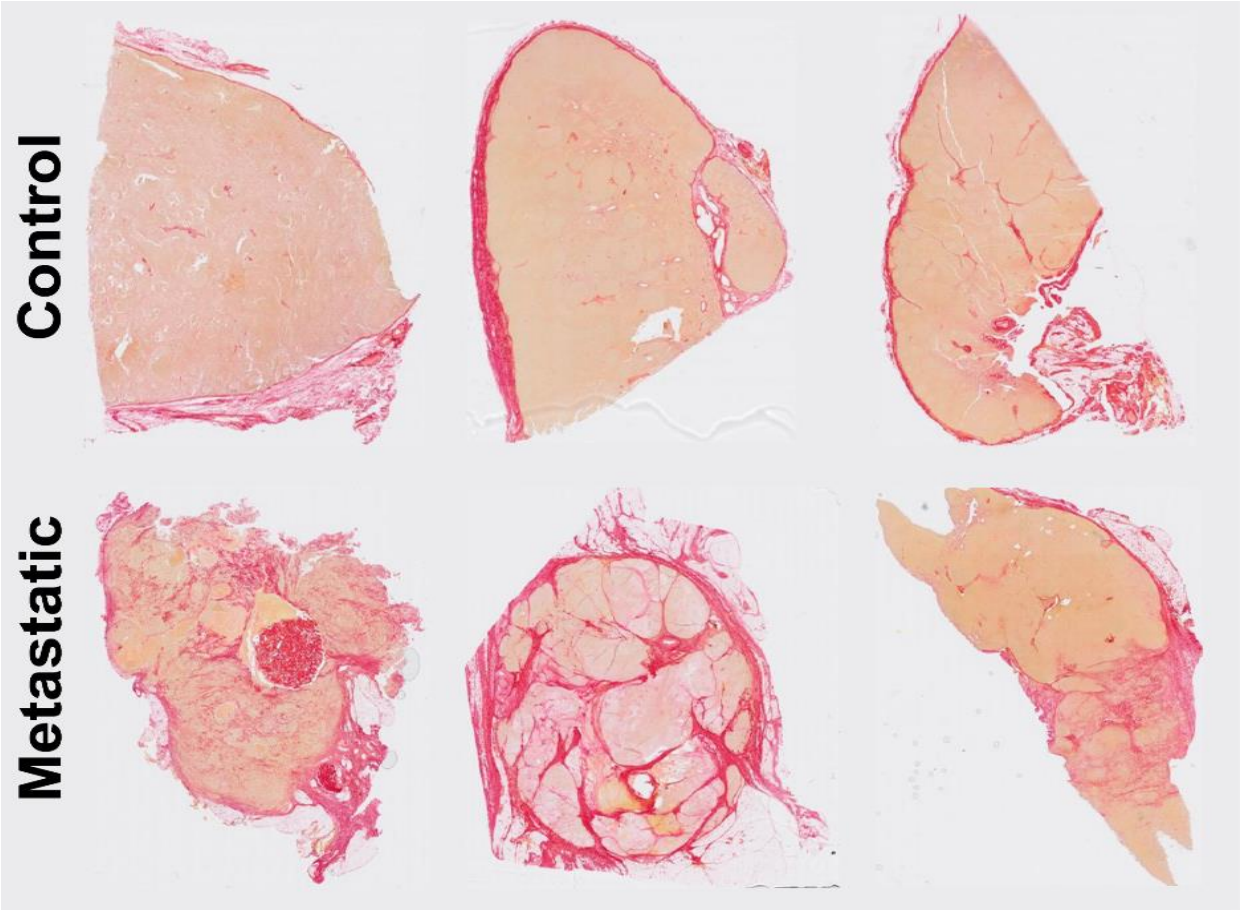

Figure 3.1. Enhanced collagen deposition in metastatic lymph nodes. *Representative images of PSR staining under brightfield. Collagen is visualized in dark pink and red.*

Collagen deposition is enhanced in metastatic nodes

We first imaged PSR stained lymph nodes under brightfield to observe whole-tissue changes. Within control lymph nodes, there is little to no collagen within the parenchyma of the tissue, where densely packed immune cells are found. Instead, thick collagen fibers are found surrounding the node, forming the capsule. In metastatic lymph nodes, the observed collagen structure is drastically altered. Collagen deposition is observed throughout the parenchyma (**Figure 3.1**).

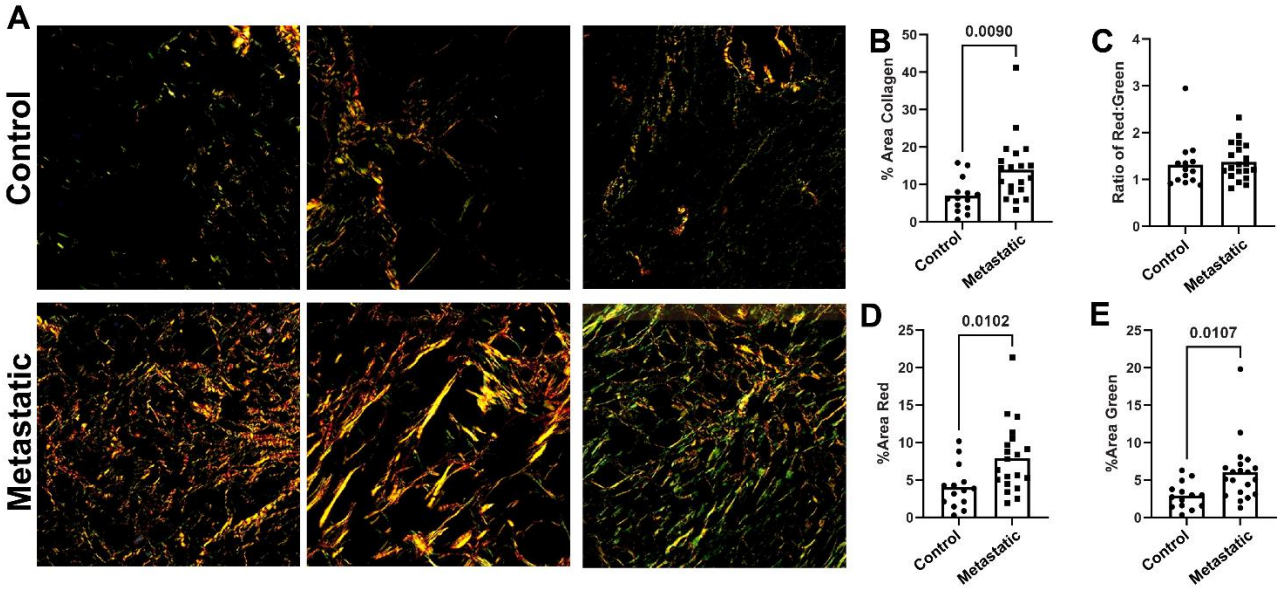

Figure 3.2.The area of collagen is increased in metastatic lymph nodes. *Representative images demonstrate collagen fibers in control and cancer lymph nodes (A). Total area of collagen is quantified (B). The color of the fiber represents its size and complexity. Red represents larger collagen fibers while green represents smaller. The ratio of red:green (C), the area of red fibers (D), and the area of green fibers (E) are reported. Each data point represents a different patient sample. Significance was determined by students' t-test, with significant p values (<0.05) reported on each graph.*

Increased collagen fibers in metastatic lymph nodes

We next examined PSR staining under polarized light. In this methodology, the color of the fibers corresponds to size: red meaning large, and green meaning small. Representative images show drastically more collagen fibers in metastatic nodes (**Figure 3.2.A**). Upon quantification, the %area collagen was significantly increased in metastatic nodes (**Figure 3.2.B**). We also sought to determine if the ratio of red:green fibers would be altered, demonstrating a preference for certain types of collagen. Interestingly, the ratio was unchanged between control and metastatic lymph nodes (**Figure 3.2.C**). However, both red (**Figure 3.2.D**) and green (**Figure 3.2.E**) area were significantly increased in metastatic nodes.

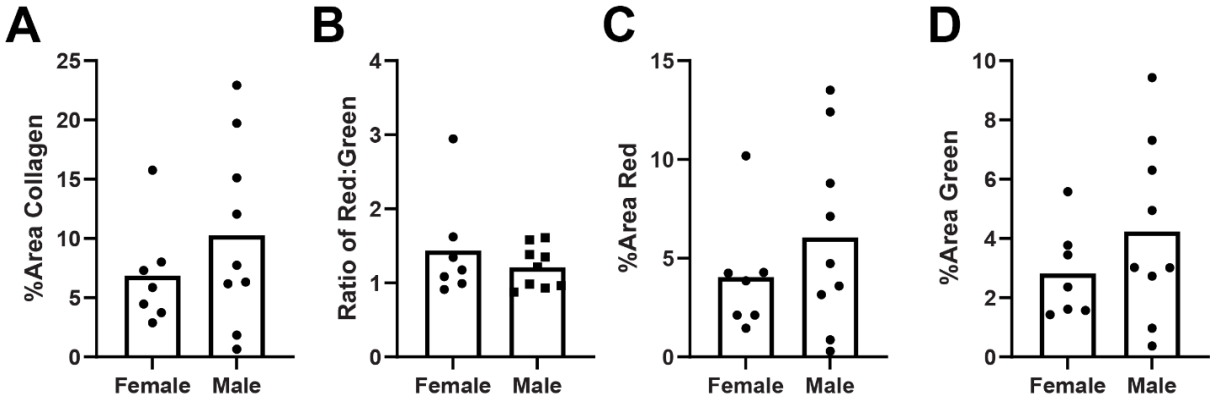

Figure 3.3. No significant differences in collagen metrics observed between sexes. *In the control samples, %area collagen (A), ratio of red:green (B), %area red (C), and %area green (D) are separated by sex of patient.*

Stratifying PSR metrics by sex and hormone receptors demonstrated no significance

Within our controls, we sought to have an approximately equal balance of male and female patient samples to examine PSR metrics between the sexes. Overall, %area collagen varied widely by patient, particularly in male samples (**Figure 3.3.A**). The ratio of red:green fibers was unchanged between male and female patients (**Figure 3.3.B**). Finally, the %area red (**Figure 3.3.C**) and %area green (**Figure 3.3.D**) were also unchanged between male and female samples, and had high variability. It is important to note that our control samples had no health records to go along with them, and thus, confounding factors are almost certainly present.

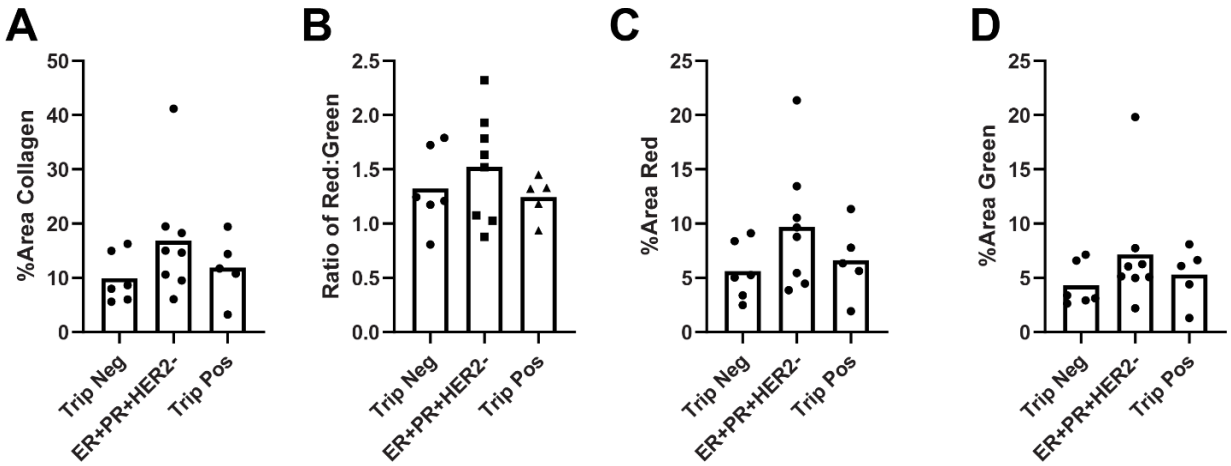

Figure 3.4. No significant differences in collagen metrics in metastatic lymph nodes when stratified by hormone receptors. *In the metastatic lymph nodes, %area collagen (A), ratio of red:green (B), %area red (C), and %area green (D) are separated by hormone receptor status.*

Within our metastatic lymph nodes, we sought out a mix of hormone receptors. The key hormone receptors in breast cancer are estrogen receptor (ER), progesterone receptor (PR), and human epidermal growth factor receptor 2 (HER2). Typically, these receptors are targeted for treatment. We sought to examine if the expression of these hormone receptors would alter collagen in the metastatic node. Overall, we saw no significant differences in %area collagen (**Figure 3.4.A**), ratio of red:green (**Figure 3.4.C**), %area red (**Figure 3.4.C**), or %area green (**Figure 3.4.D**).

Fiber alignment trends upward in cancer

In addition to amount of fibers, the orientation can also be examined. Overall, we saw a trend toward more coherency in metastatic nodes compared to the controls (**Figure 3.5.A**). Using a color map that identifies +45 degrees as purple and -45 degrees as green, we visualized the orientation of fibers in control (B,C), and metastatic (D,E) lymph nodes. Future work will include characterizing on a fiber-by-fiber basis.

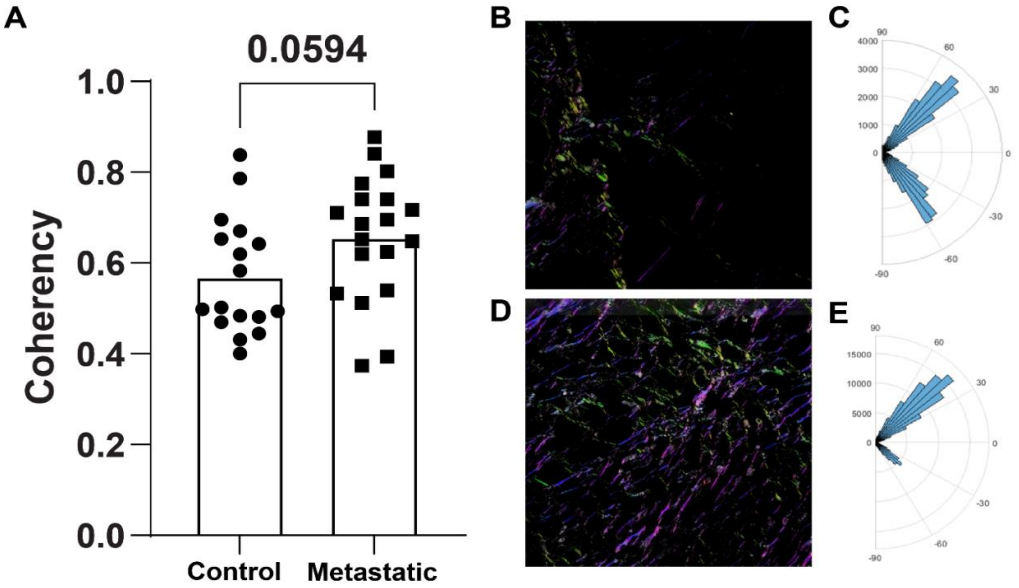

Figure 3.5. There are potential differences in coherency and orientation of collagen fibers in metastatic lymph nodes. *The coherency (A) of the fibers trends upward in metastatic nodes. Alignment of fibers with purple representing +45 degrees and green representing -45 in the control (B,C) and cancer (D,E) demonstrate trends toward more alignment in metastatic nodes.*

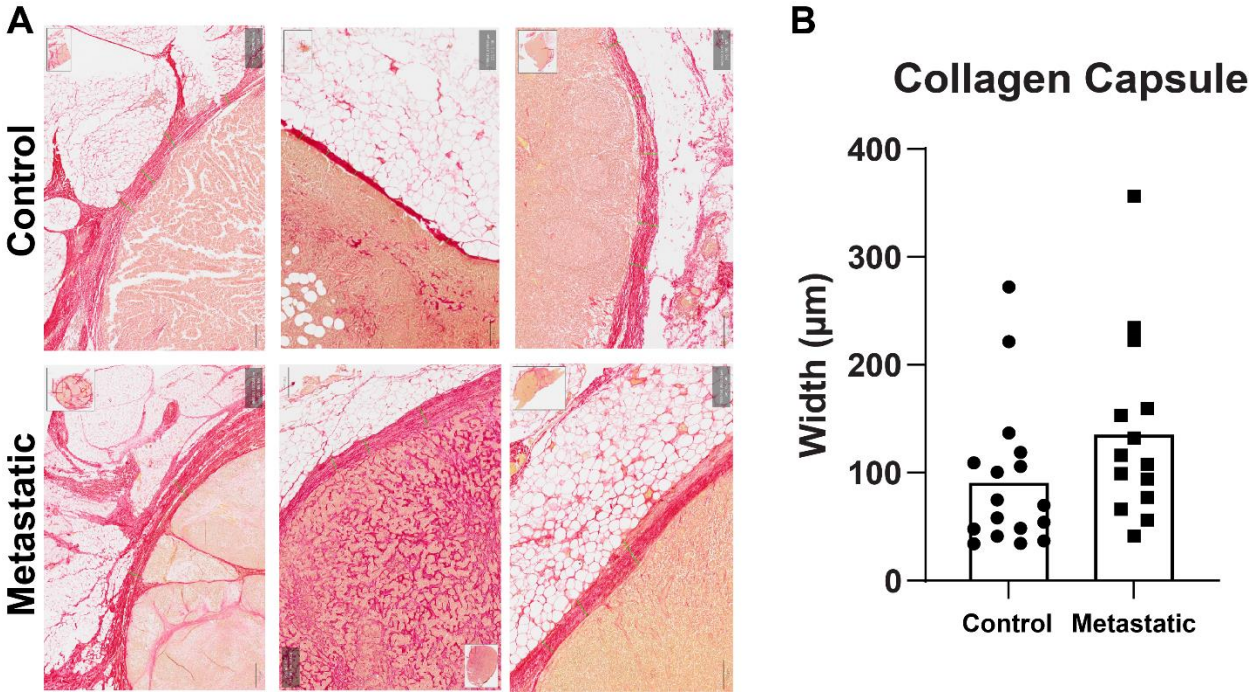

Figure 3.6 Collagen capsule thickness is unchanged between control and metastatic lymph nodes. *Within the tissue, collagen capsules separate adipose tissue from the lymph node (A). Quantification shows no significant differences in capsule thickness between control and cancer lymph node (B).*

Collagen capsules are unchanged by tumor presence

Next, we utilized PSR staining to quantify the collagen capsules (**Figure 3.6.A**). Lymph nodes are often embedded in adipose tissue, visualized in the images as circular cells surrounded by collagen. The capsule separates the lymph node from the body, so that only afferent lymph may enter. As we saw changes to collagen deposition within the node, we sought to determine if collagen structures in the capsules were altered. Overall, we saw a wide variety of capsule thicknesses. There were no significant differences between the control and metastatic nodes (**Figure 3.6.B**). This is likely due to cancer cells infiltrating the lymph node through the afferent lymph and remaining contained within the node until exiting via the efferent lymph.

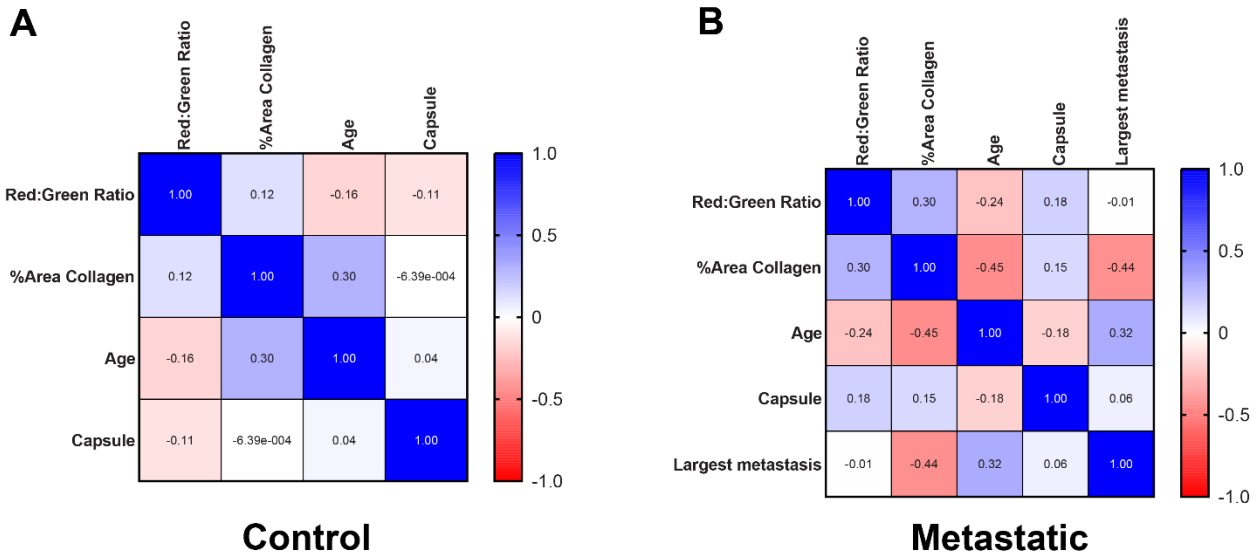

Figure 3.7. There are no significant correlations between collagen and other metrics. *Correlation charts of PSR metrics with age and metastasis in control (A) and metastatic (B) lymph nodes. Positive correlations are blue and negative correlations are red, with saturation indicating strength of the correlation.*

Correlating collagen to age and metastasis

Next, we sought to examine whether the alterations in collagen metrics correlated to age or size of metastasis. Age-related changes to the matrix are well-established, and our patient samples ranged from age 30 to 68 in our control samples and 33 to 81 in our metastatic samples. There were no significant correlations in control lymph nodes between age and other metrics (**Figure 3.7.A**). In the metastatic lymph nodes, no statistically significant correlations were found, but two trends stood out. First, that age is negatively correlated with %area collagen (*p=0.061*). And second, that %area collagen is associated with the largest metastasis as per pathology reports (*p=0.102*). With a larger sample size, these metrics could be examined in more depth.

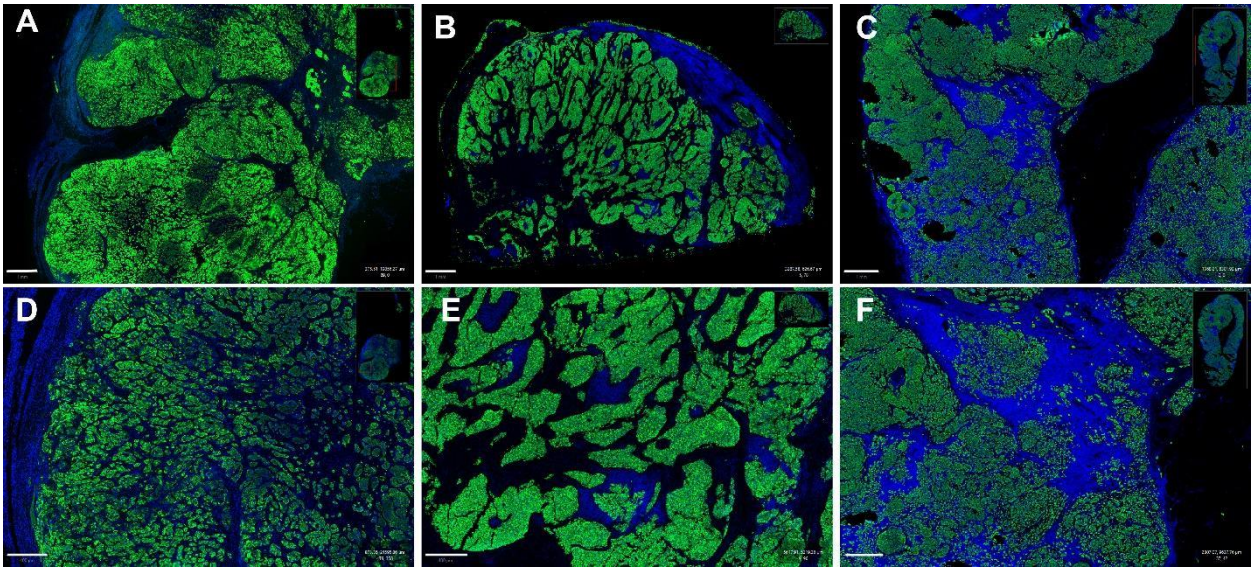

Figure 3.8. Pan-cytokeratin staining in metastatic lymph nodes demonstrates high tumor burden. *Nuclei are stained with DAPI (blue) and pan-cytokeratin is visualized in green. Lymph nodes at lower magnification (A, B, and C) demonstrate pan-cytokeratin throughout the lymph node. Scale bar is 1mm. Higher resolution demonstrates varying patterns of pan-cytokeratin (D,E and F). Scale bar is 400 microns.*

Examining tumor burden in lymph nodes

Next, we sought to examine how tumor burden may correlate to altered collagen within the lymph nodes. A portion of samples were selected to undergo multi-plex fluorescence staining. Among the panel, pan-cytokeratin was visualized. Among the lymph node samples imaged, a high tumor burden was observed. Generally, tumor cells were found all throughout the lymph nodes (**Figure 3.8**). With some samples, non-tumor cells are mostly found at the edge of the lymph node (**Figure 3.8.A and 3.8.B**). In others, non-tumor cells are distributed throughout (**Figure 3.8.C**). Taking a closer look, we see varying organizations of tumor cells (**Figure 3.8.D, E, and F**).

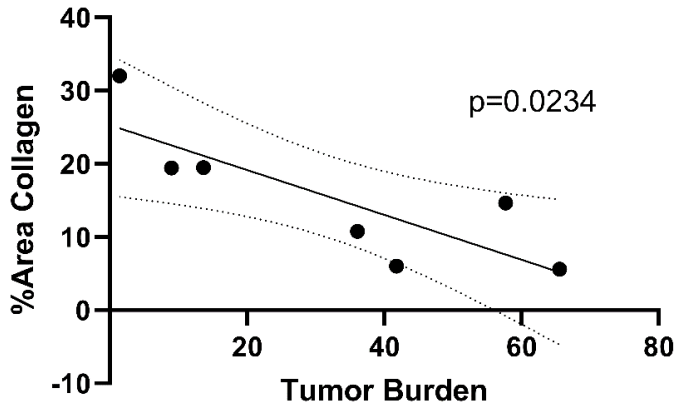

Figure 3.9. Tumor burden negatively correlates with %area collagen.

Increasing tumor burden correlates to less %area collagen

Next, we sought to correlate the amount of pan-cytokeratin staining with the % area collagen in our select samples. Though we were limited in sample size, we saw a significant correlation between the two. As tumor burden increased, the %area of collagen decreased (**Figure 3.9**).

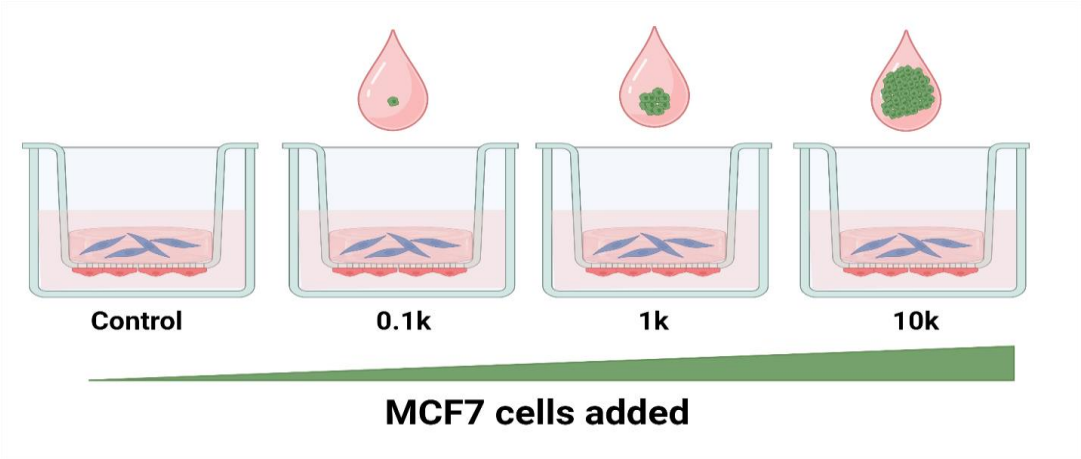

Figure 3.10. Experimental schematic of varying tumor burden. *MCF7 cells are added at different numbers to the lymph node stroma model. Created with biorender.com.*

Adapting the lymph node stroma model to examining tumor burden

As we established that tumor presence and burden are correlated with altered collagen matrix, we wanted to connect altered matrix back to changes in transport. To do this, we took our

previously developed lymph node stroma model (**Chapter 2**) and added varying numbers of MCF7 tumor cells (**Figure 3.10**) to create a metastatic LN stroma model. First, we sought to examine how varying tumor presence would impact the morphology of the LN stroma model.

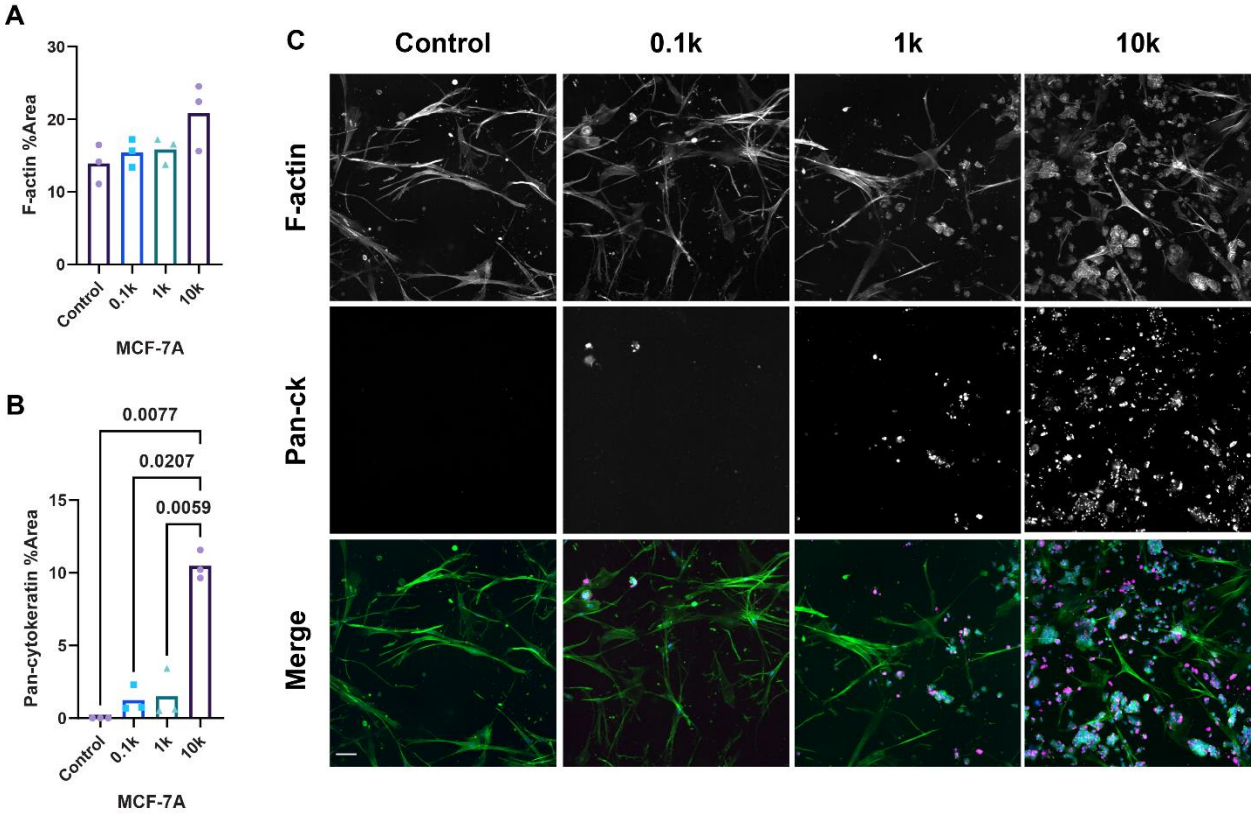

Figure 3.11. A portion of tumor cells are retained at the top of the LN stroma. *Area of f-actin was quantified (A) and normalized to pan-cytokeratin area to only account for FRCs. Pan-cytokeratin area represents tumor cell presence (B). Representative images demonstrate each cell type at the top of the LN stroma model (C). Scale bar is 100 µm. Significance was determined by one-way ANOVA followed by Tukey's t-test, with significant p values (<0.05) reported on each graph.*

Tumor cell presence does not impact FRC network

We first sought to examine where the tumor cells were originally added to the model, to determine how many remained and look at FRC-tumor cell interactions. Overall, the presence of tumor cells did not significantly alter the amount of FRC networking (**Figure 3.11.A**). As

expected, there was significantly more pan-cytokeratin area in the LN stroma models where 10,000 tumor cells were added, compared to all other conditions (**Figure 3.11.B**). Visually, FRCs are very large and elongated cells, while MCF7s are smaller, rounded, and found in clusters (**Figure 3.11.C**).

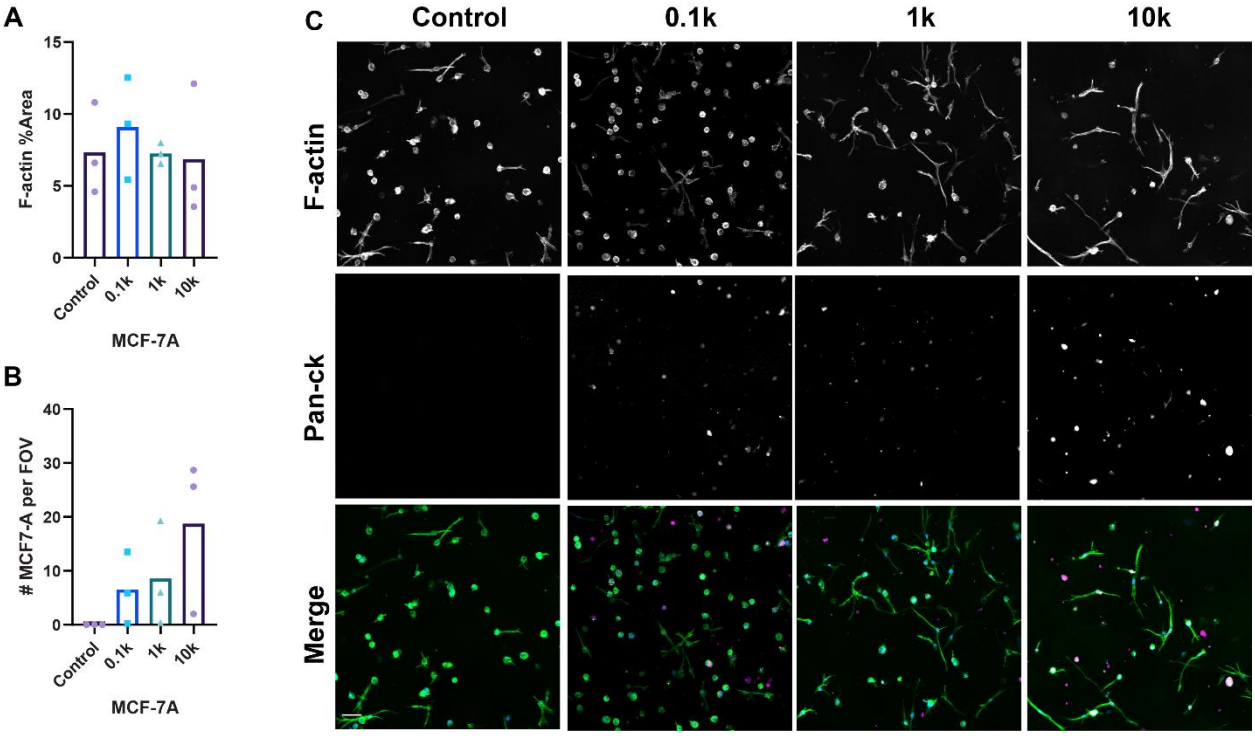

Figure 3.12 Tumor cells invade into the bulk hydrogel in the LN stroma model. *Area of f-actin (A) and area of pan-cytokeratin (B) are quantified. Each data point represents a biological replicate. Representative images demonstrate FRC spread and tumor cell presence (C). Scale bar is 100 microns. Significance was determined by one-way ANOVA followed by Tukey's t-test, with significant p values (<0.05) reported on each graph.*

Tumor cell presence within the hydrogel is variable

Next, we examined within the hydrogel, to capture tumor cells that were in the process of invading. Overall, the area of FRC networks within the gel were not altered by tumor cell presence (**Figure 3.12.A**). Interestingly, the number of MCF7s within the hydrogel varied greatly, though it trended upward with increasing original number of tumor cells added (**Figure 3.12.B**). Visually, it does appear that FRCs had enhanced spreading in the presence of tumor cells (**Figure 3.12.C**).

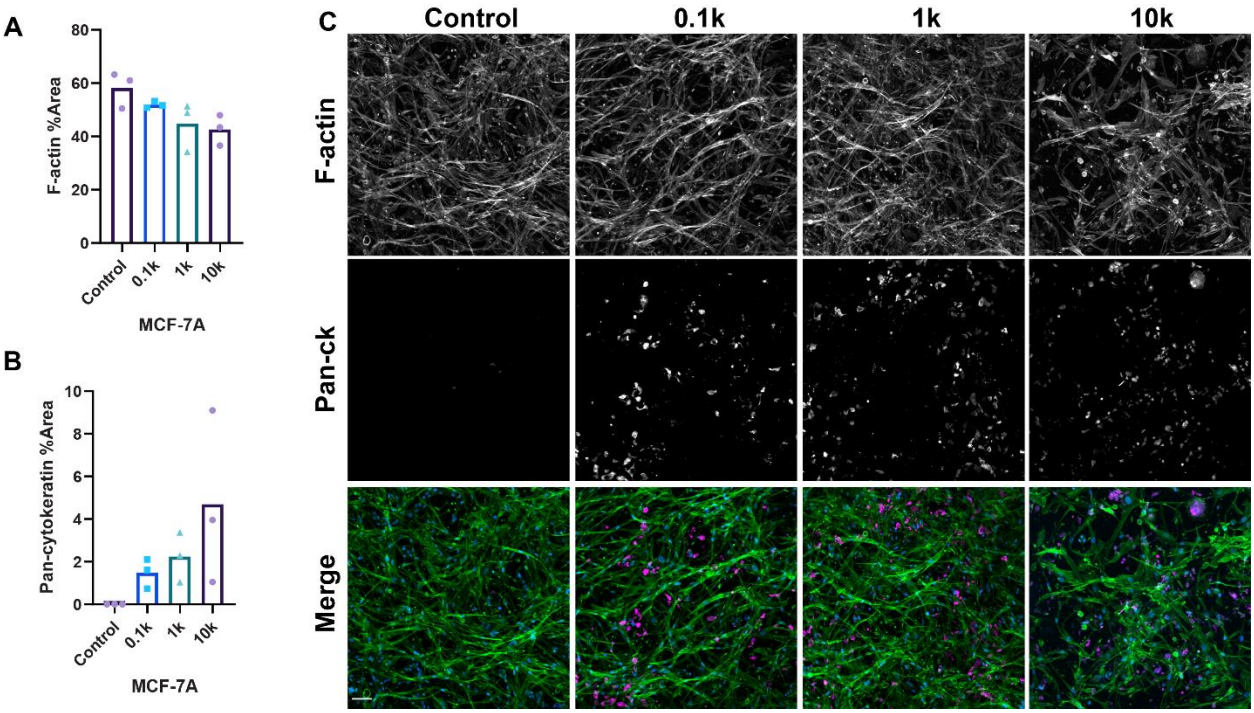

Figure 3.13. Tumor cells invade to the membrane of the LN stroma model. *Area of f-actin (A) and area of pan-cytokeratin (B) are quantified. Each data point represents a biological replicate. Representative images demonstrate FRC coverage and tumor cell presence (C). Scale bar is 100 microns. Significance was determined by one-way ANOVA followed by Tukey's t-test, with significant p values (<0.05) reported on each graph.*

Tumor cells are found associated with FRCs on upper membrane of the LN stroma model

Next, we sought to examine the layer of FRCs found at the bottom of the LN stroma model. These FRCs are in contact with the membrane, and thus, have close crosstalk with the LECs on the other side of the membrane. Overall, FRC coverage trended downward as tumor burden was increased, though this trend was not significant (**Figure 3.13.A**). Additionally, pan-cytokeratin area trended upward as tumor burden was increased, but this was also not significant due to high variability (**Figure 3.13.B**).

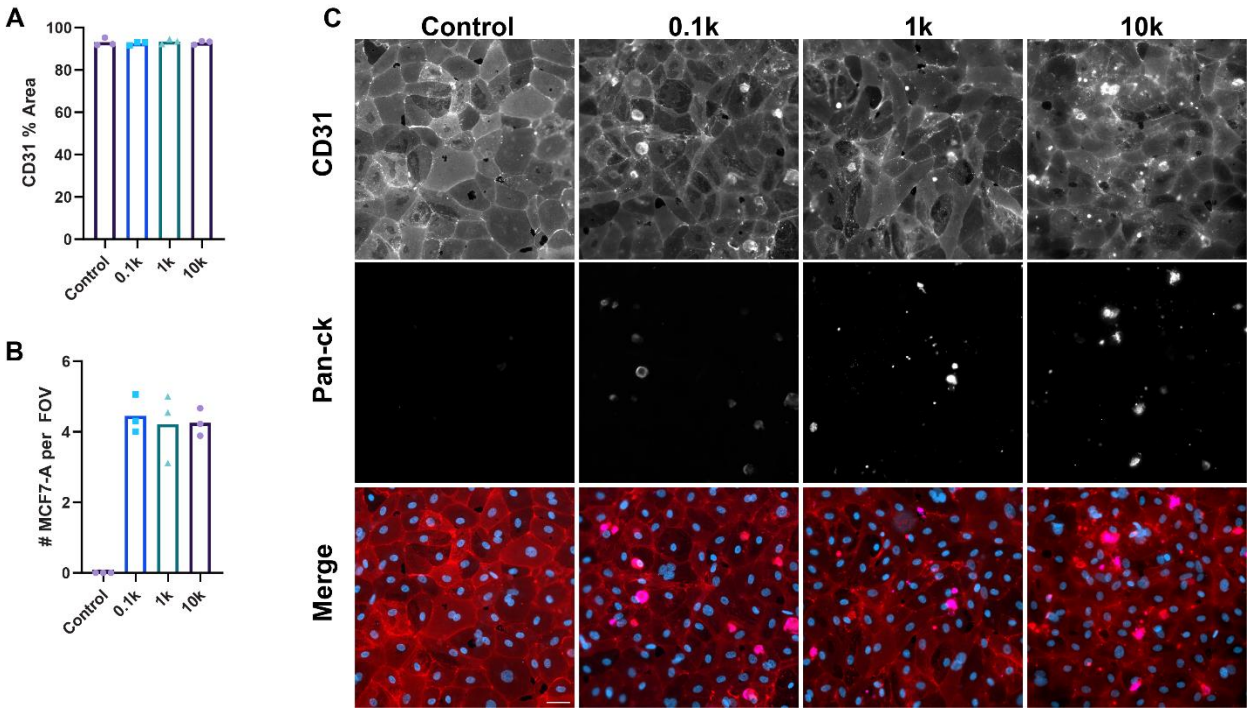

Figure 3.14. Tumor cells traverse the membrane and are found associated with LECs. *CD31 coverage (A) and MCF7 cells per field of view (B) are reported. Representative images demonstrate LEC coverage and tumor cell presence (C). Scale bar is 50 microns. Significance was determined by one-way ANOVA followed by Tukey's t-test, with significant p values (<0.05) reported on each graph.*

Tumor cells traverse the LEC membrane at similar rates, regardless of original burden

Finally, we examined the LEC monolayers. Overall, LEC coverage was not impacted by the presence of tumor cells (**Figure 3.14.A**). Strikingly, a similar number of MCF7s per FOV were found across all original seeding densities (**Figure 3.14.B**). Visually, there are no disrupted junctions in the LEC monolayers, and tumor cells are found in clumps atop the layer, rather than incorporated into it (**Figure 3.14.C**).

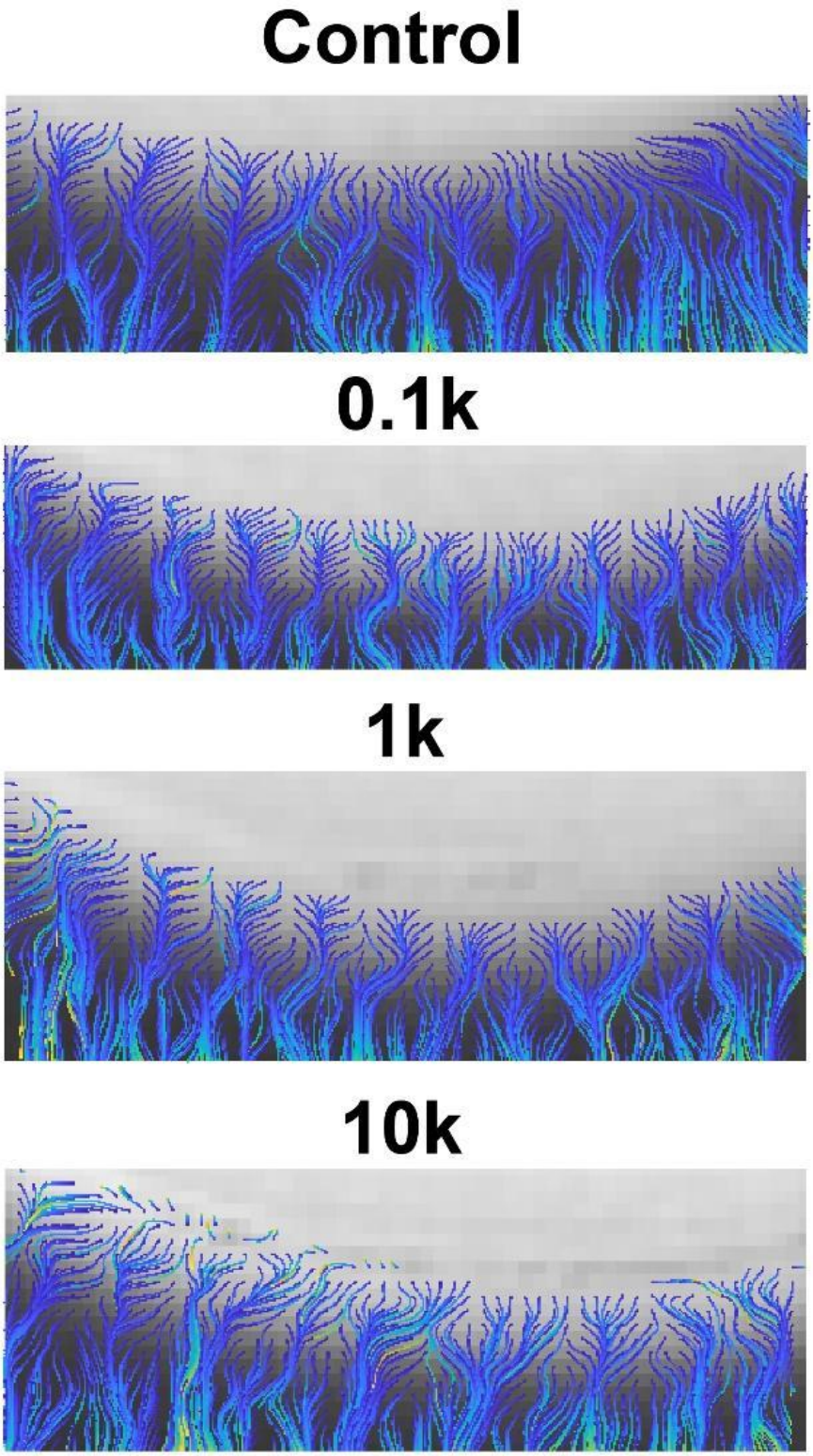

Figure 3.15. Fluid pathways in the LN stroma models are similar across groups. *Streamlines of fluid transport are produced via DCE-MRI imaging.*

Flow magnitude and divergence in the LN stroma model are unchanged with tumor cell presence

Next, we sought to examine how tumor presence might impact fluid movement in our LN stroma models. Using DCE-MRI, the movement of contrast can be used to obtain flow paths and metrics. Streamlines of fluid movement across the models demonstrate no distinct visual differences to fluid paths as tumor burden increases (**Figure 3.15**).

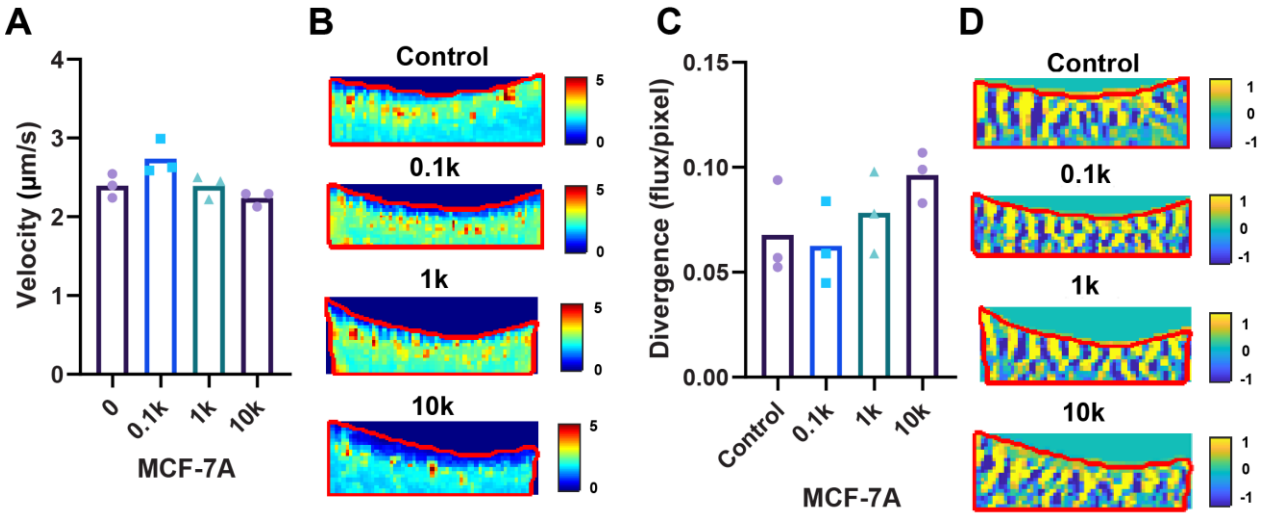

Figure 3.16. Flow magnitude and divergence are unchanged by tumor cell presence. *Average velocity of fluid flow across the entire LN stroma model (A). Each data point represents a biological replicate. Maps of pixel by pixel measurements of flow across the LN stroma models (B). Average divergence of fluid flow across the entire LN stroma model (C). Each data point represents a biological replicate. Maps of pixel by pixel measurements of divergence across the LN stroma models (D). Significance was determined by one-way ANOVA followed by Tukey's t-test, with significant p values (<0.05) reported on each graph.*

Further, there were no significant differences in average flow velocity based on tumor burden (**Figure 3.16.A**). Entire-gel flow maps demonstrate the velocity within each pixel of the image, demonstrating punctate regions of increased interstitial fluid flow (**Figure 3.16.B**).

This methodology also provides measurements of divergence. Divergence represents whether the flow is moving toward a common point (convergence) or away (divergence). Average divergence had more variability between runs than other metrics, but was not

significantly altered by tumor presence (**Figure 3.16.C**). Overall, average divergence values were slightly above zero, demonstrating a slight preference for divergence rather than convergence (**Figure 3.16.C**). Visually, there are alternating regions of positive and negative divergence across the LN stroma models (**Figure 3.16.D**).

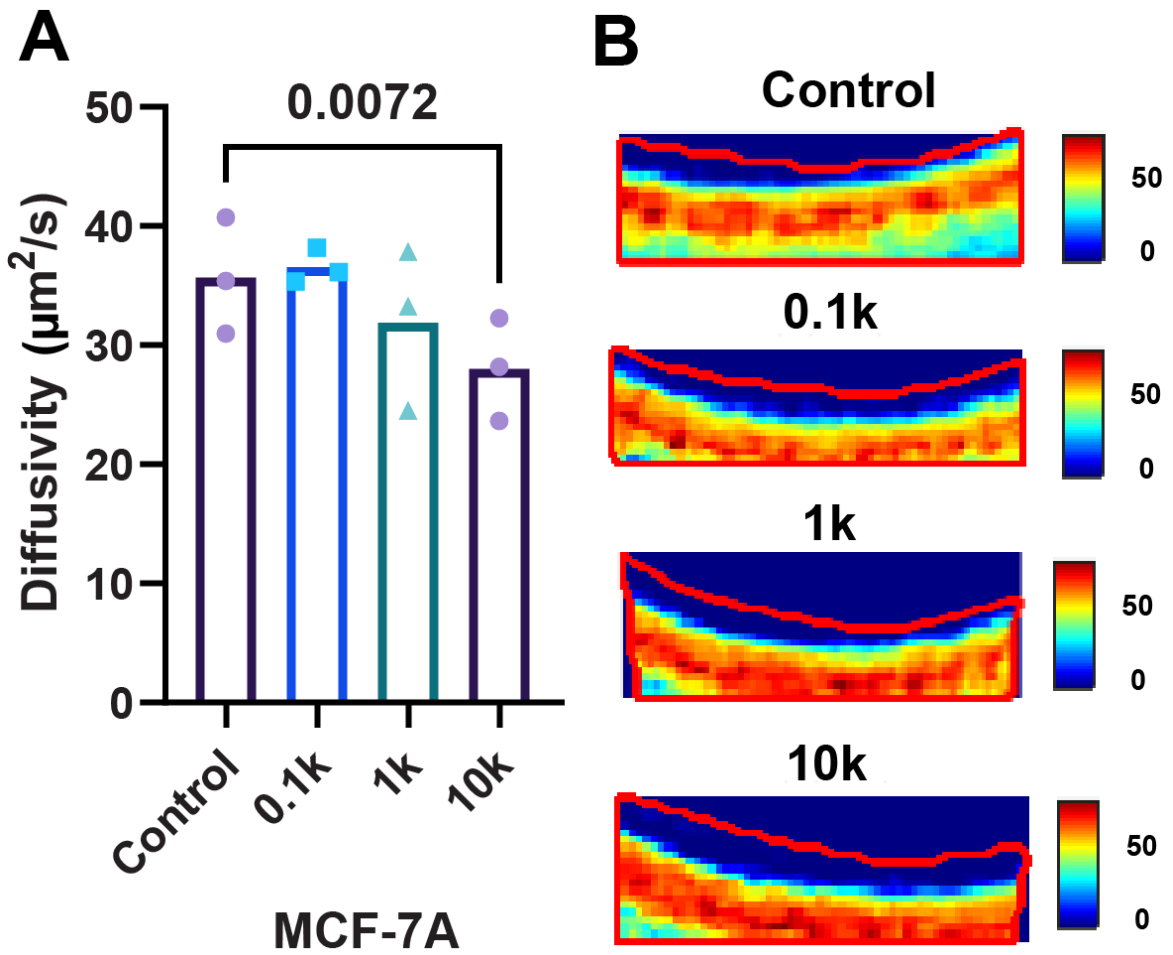

Figure 3.17. Diffusivity decreases with increasing tumor cell burden in vitro. *Average diffusivity across the entire LN stroma model (A). Each data point represents a biological replicate. Maps of pixel by pixel measurements of diffusivity across the LN stroma models (B). Significance was determined by one-way ANOVA followed by Tukey's t-test, with significant p values (<0.05) reported on each graph.*

Diffusivity is decreased in high burden metastatic LN stroma models

Finally, we examined diffusivity. Interestingly, diffusivity was significantly decreased in the highest tumor burden condition, compared to the no-tumor control (**Figure 3.17.A**). Visually,

the highest diffusivity rates are observed in the middle of the LN stroma model, with decreasing diffusivity moving away from the hydrogel (**Figure 3.17.B**).

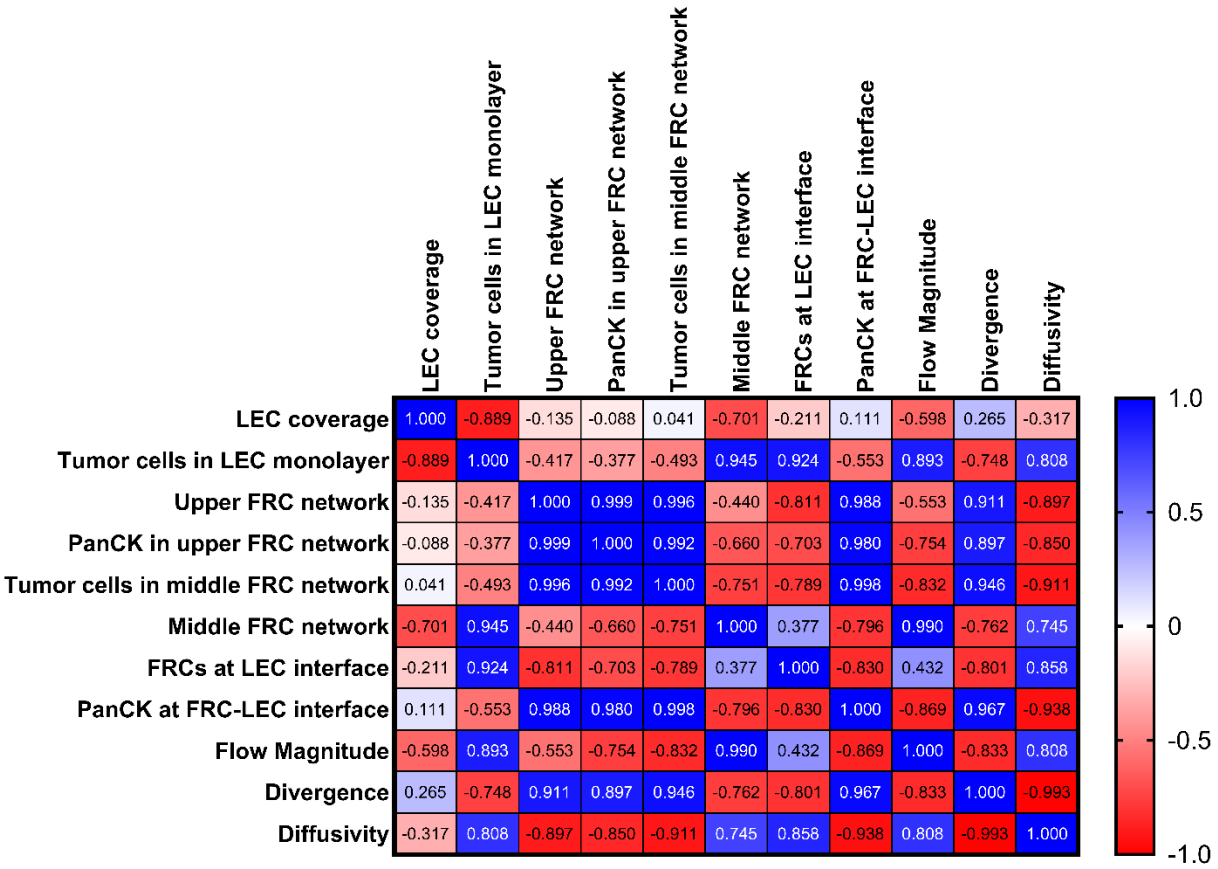

Figure 3.18. There are strong correlations between transport and model morphology. *Positive correlations are blue and negative correlations are red, with saturation indicating strength of the correlation.*

Magnitude correlates to FRC spread within the bulk hydrogel

Next, we sought to determine if any of the morphological measurements obtained in the LN stroma model would correlate to transport metrics (**Figure 3.18**). Interestingly, we found two statistically significant correlations. First, that there is a positive correlation between the area of pan-cytokeratin at the FRC-LEC interface and the amount of tumor cells within the hydrogel

(*p=0.045*). Logically, it is reasonable that a higher number of tumor cells penetrating the LN stroma model would result in more of them reaching the bottom of the stroma. Second, that there is a positive correlation between the area of FRC coverage within the hydrogel and the flow magnitude (*p=0.010*). This finding demonstrates that FRC remodeling does in fact alter transport through the LN stroma.

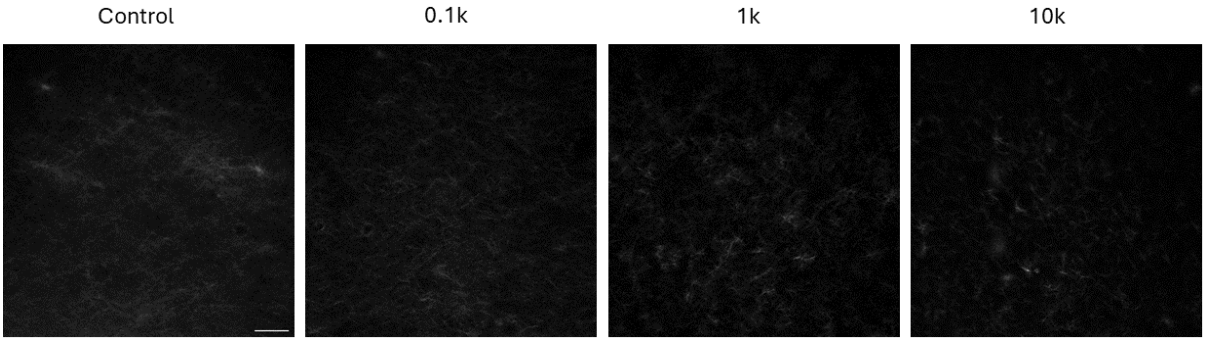

Figure 3.19. Second harmonic generation imaging of lymph node stroma models demonstrates faint collagen fibers. *Scale bar is 50 µm.*

Imaging collagen structure in the LN stroma models

Finally, we sought to utilize second harmonic generation to image the collagen structure in our LN stroma models. Collagen fibers were very small, making visualization difficult. Overall, there are some brighter, and thus larger, fibers, within the 1k and 10k tumor burden models. Future work will emphasize improving matrix visualization via fluorescent staining.

3.5 Discussion

Prior to and after breast cancer metastasis, the lymph node undergoes a number of changes, including matrix remodeling, immunosuppression, enlargement, and changes to interstitial fluid flow. Interestingly, many studies of breast cancer matrix focus on the primary tumor. It has been shown that higher collagen in the primary tumors predicts lymph node metastasis (253,254). When examining the lymph node itself, Rizwan et al demonstrated that breast cancer metastasis increased collagen density in mouse models (239). Herein, we first

sought to confirm this finding in human lymph node samples, and further examine how tumor burden in the node may correlate to matrix changes.

Picrosirius red (PSR) is a well-established stain to label collagen. When visualized under brightfield, collagen fibers appear dark pink to red. Under polarized light, collagen fibers are green and red. This phenomenon is based on the strength of birefringence which correlates to size of the collagen fiber. Under brightfield, we demonstrated that collagen is much more prevalent in the parenchyma of metastatic lymph nodes. Under polarized light, we demonstrated the presence of both red and green collagen fibers, and that there was significantly more of each in metastatic nodes. A benefit of our study was the range of samples collected. In our controls, we examined both male and female lymph nodes. Although sex differences in the immune system are well established (130), we did not see any significant sex differences in collagen structure. A larger, and more controlled, patient cohort could be utilized in the future to examine potential differences further. However, the most striking sex differences in the immune system are in the number and phenotype of lymphocytes. Therefore, collagen structure could be an irrelevant factor.

Additionally, we selected a range of hormone receptor expressions in our metastatic lymph nodes. As there are studies implicating hormone receptors in extracellular matrix remodeling in breast cancer, we sought to determine if these receptors altered collagen deposition in the metastatic lymph node (255,256). However, we saw no differences between triple negative, ER+PR+HER2-, and triple positive metastatic lymph nodes. A larger sample size and more in depth examinations of the matrix will be necessary to determine the involvement of hormone receptors.

Next, we sought to correlate additional metrics, such as age and largest metastasis, to the collagen metrics we measured. Generally, there were not many strong correlations. However, age stood out as a potentially important correlation with %area collagen. Aging is associated with a decline in immune function. Particularly, lymph nodes have reduced immune cell trafficking and sweeping changes to structure, including fibrosis (257). In our control samples, there was a slight positive correlation between age and %area collagen, but it was not statistically significant. Interestingly, the opposite was observed in the cancer samples: a negative correlation that was not statistically significant. As age is one of the most significant risk factors for cancer, it would be of interest to develop models examining how the aging lymph node may be more susceptible to metastasis due to altered collagen structure.

We followed up our examinations of the matrix with looking at tumor burden in a select sample grouping. Fascinatingly, we found a significant negative correlation between tumor burden and % area collagen. This was surprising, as metastasis is associated with higher matrix deposition. However, breast cancer cells are known to secrete high levels of proteolytic enzymes. Further, there is evidence that cancer-associated fibroblasts are the main matrix depositors, rather than cancer cells themselves (258). Thus, if tumor cells have grown so uncontrollably that the fibroblasts have been pushed out or starved, there could be an imbalance in matrix degradation and deposition.

We next began to develop an in vitro model of tumor burden in the LN stroma. The LN stroma model, developed in Chapter 2, consists of FRC-laden PhotoHA-collagen hydrogel within a tissue culture insert. On the bottom of the tissue culture insert membrane, a monolayer of LECs is seeded. Throughout the LN, the FRCs maintain an extensive conduit network made of extracellular matrix. Thus, the hydrogel represents the LN parenchyma. The LEC monolayer

represents the efferent lymphatics, where immune cells, and potentially cancer cells, egress. We added differing numbers of MCF7 breast cancer cells to the top of the model. Notably, the vast majority of the tumor cells remained at the top and did not penetrate the model. A variable amount of tumor cells were found within the bulk hydrogel. Most interestingly, regardless of how many tumor cells were originally added to the model, the same number of MCF7s invaded all the way through and were found adhered to the LEC monolayer, which was left completely intact post-invasion. Notably, our studies were performed under static conditions. However, transmural flow and luminal flow are implicated in enhancing tumor cell transmigration across LEC monolayers in vitro (165,259). Thus, adding flow could alter MCF7 invasion in the model. Additionally, the presence of tumor cells did not negatively impact the FRCs at the top or middle of the model. With notable displacement of healthy lymph node tissue in the human samples we observed, it is possible that more tumor cells, or a longer culture time, would be necessary to represent advanced metastasis. Interestingly, there was a trend toward decreased F-actin area at the interface between the FRCs and LECs. This could represent a decrease in invasive behavior from the FRCs.

Next, we sought to utilize our model to determine if tumor cell presence would alter transport properties in the LN stroma model. Largely, transport was unaffected. Visually, fluid pathways were unchanged. Additionally, flow velocity and divergence were consistent throughout all conditions. However, diffusivity was significantly decreased in the 10k tumor cell condition. Matrix density is known to alter diffusivity in hydrogels (260,261). Interestingly, tumors with higher collagen content have lower diffusion (262). We did attempt to examine the collagen structure in our models using second harmonic generation. Collagen fibers were small and difficult to visualize. However, some brighter fibers were observed in the 1k and 10k tumor

cell models. It will be essential to optimize matrix visualization by fluorescent staining or higher magnification to make a connection between FRC spread, collagen structure, and transport through the model.

Most strikingly, upon correlating the morphology of the models with transport metrics, we found a strong positive correlation between FRC area coverage within the bulk hydrogel and the magnitude of flow velocity. We established in Chapter 2 that the presence of LN stroma altered the divergence of flow, thus demonstrating the ability of FRCs to alter transport. In this chapter, we have now proven that the extent of FRC spread directly correlates to increasing magnitude, strengthening the evidence that FRCs play an essential role in modulating fluid flow in the lymph node.

Overall, we have adapted the LN stroma model toward studying tumor burden, breast cancer migration, and transport properties within the stroma. Future work will emphasize the study of how FRCs are altering transport in the microenvironment under static conditions and will further physiologically relevance with the addition of interstitial fluid flow.

CHAPTER 4

MODELING THE MENINGEAL LYMPHATICS LUMEN FOR APPLICATIONS IN OFF-TARGET CHEMOTHERAPEUTICS AND CENTRAL NERVOUS SYSTEM METASTASIS

4.1 Summary

The meningeal lymphatics are essential for fluid regulation and immunosurveillance in the central nervous system (CNS), delivering waste to the cervical lymph nodes. Only conclusively proven to exist less than a decade ago (167,168), the field of meningeal lymphatic biology is ever-expanding. With implications in cancer metastasis and cognition, additional tools are needed to study this system's physiology. Within, we establish the first in vitro model of the meningeal lymphatics. Consisting of a monolayer of lymphatic endothelial cells and a monolayer of meningeal fibroblasts on either side of a tissue culture insert membrane, we provide a facile and accessible model that can be used to examine barrier integrity and immune cell trafficking. We first apply our model to examining off-target effects of systemic chemotherapeutics commonly used to treat breast cancer. We show that docetaxel, a taxane chemotherapy, caused significant disruption to the meningeal lymphatic model. We next apply our model toward examining CNS leukemia. We show that methotrexate, commonly used as a CNS-directed chemotherapy to treat leukemia, also caused significant disruption to the meningeal lymphatics. These results suggest that off-target impacts to the meningeal lymphatics are an essential consideration in chemotherapy regimen development. Additionally, we show that leukemia cells egressed from the meningeal lymphatics model and that conditioned media from a lymph node stroma model under flow acted as a chemoattractant. Finally, we begin to examine leukemia cells in the lymph node stroma, toward developing a model that connects the meningeal lymphatics and lymph node models. Overall, the meningeal lymphatic model developed within has broad reaching applications toward studying the contribution of the meningeal lymphatics in cancer treatment and metastasis.

4.2 Docetaxel-mediated disruption to meningeal lymphatics integrity in vitro

Portions of this chapter are the author's original writing taken from "Demonstration of chemotherapeutic mediated lymphatic changes in meningeal lymphatics in vitro, ex vivo, and in vivo" by Roberts and Hammel* et al* (263).

4.2.1 Introduction

The meningeal lymphatics, which drain the central nervous system (CNS) have been implicated in a variety of CNS diseases (167,168). The meninges in which they reside consist of three protective layers surrounding the brain that provide insulation between the skull and the brain, serve as an immune cell reservoir, and drain cerebrospinal fluid (CSF) from the CNS. Within the meninges, the lymphatic system consists of dural and basal meningeal lymphatic vessels that regulate immune cell trafficking and allow CSF drainage to the cervical lymph nodes. Previous studies show that the meningeal lymphatics are involved in brain tumor drainage (172,264), Alzheimer's disease (170), and traumatic brain injury (171). However, the degree to which the meningeal lymphatics contribute to CNS pathophysiology in response to chemotherapeutic treatment has yet to be determined.

Chemotherapy is one of the most conventional forms of cancer treatment as a primary or adjuvant therapy following resection and/or radiotherapy. However, there are still known and unknown risks and side effects in response to chemotherapeutics (6,265). Most chemotherapeutics are intravenously injected into patients, circulating throughout the body to encounter all tissues, including the target tumor. After entering a tissue, chemotherapy drains via the lymphatic system, where it can have counter-therapeutic effects. Systemic chemotherapy recapitulating a breast cancer treatment regimen using either carboplatin or docetaxel in pre-clinical models leads to lymphangiogenesis in the primary tumor site and draining lymph nodes

that can promote invasion of cancer cells (6,265). However, the potential impact of chemotherapy on the distant meningeal lymphatics following systemic circulation in breast cancer is not fully defined.

With the renewed interest in the meningeal lymphatics, the development of in vitro models is crucial to answering biological questions and understanding the physiology of this essential lymphatic system. In vitro models allow the examination of crosstalk between cell types in an isolated and customizable system. Here we have developed an in vitro human cell–based model of the meningeal lymphatics to compare to in vivo studies. This model can provide future insights to better inform treatment of patients and efforts to ameliorate cognitive deficits post-treatment and increase patient quality of life.

4.2.2 Methods

Cell culture

Human lymph node lymphatic endothelial cells (LECs) (Sciencell) were cultured on fibronectin coated flasks in VascuLife® VEGF-Mv media (Lifeline Cell Technology). Human meningeal cells (MCs) were cultured on poly-L-lysine coated flasks in MenCM complete media (Sciencell).

Tissue culture insert model

12-mm tissue culture inserts with 8 µm pore size (Corning) were inverted in 6 well plates. LECs were seeded on the underside of the insert at 50,000 per insert and cultured for 2 h before re-inverting in a tissue culture plate. After 48 h, 75,000 MCs were seeded within the tissue culture insert. The co-culture model was grown for an additional 24 h to reach confluence before assays were performed. At confluence, models were treated with either 1 µM carboplatin, 1 µM docetaxel, both carboplatin and docetaxel, or vehicle (DMSO) in Vasculife® for 24 h. For

blocking studies, 100 µg of VEGF Receptor 3 Monoclonal Antibody (ThermoFisher Cat.#16-5988-85) or isotype control (rat monoclonal IgG2a kappa, Cat.#16-4321-85) were added during the course of chemotherapy treatment for 24 hours. For T cell transmigration, the chemotherapeutic agent and blocking antibodies were removed and the model was inverted. Activated T cells were added to the membrane at 50,000 per insert for 20 minutes to allow attachment. Then, the model was re-inverted and cultured for 24 hours, followed by collection of media above the insert and manual counting of T cells.

Permeability assays

300 µL of 10 µg/mL FITC dextran 10,000 MW, anionic, lysine fixable (Invitrogen) in basal Vasculife® was added inside the tissue culture insert. 300 µL of basal Vasculife® was placed underneath the insert. After 6 h, media from underneath the insert was collected and analyzed on a CLARIOstar plate reader. Samples were compared to a control of 300 µL of 10 µg/mL FITC dextran diluted with 300 µL of basal Vasculife® to represent 100% transport.

Immunofluorescence

Tissue culture inserts were fixed in 4% PFA for 15 min. The membranes of each insert were carefully cut out and mounted on positively charged slides for staining. Donkey serum was used to block nonspecific binding. Membranes were stained with sheep anti-human CD31 (R&D) at a 1:40 dilution and mouse anti-human alpha smooth muscle actin (Abcam) at a 1:200 dilution for 2 h at room temperature (RT) followed by donkey anti-sheep Alexa Fluor 647 secondary antibody (Invitrogen) at a 1:400 dilution and donkey anti-mouse Alexa Fluor 555 antibody (Invitrogen) at a 1:1000 dilution for 1 h at RT. Membranes were then stained with 488 Phalloidin for F-actin (Invitrogen) at a 1:400 dilution and DAPI (Invitrogen) at a 1:5000 dilution

for 45 min. Slides were then mounted with Fluoromount, allowed to dry overnight, sealed with nail polish, and stored at 4°C. Slides were imaged on a Zeiss Axio Observer.

Proliferation assay

The Click-iT™ EdU Cell Proliferation Kit for Imaging, Alexa Fluor™ 488 dye (ThermoFisher) was utilized to quantify proliferation in the meningeal lymphatic (ML) model. During the last 6 h of culture, 10 µM EdU was added to the culture media. At 24 h, tissue culture inserts were fixed in 4% PFA. EdU was then detected as specified by the manufacturer. Finally, insert membranes were stained for CD31 and αSMA as described above.

Image Quantification

For total area of fluorescence in the tissue engineered model, images were thresholded using Fiji and total area of signal was measured. For proliferation, total nuclei were quantified via DAPI stain and proliferating cells were quantified via positive EdU staining. Proliferation was reported as a percentage of EdU+ cells out of total cell number. For LEC morphology, LECs were traced using Fiji and area and aspect ratio were recorded. Cells with disrupted junctions were counted and reported as a percentage of total cell count.

Statistical analysis

All statistical analysis was conducted through Graphpad Prism 10.2.2 (GraphPad Software). One-way ANOVA was performed for groups of three or more with statistical significance indicated by $p<0.05$. When significance was identified, ad hoc *t*-tests (ratio paired or unpaired Student's t-test) were performed to assess significance between groups with $p<0.05$ indicating significance. For comparison of multiple factors comparing coverage, proliferation, and cell count of cells alone or in combination in response to vehicle, carboplatin, or docetaxel within our in vitro model, two-way ANOVA (statistical significance $p<0.05$) followed by a

Tukey's multiple comparison test was used. All graphs represent mean ± standard error mean with individual statistical results discussed with the presented data.

4.2.3 Results

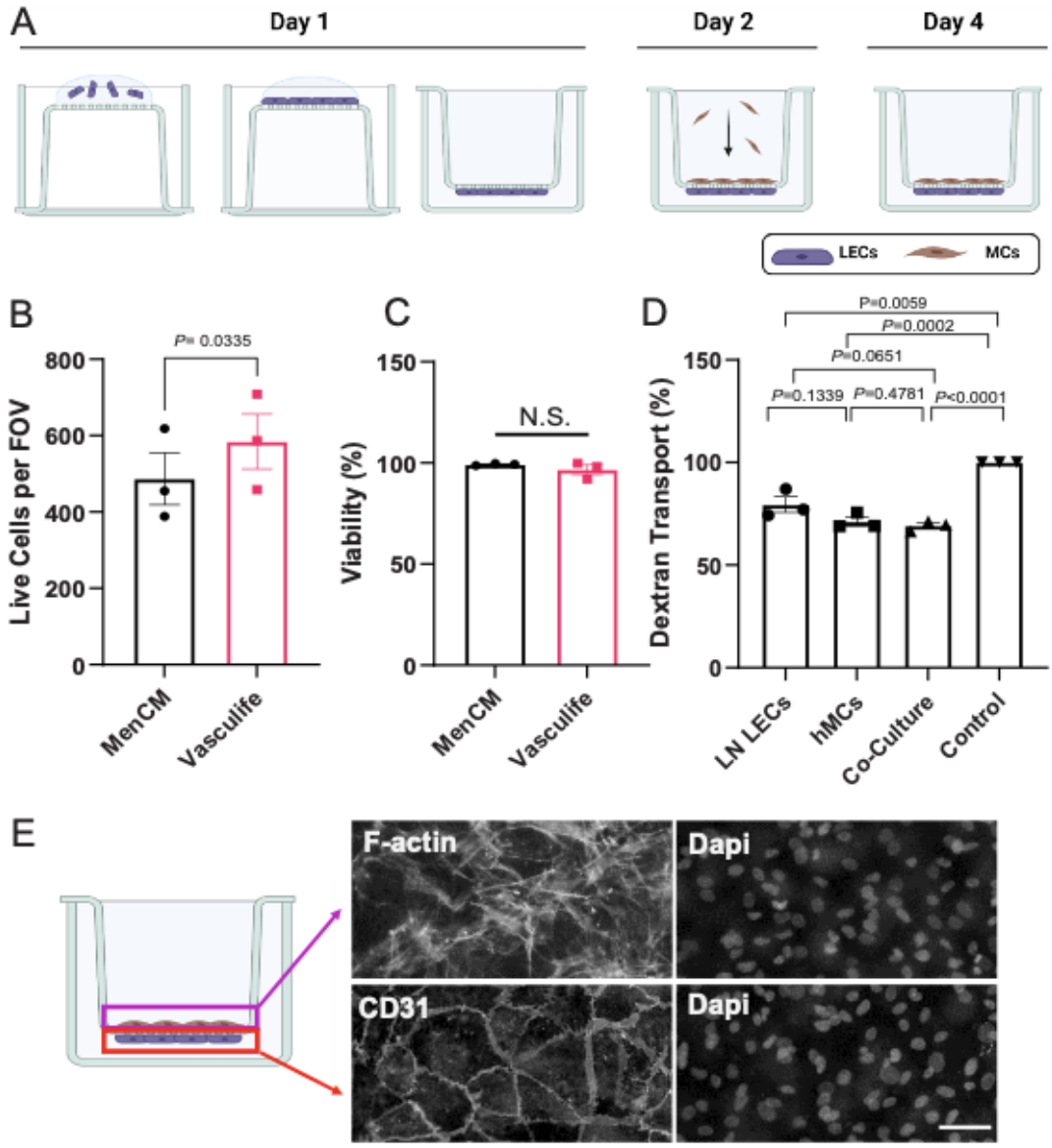

Figure 4.1. In vitro meningeal lymphatic model development. *LECs are seeded on the underside of a tissue culture and meningeal cells are seeded into the tissue culture insert (A). Suitability of co-culture media is verified via total meningeal cells per field of view (B) and viability of meningeal cells in Vasculife (C). Permeability is quantified via dextran transport assay (D). Representative images of each monolayer are shown, with meningeal cells stained for F-actin, LECs stained for CD31, and nuclei stained with DAPI (E). Scale bar is 50 µm. Data in bar graphs represents mean +/- SEM with each biological replicate shown (n=3). Significance was determined via one-way ANOVA with a post hoc unpaired Students' t-test.*

Development of in vitro meningeal lymphatics model

We first sought to develop a novel in vitro model of the meningeal lymphatics to probe chemotherapy response in a controllable high-throughput and high-volume setting. To represent the lumen of a meningeal lymphatic model, LECs were seeded and allowed to grow a complete monolayer on the underside of a tissue culture insert followed by meningeal cells (MCs) seeded inside of the insert (**Figure 4.1.A**). To support LEC viability, Vasculife® was selected as the model's media. In Vasculife®, MCs had significantly more live cells per field of view compared to their preferred media, MenCM (**Figure 4.1.B**). Additionally, MC viability was unchanged between MenCM and Vasculife® (**Figure 4.1.C**). Further, barrier function of the model compared to monoculture controls was examined via dextran permeability assay where MCs had higher barrier function than LECs (**Figure 4.1.D**). Distinct monolayers were visualized in the complete model via CD31 and F-actin staining, overall demonstrating minimal transmigration and confirming integrity of our in vitro model (**Figure 4.1.E**).

Docetaxel induces meningeal cell disruption in the ML model

Informed by our previous studies examining the impact of standard-of-care platinum and taxane chemotherapy on lymphatic endothelial cells, our in vitro model was then utilized to examine response to carboplatin and docetaxel treatment on the meningeal lymphatics. MCs in the model were highly aligned and elongated when in a confluent monolayer under vehicle and carboplatin treatment (**Figure 4.2.A**). Alone, MCs demonstrate a typical fibroblast morphology and are elongated (**Figure 4.3**). However, docetaxel treatment causes morphological changes with the MCs beginning to form clumps or plaques (**Figure 4.2A, Figure 4.3**). In co-culture with LECs, MCs formed a significantly more complete monolayer compared to when cultured alone (**Figure 4.2.B**), which was also evident during

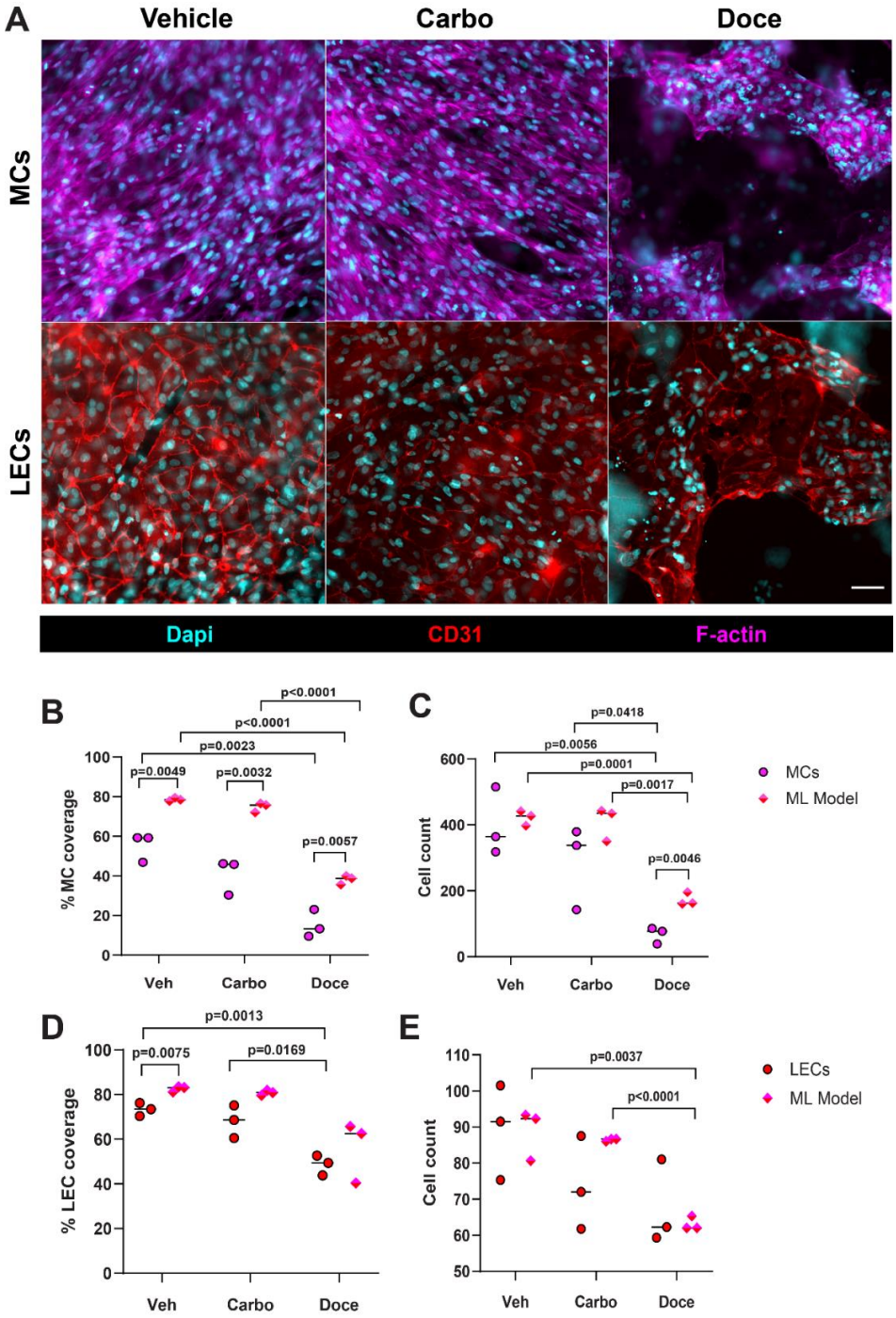

Figure 4.2. Docetaxel disrupts LEC and MC coverage and alters proliferation. *ML models were treated with 1 µM carboplatin, 1 uM docetaxel, or vehicle (DMSO) for 24 hours. Representative images of ML models are shown with nuclei stained with DAPI (cyan), MCs stained for F-actin (magenta), and LECs stained for CD31 (red) (A). Scale bar is 50 µm. Coverage (B,D) and count (C,E) of MCs and LECs is reported. Data shown represents the mean with each biological replicate shown (n=3). Significance was determined via two-way ANOVA between the vehicle and chemotherapeutic treatments with post hoc Tukey's multiple comparison test.*

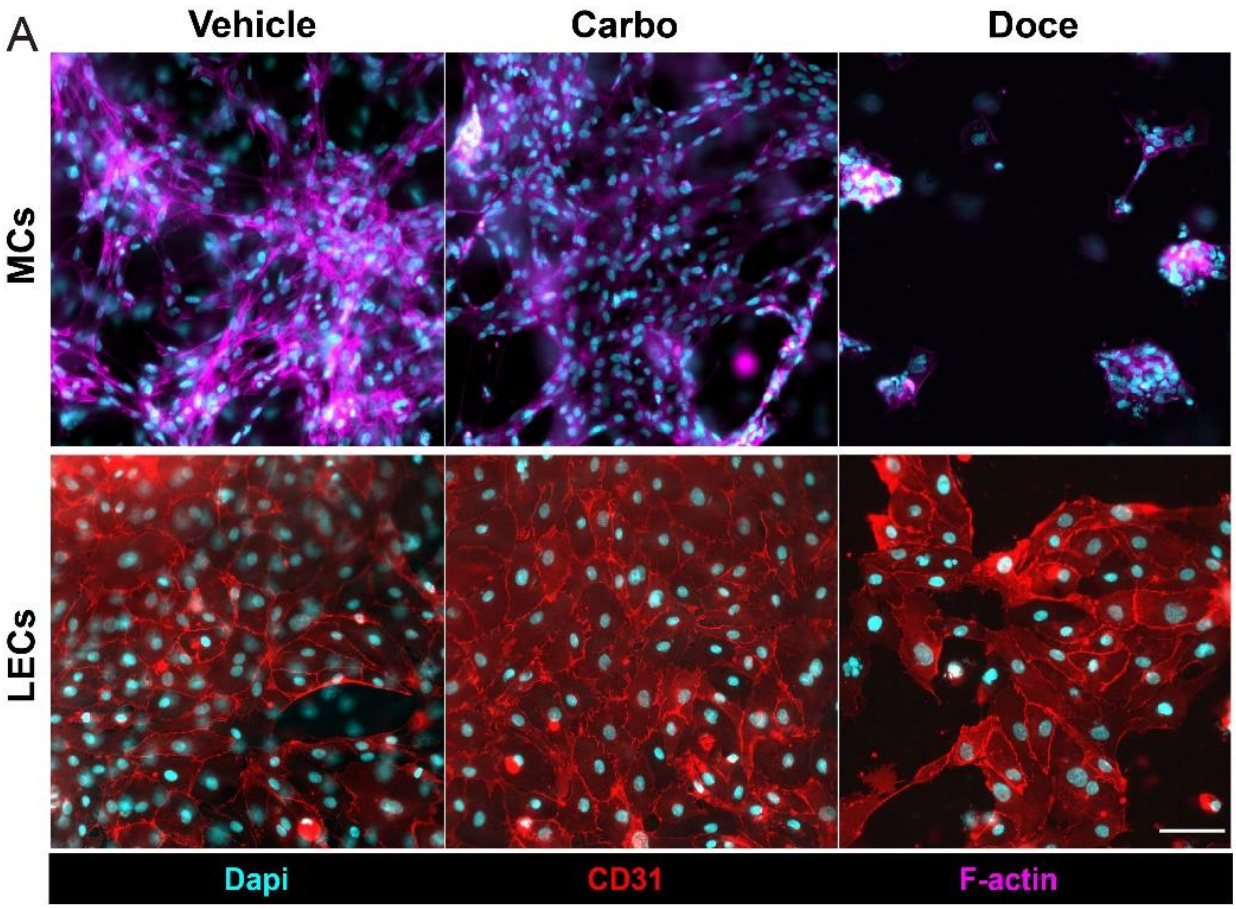

Figure 4.3. Monoculture controls are treated with 1 µM carboplatin, 1 µM docetaxel, or vehicle (DMSO) for 24 h. *Representative images of monocultures controls are shown with nuclei stained with DAPI (cyan), MCs stained for F-actin (magenta) and LECs stained for CD31 (red). Scale bar is 50 µm.*

chemotherapy treatment (**Figure 4.2.B**). Carboplatin did not significantly decrease the MC coverage in the ML model compared to the vehicle but showed a more complete monolayer in co-culture than alone (**Figure 4.2.B**). MCs also had higher MC coverage in co-culture than alone when treated with docetaxel (**Figure 4.2.B**). Further, docetaxel caused significant disruption of the monolayer compared to the vehicle and carboplatin for both co-culture and MCs alone (**Figure 4.2.B**). Additionally, MC count was not significantly different when alone vs in co-culture in the vehicle or carboplatin controls but was higher in co-culture for docetaxel treated groups (**Figure 4.2.C**), suggesting differences in cell spread. Overall, co-culture with LECs had a

positive impact on MC coverage and showed decreased disruption during chemotherapy treatment.

LEC coverage is decreased with docetaxel treatment in the ML model

LECs showed less benefit from co-culture during chemotherapy treatment. Representative images demonstrate similarly intact monolayers of LECs (**Figure 4.2A, Figure 4.3**) in the vehicle and carboplatin groups. Docetaxel-treated groups show incomplete LEC monolayers and altered CD31 staining (**Figure 4.2.A, Figure 4.3**). In the vehicle group, LEC coverage was unchanged between co-culture and when cultured alone (**Figure 4.2.D**). Interestingly, LEC coverage was significantly higher in co-culture compared to alone when treated with carboplatin (**Figure 4.2.D**). Additionally, LEC count (**Figure 4.2.E**) was not significantly different between co-culture and the LEC-only control for any of the chemotherapy groups. Carboplatin was shown not to disrupt LEC monolayer coverage compared to vehicle controls (**Figure 4.2.D**). Docetaxel significantly decreased LEC coverage in co-culture and alone compared to the vehicle (**Figure 4.2.D**). Compared to carboplatin, docetaxel significantly decreased LEC coverage in LECs cultured alone (**Figure 4.2.D**).

LEC junctions are disrupted by docetaxel treatment in the ML model

In addition to coverage, LEC junctions, area, and aspect ratio were examined. LECs had more disrupted junctions when cultured alone than in co-culture in the vehicle and docetaxel groups (**Figure 4.4.A,B**). Chemotherapy did not increase junction disruption in LEC monocultures (**Figure 4.4.A,B**). However, in co-culture, LECs had more disrupted junctions when treated with docetaxel (**Figure 4.4.A,B**). To further examine changes to LEC morphology, area and aspect ratio were quantified. LECs did not have significant changes to area across any

groups or treatments (**Figure 4.4.C**). However, LECs had a higher aspect ratio, meaning they were more elongated, when cultured alone compared to co-culture in both the vehicle and carboplatin treated groups (**Figure 4.4.D**). In the meningeal lymphatics model, LECs were more elongated when treated with docetaxel compared to the vehicle and carboplatin (**Figure 4.4.D**). These data further suggest differences in cell spread and size during co-culture and chemotherapy treatment.

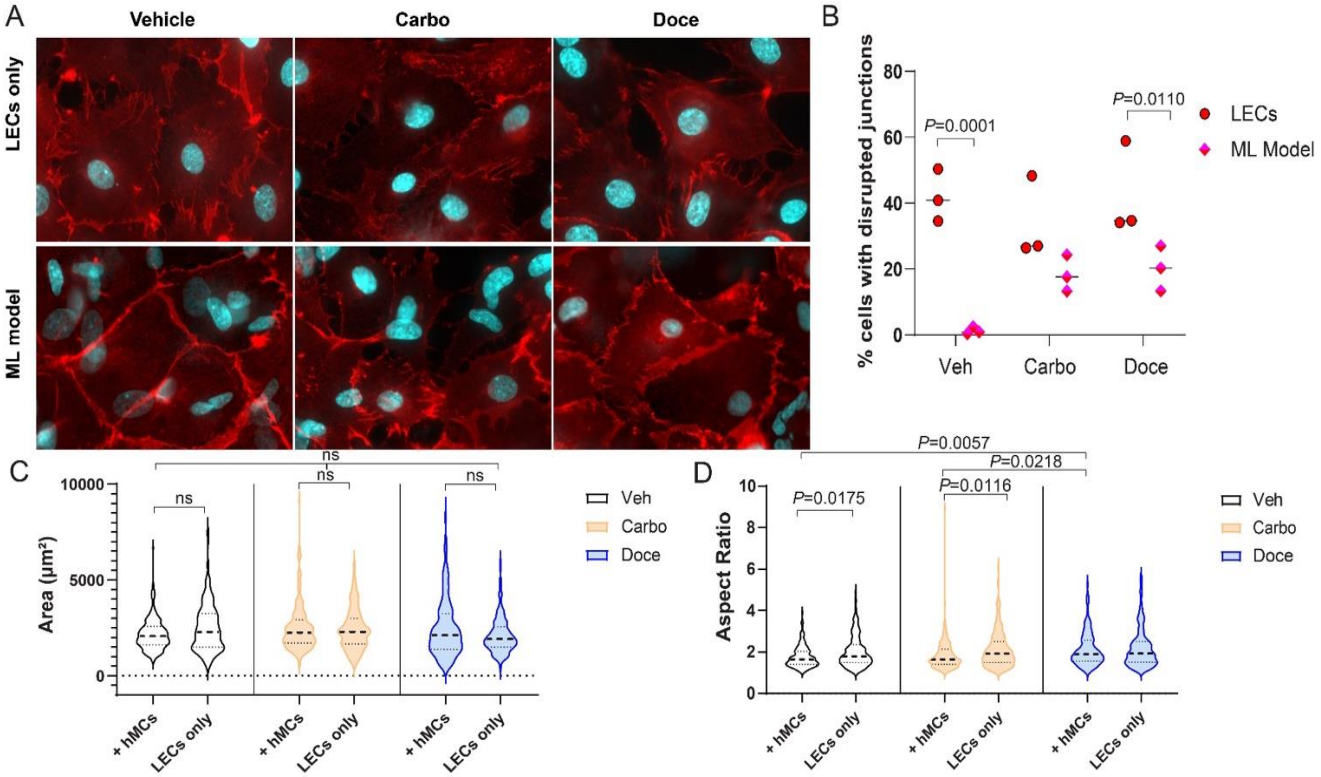

Figure 4.4 LEC junctions and morphology are impacted by chemotherapy treatment and co-culture. *ML models were treated with 1 µM carboplatin, 1 µM docetaxel, or vehicle (DMSO) for 24 hours. (A) Representative images of LECs are shown with nuclei stained with Dapi (turquoise) and LECs stained with CD31 (red). (B) Quantification of percentage of LECs with disrupted junctions. Significance was determined via two-way ANOVA (P<0.0001) with a post-hoc Tukey's multiple comparison test to calculate represented p-values. (C, D) Quantification of LEC area alone and within the in vitro model in co-culture conditions. (D,E) Quantification of aspect ratio of LECs alone and within the in vitro model in co-culture conditions. For LEC morphology, data shown represents mean ± SEM from 80 LECs that were quantified (n=3). Significance was determined via two-way ANOVA (P<0.01) with a post-hoc Tukey's multiple comparison test to calculate represented p-values.*

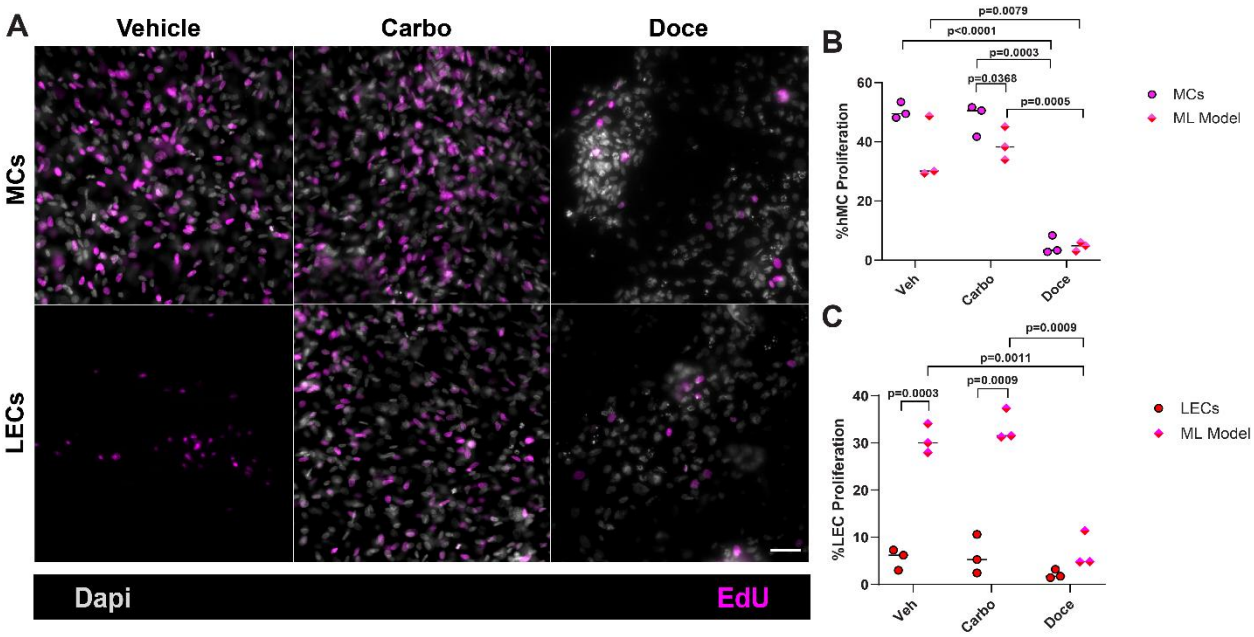

Figure 4.5. Proliferation in the ML model is altered by chemotherapy. *10 µM EdU is added to the culture media during the last 6 hours of treatment. Representative images of proliferation in the ML model are shown with all nuclei stained with DAPI (gray) and EdU-positive cells (magenta) (A). Scale bar is 50 µm. Percentage of proliferation of MCs (B) and LECs (C) is quantified. Data shown represents the mean with each biological replicate shown (n=3). Significance was determined via two-way ANOVA between the vehicle and chemotherapeutic treatments with post hoc Tukey's multiple comparison test.*

LEC and MC proliferation is altered by chemotherapy in vitro.

The mechanism of action of carboplatin and docetaxel relies on proliferation. Next, we sought to identify how crosstalk and chemotherapy altered the proliferation of each cell type. MCs had higher proliferation alone compared to co-culture in the vehicle control (**Figure 4.5.A,B, Figure 4.6**). With carboplatin treatment, proliferation was unchanged in MCs in co-culture compared to MCs cultured alone (**Figure 4.5.A,B, Figure 4.6**). Docetaxel-treated groups had very low levels of proliferation in co-culture and alone and were significantly lower than vehicle and carboplatin groups (**Figure 4.5.A,B, Figure 4.6**). LECs were shown to have higher proliferation in co-culture than alone for the vehicle (**Figure 4.5.A,C, Figure 4.6**). Carboplatin treatment showed the same result of higher proliferation in co-culture than alone (**Figure 4.5.A,C, Figure 4.6**). However, there was no significant difference in LEC proliferation between

co-culture and LECs alone for docetaxel (**Figure 4.5.A,C, Figure 4.6**). Interestingly, proliferation in the LEC-only control was not significantly altered by any chemotherapy treatment (**Figure 4.5.C**). However, LEC proliferation in co-culture was significantly lower in docetaxel compared to both vehicle and carboplatin (**Figure 4.5.C**).

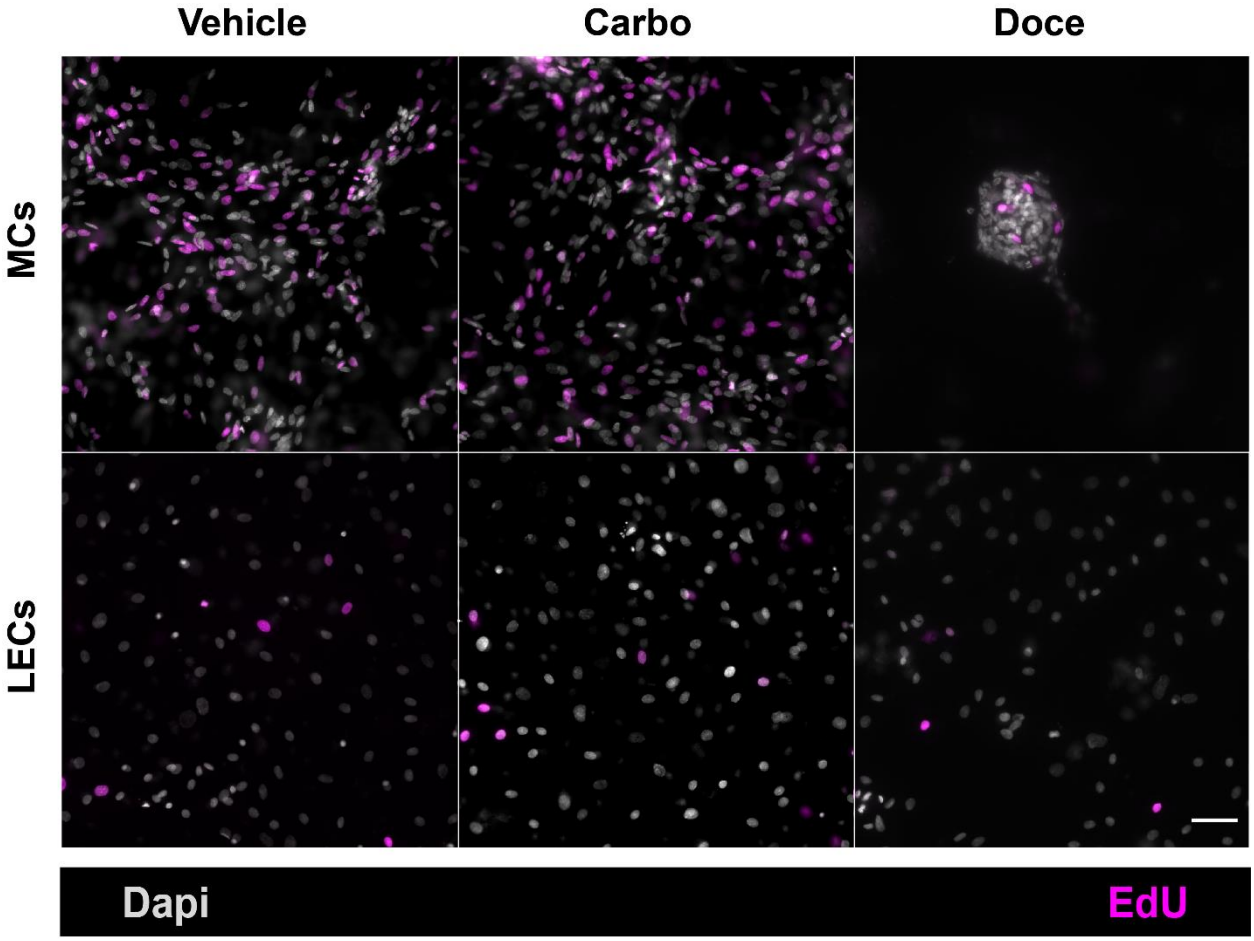

Figure 4.6. Proliferation in monoculture controls. *ML models are treated with 1 µM carboplatin, 1 µM docetaxel, or vehicle (DMSO) for 24 hours. During the last 6 h of treatment, 10 µM EdU was added to the culture media. Representative images of proliferation in the monoculture controls are shown with all nuclei stained with Dapi (gray) and EdU-positive cells in magenta. Scale bar is 50 µm.*

Combination treatment does not significantly differ from docetaxel alone.

We additionally sought to examine whether combining both carboplatin and docetaxel, as patients commonly receive multiple types of chemotherapy, would be more deleterious than either therapeutic alone. Representative images demonstrate disrupted MCs and LECs after

combination therapy (**Figure 4.7.A**). Combination treatment resulted in significantly decreased MC coverage compared to the vehicle and carboplatin alone, but not docetaxel alone (**Figure 4.7.B**). This trend was consistent among MC proliferation (**Figure 4.7.C**), LEC coverage (**Figure 4.7.D**), and LEC proliferation (**Figure 4.7.E**). Interestingly, LEC junctions were significantly disrupted by combination therapy compared to the vehicle, but not either treatment alone (**Figure 4.7.F**), suggesting that any chemotherapy presence will cause disrupted junctions.

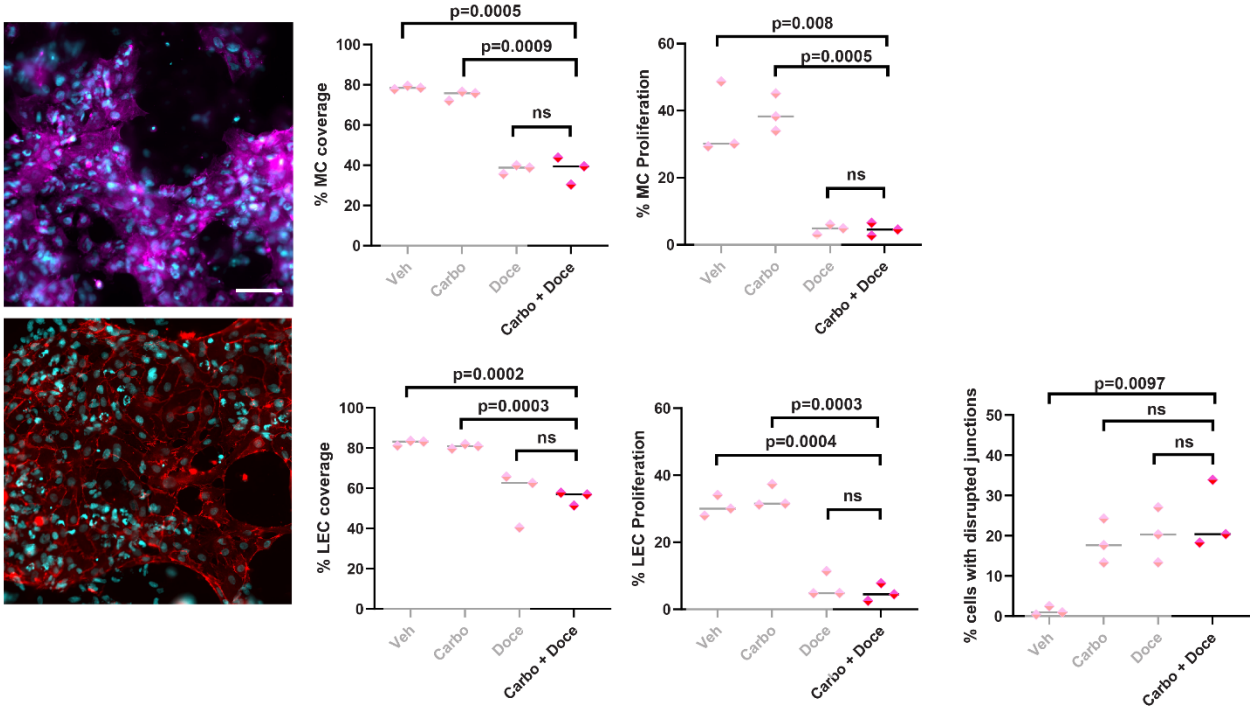

Figure 4.7. Combination treatment does not demonstrate more disruption than docetaxel alone. *Representative images of MCs stained for f-actin (magenta) and LECs stained for CD31 (red) with nuclei shown in turquoise (A). Scale bar is 50 µm. MC coverage (B) and proliferation (C) are reported. LEC coverage (D), proliferation (E), and junction disruption (F) are reported. Data shown represents the mean with each biological replicate shown (n=3). Significance was determined via two-way ANOVA between the vehicle and chemotherapeutic treatments with post hoc Tukey's multiple comparison test.*

VEGFR3 blocking does not ameliorate docetaxel-mediated disruption.

We next sought to determine whether the VEGF-C/VEGFR3 pathway was involved in our observed effects. In a previous study, blocking vascular endothelial growth factor-3 (VEGFR-3)

prevented LEC junction disruption caused by carboplatin treatment (265). Therefore, we tested VEGFR-3 blocking to determine if LEC disruption would be reduced. Overall, we saw no

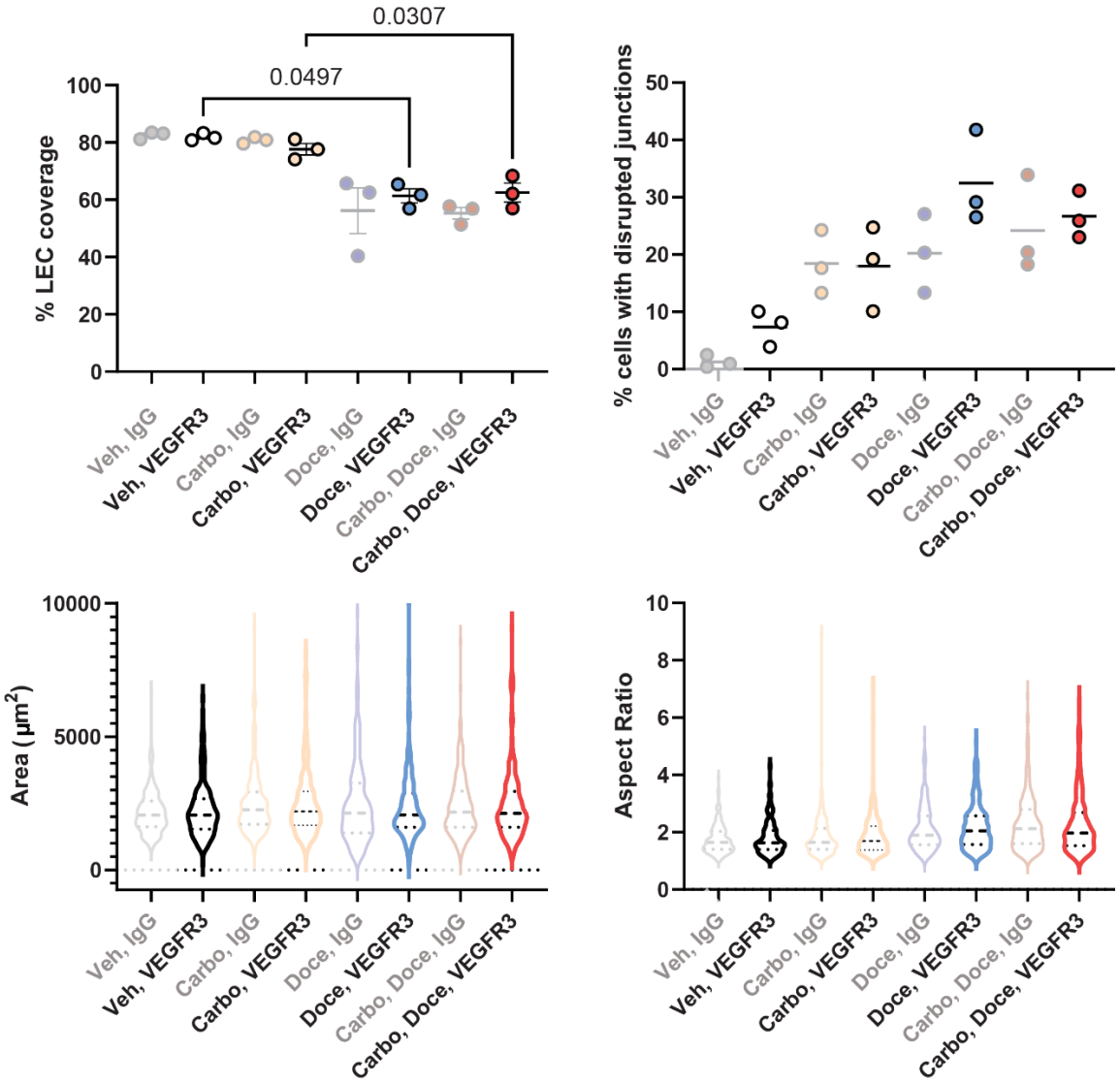

Figure 4.8. Blocking VEGFR3 does not ameliorate chemotherapy-induced changes to LECs. *LEC coverage (A), disrupted junctions (B), area (C), and aspect ratio (D) are reported. Data shown in A-B represents the mean with each biological replicate shown (n=3). Significance was determined via two-way ANOVA between the vehicle and chemotherapeutic treatments with post hoc Tukey's multiple comparison test. Data shown in C-D represent 80 measured LECs from each of 3 biological replicates (n=3).*

significant differences between the control and the VEGFR3 blocking. LEC coverage was still significantly decreased by docetaxel or combination treatment with the VEGFR3 blocking

antibody present (**Figure 4.8.A**). Additionally, no significant differences in disrupted junctions were observed, though disruption trended upward in the vehicle with VEGFR3 compared to an isotype control (**Figure 4.8.B**). Finally, no significant changes in LEC area (**Figure 4.8.C**) or aspect ratio (**Figure 4.8.D**) were observed. Beyond treatment response, these results demonstrate that the ML model is not particularly responsive to VEGFR3 blocking.

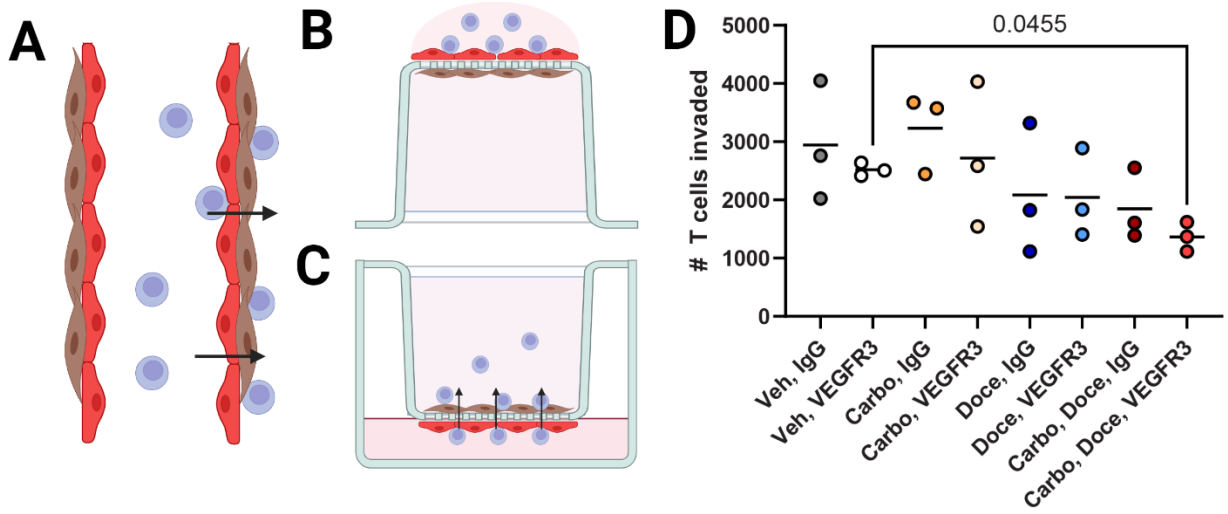

Figure 4.9. T cell transmigration is unchanged after treatment. *Immune cell transmigration into the meninges from the meningeal lymphatics (A). T cells are seeded on the underside of the ML model (B), then ML models are re-inverted and cultured for 24 hours (C). T cells invaded into the upper chamber are counted (D). Data shown represents the mean with each biological replicate shown (n=3). Significance was determined via two-way ANOVA between the vehicle and chemotherapeutic treatments with post hoc Tukey's multiple comparison test.*

T cell transmigration in the ML model.

Finally, as the meningeal lymphatics are heavily implicated in immune cell trafficking, we sought to test whether T cells could transmigrate in our model (**Figure 4.9.A**). We seeded T cells on the underside of the insert (**Figure 4.9.B**), then, reinverted and cultured for 24 hours (**Figure 4.9.C**). T cells from the upper chamber were counted to determine transmigration (**Figure 4.9.D**). Overall, we saw successful T cell transmigration across all conditions. Though

transmigration on average trended downward with treatment, this was only significant between the vehicle VEGFR3 blocking group and the combination treatment VEGFR3 blocking group (**Figure 4.9.D**). Overall, these results do not clearly elucidate how chemotherapy may alter T cell transmigration, but do demonstrate the functionality of the ML model for future in depth studies.

4.2.4 Discussion

Although a plethora of tools and experimental methods can be applied to develop a better understanding of the meningeal lymphatics, most have been in vivo studies. There are no existing in vitro models that examine changes in both lymphatic endothelial cells and meningeal fibroblasts together to recapitulate meningeal lymphatic tissue composition. For this purpose, we developed a novel tissue culture insert model of the meningeal lymphatics that allows for examination of immune cell transmigration, cellular crosstalk, cell morphology, and protein secretion. In vitro models are ideal for quick, large screening experiments that allow potential targets to be narrowed down quickly prior to moving into animal work.

Within, the goal was to model the lumen of a meningeal lymphatic vessel. The chosen cell types included in this model, MCs and LECs, have specific key functions. Meningeal fibroblasts have a variety of functions (266), but generally make up the bulk tissue, maintain meningeal integrity, and contain CSF. Lymphatic endothelial cells are responsible for collecting fluid, altering their junctions and structure to follow the needs of fluid balance. Culturing LECs in vitro comes with a variety of challenges, and initial attempts to optimize a co-culture media were not as successful as transitioning the MCs to LEC media. Candidate co-culture medias included AIM-V with VEGF-C and EGF supplementation and Neurobasal media with Glutamax, B27, and N2 (Gibco). AIM-V is a serum-free defined media considered to be universal that has

been used for lymphocytes, breast cancer cells, and tissue explants (267–269). We supplemented with VEGF-C and EGF, as these factors are known to support LECs in culture (270–272). Additionally, we sought to test Neurobasal media to determine if future work could include brain-resident cells, such as astrocytes, microglia, and neurons (273,274). Preliminary data showed LECs had decreased viability in all tested media compared to Vasculife® (**Appendix A**). However, MC viability was not changed between preferred media, MenCM, and Vasculife®. Therefore, Vasculife® was chosen to culture the model. Future applications may require optimization of a different co-culture media, especially in the event of adding additional cells that are also known to be sensitive to media formulation, such as neural cells or immune cells.

Recently, the impact of localized radiation treatment on the meningeal lymphatics has been explored (174). However, lymphatic remodeling in response to systemic cancer treatment has not been fully characterized. It is established that platinum and taxane systemic chemotherapy have impacts on ex vivo mesentery lymphatics and lymphatic endothelial cells in vitro (6,265). Findings from our in vitro model yielded interesting insights regarding cellular behavior and proliferation that correlate to the mechanisms of action of the chemotherapeutic agents used. Overall, we demonstrated that docetaxel treatment is deleterious to both MCs and LECs in the model, whereas carboplatin had little to no impact. These results match changes to meningeal lymphatic morphology seen in mouse models (263). Carboplatin, a platinum-based chemotherapy, prevents proliferation by binding to DNA and inhibiting replication and triggering apoptosis (275). Docetaxel, a taxane chemotherapy, interferes with microtubules, leading to cell cycle arrest and preventing cell division (276,277). These chemotherapies are known to have off-target side effects, as they can often impact rapidly dividing healthy cells, such as hair, nails, and skin. Specifically, fibroblasts are highly proliferative cells that are

prevalent all over the body, but also in the bulk structure of the meninges and surrounding meningeal lymphatic vessels. Thus, they could also be impacted during treatment based on their proliferative nature. In tandem with the established accumulation of docetaxel in the lymphatics, this system is particularly susceptible to taxanes, potentially due to physiology. The meninges are a fluid filled organ with a high presence of inflammatory cells, such as macrophages, and has quick turnover of meningeal fibroblasts. Docetaxel likely accumulates in the meningeal lymphatics, particularly as there is not much tissue bulk or many cells to take up the docetaxel in the meninges as compared to larger tissues.

As these chemotherapeutics target proliferating cells, we next sought to quantify proliferation in our ML model during treatment. We demonstrated a decrease in percentage of proliferating meningeal cells in docetaxel-treated groups compared to both the vehicle and the carboplatin, both alone and in the meningeal lymphatic model. In contrast, LECs only exhibited decreased proliferation in co-culture with meningeal cells when treated with docetaxel. Thus, LEC response is dependent on crosstalk with other cell types. Further, there is potential for differences in LEC response to chemotherapy based on source and physiological function. For instance, in this study we used lymph node LECs, specialized cells that are highly relevant, but other types, such as dermal LECs were used in previous studies (265). In our studies, carboplatin did not change proliferation or disrupted junctions. In contrast, docetaxel disrupted junctions and decreased proliferation. Previous work revealed that, although dermal LECs are activated by carboplatin and display disrupted junctions, docetaxel did not disrupt junctions in dermal LECs (6,265). Dermal LECs have been previously shown to possess a decreased ability to migrate and form tubes when treated with docetaxel (278). Overall, these findings paired with prior work

demonstrate the importance of LEC source and microenvironment in altering response to chemotherapy.

Our work emphasizes that chemotherapeutics can attune the delicate balance between lymphatic structural maintenance and function. Docetaxel has been shown to cause lymphatic dysfunction with common occurrences of lymphedema following treatment during breast cancer (279–281). Prior work has also shown that docetaxel accumulates in the lymphatics with both subcutaneous and intravenous delivery, whereas carboplatin does not (282). Further, docetaxel cannot cross the blood-brain barrier (BBB), further suggesting it could accumulate in the meninges through their unique blood supply and then interact at high concentrations with the meningeal lymphatics. Moreover, though it cannot cross the BBB in its normal form, docetaxel can potentially disrupt the BBB as it is associated with higher occurrence of breast cancer metastasis to the brain (283). Thus, these findings suggest that docetaxel may have uniquely deleterious impacts on the meningeal lymphatics.

4.3 Applications in CNS Leukemia

4.3.1 Introduction

Acute lymphoblastic leukemia (ALL) is a hematological cancer wherein lymphoblasts become malignant rather than properly differentiating into functional white blood cells. Leukemia cells, though produced in the bone marrow, are then able to travel through the circulatory system and metastasize to distant organs. Early treatment consisted of systemic chemotherapy but saw high rates of CNS relapse. With the inclusion of CNS-directed therapy into treatment regimens, CNS relapse has decreased from 80% to 5% (284). Recent work has implicated the meninges in leukemia CNS relapse, with meningeal cells protecting leukemia cells from chemo-induced apoptosis due to quiescence upon direct contact (285). However, the route that leukemia cells utilize to traffic in and out of the meninges is unclear.

Within the meninges, there are blood vessels that feed the meninges and meningeal lymphatic vessels that maintain fluid balance, drain waste to the cervical lymph nodes, and support immune cell trafficking (167,168). We previously demonstrated chemotherapy-mediated disruption to an in vitro model of the meningeal lymphatics (263). Thus, examining the impacts of CNS-directed chemotherapies used to treat leukemia is of great interest. Disrupted meningeal lymphatics could result in decreased cell trafficking to the cervical lymph nodes, in turn helping to prevent leukemia relapse.

Outside of treatment, the homeostatic meningeal lymphatics could be a route for leukemia cells to reach the cervical lymph nodes and dampen tumor-specific immune responses during disease progression. Lymphatic endothelial cells secrete a number of cytokines that act as a chemoattractant for immune cells (30), and thus, could attract leukemia cells as an unintended effect. Further, leukemia cells migrate in the direction of shear stress (286), and could therefore

utilize drainage pathways to the lymph node. However, as the meningeal lymphatics have only recently begun to gain notoriety, these interactions have never been explored.

Upon reaching the lymph node, leukemia cells are poised to reach distant organs in the body and cause relapse. The lymph node microenvironment has been implicated in regulating ALL cell proliferation (287), but has primarily been studied in chronic lymphocytic leukemia (288,289). Thus, many questions remain about the interactions of lymph nodes and ALL. The lymph node is a complex and dynamic microenvironment, with constant immune cell recirculation and interstitial fluid flow delivering pathogens for immunosurveillance (42,47). During inflammation, interstitial flow is greatly enhanced, and immune cells are retained. Yet, the impact of interstitial fluid flow on leukemia cells in the lymph node has never been examined.

Creating tools to study leukemia cell behavior in the brain to cervical lymph node pathway will provide a platform to develop targeted therapeutics for CNS leukemia. Toward that goal, herein we apply a simple in vitro model of the meningeal lymphatics to understanding CNS leukemia. First, we examine the impacts of CNS-directed chemotherapeutics, cytarabine and methotrexate, that are commonly used to treat leukemia and prevent CNS relapse. Then, we examine leukemia cell egress from the meningeal lymphatic model. Finally, we apply the LN stroma model established in Chapter 2 toward answering questions around chemoattraction and flow-mediated migration.

4.3.2 Methods

Cell culture

LECs and MCs were cultured and incorporated into the meningeal lymphatic model as described in 4.2.2. LECs and FRCs were cultured and incorporated into the lymph node stroma

model as described in Chapter 2. Jurkat leukemia cells were cultured in RPMI + 10% characterized fetal bovine serum (Cytiva Hyclone).

Chemotherapy treatment

ML model was treated with 500 nM methotrexate (MTX) or cytarabine (Ara-C) for 24 hours. ML models were fixed, stained, imaged, and quantified as described above in 4.1.

Leukemia cell egress from the meningeal lymphatic model

Jurkat cells were added to the upper compartment of the meningeal lymphatic model at 50,000 per tissue culture insert. After 24 hours, media from underneath the tissue culture insert was collected and Jurkat T cells were counted manually. For conditioned media studies, supernatant was collected from lymph node stroma models under static and flow conditions (Chapter 2) and kept at 4°C until use. Conditioned media was placed in the well underneath the ML model insert and fresh vasculife was placed within the insert. Jurkats were added and counted as described above.

Jurkat invasion assay

Jurkat leukemia cells are encapsulated at 1 million/mL in PhotoHA/collagen gels in tissue culture inserts, with pressure head induced 0.8 µm/s interstitial fluid flow as described in Chapter 2. Briefly, 700 µL of media is placed underneath the tissue culture insert and 100 µL is placed atop the hydrogel for static conditions. For 0.8 µm/s flow, 100 µL is placed underneath the tissue culture insert and 700 µL is placed atop the gel. After 24 hours, hydrogels are removed from the tissue culture insert. The membranes are fixed with 4% formaldehyde in 1X PBS for 15 minutes. Then, membranes are stained with DAPI and three regions of interest are imaged on an EVOS at 10X. Invaded cells are counted and converted to % invasion.

Leukemia cell egress from the lymph node stroma model

Jurkat cells were labeled with CellTracker Orange and added to the upper compartment of the LN stroma model at 50,000 per tissue culture insert. After 24 hours, media from underneath the tissue culture insert was collected and Jurkat T cells were counted manually. LN stroma models were fixed in 4% formaldehyde in 1X PBS for 45 minutes. Blocking with donkey serum in 0.01% triton x-100 was performed for 6 hours at room temperature (RT) on a rocker. LN stroma models are then incubated with 1 µg/mL mouse anti-human alpha smooth muscle actin antibody [1A4] (abcam) in blocking solution overnight at 4°C on a rocker. LN stroma models were rinsed with PBS three times for 20 minutes on a rocker at RT. Next, gels were incubated with 2 µg/mL donkey anti-mouse AlexaFluor 555 in blocking solution overnight at 4°C on a rocker, followed by a rinse as previously described

4.3.3 Results

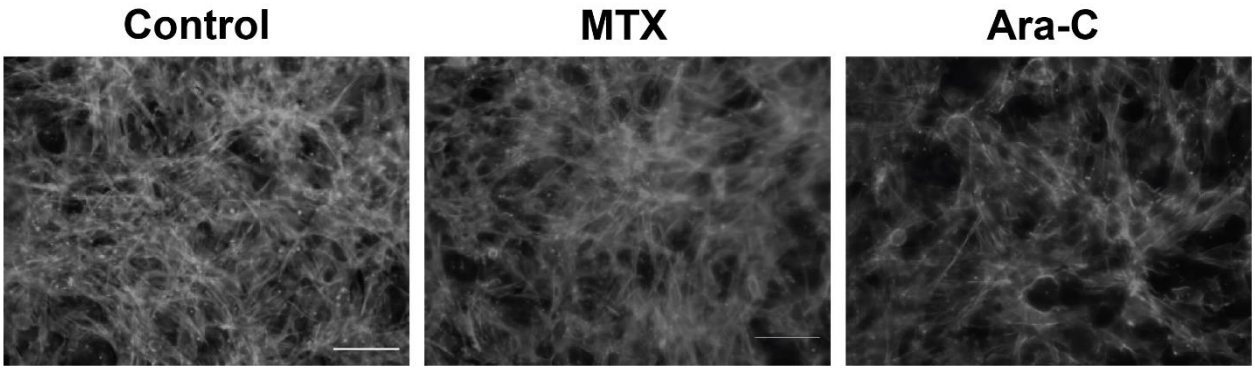

Figure 4.10. ***Meningeal cells are not disrupted by MTX or Ara-C.*** *MCs are visualized via F-actin stain. Scale bars are 50 µm.*

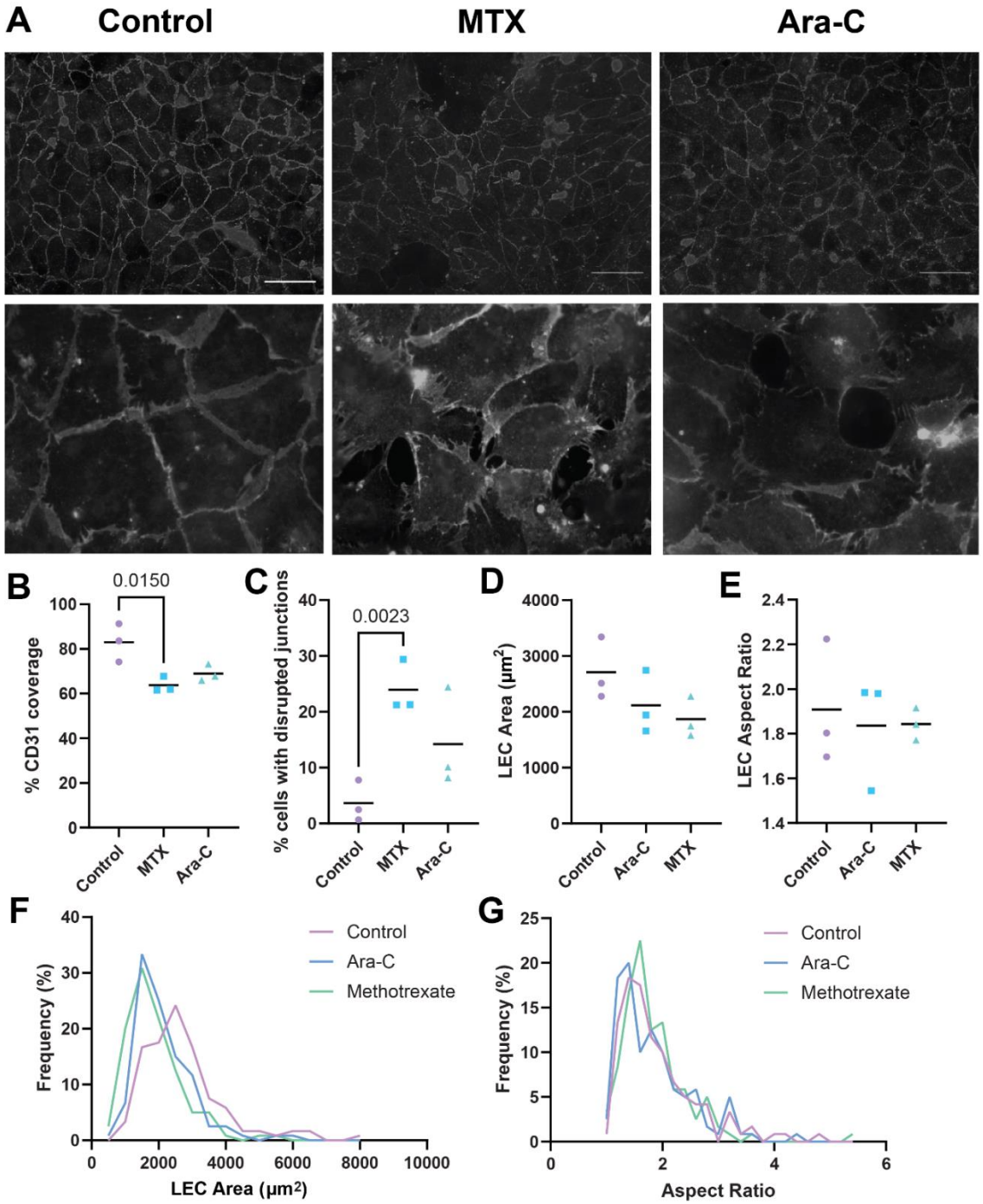

Figure 4.11. Methotrexate disrupts LEC monolayer integrity. *ML models were treated with 500 nM methotrexate (MTX), 500 nM cytarabine (Ara-C), or vehicle for 24 hours. Representative images are shown with LECs stained for CD31 (A). Scale bar is 50 µm. LEC coverage (B), disrupted junctions (C), average area (D), and average aspect ratio (E) are reported. Data shown represents the mean with each biological replicate shown (n=3). Significance was determined via one-way ANOVA between the vehicle and chemotherapeutic treatments with post hoc Tukey's multiple comparison test. Histograms of LEC area (F) and aspect ratio (G) contain the measurements of 80 LECs from each of 3 biological replicates, to total 240 data points.*

Methotrexate and cytarabine do not disrupt meningeal cell integrity

Based on our prior results, we sought to examine whether commonly utilized chemotherapeutics for treating leukemia could cause disruption to the meningeal lymphatics. MCs were not significantly disrupted by the presence of methotrexate (MTX) or cytarabine (Ara-C) (**Figure 4.10**).

Methotrexate disrupts LEC integrity in meningeal lymphatic model

Next, we examined changes to the LEC barrier integrity. Representative images demonstrate alterations to LEC monolayers with chemotherapy treatment (**Figure 4.11.A**). LEC coverage was significantly decreased by MTX, but not Ara-C (**Figure 4.11.B**). This trend remained for LEC junction disruption (**Figure 4.11.C**). However, average LEC area (**Figure 4.11.D**) and aspect ratio (**Figure 4.11.E**) were unchanged. Histograms represent a trend toward smaller LECs under treatment (**Figure 4.11.F**). No trends in aspect ratio distribution were observed (**Figure 4.11.G**). Therefore, we have shown that methotrexate is deleterious to LECs, but not MCs, in a model of the meningeal lymphatics.

Leukemia cells egress from the ML model

We next sought to incorporate leukemia cells into the ML model to characterize their behavior. We sought to answer (I) – if leukemia cells could egress, and (II) – if the cell types included altered that behavior. To do so, we set up the ML model alongside two monoculture controls and added Jurkat leukemia cells to the upper chamber (**Figure 4.12.A**). After 24 hours, we collected media from underneath the tissue culture insert and counted the leukemia cells to report egress. Overall, egress was significantly lower when both LECs and MCs were present compared to MCs alone (**Figure 4.12.B**). Whether this effect is due to a double layer of cells or the physiology of the system is unknown, but will be the focus of future studies.

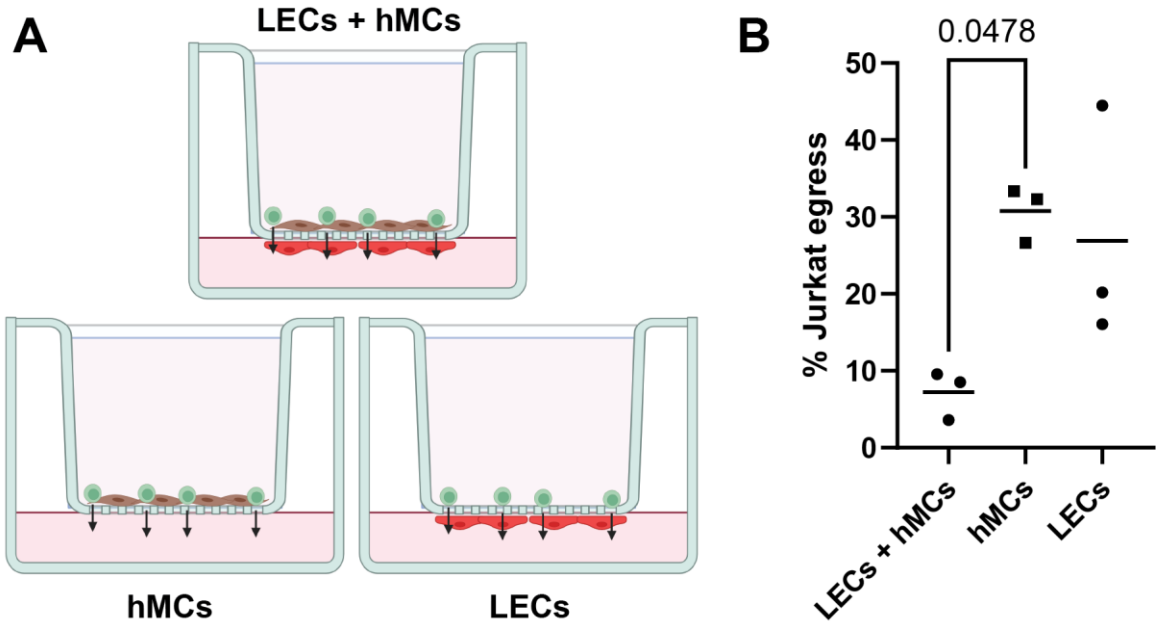

Figure 4.12. Leukemia cell egress is decreased by ML model compared to either cell type alone. *Tissue culture inserts with seeded with both LECs and hMCs or each cell type alone (A). Jurkat leukemia cells were added to the upper chamber and media from the lower chamber was collected after 24 hours to count the cells. Percent egress is reported (B). Data shown represents the mean with each biological replicate shown (n=3). Significance was determined via one-way ANOVA with post hoc Tukey's multiple comparison test.*

Lymph node stroma supernatant acts as a leukemia cell chemoattractant

We next wanted to examine whether the lymph node stroma model, established in Chapter 2, could act as a chemoattractant for leukemia cells. To do this, Jurkat leukemia cells were added to the upper compartment of the ML models as previously described. Supernatant from static and flow lymph node stroma models was collected and placed underneath the ML models as a chemoattractant (**Figure 4.12.A**).

Interestingly, conditioned media from the LN stroma under flow caused significantly more egress of leukemia cells out of the meningeal lymphatics model (**Figure 4.12.B**). Conditioned media from the static LN stroma caused an upward trend of egress, but this was not

significant (**Figure 4.13.B**). These results suggest that signaling from activated LN stroma could attract leukemia cells to circulate again after remission.

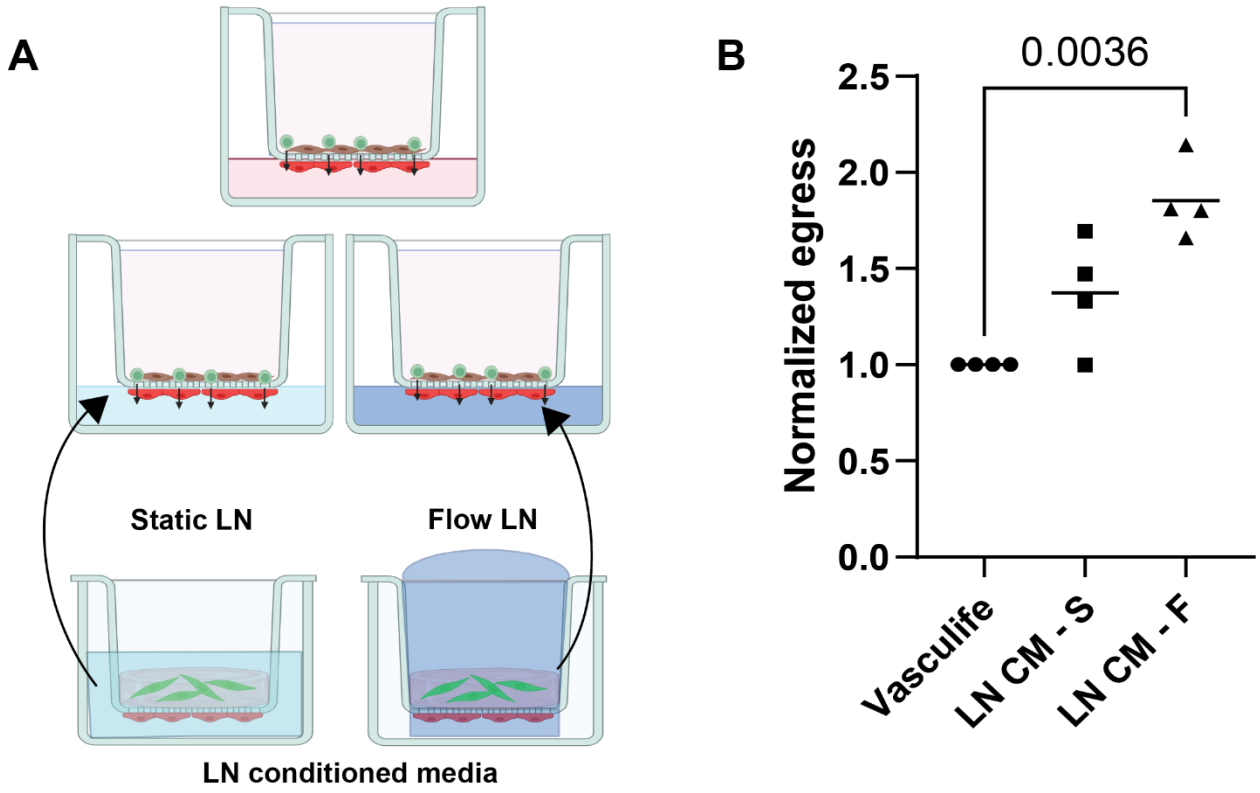

Figure 4.13. Conditioned media from flow conditioned lymph node stroma models enhances Jurkat egress from the ML model. *Schematic demonstrating conditioned media collection and positioning in the ML model (A). Egress of Jurkats was quantified and normalized to the Vasculife control (B). Data shown represents the mean with each biological replicate shown (n=4). Significance was determined via one-way ANOVA with post hoc Tukey's multiple comparison test.*

Jurkat leukemia cells have enhanced migration with interstitial flow

Having established that the LN stroma under flow acts as a chemoattractant for leukemia cells, we next sought to examine leukemia cell behavior in the model. First, we examined leukemia cell migration under interstitial fluid flow to understand their baseline behavior. We found significantly more invasion under flow conditions (**Figure 4.14**). With this baseline

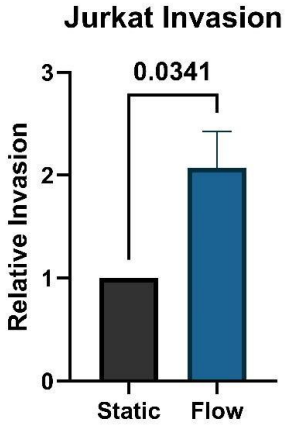

Figure 4.14. Jurkat leukemia cells have increased invasion in the presence of interstitial fluid flow. *Statistical significance determined by Students' t test with p value displayed on the graph (n=3).*

knowledge, we sought to examine Jurkat behavior in the LN stroma model under static and flow conditions. We found that Jurkats readily egressed from the LN stroma model and this egress trended upward under flow conditions (**Figure 4.15.A**). Visually, we see that Jurkats form aggregates in the static condition and remain at the top of the gel. Under flow conditions, less Jurkats are seen at the top (**Figure 4.15.B**). Therefore, Jurkat cells are able to migrate throughout the LN stroma and exhibit potential differences in the presence of interstitial fluid flow.

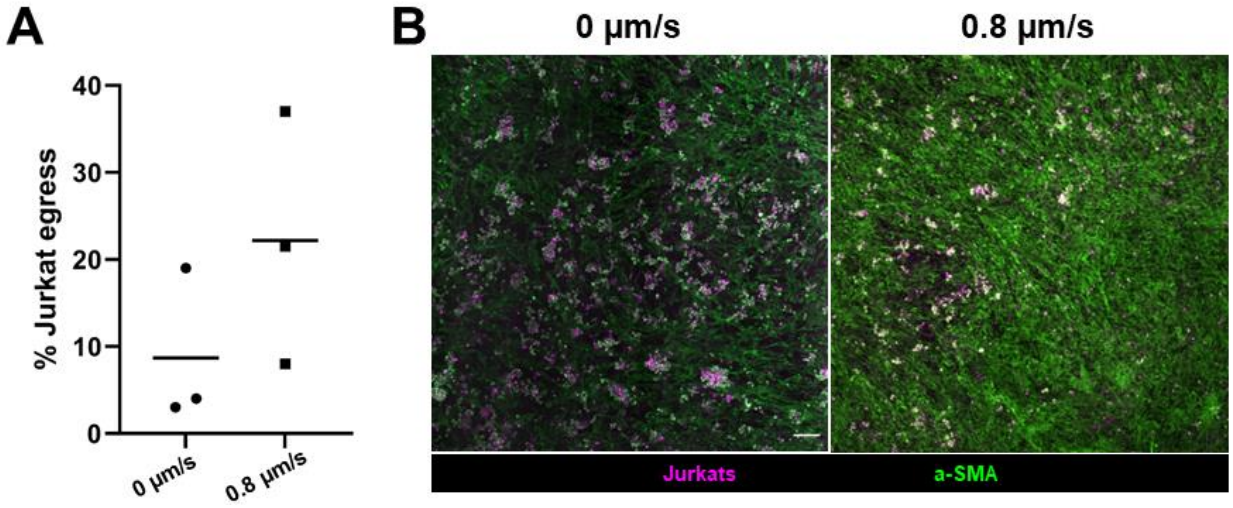

Figure 4.15. Jurkats egress from the LN stroma model. *Jurkats egress from the LN stroma (A). There are more Jurkats at the top of the gel in static compared to flow conditions, with Jurkats labeled with CellTracker in Magenta and FRCs labeled with α-SMA in green (B).*

4.3.4 Discussion

The CNS remains an important site of leukemia relapse. Though CNS-targeted therapy has decreased overall rates significantly, the CNS is involved in 30-40% of all relapses (290). Current therapeutics include cranial irradiation, methotrexate, and cytarabine (284). Cranial irradiation is utilized more sparingly, due to the harsh side effects on the developing brain of pediatric patients. Chemotherapeutic agents methotrexate and cytarabine are typically administered intrathecally, or into the cerebrospinal fluid, to target the CNS. Though these agents are extremely effective, studies have shown CNS impairment long-term after the treatment (291–293). Interestingly, methotrexate is also used to treat autoimmune disorders such as psoriasis (294). Herein, we demonstrate that methotrexate, but not cytarabine, was significantly deleterious to LECs in a model of the meningeal lymphatics. Interestingly, neither chemotherapeutic was disruptive to the meningeal cells. Previous work has demonstrated that meningeal cells enhance leukemia chemoresistance to both methotrexate and cytarabine, which was mediated mostly by direct contact, but to some degree by conditioned media (285). Meningeal cells could secrete various chemokines in response to methotrexate and cytarabine to alter leukemia survival. Thus, meningeal cell response to chemotherapy could be an interesting future direction toward understanding this CNS metastatic niche.

Further, differences between LEC response to methotrexate and cytarabine were observed, though this was likely due to biological variability, as cytarabine had trends of negative effects. However, methotrexate stood out as consistently disruptive. Generally, methotrexate delivery to the lymphatics is much more efficient when encapsulated in nanoparticles (295,296). However, our ML model directly delivers methotrexate to the cells. In intrathecal therapy, methotrexate is injected directly into the cerebrospinal fluid and thus

delivered to the meninges. The meningeal lymphatics are actively draining this system, and thus, may encounter methotrexate at higher rates than other lymphatic systems in the body. We demonstrated in Section 4.1 that docetaxel had significantly deleterious effects on the meningeal lymphatics in vitro, and have further demonstrated similar impacts in vivo (263). Thus, next steps could include validating the impact of methotrexate on the meningeal lymphatics in a mouse model.

Beyond response to chemotherapeutics, the meningeal lymphatics model can be used to examine cell trafficking. Leukemia cell trafficking in the CNS is a key area of research toward developing preventative therapies. There are multiple pathways leukemia cells can take to infiltrate or exit the meninges, including the blood-brain barrier, the blood-leptomeningeal barrier, the blood-cerebrospinal fluid barrier, or the meningeal lymphatics (297). Within, we demonstrated that leukemia cells can egress from the ML model. Additionally, when supernatant from the lymph node stroma model (Chapter 2) was placed beneath the ML model, Jurkats egressed more readily. The meningeal lymphatics drain directly to the cervical lymph nodes for immunosurveillance, and thus, these models could be used in conjunction to understand how leukemia cells may enter and exit the meninges to cause relapse. We show the first evidence that Jurkat leukemia cells are responsive to interstitial fluid flow, and that they can migrate and egress in the LN stroma model. Therefore, combining the ML model and the LN storma model into one pathway will be an essential next step toward understanding leukemia in the CNS. Ultimately, we have demonstrated the suitability of both the meningeal lymphatics and lymph node stroma models toward answering questions around CNS leukemia, and future work will aim to characterize these interactions.

4.4 Applications of the meningeal lymphatics model

Herein we have presented the first in vitro model of a meningeal lymphatic lumen. With the increasing awareness of the meningeal lymphatics' involvement in a plethora of diseases, more in vitro models will be required to tease apart key physiology. This model is a simple, robust, and easily adaptable first iteration. With commercially available cells and tissue culture inserts, this is a low cost and low barrier-to-entry model. The features of the meningeal lymphatic model include cell-level analysis, transport across the barrier, and easy adaptability (**Figure 4.16**). Together, these features power the model to answer basic questions around CNS immunosurveillance and metastasis.

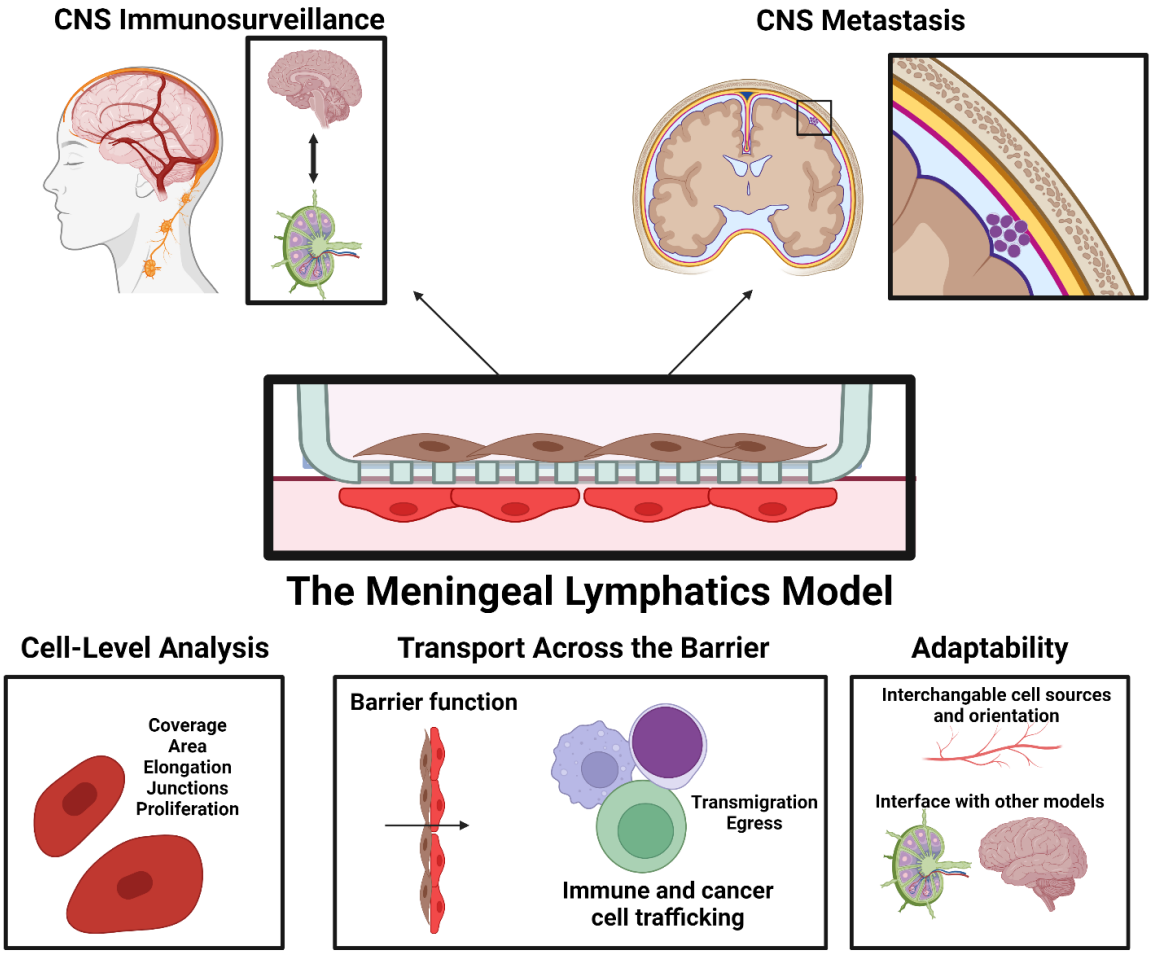

Figure 4.16. Overview of applications and features of the meningeal lymphatics model.

Looking forward, the in vitro meningeal lymphatic model presented within can be tailored to a wide variety of applications, such as modeling different pathological conditions with inflammation or tumor cells or altering the orientation of the cells to model afferent vs efferent vessels. This model could be combined with photo-crosslinkable hydrogels to represent the brain parenchyma. Additionally, the meninges are an immune cell reservoir, so incorporating immune cells such as macrophages and lymphocytes is of great interest toward increasing complexity. Herein, we demonstrated the model's capability for T cell transmigration and leukemia cell egress. The ML model provides a simple platform for immune cell trafficking. This model could also be adapted to other organ systems by employing tissue-specific lymphatic endothelial cells and fibroblasts, as we have established the impact of tissue-specific fibroblasts on the response to chemotherapy. Overall, the meningeal lymphatic model developed herein has wide applicability toward advancing the nascent field of meningeal lymphatic biology.

CHAPTER 5

DISCUSSION

5.1 Discussion

The lymphatic system is far-reaching, not only physically throughout the body, but in the regulation of fluid homeostasis and immune response. This dissertation sought to develop novel models of the lymphatics that incorporate tissue-specific fibroblasts to probe their contributions to immune function and pathophysiology. First, we developed a model of the lymph node stroma that consists of a fibroblastic reticular cell (FRC)-laden hydrogel above a monolayer of lymphatic endothelial cells (LECs) that sustains interstitial fluid flow. We found IFF-mediated changes to remodeling and chemokine secretion by FRCs, LEC junctional integrity, and T cell migration and IFNy secretion (**Chapter 2**). Moving toward pathophysiology, we examined the lymph node during breast cancer metastasis. We first demonstrated a negative correlation between tumor burden and collagen deposition in human lymph node samples. We then adapted the LN stroma model toward examining tumor burden by adding varying numbers of breast cancer cells. We found breast cancer cell invasion throughout the model, regardless of initial burden, and changes to diffusivity at the highest burden (**Chapter 3**). Next, we sought to look at a more recently discovered lymphatic system: the meningeal lymphatics. We developed the first in vitro model of this CNS-draining system and demonstrated chemotherapeutic-mediated disruption, T cell transmigration, and leukemia cell egress (**Chapter 4**). Within, we have developed two lymphatic stroma models with wide reaching applications in studying interstitial fluid flow, immune cell trafficking, cancer metastasis, and off-target chemotherapeutic effects. These models aim to provide an additional preclinical tool, both in understanding pathophysiological processes and in providing a platform for screening therapeutics.

Lymph node stroma model as a new tool for studying immunity

Adaptive immunity is essential for long-lasting protection from antigens such as viruses. Indeed, this process is how vaccines have saved approximately 154 million lives (298) and why diseases such as smallpox can be eradicated (299). Adaptive immunity is initiated in the lymph node, and thus, physiologically relevant models are essential for isolating essential variables toward developing targeted therapeutics. Within, we developed a model of the lymph node stroma cells that play essential roles in guiding fluid transport and immune cells, adding to the toolkit available to study lymph node physiology. Our model has applications in immune cell trafficking, acute and chronic inflammation, and cancer metastasis. It allows immune cell infiltration and egress, quantification of chemokines, morphological analysis, transluminal flow, and is made with commercially available components. However, the LN stroma model does have a number of limitations. Notably, that live imaging through a tissue culture insert membrane is possible, but challenging and has low resolution. Therefore, the live dynamics of remodeling and migration in the model are not easily captured. The presence of FRC-laden hydrogel also prevents the direct analysis of lymphatic barrier function, a common metric used in lymphatic models. Additionally, while the use of commercially available cell lines does improve accessibility, it prevents patient-matched models. Therefore, it is essential to consider what functionality is necessary in a model to answer the scientific question of interest.

Interstitial fluid flow as an essential consideration in lymph node modeling

Interest in interstitial fluid flow has gained traction in recent years, with striking implications in cancer progression (162,300). Strategies to alter IFF include changing the viscosity of the media, placing engineered models on a rocker for gravity driven flow, and using pumps to drive flow. Within, we utilize varying heights of pressure heads to drive interstitial

fluid flow. This methodology is well-established (74,193), allows unidirectional flow, and the utilization of cell-specific culture medium.

IFF plays essential roles in delivering antigens throughout the lymph node for screening by APCs and is greatly enhanced during inflammation and threat. Typically, this fluid moves through extracellular matrix conduits created and maintained by FRCs. The impact of IFF on other fibroblast populations is well-established (178,181,182,185,186). However, only one study has examined IFF on FRCs, showing enhanced networking (135). Building off of this knowledge, we sought to incorporate the efferent lymphatics, that would also experience the enhanced IFF as they drain lymph, and examine how immune cell trafficking would be altered in the presence of IFF.

Serrano et al established that the presence of interstitial fluid flow enhances solute drainage by lymphatics in a microfluidic device. Further, peripheral blood mononuclear cells infiltrated into the lymphatic sprouts at the same rate regardless of added growth factors or interstitial fluid flow (301). This provides evidence that our observations of decreased egress with IFF could be due to the presence of FRCs. In Chapter 2, we demonstrated that IFF alters the behavior of every cell type in the model. FRCs had enhanced networking, proliferation. LECs had disrupted junctions and decreased coverage. CD4+ and CD8+ T cells had altered egress from the model. The chemokine secretion of the model was also significantly altered by flow. These findings underline the importance of incorporating interstitial fluid flow into models of the lymph node to understand how immune cell trafficking and immune response is altered during states of inflammation.

Considering other physical parameters in the lymph node

Beyond flow rates, inflammation and immune response produces a number of changes to physical forces in the lymph node. For example, in our system, flow and pressure are inextricable. Additionally, the protein content of lymph can change with inflammation, leading to changes in colloid osmotic pressure and viscosity. Much of this knowledge has come from animal models. In a mouse model of rheumatoid arthritis, inflamed and expanding lymph nodes had increased lymphatic pumping pressure but decreased lymph node pressure, while viscosity was unchanged (15). In a study of peritoneal infection in rats, lymph viscosity increased by about 30% (302). Lymph nodes are known to alter the colloid osmotic pressure of lymph during its transit (303). Interestingly, both lymphatic dysfunction, such as in the case of edema (304), and inflammation after treatment with lipopolysaccharide (305), have been shown to decrease colloid osmotic pressure. Thus, these parameters vary widely depending on disease and inflammatory state. Our lymph node stroma model provides a useful platform to explore these parameters in vitro. Viscosity and colloid osmotic pressure could be varied in vitro by adding dextrans, a synthetic colloid, or albumin, a protein colloid, to the cell culture media of the model. In animal studies, these experiments take place by cannulating and using artificial lymph. Therefore, our model provides a high throughput and noninvasive platform that could streamline this work.

Outside inflammation and infection, these parameters can also change during cancer progression and treatment. In humans, intraoperative measurements of intranodal pressure demonstrated values of ~12 mmHg in tumor negative sentinel lymph nodes. This increased to ~28 mmHg in tumor positive sentinel lymph nodes, and increasing pressure correlated with increasing size of metastasis (306). Interestingly, in mice, a study showed that intranodal lymph node pressure increases before any detectable enlargement of the node during cancer (307).

Examining how afferent lymph is altered by tumors, in terms of viscosity and colloid osmotic pressure, could further be an important advancement of the LN stroma model. Currently, our model experiences calculated pressures of approximately 0.7 mmHg (for 0.8 μm/s flow) and 2.3 mmHg (for 3.0 μm/s flow). These are much lower than the aforementioned values in humans. Therefore, exploration of the magnitude of pressure required for pressure-induced lymph node changes is of great interest. However, the model is poised to answer questions around altered colloid osmotic pressure in lymph draining to sentinel lymph nodes.

Understanding migration and transport in metastatic lymph nodes

As lymph node metastasis is the most important prognostic factor in breast cancer survival, we adapted our LN stroma model to study this phenomenon. In the breast tumor, increased interstitial pressure drives fluid out of the tumor, and thus, aids breast cancer cells in escape to the lymph node (161,308). We sought to understand how the presence of tumor cells may cause remodeling in the LN stroma that results in altered transport, either enhancing breast cancer cell survival, or invasion to the next LN. We demonstrated in Chapter 3 that breast cancer cells can migrate throughout the LN stroma model and invade to the LEC monolayer, regardless of the amount of tumor cells added. Interestingly, we only observed decreased diffusivity at the highest tumor cell density. However, taken together with our findings of altered collagen deposition in metastatic lymph nodes, we have uncovered new directions in how matrix and transport are connected in metastasis. Indeed, we have also uncovered a limitation of our model. Visualization of collagen fibers via techniques such as second harmonic generation proved challenging. Thus, developing new protocols for staining the matrix will be essential toward answering these questions. Additionally, analyzing other breast cancer cell lines will provide insight into how patient-specific these effects may be. Ayuso et al demonstrated that MCF7 and

MDA-MB-231 breast cancer cells had differing impacts on LEC gene expression and barrier function (309). Thus, it will be essential to understand how varying cancer cell lines impact the LN stroma model.

Metastatic lymph nodes and perinodal adipose tissue

Lymph nodes are typically embedded in adipose tissue, the primary regulator of whole-body metabolism that consists largely of adipocytes. Peri-nodal adipocytes serve as an energy source for the lymph node and release more energy during immune response than distant adipocytes (310,311). Interestingly, a recent study found that lymph node FRCs can drive cold-induced beiging of adipose tissue, where adipocyte function shifts from energy storage to thermogenesis (312). Beiging is considered a potential therapeutic for obesity. However, obesity has profound negative impacts on lymph nodes, impairing fluid transport and immune cell trafficking and decreasing the size and T cell count of lymph nodes (313,314). More research is required to fully understand the crosstalk between the lymph node, particularly the stroma, and the perinodal adipose tissue.

Additionally, adipose tissue plays many roles in breast cancer progression. Much work has been done to examine breast cancer – adipocyte interactions, showing that adipocytes promote breast cancer survival and migration through metabolism, inflammation, and drug resistance (315–318). However, the contributions of local sentinel lymph nodes to adipocyte-mediated breast cancer growth are not yet understood. Though lymph nodes are separated from the surrounding adipose tissue by a thick collagen capsule, tumor cells are known to penetrate the capsule and infiltrate the surrounding tissue (extranodal extension), impacting prognosis (319,320). As this process is poorly understood, many questions remain in defining the role of the lymph node stroma in extranodal extension.

In Appendix B, we utilized engineered adipose tissue models to study transport with the goal of developing models of lipedema. However, these engineered adipose tissue models could be adapted to study breast cancer and interfaced with the LN stroma model to answer these questions around crosstalk. In the next section, we discuss the various chemokines that are secreted by the LN stroma model and how they may impact breast cancer progression.

Stroma-derived chemokines as potential modulators of tumor cell migration

Chemokine secretion is an essential method of communication in the tissue microenvironment. However, tumor cells can intercept these signals to promote their survival and migration and can secrete their own chemokines to recruit supporting cells. We established the secretion of interleukin-6, CXCL12, CCL2, and CXCL8 by our LN stroma model in Chapter 2. Each of these chemokines have implications in breast cancer metastasis and progression.

Interleukin-6

IL-6 is an inflammatory chemokine secreted by stromal and immune cells in response to pathogens or tissue damage to help regulate the immune response. IL-6 is well studied in breast cancer and is known to enhance tumor cell migration and invasiveness as well as epithelial-to-mesenchymal transition (EMT) (321). Increasing serum IL-6 is associated with increasing stage and worse prognosis (322,323). Many cell types, including lymphatic endothelial cells, macrophages, fibroblasts, adipocytes, and tumor cells, all secrete IL-6, potentially contributing to a pro-tumor microenvironment.

The involvement of IL-6 in lymphatic metastasis has been well studied. Van de Velde et al showed that tumor-exposed lymphatic endothelial cells produce significantly increased levels of IL-6 that enhance tumor cell invasion and proliferation (324). Cho et al examined the impact of IL-6 on breast cancer metastasis through lymphatic vessels in a microfluidic device (325).

First, they demonstrated increased MCF7 invasion with IL-6 in the presence of LECs. They also showed that IL-6 induced the secretion of VEGF by LECs, recruiting blood vascular endothelial cells (325). Further, IL-6 derived from cancer-associated fibroblasts has been shown to enhance tumor growth and migration (326). In our work, we demonstrated that IL-6 was secreted by the LN stroma model into the supernatant at higher rates under high magnitude interstitial fluid flow. Interestingly, when looking at IL-6 sequestered in the hydrogel, the opposite trend was observed. This suggests that flow could be driving IL-6 out of the hydrogel and into the supernatant. From these results, we know that IL-6 is secreted by the LN stroma, even under the static conditions that we added tumor cells in. Interestingly, regardless of the amount of tumor cells added, we saw similar rates of invasion all the way through the model. If high magnitude flow can alter chemokine secretion, it introduces the question as to whether high magnitude flow would also help drive tumor cell migration in the LN stroma. Further, examining how IL-6 secretion by the LN stroma was altered in the presence of tumor cells could help advance our understanding of breast cancer metastasis in the LN.

As adipose tissue is in close proximity to primary breast tumors, adipocyte-derived IL-6 is also of particular interest. Indeed, adipocyte-derived IL-6 promotes breast cancer migration (327). Additionally, serum levels of IL-6 also correlate with body mass in breast cancer patients with obesity (328). As we have demonstrated the secretion of key chemokines in our LN stroma, adapting the model to incorporate adipose tissue and study extranodal extension is of great interest.

CXCL12

Also of note, we characterized the secretion of stromal cell-derived factor 1, also known as SDF-1 and CXCL12, in our LN stroma model. CXCL12 binds to C-X-C chemokine receptor

type 4 (CXCR4). The CXCR4/CXCL12 axis is well characterized in breast cancer, with involvement in tumor cell proliferation and migration as well as cancer-associated fibroblast transformation. CXCR4+ breast cancer cells exhibit more lymph node metastasis, and thus, poor prognosis (160). Interestingly, the CXCR4/CXCL12 axis has been implicated in interstitial fluid flow driven cancer cell invasion in breast cancer, glioblastoma, and hepatocellular carcinoma (74,193,329,330).

In the normal lymph node, CXCL12 is implicated in homing of lymphocytes (331,332) and dendritic cells (29). We found that secreted CXCL12 was significantly increased in the supernatant and decreased in the hydrogel under 3.0 µm/s flow. As CXCL12 has already been implicated in breast cancer invasion under interstitial fluid flow in simple mono-culture models (330), turning to tissue-specific models will help understand the contribution of this pathway in lymph node metastasis.

CCL2

Another inflammatory chemokine of note is CCL2. Both FRCs and LECs are known to secrete CCL2 (216,217) and there are known effects of CCL2 on T cell chemotaxis (218,219) and accumulation in LNs (221). However, in the application of breast cancer, CCL2 has more implications in the recruitment of macrophages. Indeed, CCL2 promotes tumor-associated macrophage conversion that promotes tumor growth (333,334). Additionally, fibroblasts in co-culture with breast tumor cells produce higher amounts of CCL2 that in turn promotes cancer stem cell behavior (335).

In our LN stroma model, we found that gene expression of CCL2 was upregulated by 0.8 µm/s flow while the secretion of CCL2 was upregulated by 3.0 µm/s flow. The secretion of CCL2 could modulate the behavior of tumor cells when added to the LN stroma, promoting

survival and migration (335,336). Additionally, CCL2 enhanced macrophage infiltration into breast tumor and tumor-derived fibroblast spheroids (337). Thus, adding macrophages to the metastatic LN stroma model under interstitial fluid flow is of great interest toward understanding crosstalk and progression in lymph node metastasis.

CXCL8

Finally, CXCL8 is another chemokine of interest in breast cancer progression. CXCL8, also known as IL-8, is primarily responsible for recruiting neutrophils during the inflammatory response (338). However, in breast cancer, CXCL8 promotes tumor cell proliferation, migration and drug resistance as well as matrix remodeling (338,339). Similar to the other chemokines, CXCL8 secretion into the supernatant was increased by 3.0 µm/s fluid flow and sequestering in the hydrogel was decreased by 3.0 µm/s flow. Therefore, CXCL8 could also be a modulator of breast cancer invasion under flow in the LN stroma.

As evidenced by the last few sections, the mosaic of chemokines in the microenvironment is dynamic and complicated. We have proposed four different chemokines as potentially playing a role in breast cancer metastasis and growth in the lymph node, and our list is by no means exhaustive. However, no singular factor is likely to explain the complexity of this phenomenon. Simple and adaptable in vitro models like the ones developed herein provide an essential platform for screening these mechanisms with precise control over which cell types are included to minimize confounding factors.

Combining immune cells and tumor cells in the LN stroma

Beyond the impact of stromal cell-derived chemokines, the immune cell populations within the lymph node are of interest in understanding lymph node metastasis. Metastatic lymph nodes exhibit profound immunosuppression and reduced T cell and B cell populations. Notably,

the lack of in vitro lymph node models has also led to a lack of studies examining cancer-immune cell crosstalk in the lymph node microenvironment. Within, we examined the LN stroma model in co-culture with T cells under interstitial fluid flow and we examined varying tumor burden. Each of these studies demonstrated the complexity of crosstalk in co-culture. In combining these studies, many questions about the necessary components of a lymph node stroma model could be answered.

Outside of the lymph node, many studies have aimed to co-culture breast cancer cells with varying immune cells. Regier et al demonstrated that tri-culture between breast cancer cells, monocytes, and bone marrow stromal cells impacted the gene expression of all three cell types (340). Indeed, the function and phenotype of immune cells in co-culture with cancer cells is drastically altered. Shao et al found that CD8+ T cells in co-culture with MCF7s had decreased activation, proliferation, and interferon-gamma secretion (341). However, Saraiva et al demonstrated that peripheral blood mononuclear cells were able to infiltrate breast cancer spheroids, and as their interferon-gamma secretion went up, tumor cell viability was decreased (342). Interestingly, as we found enhanced interferon-gamma secretion by activated T cells under high magnitude flow, this could suggest that cancer cell viability could be decreased if combined with the LN stroma and T cells. Additionally, other studies shed light into the timing of such a complex experimental system. Raffo-Romero et al showed macrophage infiltration into hydrogel containing tumor spheroids. Initial infiltration took three days, whereas complete infiltration occurred around day 7. We examined LN stroma and T cell response to flow at 24 hours. We examined breast cancer invasion for 5 days. In combining these experiments, T cells could become exhausted. Optimizing a co-culture strategy and timeline will be an essential future direction.

As discussed above, the addition of macrophages could be an important variable, particularly with the secretion of CXCL12, IL-6, and CCL2 demonstrated in the LN stroma. Each of these chemokines is implicated in macrophage recruitment in support of tumor progression (160). Interestingly, lymph node resident CD169+ macrophages that line the subcapsular sinus are protective against metastasis (36,343,344). Thus, studying macrophages in this system could lean toward tumor-associated macrophages that enhance progression, or CD169+ macrophages that protect against metastasis. The combinations of immune cells, tumor cells, and stroma are nearly endless. Accessible and customizable in vitro models are essential toward beginning to tease apart the complex crosstalk that is ongoing in the healthy and tumor microenvironment.

Applying transport tools to lipedema

The tools and techniques developed and demonstrated in this dissertation go beyond the lymphatic system. Lipedema, a disorder in which adipose tissue accumulates in the lower extremities that primarily impacts females, is a poorly understood condition. With much debate over the contribution of lymphatics to this disorder, engineered models are needed to understand the pathophysiology. In Appendix B, we studied the transport of fluid and fatty acids in engineered adipose tissue and demonstrated preliminary results of the effect of interstitial fluid flow on adipocytes. Similar to observations in obesity and breast cancer, lipedema is also characterized by macrophage infiltration, causing excess inflammation and pain (345–347). Concepts demonstrated above, such as altering immune cell infiltration and egress with interstitial fluid flow, could be applied to developing a more physiologically relevant model of lipedema.

Future work will also include incorporating monolayers of LECs into the engineered adipose tissue to look at tissue-specific drainage. Interstitial fluid flow matters everywhere in the body, and the tools described within can be applied toward a range of organs and pathophysiologies.

Meningeal lymphatics model for cell and fluid transport in the CNS

Voyaging to a less well-known lymphatic system, we also developed the first in vitro model of the meningeal lymphatics that drain the central nervous system. The meningeal lymphatics are under intense scrutiny in a wide range of diseases. We utilized our knowledge in lymphatics and fibroblasts to develop a simple and accessible model. The ML model consists of a layer of meningeal cells on the upper side of a tissue culture insert, representing the meninges, and a layer of LECs on the underside of the insert, representing the luminal compartment of the meningeal lymphatic vessel. This is an extremely simple and high-throughput model that can be widely applied. Barrier function, immune cell transmigration and egress, and morphological analysis are all possible with this model. Additionally, by using commercially available cell lines, this model can be easily reproduced. However, this model does have limitations, particularly in complexity. In vivo, metrics such as branches and loops are essential for studying meningeal lymphatic activation and disruption. As this model is not 3-dimensional, it cannot account for bulk changes in morphology. Additionally, meningeal cells are extremely proliferative, and thus, long-term cultures with this model are not possible. However, when applied to the appropriate questions, the model can prove a quick and efficient screening tool. Adding complexity to the meningeal lymphatic model could come in the form of additional cell types, such as the macrophages found in high density in the meninges, or in switching to artificial cerebrospinal fluid as a culture medium.

Potential link between the meningeal lymphatics and cognition

Cancer patients often report symptoms such as challenges with attention and memory while undergoing systemic chemotherapy, dubbed “chemo brain” (348). Docetaxel has known impacts on cognitive function (349,350). In Chapter 4, we demonstrated that docetaxel had negative impacts on the meningeal lymphatics in vitro as part of a greater study including in vivo and ex vivo studies. In the engineered model, docetaxel caused decreased LEC and MC coverage and disrupted junctions. In vivo work by M. Roberts demonstrated decreased meningeal lymphatic vessel diameter and insussceptions/loops in docetaxel-treated mice (15). We hypothesize that disrupted meningeal lymphatics may be related to cognitive impairment. We showed that the meningeal lymphatics model can replicate the disruption we see in vivo, and thus, it could be used as a platform to screen chemokines or antibodies that could rescue the meningeal lymphatics.

Completing the meninges to cervical lymph node pathway for modeling CNS immunosurveillance

As the meningeal lymphatics drain directly to the cervical lymph nodes, many in vivo studies have examined this pathway as a whole. When Evans blue, a tracer, is injected into the cerebrospinal fluid (CSF), it takes approximately 3 hours to reach the deep cervical lymph nodes (dCLNs), with a peak in concentration around 24 hours (351), giving insight into the dynamics of CSF drainage. This pathway delivers antigen-rich lymph and immune cells such as T cells and dendritic cells, allowing for CNS immunosurveillance.

Prior to the establishment of the meningeal lymphatics, a study showed that surgical resection of the dCLNs resulted in the accumulation of CD4+ T cells in the meninges and caused cognitive impairment (352). After the meningeal lymphatics were conclusively proven to drain

CSF (167,168), studies began examining both the meningeal lymphatics and the dCLNs. Da Mesquita et al demonstrated that aged mice had decreased meningeal lymphatic vessel (MLV) diameter and coverage, leading to reduced drainage to the dCLNs (170). Wang et al demonstrated that ligating the dCLNs led to enhanced amyloid beta accumulation, neuroinflammation, and cognitive deficits in an Alzheimer's disease model (353). Liu et al examined a mouse model of Parkinson's disease and found enlarged dCLNs with reduced lymphatic flow and enhanced inflammation (354). Li et al found that MLVs can drain viruses to the dCLNs and that disruption of this pathway resulted in enhanced neurological damage and mortality (355). These studies show the multitude of roles that the MLV to dCLN pathway plays in regulating immunity and cognition.

Most interestingly, Hu et al examined how the MLVs and dCLNs are impacted by brain tumors. Both glioblastoma and metastatic melanoma tumors induced extensive remodeling of MLVs and lymphangiogenesis in the dCLNs. When the MLVs were ablated, these effects were fully mitigated, tumor growth was not impacted, and cerebral edema was enhanced. Further, metastasis to the dCLNs was significantly inhibited by ablating the MLVs. Finally, ablation of the MLVs caused impaired trafficking of dendritic cells to the dCLNs (172). This study provides evidence that the MLV to dCLN pathway is essential toward understanding CNS metastasis.

The in vivo studies described above are essential toward advancing our knowledge of this pathway. Indeed, they provide much insight into how dysfunctional MLVs can aggravate CNS disease. However, the development of in vitro models is paramount for high throughput screening and experimentation. From these in vivo studies, we can understand the essential functions of the MLVs and the dCLNs to recapitulate in our models: fluid drainage and immune cell trafficking.

Within, we established models of lymph node stroma (Chapter 2 & 3) and the meningeal lymphatics (Chapter 4). These models are both cultured in the same medium and are poised to be connected for studying this pathway. The meningeal lymphatic model is designed with enhancements in mind. Adding a photocrosslinkable hydrogel laden with tumor cells, neurons, astrocytes, or microglia to replicate the brain microenvironment can be performed with the same techniques used to establish the LN stroma model in Chapter 2. Ideally, immune cells would be added to this model to observe how the brain tumor microenvironment alters their functionality and behavior upon reaching the lymph node stroma. Another key focus could be inflammation in this pathway, as we have demonstrated the LN stroma model secretes various inflammatory chemokines. We can examine how inflammation in the LN versus the MLVs impacts immune cell trafficking and crosstalk. We can examine how cancer metastasis in each tissue impacts the other. The models within are designed with these future experiments in mind: easily modifiable, interfaceable, and accessible.

Implicating the meningeal lymphatics in CNS leukemia

Another new frontier comes in the form of elucidating how leukemia cells invade the meninges and why relapse occurs. With the increased interest in the meningeal lymphatics, they stand out as a potential pathway for leukemia cell migration. Leukemia cells, once in the meninges, become quiescent and chemoresistant (285), remaining in this state for years until a relapse is triggered and they circulate once more. Though it is more likely that leukemia cells invade the meninges through their blood supply, it is unknown why, and how, leukemia cells begin circulating again. Within Chapter 4, we began to explore Jurkat egress from the meningeal lymphatic model and how it is augmented by lymph node crosstalk. We can utilize the two models developed within to begin to probe this connection. Understanding why leukemia cells

egress from the meninges and begin to recirculate will help develop novel strategies and therapeutics for treating CNS leukemia and preventing relapse.

5.2 Future Directions

Increasing lymph node model complexity

In vitro lymphatic vessel models can come in the format of monolayers for the lumen (e.g. tissue culture inserts), self-assembled vessels (e.g. 3D hydrogels), or seeded hollow constructs (e.g. microfluidic devices). We sought to develop a model that was easily accessible with commercially available components, and thus, we utilized tissue culture inserts rather than microfluidic devices. Additionally, self-assembled vascular networks often do not form a perfusable structure, and thus, examining immune cell transmigration would be a major challenge. Considering the structure of the lymph node and the ease of answering biological questions about transmigration, we decided to develop a spatially separated system, with bulk networks of FRCs to model the conduit system and a monolayer of LECs to model the efferent lymphatics. However, future models could transition to a microfluidic device for increasing complexity. Indeed, a plethora of lymphatic vessel microfluidics devices already exist, many in co-culture with breast cancer cells (325,356–359). To highlight a few, Ayuso et al seeded LECs into hollow channels in type I collagen to create a perfusable lymphatic vessel capable of barrier function and sprouting and further co-cultured it with breast cancer cells (309). Serrano et al seeded LECs into channels adjacent to fibrin gels. This device is further combined with interstitial fluid flow, and demonstrated sprouting and increased drainage (301).

Beyond adding complexity in the structure of the lymphatics, we can also advance the model by including more cell types to replicate adaptive immunity. Within Chapter 2, we

focused on T cells specifically. However, the lymph node is also home to dendritic cells, B cells, macrophages, and blood vessels. In Chapter 1, we discussed the necessity of dendritic cells to present antigens to T cells. We further explored how CD4+ T cells can help B cell activation and response. Many in vitro models of the lymph node focus specifically on these immune cell types, as discussed in Chapter 1. In an artificial human lymph node model combining T and B cells with dendritic cells, immune cell activation and antibody secretion were observed (133). Therefore, adding dendritic cells to our model would greatly advance the functional responses. Thus, adding the LN stroma to the well-characterized dynamic of T cells, B cells, and dendritic cells in vitro proves an exciting next step.

We can also improve our model by incorporating more sophisticated techniques. Within Chapter 2, we examined IFNg secretion into the media. However, with flow cytometry techniques, we can quantify chemokines on a per-cell basis. Work is ongoing to optimize intracellular IFNg stains on the flow cytometer. We can further expand our staining panel to include markers of T cell activation, such as CD25, CD26, CD40L, and CD69, and markers of T cell exhaustion, such as PD1, TIM-3, and LAG3 (360,361). Interestingly, lymph node stromal cells, notably LECs and FRCs, have been shown to express major histocompatibility complex-II in order to suppress autoreactivity (362). These stromal cells are known to convert naïve CD4+ T cells into Tregs (363). Therefore, examining T cell phenotype via flow cytometry is also of great interest. Expanding our repertoire of added immune cells and characterizations of immune function will be an exciting next step.

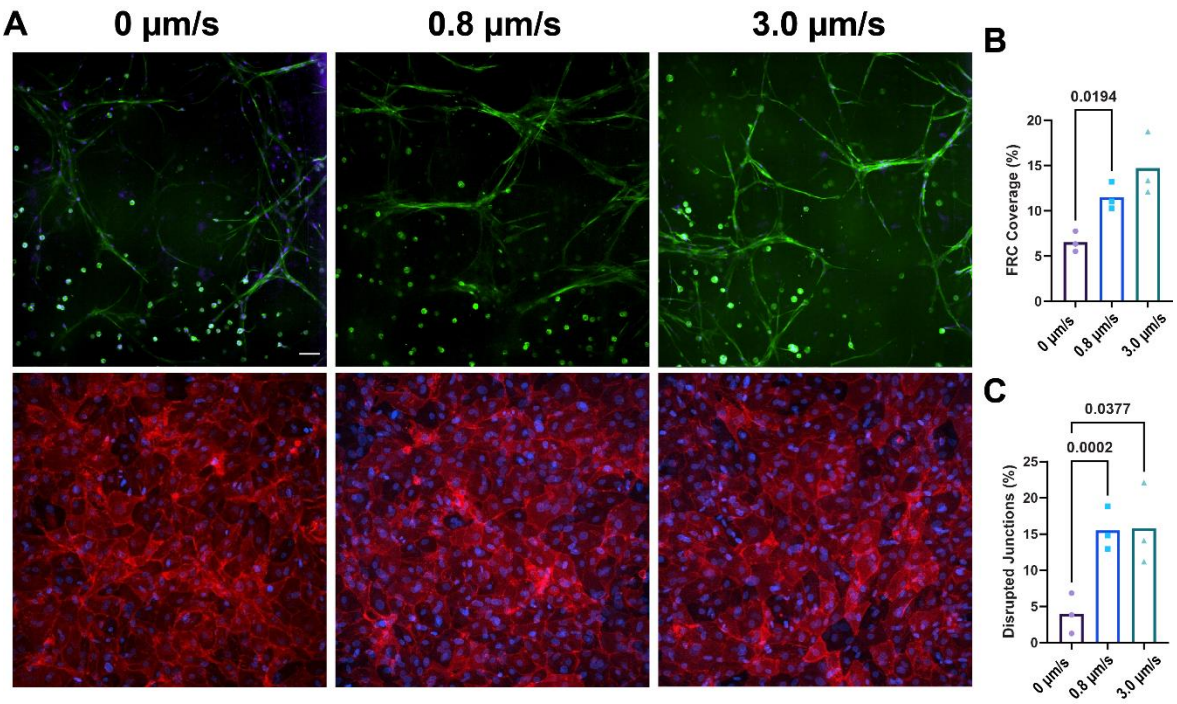

Figure 5.1. LN stroma model morphology after 5 days of culture. *Representative images of FRCs (green) and LECs (red) in the model, visualized with F-actin and CD31 respectively (A). FRC coverage (B) and disrupted LEC junctions (C) are reported. Each data point represents a biological replicate (n=3). Significance was determined by one-way ANOVA followed by Tukey's t-test, with significant p values (<0.05) reported on each graph.*

Temporal dynamics of IFF

In Chapter 2, we examined IFF-mediated impacts after 24 hours. This timing allows us to look at how cells respond to enhanced fluid flow at the beginning of the immune response. However, in the body, inflammation and enhanced lymphatic drainage can persist for days. Extending the time of flow conditioning may provide a methodology to look at the temporal dynamics of acute inflammation. We demonstrated in Chapter 2 that 0.8 µm/s flow rate did not significantly impact morphology in the LN model. However, after 5 days of flow, we found that 0.8 µm/s flow caused significant morphological changes (**Figure 5.1A**). FRC coverage was significantly higher compared to the static control (**Figure 5.1.B**) and LEC junctions were significantly disrupted compared to the static control (**Figure 5.1.C**).

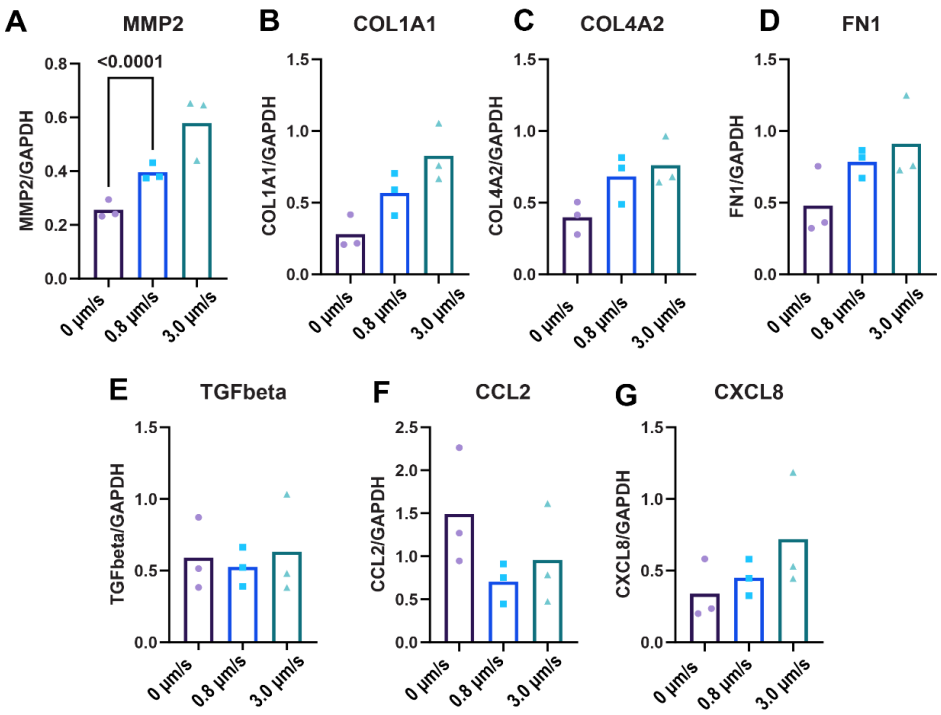

Figure 5.2. Gene expression of LN stroma under flow conditions for 5 days. *Relative expression of matrix remodeling-related genes MMP2 (A), COL1A1 (B), COL4A2 (C) and FN1 (D) are reported. Relative expression of chemokines TGFbeta (E), CCL2 (F), and CXCL8 (G) are reported. Each data point represents a biological replicate (n=3). Significance was determined by one-way ANOVA followed by Tukey's t-test, with significant p values (<0.05) reported on each graph.*

Additionally, matrix remodeling is a long-term process that we could not visualize strongly after only 24 hours of flow. Thus, we examined matrix-related genes in our 5-day models. Interestingly, MMP2 was significantly upregulated in the 0.8 µm/s flow rate (**Figure 5.2A**). COL1A1 (**Figure 5.2B**), COL4A2 (**Figure 5.2C**), and FN1 (**Figure 5.2.D**), all showed upward trends under flow, though these were not statistically significant. Next steps will include second harmonic generation to visualize collagen fibers and immunofluorescent staining.

We further examined gene expression of key chemokines. In Chapter 2, we showed that at 24 hours these chemokines trended upward under 0.8 µm/s flow, but not 3.0 µm/s flow. Interestingly, at 5 days, no trends are readily apparent. TGF-beta appears variable, but

unchanged, across all conditions (**Figure 5.2.E**). CCL2, which was significantly upregulated at 24 hours, trends downward at 5 days (**Figure 5.2.F**). CXCL8 demonstrated high variability (**Figure 5.2.G**). Next steps will include examining the secretion of these key chemokines as done in Chapter 2.

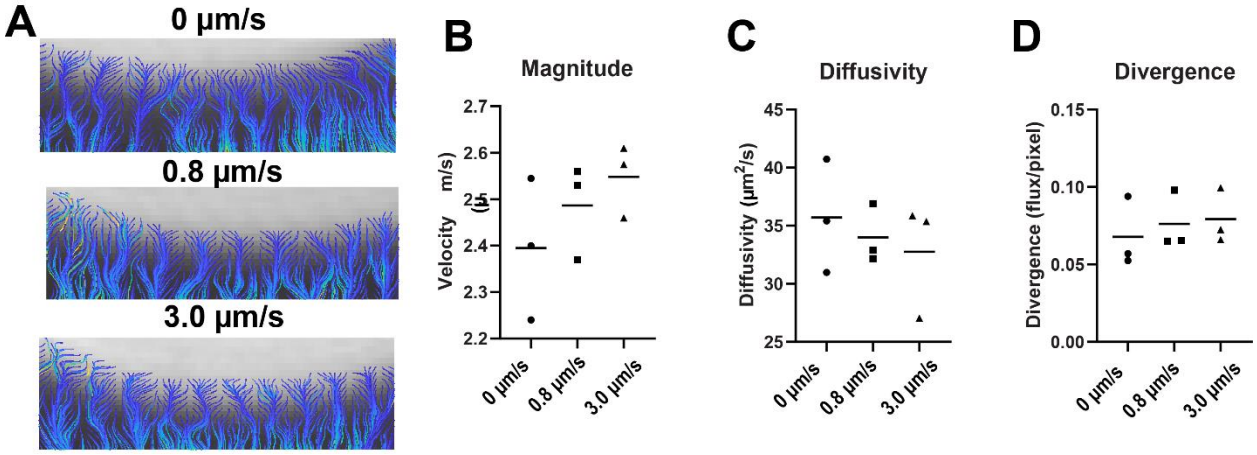

Figure 5.3. Transport metrics in LN stroma after 5 days of flow conditioning. *Streamlines demonstrate similar fluid pathways among all conditions (A). Flow magnitude (B), diffusivity (C), and divergence (D) are reported. Each datapoint represents a biological replicate (n=3).*

Finally, we sought to determine if 5 days of flow conditioning would result in significantly altered transport through the LN stroma model. Visualization of fluid pathways in the LN stroma model show no striking differences (**Figure 5.3.A**). Additionally, flow magnitude (**Figure 5.3.B**) had upward trends with flow conditioning, but this was not statistically significant. Interestingly, diffusivity trended downward under flow (**Figure 5.3.C**). Divergence was unchanged across conditions (**Figure 5.3.D**). Next steps will include correlating the morphology and gene expression of the 5-day flow conditioned models, to determine if there is any significant connection between flow metrics and model morphology and function.

These results demonstrate that the temporal dynamics of flow conditioning are an essential consideration in model building. In order to more accurately represent acute inflammation, longer flow conditioning is required. In Chapter 2, the LN stroma models

encountered interstitial fluid flow and T cells at the same time. Many questions remain about how T cells would behave over longer periods of time or being added to already-inflamed LN stroma.

Cancer metastasis

There are a host of new directions and applications in cancer metastasis using the LN stroma model. Within, we began to examine varying tumor burden and impacts on transport. As noted, future directions will include optimizing matrix visualization via fluorescent staining. Another area of interest is in examining how LN stroma alter breast cancer proliferation, using straightforward techniques such as EdU labeling. In addition, new technologies such as the UnipicK+™ allow for the collection of single cells from 3D cultures. With this technology, we aim to isolate breast cancer cells from the LN stroma to establish a LN-conditioned line and compare them back to the parental line.

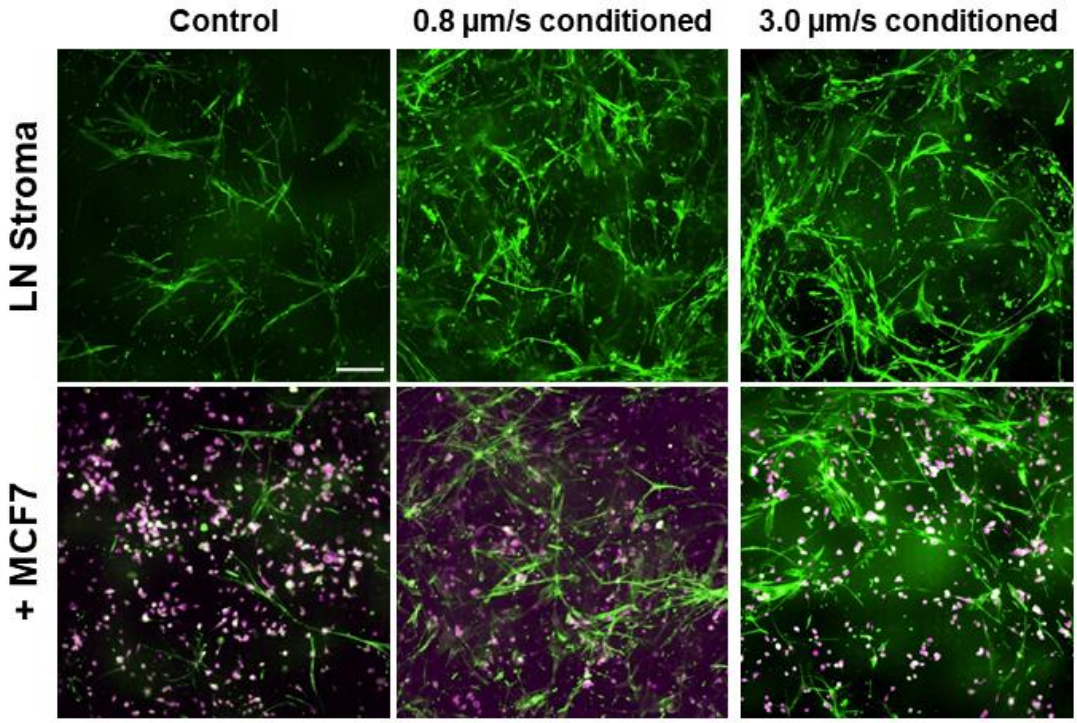

Figure 5.4. Representative images of breast cancer cells in flow conditioned LN stroma. *Fibroblastic reticular cells are visualized with F-actin in green. MCF7 cells are labeled with CellTracker Orange and visualized in magenta. Scale bar is 100 µm.*

Next, we aim to establish a model of the premetastatic node by flow-conditioning the LN stroma prior to adding breast cancer cells. Prior to metastasis, flow in the LN increases due to inflammation and chemokines in lymph draining from the tumor. This conditioning is known to cause immunosuppression and alter the LN, before cancer cells ever arrive. We added varying levels of flow to our LN stroma models for 5 days prior to adding breast cancer cells for 24 hours (**Figure 5.4**). Preliminary data shows that FRC coverage is enhanced under interstitial fluid flow, tracking with our prior results. Additionally, we can visualize MCF7 cells within the LN stroma. Interestingly, there are visibly less MCF7 cells in the high magnitude flow conditioned model. As we discussed, the 3.0 µm/s flow rate caused enhanced inflammatory chemokine secretion by the LN stroma. We demonstrated in **Figure 5.3** that flow conditioning did not cause alterations in transport in the gel, and thus, changes to MCF7 infiltration may be due to chemokines. Therefore, it will be necessary to explore what chemokines are present once breast cancer cells are added, and how they may be impacting migration through the model. Next steps also include characterizing the proliferation of the cancer cells within the flow conditioned LN stroma.

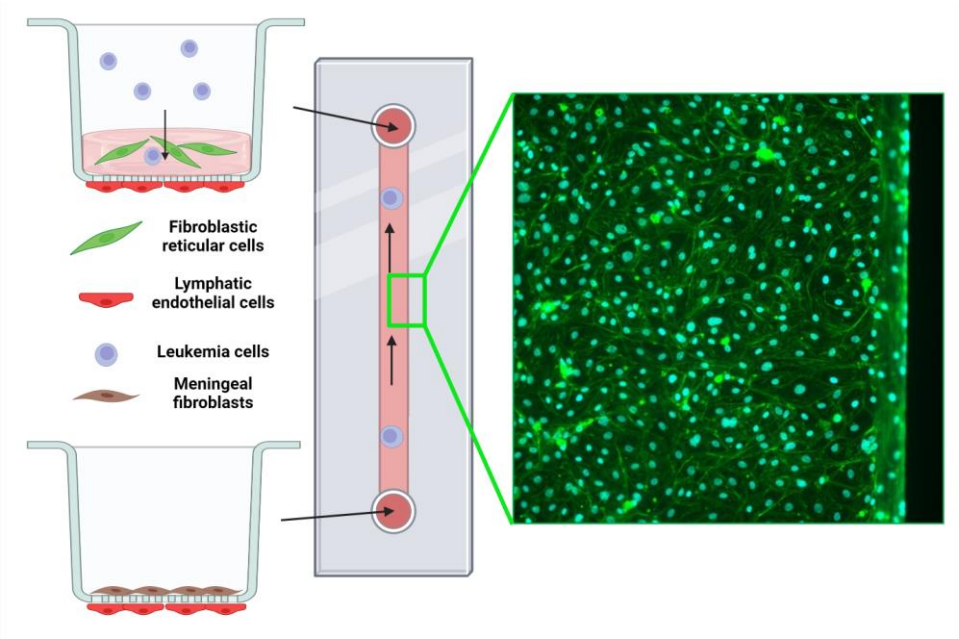

Figure 5.5. Combining the meningeal lymphatics and the lymph node engineered models.

Steps toward a meninges to cervical lymph node pathway model

Finally, we aim to combine our models of the meningeal lymphatics and the lymph node stroma into a complete pathway. We seeded the channel of an Ibidi µ-Slide I microfluidic chip with LN LECs to represent a lymphatic vessel connecting the two models. The media chambers on either side are large enough to accommodate tissue culture inserts. As both models use the same culture media, they are easily connected using this methodology. Next steps include adding immune cells and leukemia cells to the ML model and observing whether they traffic to the LN. This chip is also compatible with live imaging to track cell migration in real time. Upon optimization, this device will be an exciting leap toward developing an in vitro model of the brain to cervical lymph node pathway.

5.3 Final remarks

Engineered models have proven an advanced and efficient tool toward streamlining pre-clinical screening. Approximately 85% of therapeutics fail during clinical trials with traditional pre-clinical screening in animals (364). Knowing that mouse models are not fully representative of human physiology, increasing the complexity of in vitro models can help bridge the gap between cells on tissue culture plastic and clinical trials. By identifying suitable therapeutics in vitro, effective treatments can make it to patients safer and quicker. Within, we sought to develop engineered models of the lymphatic stroma. The lymphatic system is of great interest in drug delivery, metastasis and drug resistance of tumors, post-surgical complications, and now, central nervous system disorders. These models serve as starting points to begin understanding the complexity of transport across healthy and pathological conditions. In the future, adding complexity will increase their suitability for pre-clinical screening. As of now, fully

characterizing the biology within the model will aid in designing and interpreting experiments toward drug testing. The field of tissue engineering is burgeoning with technological developments and ever-sophisticated models. It is our hope that drawing attention to the contributions of the lymphatic system and interstitial flow will help to inform model design for tissues throughout the body.

Appendix A

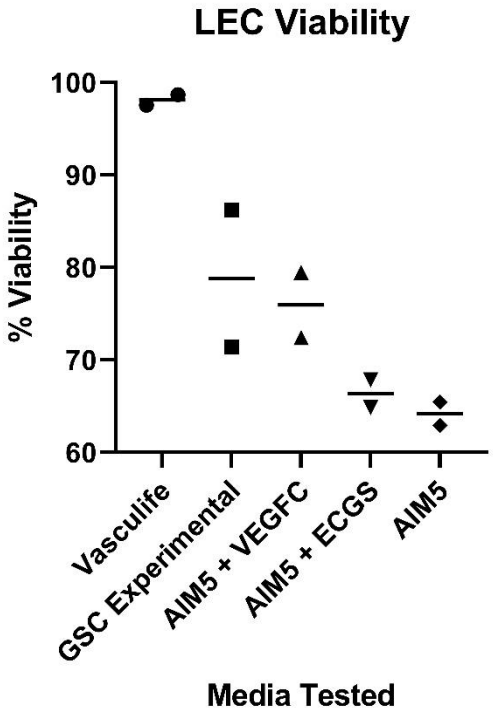

Figure A.1. Vasculife is the optimal media for LECs in the in vitro model compared to other tested experimental medias. *Viability of LN LECs after 24 h in various cell culture medias as determined by LIVE/DEAD kit. N=2.*

Appendix B

Sex differences and transport in engineered adipose tissue toward studying lipedema

B.1 Introduction

Adipose tissue (AT) is the master regulator of whole-body metabolism. AT stores excess energy, regulates body temperature, secretes hormones to regulate appetite, and participates in insulin signaling and glucose homeostasis (365)**.** This tissue consists mainly of adipocytes, or fat cells, that store energy in the form of a large lipid droplet. AT requires extensive vascularization to allow nutrients and oxygen to reach each adipocyte (366)**.** The diffusion limit for oxygen is is approximately 100 microns (367).

During pathological states, such as obesity, AT expands rapidly without adequate vascularization, leading to hypoxia. AT expansion can come in two forms – hyperplasia and hypertrophy. In hyperplasia, the number of adipocytes increases. In hypertrophy, the size of adipocytes increases. The average adipocyte is around 90 microns in diameter. During obesity, that number can reach 300 microns or more, preventing sufficient oxygen diffusion and resulting in hypoxia (368)**.** This can lead to necrosis in the tissue, increased inflammation, and metabolic dysfunction. Hypoxia can also drive fibrosis – the pathological deposition of extracellular matrix (ECM), which is known to alter interstitial transport

Lipedema, a disorder characterized by excess adipose tissue deposition, most frequently in the lower extremities, primarily affects women, and is both underdiagnosed and understudied (**Figure B.1**). The onset of lipedema typically occurs around puberty (age 12-14), but the average patient seeks out medical treatment around age 40 and on average receives a diagnosis at age 48 (lipedema.org). There are four stages of lipedema that track with progression of adipose tissue accumulation, pain, and changes to the skin. Stage 4 is called lipolymphedema, and is

characterized by the addition of lymphatic dysfunction, resulting in swelling (369). Lipedema is frequently misdiagnosed as obesity, adding an alternative challenge to receiving the proper diagnosis. There is no cure for lipedema, but treatments aim to manage pain and discomfort. Current treatments include liposuction, lymphatic massage, compression socks, and an anti-inflammatory diet (370).

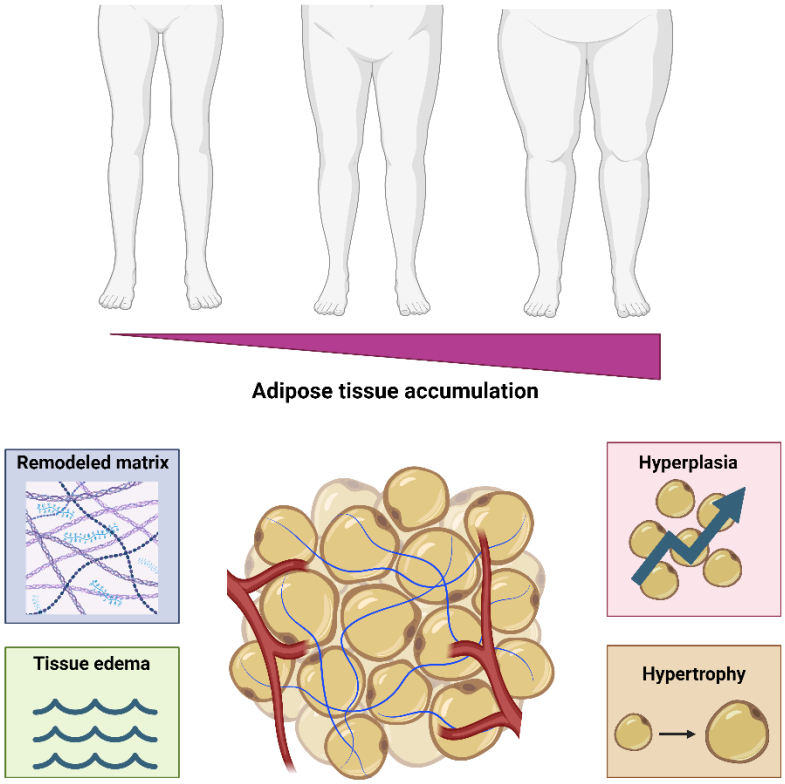

Figure B.1. Lipedema is the excess accumulation of adipose tissue in the lower extremities. *It results in remodeled matrix, tissue edema, hyperplasia, and hypertrophy in adipose tissue. Created with biorender.com*

Though there are limited tissue-level studies performed on lipedemic adipose tissue, some key characteristics are widely agreed upon. There is both hyperplasia (more adipocytes) (371,372) and hypertrophy (larger adipocytes) (346,371,373) in lipedema adipose tissue compared to a BMI-matched control. These adipocytes experience hypoxia (371), remodeled matrix (373), and enhanced interstitial fluid accumulation (374). However, the etiology and progression of these symptoms is not well understood.

Though edema is a well-established feature of lipedema (375), the pathophysiology is not yet understood. The lymphatic system is a key area of study, as it is responsible for fluid balance and waste clearance. In 2009, a magnetic resonance lymphangiography study by Crescenzi et al showed that lipedema patients did not exhibit lymphedema, but some patients exhibited enlarged lymphatics (376). In 2018, Crescenzi et al further demonstrated that lipedema patients had increased sodium content in skin and subcutaneous adipose tissue, suggesting a lack of clearance by the lymphatic system (377). However, studies since then have produced confounding results about the lymphatic system during lipedema. In 2017, Gould et al demonstrated impaired lymphatic transport in the majority of lipedema patients in their study cohort. Notably, over one third of patients had clinically normal lymphatic transport. These patients represented all four stages of lipedema (378). A 2022 study by Rasmussen et al demonstrated lymphatic vessel dilation and intravascular pooling in stage I and II lipedema patients. However, the propulsion rates within the vessels were higher than controls, suggesting there is not dysfunction in early stages (379). Finally, in 2023, Zaleska et al demonstrated reduced lymphatic flow in lipedema patients (380). It is clear that the lymphatic system during lipedema requires additional study.

An additional area of transport that is understudied in lipedema is interstitial transport. In adipose tissue, slow levels of interstitial flow are consistently bathing the tissue and allowing chemokine, nutrient, and oxygen diffusion through the tissue to eventually collect in the lymphatics (381,382). It is possible that the key to understanding fluid accumulation during lipedema lies not in the lymphatics, but within the interstitial spaces of the tissue itself. Developing preclinical models of interstitial transport could provide a high-throughput and highly customizable system to probe this mechanism.

Currently, in vitro studies of this disease focus on characterizing adipose-derived stem cells (ASCs) from lipedema tissues. Typically, these cells are isolated from liposuction aspirates. A 2019 study demonstrated reduced adipogenic capacity in lipedema ASCs compared to control tissue, shown via decreased lipid accumulation and adipokine secretion (383). In contrast, a 2020 study demonstrated upregulated leptin and PPAR-gamma gene expression in lipedema ASCs compared to controls, suggesting increased adipogenic potential (384). A follow up study with 3D spheroids of lipedema and control ASCs demonstrated similar findings, alongside altered matrix-related gene expression (385). A 2023 study attempted to parse out the contributions of lipedema and body mass index to ASC function and differentiation potential. The authors demonstrated upregulated adipogenic gene expression in nonobese lipedema ASCs compared to nonobese controls. However, there were no differences between obese lipedema ASCs and obese controls (386)**,** underscoring the importance of confounding factors in lipedema studies.

Recently, in vitro studies of lipedema have begun to expand beyond characterizing ASCs alone. A 2023 study showed enhanced angiogenesis of human umbilical vein endothelial cells after treatment with media differentiated lipedema-derived ASCs (387)**.** A 2024 study demonstrated that healthy ASCs and lipedema ASCs respond differently to estrogen (388). These studies are at the forefront of lipedema research. However, these studies primarily rely on 2D cultures or spheroids, where there is limited control of the microenvironment.

The field of adipose tissue engineering aims to develop physiologically relevant models to dissect the progression of AT dysfunction (389–394). In vitro modeling allows for precise control over the microenvironment, including factors such as hypoxia, adipocyte size, and adipocyte density, all known to play a role in lipedema. Herein, we aimed to develop human

engineered lipedemic AT models, benchmarked to human ex vivo lipedema tissue, to understand how lipedema may impact fluid and lipid transport in this key tissue.

B.2 Materials and Methods

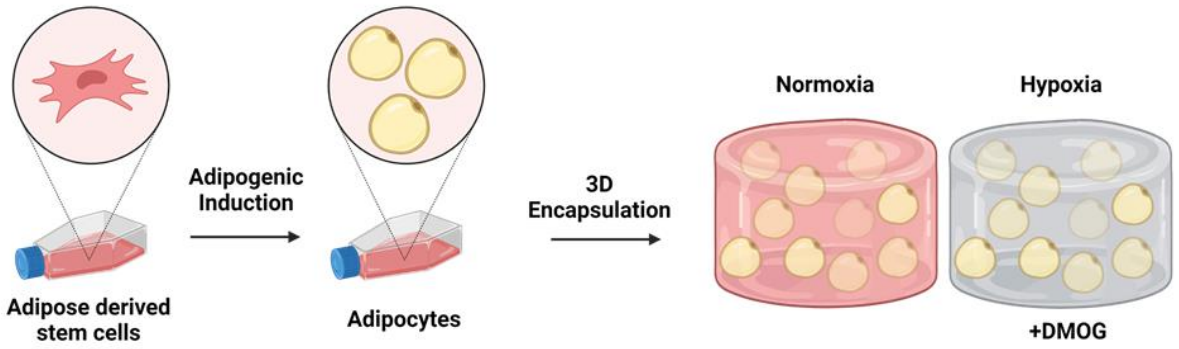

Figure B.2. Workflow for engineered adipose tissue. *Adipose derived stem cells are grown to confluency and differentiated for one week into adipocytes. Then, they are encapsulated in collagen hydrogels and cultured under various experimental conditions. Schematic made with biorender.com.*

Adipocyte stem cell culture and differentiation

Human adipose derived stem cells (ADSCs) are isolated from patients undergoing either abdominoplasty or thigh plasty. ADSCs are cultured in adherent tissue culture flasks and fed every 2-3 days with DMEM/F-12 supplemented with 3% fetal bovine serum and 1% penicillin-streptomycin. Once confluent, differentiation is initiated with the addition of rosiglitazone (2 μM), isobutylmethylxanthine (500 μM), dexamethasone (1 μM), D-calcium pantothenate (17 μM), biotin (33 μM) and insulin (20 nM) for 7 days.

Collagen hydrogel

Adipocytes are encapsulated at 2 million/mL in 2 mg/mL Type I collagen gels. Briefly, rat tail collagen I stored in acetic acid is neutralized with 10 mM HEPES, 28.4 μM sodium hydroxide, 1X M199, 0.4 μM sodium bicarbonate, and water, according to established protocols

(395). 100 µL of adipocyte-laden collagen gel solution is placed into 12-mm tissue culture inserts and incubated at 37C for 30 minutes to complete gelation.

Methacrylated hyaluronic acid and collagen hydrogel

Adipocytes are encapsulated at 1 million/mL (static/flow assays) or 4 million/mL (for MRI experiments) in methacrylated hyaluronic acid/collagen gels as described in Chapter 2. Pressure head driven interstitial fluid flow was applied as described in Chapter 2. Briefly, 700 µL of media was placed above the hydrogel and 100 µL of media was placed beneath the tissue culture insert to drive ~0.8 µm/s interstitial flow.

Engineered adipose tissue treatments

After 24 hours, hypoxia is initiated with 1 µM Dimethyloxalylglycine (DMOG), matched with a vehicle control in DMSO. For hormone treatment, 17 beta estradiol is added to the constructs at 0.5, 5, 25, and 50 ng/mL for one week. For oleic acid (OA) supplementation, 2mM bovine serum albumin is dissolved in 1X PBS until clear. Next, 10 mM OA is added and dissolved for one hour. Engineered adipose tissue cultures are treated with 500 µM OA every other day. For all experiments, AT models are fixed in 4% paraformaldehyde and stained with bodipy 488 at 1:500 and DAPI at 1:5000 for one hour.

Fatty acid transport

Rhodamine Palmitic Acid (PA) or TopFluor Oleic Acid (OA) is conjugated to bovine serum albumin and added above the AT models after one week of normoxia or hypoxia. Flow through media is collected and gels are homogenized to determine PA transport and uptake. For OA, AT models are fixed and imaged for adipocyte uptake.

Imaging and analysis

A Nikon Spinning Disk confocal is used to take z-stacks through entire engineered constructs with a 10 micron step size. Image analysis is performed manually in ImageJ. Individual adipocytes are hand-traced and area, circularity, and aspect ratio are recorded (**Figure B.3**). For lipid droplet size, images are thresholded and the 'analyze particles' function is used to detect and measure lipid droplet size.

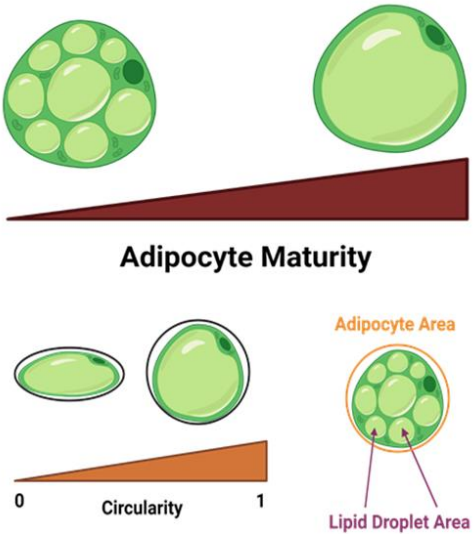

Figure B.3. Metrics for adipocyte maturity. *A fully mature adipocyte is unilocular with a lipid droplet taking up the bulk of the cell body. For in vitro quantification, adipocyte circularity, adipocyte area, lipid droplet area, and number of lipid droplets per adipocyte are measured.*

Dynamic contrast enhanced MRI

Thigh AT from a male lymphedema patient was cut to approximately 0.4 grams, secured in a tissue culture insert with transglutaminase, and placed inside of a Bruker 9.4T ClinScan MRI. Gado-DTPA (BioPal) was added to the upper well above the tissue at a 1:100 dilution. T1-weighted images were then taken every 3 minutes for 30 minutes. Lymph4D in Matlab is used to create maps of diffusivity, magnitude of flow, and direction of flow. MRI of in vitro constructs was performed as described in Chapter 2.

Statistical Analysis

Statistical tests are performed in GraphPad Prism. Two-way ANOVA and Tukey's multiple comparison t-test are performed with $p<0.05$ representing significant differences.

B.3. Results

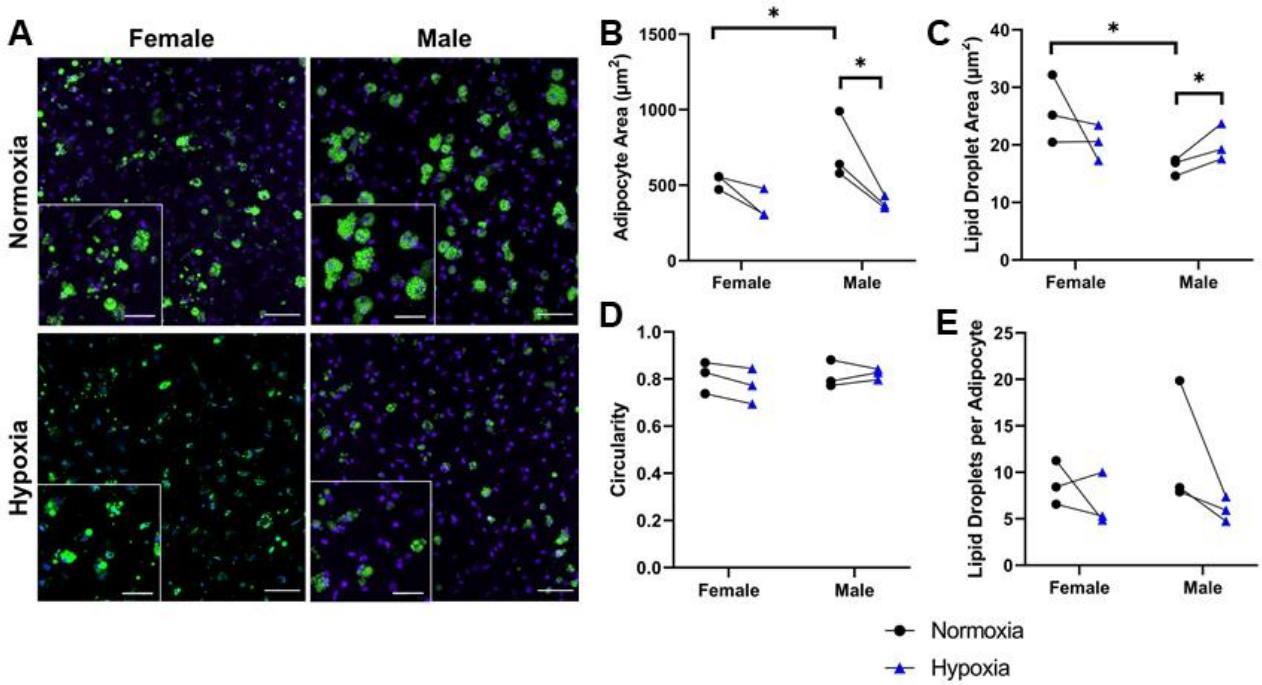

Figure B.4. Male adipocytes are larger and more responsive to hypoxia. *Representative images demonstrate adipocytes visualized with bodipy in green, with nuclei in blue (A). Scale bars are 100 microns. Adipocyte area (B), lipid droplet area (C), circularity (D), and lipid droplets per adipocyte (E) are quantified for each experimental condition. Significance is measured two-way ANOVA and Tukey's multiple comparison test. Significance (p<0.05) is denoted by *.*

Sex differences in adipocyte morphology and response to hypoxia

Representative images of adipocytes in engineered tissue show rounded morphology with lipid droplet accumulation (**Figure B.4.A**). Under normoxia, female adipocytes are smaller than male, regardless of depot. Female adipocytes were approximately 529 ± 40 μm^2 in area, while male adipocytes were significantly larger at 736 ± 180 μm^2 in area (**Figure B.4.B**). Interestingly, female adipocytes, though smaller, did have significantly larger lipid droplets (LDs). In female

adipocytes, LDs were 26.0 ± 4.8 μm^2, while male LDs were 16.3 ± 1.2 μm^2 (**Figure B.4.C**). There were no significant differences in circularity or number of LDs per adipocyte between male and female donors (**Figure B.4.D,E**).

Hypoxia had varying impacts on adipocyte maturity and morphology based on sex. In female cells, adipocyte area trended downward under hypoxia (**Figure B.4.B**). In male cells, adipocyte area significantly decreased from 736 ± 180 μm^2 to 383 ± 35 μm^2 (**Figure B.4.B**). While LD area was unchanged in female adipocytes under hypoxia, male adipocytes had a significant increase in LD area, from 16.3 ± 1.2 μm^2 to 20.2 ± 2.6 μm^2 (**Figure B.4.C**). Similar to normoxia, neither circularity or LDs per adipocyte were significantly changed by hypoxia (**Fig B.4.D,E**).

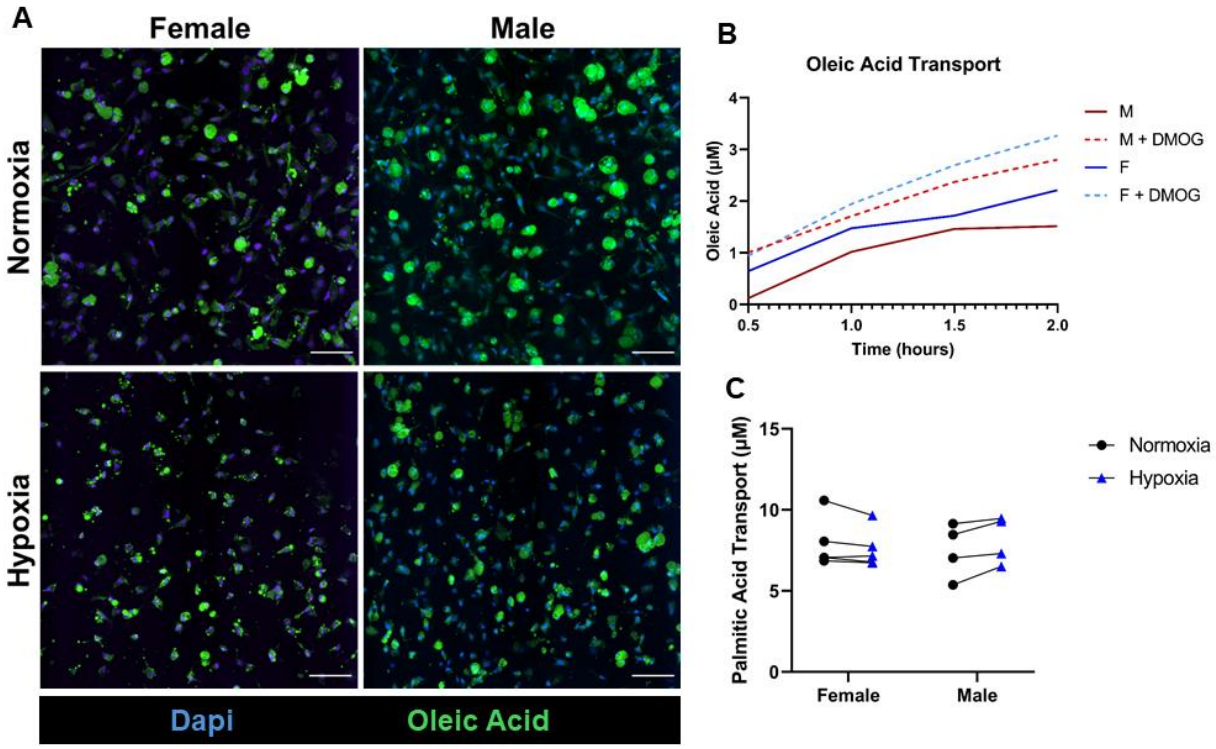

Figure B.5. Fatty acid transport in engineered AT. *Oleic acid uptake is visualized in engineered adipose tissue (A). Scale bar is 100 microns. The transport of oleic acid through the engineered AT and into the flow through media is quantified over time (B). Palmitic acid transport though the engineered AT is quantified at the endpoint (C).*

Fatty acid transport and hormone response

To probe the impact of sex differences and hypoxia on fatty acid transport, constructs were treated with TopFluor Oleic Acid (OA). Representative images show that adipocytes take up OA (**Figure B.5.A**). Media was taken from beneath the construct and measured on a fluorescent plate reader to determine OA transport. Preliminary data suggests more OA is transported through the engineered adipose tissue under hypoxia (**Figure B.5.B**), which is in line with the increased uptake visualized in representative images (**Figure B.5.A**). Additionally, palmitic acid transport was quantified and demonstrated no significant changes under hypoxia, though female adipocytes trended downward and male adipocytes trended upward (**Figure B.5.C**).

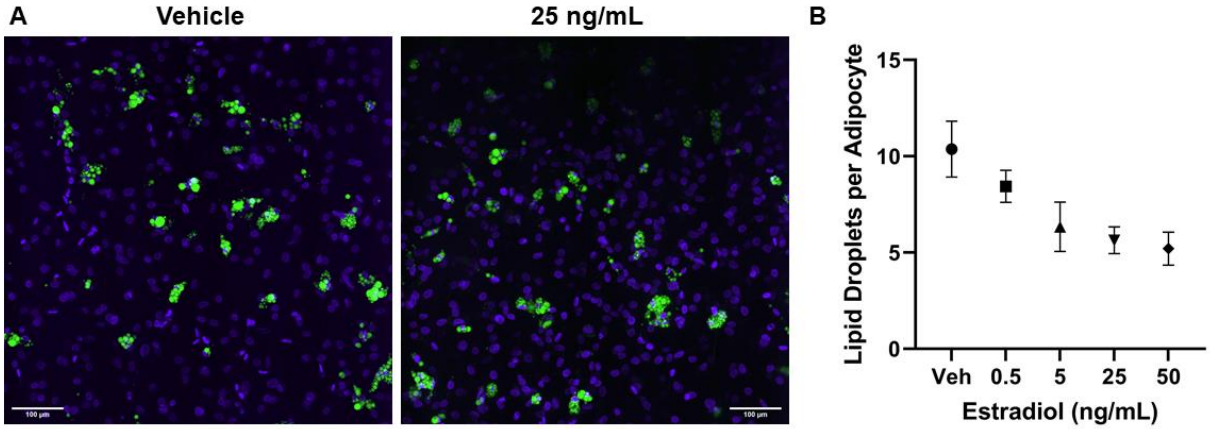

Figure B.6. Estradiol treatment pilot study suggests changes in adipocyte maturity. *Adipocytes are visualized in the engineered adipose tissue under treatment (A). Scale bars are 100 microns. The number of lipid droplets per adipocyte is quantified (B).*

Pilot data of adipocyte response to estradiol

To begin examining the contribution of female sex hormones to adipose tissue function, we treated engineered adipose tissue with adipocytes from female donors with varying

concentrations of estradiol. Representative images show LDs visualized in green with bodipy (**Figure B.6.A**). Data analysis of a pilot study suggests that LDs per adipocyte decreases as the dosage of estradiol increases (**Figure B.6.B**).

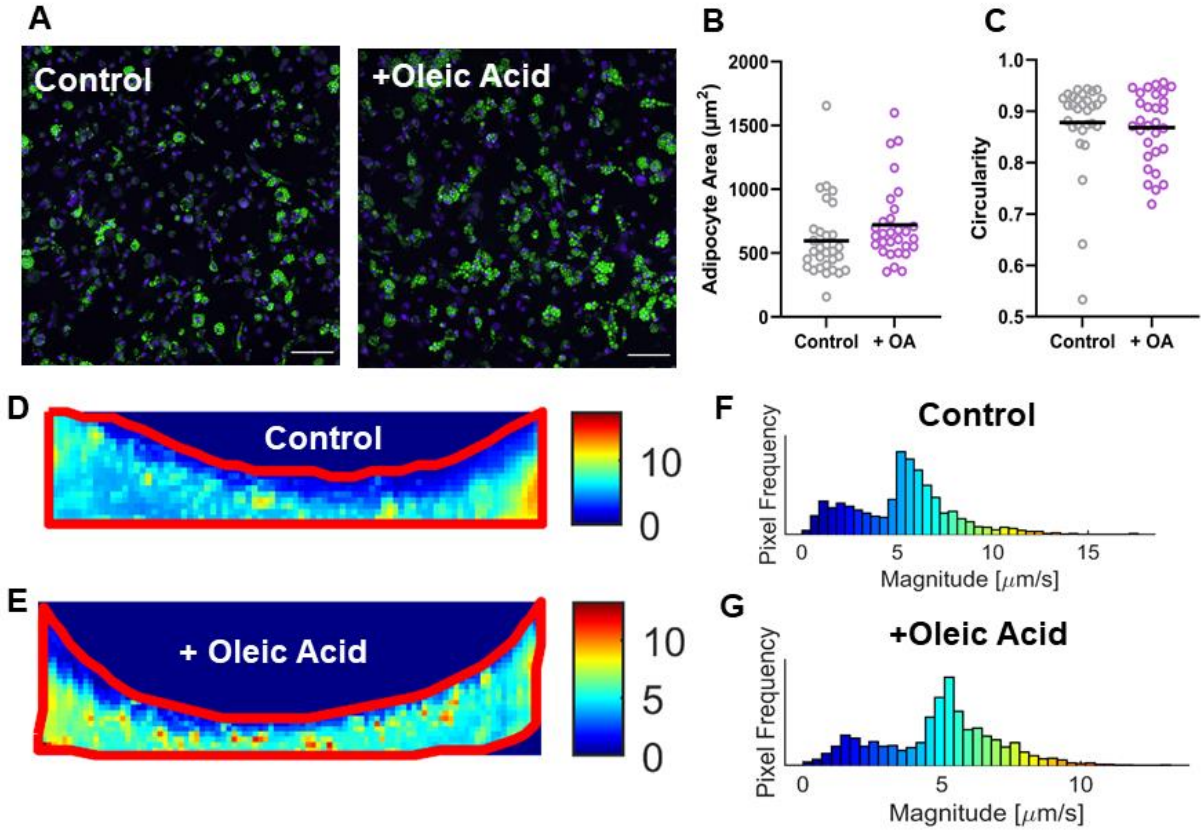

Figure B.7. Flow mapping of engineered adipose tissue. *Oleic acid supplementation is performed to enlarge adipocytes in engineered tissue. Representative images show adipocytes labeled with bodipy (green) and nuclei with DAPI in blue (A). Scale bars are 100 microns. Adipocyte area (B) and circularity (C) are quantified. Flow maps demonstrate the spatial map of flow velocity (D,E). Histograms of velocity demonstrate frequency (F,G).*

Altering adipocyte size in engineered adipose tissue for flow mapping via DCE-MRI

To control adipocyte size in vitro, cultures are supplemented with 500 µM oleic acid for one week. Oleic acid resulted in visibly larger adipocytes (**Figure B.7.A**). Pilot data suggests that oleic acid results in larger (**Figure B.7.B**), but not more circular (**Figure B.7.C**), adipocytes.

MRI imaging and flow analysis demonstrated pockets of high interstitial flow with OA treatment (**Figure B.7.D,E**). We hypothesize that these regions had dense and large adipocytes. In this pilot, the control eAT had an average velocity of 5.3 µm/s (**Figure B.7.F**), while the OA treated eAT had an average velocity of 4.9 µm/s (**Figure B.7.G**).

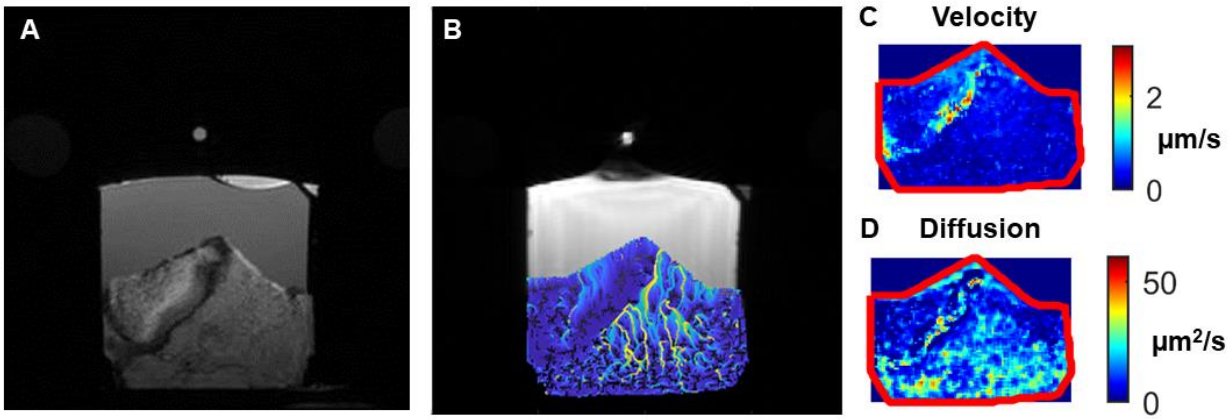

Figure B.8. Ex vivo flow mapping of adipose tissue. *Tissue structure is visualized via T2 imaging (A). Streamlines demonstrate contrast transport through the tissue (B). Flow velocity (C) and diffusion (D) maps demonstrate heterogeneity of metrics.*

Flow mapping in ex vivo adipose tissue

Finally, we sought to test out our MRI flow mapping tool on ex vivo tissue. We were successfully able to mount excised adipose tissue in tissue culture inserts for MRI imaging utilizing transglutaminase. T2 imaging demonstrates the structure of ex vivo tissue (**Figure B.8.A**). After DCE-MRI, streamlines are produced (**Figure B.8.B**) and flow metrics are quantified. The ex vivo tissue demonstrated much slower velocities and diffusion than our engineered adipose tissue models, with flow velocity around 0.6 µm/s (**Figure B.8.C**) and diffusivity around 36 $\mu m^2/s$ (**Figure B.8.D**). Spatial mapping of flow (**Figure B.8.C**)

demonstrates that transport in AT is heterogeneous and correlates with structures visualized in T2 images (**Figure B.8.A**).

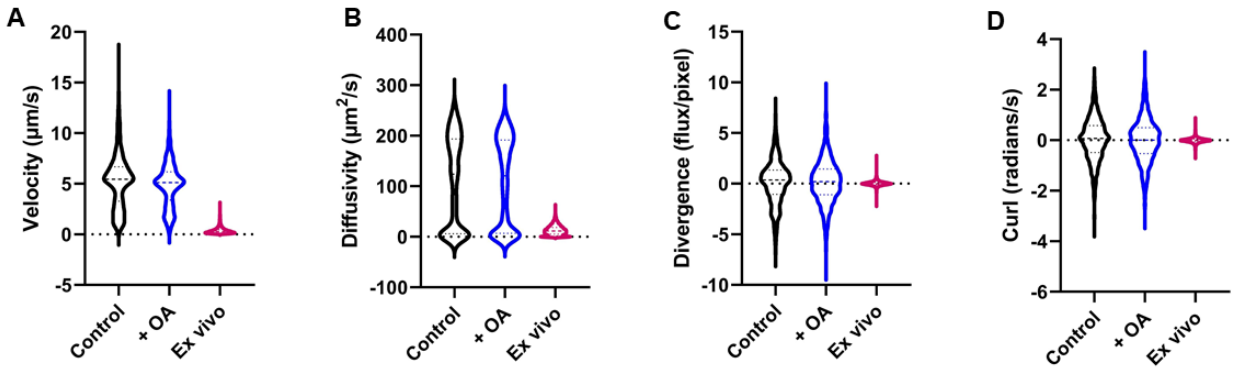

Figure B.9. Flow metrics are more consistent in ex vivo tissue. *Histograms of velocity (A), diffusivity (B), divergence (C), and curl (D) are reported for engineered adipose tissue with and without oleic acid supplementation and ex vivo tissue.*

Finally, we sought to compare our engineered AT transport metrics to the ex vivo tissue. Across velocity (**Figure B.9.A**) and diffusivity (**Figure B.9.B**), ex vivo tissue had much lower values and a smaller range. For divergence (**Figure B.9.C**), and curl (**Figure B.9.D**), though the average values were similar between ex vivo tissue and engineered tissue, once again the range in ex vivo tissue was much smaller.

Adipocyte response to interstitial fluid flow

Next, we sought to understand how adipocytes themselves might respond to altered transport. Adipocyte response to IFF was highly variable based on donor. Representative images show varying flow responses (**Figure B.10.A**). Donor 1 responded to flow via increased adipocyte area (**Figure B.1-.B**). Donor 2 showed decreased adipocyte area in response to flow, and donor 3 adipocyte area was unchanged (**Figure B.10.B**). Adipocyte circularity was not altered by flow (**Figure B.10.C**).

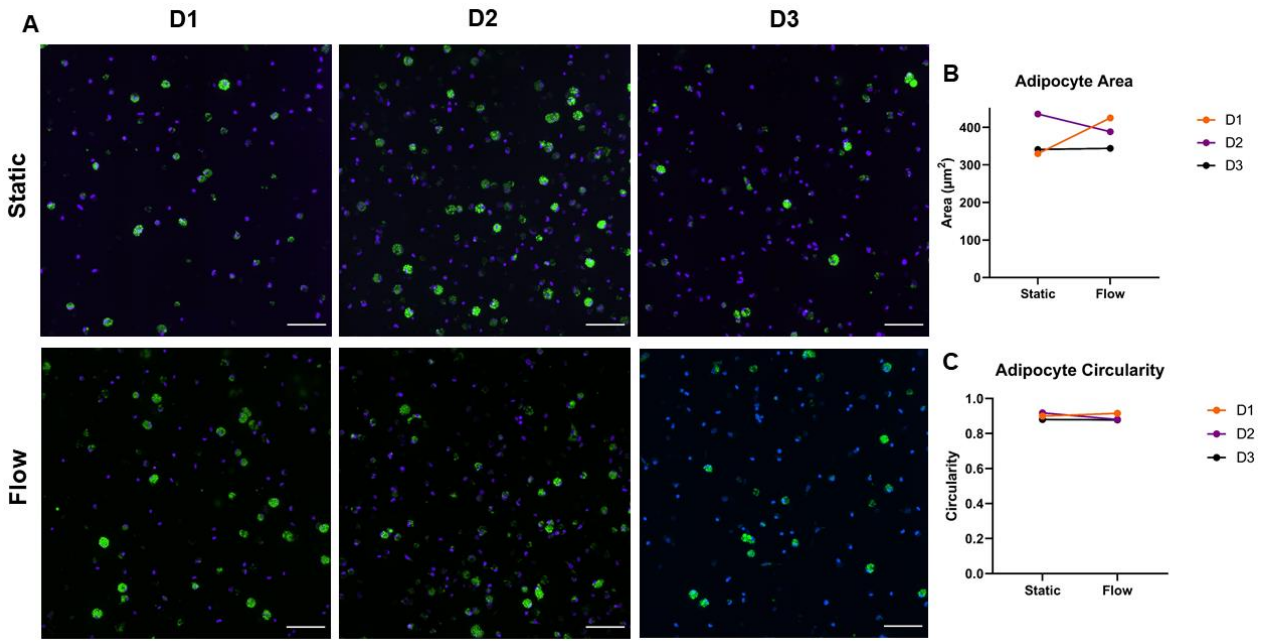

Figure B.10. Adipocyte response to IFF is variable. *Representative images demonstrate adipocyte morphology in response to flow (A). Scale bars are 100 microns. Adipocyte area (B) and circularity (C) are reported for each donor.*

B.4 Discussion

With the growing appreciation of adipose tissue as a master regulator of the body's metabolism, more physiologically relevant models are required. Adipose tissue disorders affect a large portion of the population, with over 40% of U.S. adults suffering from obesity (CDC.gov). The prevalence of lipedema has been a source of debate, with some estimates of lipedema in up to 10% of females (396), though this estimate has been challenged and is considered too high (397,398). We utilized previously established 3-dimensional engineered adipose tissue models (389,390) to begin to develop an in vitro model of lipedema. Key characteristics of lipedema tissue include (I) female adipocytes, (II) control over tissue microenvironment for aspects such as hypoxia, edema, and fibrosis, and (III) fluid and fatty acid transport.

We first sought to examine the differences between female and male adipocytes differentiated from adipose derived stem cells. In the burgeoning field of sex differences, adipose tissue is particularly well studied (399–403). Hormonal differences between females and males result in drastically different body composition. Generally, females are more likely to accumulate subcutaneous adipose tissue (SAT) in the lower extremities. Males are more likely to accumulate visceral adipose tissue (VAT) in the abdomen, which is correlated with metabolic dysfunction and inflammation. Notably, estrogen plays a large role in guiding AT distribution in females, as well as protecting from metabolic dysfunction.

Herein, we have demonstrated that male ADSC-derived adipocytes are larger in size than female. In contrast, lipid droplet area was significantly higher in female ADSC-derived adipocytes than male. These conflicting results could suggest differences in adipocyte maturity, where an adipocyte with a single, large lipid droplet is considered mature. Female adipocytes could therefore be smaller, but more mature, or more effective at lipid storage. There were no differences in circularity or number of lipid droplets per adipocyte. Adipocyte size is impacted by several confounding variables, including depot, BMI, and other metabolic complications. In the literature, some studies demonstrate larger adipocytes in obese males compared to females (404,405), while others found limited differences (406), or larger adipocytes in females (407,408). Interestingly, when male and female mice were both given a high fat diet, females gained weight at a slower pace than male mice, though at the same weight, they had larger adipocytes (409). It is important to note that some of these studies looked at different depots, and generally it was reported that female adipocytes are larger in the lower extremities and male adipocytes are larger in the abdomen. Sourcing ADSCs from various depots will be essential toward understanding sex differences in this context.

Next, we sought to examine sex differences in response to hypoxia. Previous work demonstrated hypoxia treatment in vitro results in smaller adipocytes (390). We report that adipocyte area trended downward in female adipocytes but was significantly decreased in male adipocytes. Interestingly, male lipid droplet area was significantly increased by hypoxia, while female lipid droplet area was not. Similar to normoxia, circularity and lipid droplets per adipocyte were unchanged. These results suggest that male adipocytes are more susceptible to changes after hypoxia exposure.

Beyond adipocyte morphology, we sought to understand the effect of sex and hypoxia on engineered adipose tissue function. We have chosen to focus on the transport of fatty acids as a key element toward eAT function. Oleic acid, which is prevalent in olive oil, is an unsaturated fatty acid that is considered to have beneficial impacts on metabolism and weight (410,411). Oleic acid uptake by adipose tissue is on the scale of hours (412). Palmitic acid is a saturated fatty acid that makes up 20-30% of fatty acids in human adipose tissue and is prevalent in animal fat and vegetable oils (413). Palmitic acid is associated with increased inflammation and insulin resistance (414–417). It is hypothesized that transport of fatty acids in lipidemic tissue is impaired. Using fluorescently labeled oleic acid, we were able to observe OA uptake in engineered adipose tissue. Visually, more OA uptake occurred under normoxia than hypoxia. Preliminary data of OA transport over time was measured via fluorescence readings in the media that had passed through the eAT. Overall, more OA was measured in the flow through media under hypoxia, matching the visual observations of decreased uptake. More replicates are required to understand how hypoxia and sex differences impact OA transport. Palmitic acid transport, measured by the concentration of PA in the flow through media, did not demonstrate significant differences based on sex or hypoxia. Generally, PA transport in females under

hypoxia trended down, while in males, it trended up. Overall, these results demonstrate that we can quantify fatty acid uptake and transport through engineered adipose tissue.

A major player in adipose tissue dimorphism is the estrogen signaling pathway. Preliminary data testing estradiol dilutions on engineered adipose tissue showed that lipid droplets per adipocyte trended downwards as estradiol concentration increased. More replicates are required to understand the impacts of estradiol on adipocyte maturity and function in vitro.

Beyond cellular level behavior, we also sought to understand the physical forces at play during lipedema progression. To see whether we could alter adipocyte size in vitro and directly observe changes to transport, we supplemented engineered adipose tissue with oleic acid to increase adipocyte size. This preliminary study demonstrated adipocyte size was trending upwards, while circularity was unchanged. We used DCE-MRI to observe flow velocities throughout the tissue and demonstrated that average flow velocity was trending downward in OA-treated eAT. However, more pockets of high interstitial flow were observed on the velocity map.

We next sought to benchmark transport parameters in our engineered adipose tissue to ex vivo tissue. By securing ex vivo thigh adipose tissue in a tissue culture insert with transglutaminase, we were able to add contrast and image fluid transport through the tissue. Generally, transport was much slower in ex vivo tissue compared to engineered tissue. Interestingly, ex vivo transport parameters were also much less variable than eAT. These results demonstrate that engineered adipose tissue will be ideal for precise control of experimental factors, but does not match the transport values of ex vivo tissue. This is likely due to the very high density of adipocytes in ex vivo tissue that is challenging to replicate in a hydrogel. However, the hydrogel system provides a plethora of benefits, including throughput,

experimental control, and ease of visualization. Therefore, the ex vivo and eAT models will be applied to different experimental questions.

The impacts of mechanical forces on adipocyte differentiation and function are well studied (418), but there is a major gap in the study of interstitial fluid flow. In lipedema, decreased fluid flow could lead to compression of adipocytes by retained fluid. One study has demonstrated that compression of adipocytes induced inflammation (419). Using our pressure-head driven flow system (sources), we sought to examine adipocyte response to IFF. Amongst three donors, response to flow varied widely. Interestingly, one donor had decreased adipocyte area in response to flow, one donor had increased area, and one donor was unchanged. The factors that contribute toward adipocyte flow response are not currently understood, but it is well established that adipocytes are mechanosensitive (420). Further, PIEZO1, a mechanosensory of fluid flow, is known to impact adipogenesis (421). Thus, exploration of flow-mediated impacts of adipocytes is of great interest.

Overall, these results suggest sex differences among adipocytes which may advance our understanding of why lipedema primarily affects female patients. Adipocyte maturity and size could alter transport biochemically, in terms of lipid uptake and storage, as well as physically, by altering the microenvironment. Understanding changes to transport in healthy and dysfunctional AT and how flow impacts adipocyte function will provide essential information toward understanding AT-related disorders.

References

1. Hammel JH, Cook SR, Belanger MC, Munson JM, Pompano RR. Modeling Immunity In Vitro: Slices, Chips, and Engineered Tissues. Annu Rev Biomed Eng. 2021 Jun 4;23(1):annurev-bioeng-082420-124920.

2. Nipper ME, Dixon JB. Engineering the Lymphatic System. Cardiovasc Eng Technol. 2011 Dec;2(4):296–308.

3. Card CM, Yu SS, Swartz MA. Emerging roles of lymphatic endothelium in regulating adaptive immunity. J Clin Invest. 2014 Mar 3;124(3):943–52.

4. Randolph GJ, Ivanov S, Zinselmeyer BH, Scallan JP. The Lymphatic System: Integral Roles in Immunity. Annu Rev Immunol. 2017 Apr 26;35:31–52.

5. Shields JD. Lymphatics: At the Interface of Immunity, Tolerance, and Tumor Metastasis: Lymphatics in Cancer and Inflammation. Microcirculation. 2011 Oct;18(7):517–31.

6. Harris AR, Perez MJ, Munson JM. Docetaxel facilitates lymphatic-tumor crosstalk to promote lymphangiogenesis and cancer progression. BMC Cancer. 2018 Dec;18(1):718.

7. Baluk P, Fuxe J, Hashizume H, Romano T, Lashnits E, Butz S, et al. Functionally specialized junctions between endothelial cells of lymphatic vessels. J Exp Med. 2007 Oct 1;204(10):2349–62.

8. Sen D, Forrest L, Kepler TB, Parker I, Cahalan MD. Selective and site-specific mobilization of dermal dendritic cells and Langerhans cells by Th1- and Th2-polarizing adjuvants. Proc Natl Acad Sci. 2010 May 4;107(18):8334–9.

9. Jackson DG. Leucocyte Trafficking via the Lymphatic Vasculature— Mechanisms and Consequences. Front Immunol. 2019 Mar 14;10:471.

10. Weber M, Hauschild R, Schwarz J, Moussion C, De Vries I, Legler DF, et al. Interstitial Dendritic Cell Guidance by Haptotactic Chemokine Gradients. Science. 2013 Jan 18;339(6117):328–32.

11. Dixon JB, Greiner ST, Gashev AA, Cote GL, Moore JE, Zawieja DC. Lymph Flow, Shear Stress, and Lymphocyte Velocity in Rat Mesenteric Prenodal Lymphatics. Microcirculation. 2006 Oct 11;13(7):597–610.

12. Fischer M, Franzeck UK, Herrig I, Costanzo U, Wen S, Schiesser M, et al. Flow velocity of single lymphatic capillaries in human skin. Am J Physiol-Heart Circ Physiol. 1996 Jan 1;270(1):H358–63.

13. Breslin JW. Mechanical forces and lymphatic transport. Microvasc Res. 2014 Nov;96:46–54.

14. Blatter C, Meijer EFJ, Nam AS, Jones D, Bouma BE, Padera TP, et al. In vivo label-free measurement of lymph flow velocity and volumetric flow rates using Doppler optical coherence tomography. Sci Rep. 2016 Jul 5;6(1):29035.

15. Bouta EM, Wood RW, Brown EB, Rahimi H, Ritchlin CT, Schwarz EM. *In vivo* quantification of lymph viscosity and pressure in lymphatic vessels and draining lymph nodes of arthritic joints in mice. J Physiol. 2014 Mar 15;592(6):1213–23.

16. Renkin EM. Some consequences of capillary permeability to macromolecules: Starling's hypothesis reconsidered. Am J Physiol-Heart Circ Physiol. 1986 May 1;250(5):H706–10.

17. Moore JE, Bertram CD. Lymphatic System Flows. Annu Rev Fluid Mech. 2018 Jan 5;50(1):459–82.

18. Maclellan RA. The Lymphatic System. In: Greene AK, Slavin SA, Brorson H, editors. Lymphedema [Internet]. Cham: Springer International Publishing; 2015 [cited 2024 Aug 16]. p. 3–7. Available from: https://link.springer.com/10.1007/978-3-319-14493-1_1

19. Smith JB, McIntosh GH, Morris B. The traffic of cells through tissues: a study of peripheral lymph in sheep. J Anat. 1970 Jul;107(Pt 1):87–100.

20. Schwager S, Detmar M. Inflammation and Lymphatic Function. Front Immunol. 2019 Feb 26;10:308.

21. Cromer WE, Zawieja SD, Tharakan B, Childs EW, Newell MK, Zawieja DC. The effects of inflammatory cytokines on lymphatic endothelial barrier function. Angiogenesis. 2014 Apr;17(2):395–406.

22. Chaitanya GV, Franks SE, Cromer W, Wells SR, Bienkowska M, Jennings MH, et al. Differential Cytokine Responses in Human and Mouse Lymphatic Endothelial Cells to Cytokines *in Vitro*. Lymphat Res Biol. 2010 Sep;8(3):155–64.

23. Kataru RP, Kim H, Jang C, Choi DK, Koh BI, Kim M, et al. T Lymphocytes Negatively Regulate Lymph Node Lymphatic Vessel Formation. Immunity. 2011 Jan;34(1):96–107.

24. Aldrich MB, Sevick-Muraca EM. Cytokines are systemic effectors of lymphatic function in acute inflammation. Cytokine. 2013 Oct;64(1):362–9.

25. Johnson LA, Jackson DG. The chemokine CX3CL1 promotes trafficking of dendritic cells through inflamed lymphatics. J Cell Sci. 2013 Jan 1;jcs.135343.

26. Johnson LA, Jackson DG. Inflammation-induced secretion of CCL21 in lymphatic endothelium is a key regulator of integrin-mediated dendritic cell transmigration. Int Immunol. 2010 Oct;22(10):839–49.

27. Vaahtomeri K, Brown M, Hauschild R, De Vries I, Leithner AF, Mehling M, et al. Locally Triggered Release of the Chemokine CCL21 Promotes Dendritic Cell Transmigration across Lymphatic Endothelia. Cell Rep. 2017 May;19(5):902–9.

28. Zhuo W, Jia L, Song N, Lu X an, Ding Y, Wang X, et al. The CXCL12–CXCR4 Chemokine Pathway: A Novel Axis Regulates Lymphangiogenesis. Clin Cancer Res. 2012 Oct 1;18(19):5387–98.

29. Kabashima K, Shiraishi N, Sugita K, Mori T, Onoue A, Kobayashi M, et al. CXCL12-CXCR4 Engagement Is Required for Migration of Cutaneous Dendritic Cells. Am J Pathol. 2007 Oct;171(4):1249–57.

30. Farnsworth RH, Karnezis T, Maciburko SJ, Mueller SN, Stacker SA. The Interplay Between Lymphatic Vessels and Chemokines. Front Immunol. 2019 Apr 12;10:518.

31. Johnson LA. In Sickness and in Health: The Immunological Roles of the Lymphatic System. Int J Mol Sci. 2021 Apr 24;22(9):4458.

32. Tammela T, Alitalo K. Lymphangiogenesis: Molecular Mechanisms and Future Promise. Cell. 2010 Feb;140(4):460–76.

33. Huggenberger R, Siddiqui SS, Brander D, Ullmann S, Zimmermann K, Antsiferova M, et al. An important role of lymphatic vessel activation in limiting acute inflammation. Blood. 2011 Apr 28;117(17):4667–78.

34. Huggenberger R, Ullmann S, Proulx ST, Pytowski B, Alitalo K, Detmar M. Stimulation of lymphangiogenesis via VEGFR-3 inhibits chronic skin inflammation. J Exp Med. 2010 Sep 27;207(10):2255–69.

35. Dieterich LC, Seidel CD, Detmar M. Lymphatic vessels: new targets for the treatment of inflammatory diseases. Angiogenesis. 2014 Apr;17(2):359–71.

36. Louie DAP, Liao S. Lymph Node Subcapsular Sinus Macrophages as the Frontline of Lymphatic Immune Defense. Front Immunol. 2019 Feb 28;10:347.

37. Pape KA, Catron DM, Itano AA, Jenkins MK. The Humoral Immune Response Is Initiated in Lymph Nodes by B Cells that Acquire Soluble Antigen Directly in the Follicles. Immunity. 2007 Apr;26(4):491–502.

38. Mandl JN, Liou R, Klauschen F, Vrisekoop N, Monteiro JP, Yates AJ, et al. Quantification of lymph node transit times reveals differences in antigen surveillance strategies of naïve $CD4^+$ and $CD8^+$ T cells. Proc Natl Acad Sci. 2012 Oct 30;109(44):18036–41.

39. Nutt SL, Hodgkin PD, Tarlinton DM, Corcoran LM. The generation of antibody-secreting plasma cells. Nat Rev Immunol. 2015 Mar;15(3):160–71.

40. Allie SR, Randall TD. Resident Memory B Cells. Viral Immunol. 2020 May 1;33(4):282–93.

41. Jafarnejad M, Woodruff MC, Zawieja DC, Carroll MC, Moore JE. Modeling Lymph Flow and Fluid Exchange with Blood Vessels in Lymph Nodes. Lymphat Res Biol. 2015 Dec;13(4):234–47.

42. Acton SE, Onder L, Novkovic M, Martinez VG, Ludewig B. Communication, construction, and fluid control: lymphoid organ fibroblastic reticular cell and conduit networks. Trends Immunol. 2021 Sep;42(9):782–94.

43. Novkovic M, Onder L, Bocharov G, Ludewig B. Topological Structure and Robustness of the Lymph Node Conduit System. Cell Rep. 2020 Jan;30(3):893-904.e6.

44. Thierry GR, Kuka M, De Giovanni M, Mondor I, Brouilly N, Iannacone M, et al. The conduit system exports locally secreted IgM from lymph nodes. J Exp Med. 2018 Dec 3;215(12):2972–83.

45. Link A, Vogt TK, Favre S, Britschgi MR, Acha-Orbea H, Hinz B, et al. Fibroblastic reticular cells in lymph nodes regulate the homeostasis of naive T cells. Nat Immunol. 2007 Nov;8(11):1255–65.

46. Siegert S, Huang HY, Yang CY, Scarpellino L, Carrie L, Essex S, et al. Fibroblastic reticular cells from lymph nodes attenuate T cell expansion by producing nitric oxide. PloS One. 2011;6(11):e27618.

47. Gasteiger G, Ataide M, Kastenmüller W. Lymph node – an organ for T-cell activation and pathogen defense. Immunol Rev. 2016 May;271(1):200–20.

48. The route of re-circulation of lymphocytes in the rat. Proc R Soc Lond B Biol Sci. 1964 Jan 14;159(975):257–82.

49. Miller MJ, Wei SH, Parker I, Cahalan MD. Two-Photon Imaging of Lymphocyte Motility and Antigen Response in Intact Lymph Node. Science. 2002 Jun 7;296(5574):1869–73.

50. Bousso P, Robey E. Dynamics of CD8+ T cell priming by dendritic cells in intact lymph nodes. Nat Immunol. 2003 Jun 1;4(6):579–85.

51. Willard-Mack CL. Normal Structure, Function, and Histology of Lymph Nodes. Toxicol Pathol. 2006 Aug;34(5):409–24.

52. Suarez AC, Hammel JH, Munson JM. Modeling lymphangiogenesis: Pairing in vitro and in vivo metrics. Microcirculation. 2023 Apr;30(2–3):e12802.

53. Hammel JH, Zatorski JM, Cook SR, Pompano RR, Munson JM. Engineering in vitro immune-competent tissue models for testing and evaluation of therapeutics. Adv Drug Deliv Rev. 2022 Mar;182:114111.

54. Banerji S, Ni J, Wang SX, Clasper S, Su J, Tammi R, et al. LYVE-1, a new homologue of the CD44 glycoprotein, is a lymph-specific receptor for hyaluronan. J Cell Biol. 1999 Feb 22;144(4):789–801.

55. Breiteneder-Geleff S, Soleiman A, Horvat R, Amann G, Kowalski H, Kerjaschki D. [Podoplanin--a specific marker for lymphatic endothelium expressed in angiosarcoma]. Verh Dtsch Ges Pathol. 1999;83:270–5.

56. Kaipainen A, Korhonen J, Mustonen T, van Hinsbergh VW, Fang GH, Dumont D, et al. Expression of the fms-like tyrosine kinase 4 gene becomes restricted to lymphatic endothelium during development. Proc Natl Acad Sci. 1995 Apr 11;92(8):3566–70.

57. Boardman KC, Swartz MA. Interstitial Flow as a Guide for Lymphangiogenesis. Circ Res. 2003 Apr 18;92(7):801–8.

58. Wilting J, Papoutsi M, Christ B, Nicolaides KH, von Kaisenberg CS, Borges J, et al. The transcription factor Prox1 is a marker for lymphatic endothelial cells in normal and diseased human tissues. FASEB J Off Publ Fed Am Soc Exp Biol. 2002 Aug;16(10):1271–3.

59. Deng J, Dai T, Sun Y, Zhang Q, Jiang Z, Li S, et al. Overexpression of Prox1 Induces the Differentiation of Human Adipose-Derived Stem Cells into Lymphatic Endothelial-Like Cells *In Vitro*. Cell Reprogramming. 2017 Feb;19(1):54–63.

60. Shrestha S, Cho W, Stump B, Imani J, Lamattina AM, Louis PH, et al. FK506 induces lung lymphatic endothelial cell senescence and downregulates LYVE-1 expression, with associated decreased hyaluronan uptake. Mol Med. 2020 Dec;26(1):75.

61. Nishino K, Yoshimatsu Y, Muramatsu T, Sekimoto Y, Mitani K, Kobayashi E, et al. Isolation and characterisation of lymphatic endothelial cells from lung tissues affected by lymphangioleiomyomatosis. Sci Rep. 2021 Dec;11(1):8406.

62. Nandi P, Girish GV, Majumder M, Xin X, Tutunea-Fatan E, Lala PK. PGE2 promotes breast cancer-associated lymphangiogenesis by activation of EP4 receptor on lymphatic endothelial cells. BMC Cancer. 2017 Dec;17(1):11.

63. Ando T, Jordan P, Joh T, Wang Y, Jennings MH, Houghton J, et al. Isolation and Characterization of A Novel Mouse Lymphatic Endothelial Cell Line: SV-LEC. Lymphat Res Biol. 2005 Sep;3(3):105–15.

64. Garrafa E, Trainini L, Benetti A, Saba E, Fezzardi L, Lorusso B, et al. Isolation, purification, and heterogeneity of human lymphatic endothelial cells from different tissues. Lymphology. 2005 Dec;38(4):159–66.

65. Ng CP, Helm CLE, Swartz MA. Interstitial flow differentially stimulates blood and lymphatic endothelial cell morphogenesis in vitro. Microvasc Res. 2004 Nov;68(3):258–64.

66. Michalaki E, Surya VN, Fuller GG, Dunn AR. Perpendicular alignment of lymphatic endothelial cells in response to spatial gradients in wall shear stress. Commun Biol. 2020 Dec;3(1):57.

67. Amatschek S, Kriehuber E, Bauer W, Reininger B, Meraner P, Wolpl A, et al. Blood and lymphatic endothelial cell-specific differentiation programs are stringently controlled by the tissue environment. Blood. 2007 Jun 1;109(11):4777–85.

68. Schoppmann SF, Soleiman A, Kalt R, Okubo Y, Benisch C, Nagavarapu U, et al. Telomerase-Immortalized Lymphatic and Blood Vessel Endothelial Cells are Functionally Stable and Retain Their Lineage Specificity. Microcirculation. 2004 Jan;11(3):261–9.

69. Frenkel N, Poghosyan S, Alarcón CR, García SB, Queiroz K, van den Bent L, et al. Long-Lived Human Lymphatic Endothelial Cells to Study Lymphatic Biology and Lymphatic Vessel/Tumor Coculture in a 3D Microfluidic Model. ACS Biomater Sci Eng. 2021 Jul 12;7(7):3030–42.

70. Liang CC, Park AY, Guan JL. In vitro scratch assay: a convenient and inexpensive method for analysis of cell migration in vitro. Nat Protoc. 2007 Feb;2(2):329–33.

71. Vega-Avila E, Pugsley MK. An overview of colorimetric assay methods used to assess survival or proliferation of mammalian cells. Proc West Pharmacol Soc. 2011;54:10–4.

72. Boyden S. THE CHEMOTACTIC EFFECT OF MIXTURES OF ANTIBODY AND ANTIGEN ON POLYMORPHONUCLEAR LEUCOCYTES. J Exp Med. 1962 Mar 1;115(3):453–66.

73. Kramer N, Walzl A, Unger C, Rosner M, Krupitza G, Hengstschläger M, et al. In vitro cell migration and invasion assays. Mutat Res Mutat Res. 2013 Jan;752(1):10–24.

74. Munson JM, Bellamkonda RV, Swartz MA. Interstitial Flow in a 3D Microenvironment Increases Glioma Invasion by a CXCR4-Dependent Mechanism. Cancer Res. 2013 Mar 1;73(5):1536–46.

75. Kingsmore KM, Logsdon DK, Floyd DH, Peirce SM, Purow BW, Munson JM. Interstitial flow differentially increases patient-derived glioblastoma stem cell invasion *via* CXCR4, CXCL12, and CD44-mediated mechanisms. Integr Biol. 2016 Dec 5;8(12):1246–60.

76. Cornelison RC, Brennan CE, Kingsmore KM, Munson JM. Convective forces increase CXCR4-dependent glioblastoma cell invasion in GL261 murine model. Sci Rep. 2018 Dec;8(1):17057.

77. Kubota Y, Kleinman HK, Martin GR, Lawley TJ. Role of laminin and basement membrane in the morphological differentiation of human endothelial cells into capillary-like structures. J Cell Biol. 1988 Oct 1;107(4):1589–98.

78. Arnaoutova I, George J, Kleinman HK, Benton G. The endothelial cell tube formation assay on basement membrane turns 20: state of the science and the art. Angiogenesis. 2009 Sep;12(3):267–74.

79. Blacher S, Erpicum C, Lenoir B, Paupert J, Moraes G, Ormenese S, et al. Cell Invasion in the Spheroid Sprouting Assay: A Spatial Organisation Analysis Adaptable to Cell Behaviour. Kirchmair R, editor. PLoS ONE. 2014 May 7;9(5):e97019.

80. Gibot L, Galbraith T, Kloos B, Das S, Lacroix DA, Auger FA, et al. Cell-based approach for 3D reconstruction of lymphatic capillaries in vitro reveals distinct functions of HGF and VEGF-C in lymphangiogenesis. Biomaterials. 2016 Feb;78:129–39.

81. Gibot L, Galbraith T, Bourland J, Rogic A, Skobe M, Auger FA. Tissue-engineered 3D human lymphatic microvascular network for in vitro studies of lymphangiogenesis. Nat Protoc. 2017 May;12(5):1077–88.

82. Lee S, Kang H, Park D, Yu J, Koh SK, Cho D, et al. Modeling 3D Human Tumor Lymphatic Vessel Network Using High-Throughput Platform. Adv Biol. 2021 Feb;5(2):2000195.

83. Pisano M, Triacca V, Barbee KA, Swartz MA. An in vitro model of the tumor–lymphatic microenvironment with simultaneous transendothelial and luminal flows reveals mechanisms of flow enhanced invasion. Integr Biol. 2015;7(5):525–33.

84. Kim S, Chung M, Jeon NL. Three-dimensional biomimetic model to reconstitute sprouting lymphangiogenesis in vitro. Biomaterials. 2016 Feb;78:115–28.

85. Sato M, Sasaki N, Ato M, Hirakawa S, Sato K, Sato K. Microcirculation-on-a-Chip: A Microfluidic Platform for Assaying Blood- and Lymphatic-Vessel Permeability. Eddington DT, editor. PLOS ONE. 2015 Sep 2;10(9):e0137301.

86. Lugo-Cintrón KM, Ayuso JM, White BR, Harari PM, Ponik SM, Beebe DJ, et al. Matrix density drives 3D organotypic lymphatic vessel activation in a microfluidic model of the breast tumor microenvironment. Lab Chip. 2020;20(9):1586–600.

87. Cho HY, Choi JH, Kim KJ, Shin M, Choi JW. Microfluidic System to Analyze the Effects of Interleukin 6 on Lymphatic Breast Cancer Metastasis. Front Bioeng Biotechnol. 2021 Feb 15;8:611802.

88. Henderson AR, Ilan IS, Lee E. A bioengineered lymphatic vessel model for studying lymphatic endothelial cell-cell junction and barrier function. Microcirculation [Internet]. 2021 Nov [cited 2022 Apr 7];28(8). Available from: https://onlinelibrary.wiley.com/doi/10.1111/micc.12730

89. Gong MM, Lugo-Cintron KM, White BR, Kerr SC, Harari PM, Beebe DJ. Human organotypic lymphatic vessel model elucidates microenvironment-dependent signaling and barrier function. Biomaterials. 2019 Sep;214:119225.

90. Selahi A, Fernando T, Chakraborty S, Muthuchamy M, Zawieja DC, Jain A. Lymphangion-chip: a microphysiological system which supports co-culture and bidirectional signaling of lymphatic endothelial and muscle cells. Lab Chip. 2022;22(1):121–35.

91. Cho Y, Na K, Jun Y, Won J, Yang JH, Chung S. Three-Dimensional In Vitro Lymphangiogenesis Model in Tumor Microenvironment. Front Bioeng Biotechnol. 2021 Oct 4;9:697657.

92. In J, Ryu J, Yu H, Kang D, Kim T, Kim J. Microfluidic valvular chips and a numerical lymphatic vessel model for the study of lymph transport characteristics. Lab Chip. 2021;21(11):2283–93.

93. Bruyère F, Melen-Lamalle L, Blacher S, Roland G, Thiry M, Moons L, et al. Modeling lymphangiogenesis in a three-dimensional culture system. Nat Methods. 2008 May;5(5):431–7.

94. Azimi MS, Motherwell JM, Murfee WL. An Ex Vivo Method for Time-Lapse Imaging of Cultured Rat Mesenteric Microvascular Networks. J Vis Exp. 2017 Feb 9;(120):55183.

95. Eklund L, Bry M, Alitalo K. Mouse models for studying angiogenesis and lymphangiogenesis in cancer. Mol Oncol. 2013 Apr;7(2):259–82.

96. Xiang M, Grosso RA, Takeda A, Pan J, Bekkhus T, Brulois K, et al. A Single-Cell Transcriptional Roadmap of the Mouse and Human Lymph Node Lymphatic Vasculature. Front Cardiovasc Med. 2020 Apr 30;7:52.

97. Sauter B, Foedinger D, Sterniczky B, Wolff K, Rappersberger K. Immunoelectron Microscopic Characterization of Human Dermal Lymphatic Microvascular Endothelial Cells: Differential Expression of CD31, CD34, and Type IV Collagen with Lymphatic Endothelial Cells vs Blood Capillary Endothelial Cells in Normal Human Skin, Lymphangioma, and Hemangioma In Situ. J Histochem Cytochem. 1998 Feb;46(2):165–76.

98. Pusztaszeri MP, Seelentag W, Bosman FT. Immunohistochemical Expression of Endothelial Markers CD31, CD34, von Willebrand Factor, and Fli-1 in Normal Human Tissues. J Histochem Cytochem. 2006 Apr;54(4):385–95.

99. Chang C, Seibel AJ, Song JW. Application of microscale culture technologies for studying lymphatic vessel biology. Microcirculation [Internet]. 2019 Nov [cited 2022 Apr 13];26(8). Available from: https://onlinelibrary.wiley.com/doi/10.1111/micc.12547

100. Alderfer L, Hall E, Hanjaya-Putra D. Harnessing biomaterials for lymphatic system modulation. Acta Biomater. 2021 Oct;133:34–45.

101. Greenlee JD, King MR. Engineered fluidic systems to understand lymphatic cancer metastasis. Biomicrofluidics. 2020 Jan;14(1):011502.

102. Miyahara M, Tanuma J ichi, Sugihara K, Semba I. Tumor lymphangiogenesis correlates with lymph node metastasis and clinicopathologic parameters in oral squamous cell carcinoma. Cancer. 2007 Sep 15;110(6):1287–94.

103. Hirakawa S, Brown LF, Kodama S, Paavonen K, Alitalo K, Detmar M. VEGF-C–induced lymphangiogenesis in sentinel lymph nodes promotes tumor metastasis to distant sites. Blood. 2007 Feb 1;109(3):1010–7.

104. Mestas J, Hughes CCW. Of Mice and Not Men: Differences between Mouse and Human Immunology. J Immunol. 2004 Mar 1;172(5):2731–8.

105. Shoichet MS. Polymer Scaffolds for Biomaterials Applications. Macromolecules. 2010 Jan 26;43(2):581–91.

106. Singh A, Peppas NA. Hydrogels and Scaffolds for Immunomodulation. Adv Mater. 2014 Oct;26(38):6530–41.

107. Sadtler K, Wolf MT, Ganguly S, Moad CA, Chung L, Majumdar S, et al. Divergent immune responses to synthetic and biological scaffolds. Biomaterials. 2019 Feb;192:405–15.

108. Caccavo D, Cascone S, Lamberti G, Barba AA. Hydrogels: experimental characterization and mathematical modelling of their mechanical and diffusive behaviour. Chem Soc Rev. 2018;47(7):2357–73.

109. Loh QL, Choong C. Three-Dimensional Scaffolds for Tissue Engineering Applications: Role of Porosity and Pore Size. Tissue Eng Part B Rev. 2013 Dec;19(6):485–502.

110. Oyen ML. Mechanical characterisation of hydrogel materials. Int Mater Rev. 2014 Jan;59(1):44–59.

111. Ghasemiyeh P, Mohammadi-Samani S. Hydrogels as Drug Delivery Systems; Pros and Cons. Trends Pharm Sci [Internet]. 2019 Mar [cited 2021 May 14];5(1). Available from: https://doi.org/10.30476/tips.2019.81604.1002

112. Stachowiak AN, Irvine DJ. Inverse opal hydrogel-collagen composite scaffolds as a supportive microenvironment for immune cell migration. J Biomed Mater Res A. 2008 Jun 1;85A(3):815–28.

113. Katakai T. A novel reticular stromal structure in lymph node cortex: an immuno-platform for interactions among dendritic cells, T cells and B cells. Int Immunol. 2004 Jun 28;16(8):1133–42.

114. Gretz JE, Anderson AO, Shaw S. Cords, channels, corridors and conduits: critical architectural elements facilitating cell interactions in the lymph node cortex. Immunol Rev. 1997 Apr;156(1):11–24.

115. Miyaji K, Furuse A, Nakajima J, Kohno T, Ohtsuka T, Yagyu K, et al. The stiffness of lymph nodes containing lung carcinoma metastases: A new diagnostic parameter measured by a tactile sensor. Cancer. 1997 Nov 15;80(10):1920–5.

116. Arda K, Ciledag N, Aktas E, Arıbas BK, Köse K. Quantitative Assessment of Normal Soft-Tissue Elasticity Using Shear-Wave Ultrasound Elastography. Am J Roentgenol. 2011 Sep;197(3):532–6.

117. Huse M. Mechanical forces in the immune system. Nat Rev Immunol. 2017 Nov;17(11):679–90.

118. Moreau HD, Piel M, Voituriez R, Lennon-Duménil AM. Integrating Physical and Molecular Insights on Immune Cell Migration. Trends Immunol. 2018 Aug;39(8):632–43.

119. Hirsch S, Guo J, Reiter R, Papazoglou S, Kroencke T, Braun J, et al. MR Elastography of the Liver and the Spleen Using a Piezoelectric Driver, Single-Shot Wave-Field Acquisition, and Multifrequency Dual Parameter Reconstruction: Multi-frequency MR Elastography of the Liver and the Spleen. Magn Reson Med. 2014 Jan;71(1):267–77.

120. Hickey JW, Dong Y, Chung JW, Salathe SF, Pruitt HC, Li X, et al. Engineering an Artificial T-Cell Stimulating Matrix for Immunotherapy. Adv Mater. 2019 Jun;31(23):1807359.

121. Saitakis M, Dogniaux S, Goudot C, Bufi N, Asnacios S, Maurin M, et al. Different TCR-induced T lymphocyte responses are potentiated by stiffness with variable sensitivity. eLife. 2017 Jun 8;6:e23190.

122. de la Zerda A, Kratochvil MJ, Suhar NA, Heilshorn SC. Review: Bioengineering strategies to probe T cell mechanobiology. APL Bioeng. 2018 Jun;2(2):021501.

123. Moura Rosa P, Gopalakrishnan N, Ibrahim H, Haug M, Halaas Ø. The intercell dynamics of T cells and dendritic cells in a lymph node-on-a-chip flow device. Lab Chip. 2016;16(19):3728–40.

124. Miteva DO, Rutkowski JM, Dixon JB, Kilarski W, Shields JD, Swartz MA. Transmural Flow Modulates Cell and Fluid Transport Functions of Lymphatic Endothelium. Circ Res. 2010 Mar 19;106(5):920–31.

125. Wolf K, Müller R, Borgmann S, Bröcker EvaB, Friedl P. Amoeboid shape change and contact guidance: T-lymphocyte crawling through fibrillar collagen is independent of matrix remodeling by MMPs and other proteases. Blood. 2003 Nov 1;102(9):3262–9.

126. Oyler-Yaniv A, Oyler-Yaniv J, Whitlock BM, Liu Z, Germain RN, Huse M, et al. A Tunable Diffusion-Consumption Mechanism of Cytokine Propagation Enables Plasticity in Cell-to-Cell Communication in the Immune System. Immunity. 2017 Apr;46(4):609–20.

127. Farh KKH, Marson A, Zhu J, Kleinewietfeld M, Housley WJ, Beik S, et al. Genetic and epigenetic fine mapping of causal autoimmune disease variants. Nature. 2015 Feb 19;518(7539):337–43.

128. Blumenreich MS. The White Blood Cell and Differential Count. In: Walker HK, Hall WD, Hurst JW, editors. Clinical Methods: The History, Physical, and Laboratory Examinations [Internet]. 3rd ed. Boston: Butterworths; 1990 [cited 2021 May 14]. Available from: http://www.ncbi.nlm.nih.gov/books/NBK261/

129. Kleiveland CR. Peripheral Blood Mononuclear Cells. In: Verhoeckx K, Cotter P, López-Expósito I, Kleiveland C, Lea T, Mackie A, et al., editors. The Impact of Food Bioactives on Health [Internet]. Cham: Springer International Publishing; 2015 [cited 2021 May 14]. p. 161–7. Available from: http://link.springer.com/10.1007/978-3-319-16104-4_15

130. Klein SL, Flanagan KL. Sex differences in immune responses. Nat Rev Immunol. 2016 Oct;16(10):626–38.

131. Gosselin EA, Eppler HB, Bromberg JS, Jewell CM. Designing natural and synthetic immune tissues. Nat Mater. 2018 Jun;17(6):484–98.

132. Purwada A, Singh A. Immuno-engineered organoids for regulating the kinetics of B-cell development and antibody production. Nat Protoc. 2017 Jan;12(1):168–82.

133. Giese C, Lubitz A, Demmler CD, Reuschel J, Bergner K, Marx U. Immunological substance testing on human lymphatic micro-organoids in vitro. J Biotechnol. 2010 Jul 1;148(1):38–45.

134. Kuzin I, Sun H, Moshkani S, Feng C, Mantalaris A, Wu JHD, et al. Long-term immunologically competent human peripheral lymphoid tissue cultures in a 3D bioreactor. Biotechnol Bioeng. 2011 Jun;108(6):1430–40.

135. Tomei AA, Siegert S, Britschgi MR, Luther SA, Swartz MA. Fluid Flow Regulates Stromal Cell Organization and CCL21 Expression in a Tissue-Engineered Lymph Node Microenvironment. J Immunol. 2009 Oct 1;183(7):4273–83.

136. Kim J, Wu B, Niedzielski SM, Hill MT, Coleman RM, Ono A, et al. Characterizing natural hydrogel for reconstruction of three-dimensional lymphoid stromal network to model T-cell interactions: 3D LYMPHOID STROMAL NETWORK. J Biomed Mater Res A. 2015 Aug;103(8):2701–10.

137. Murakami T, Kim J, Li Y, Green GE, Shikanov A, Ono A. Secondary lymphoid organ fibroblastic reticular cells mediate trans-infection of HIV-1 via CD44-hyaluronan interactions. Nat Commun. 2018 Dec;9(1):2436.

138. Votanopoulos KI, Forsythe S, Sivakumar H, Mazzocchi A, Aleman J, Miller L, et al. Model of Patient-Specific Immune-Enhanced Organoids for Immunotherapy Screening: Feasibility Study. Ann Surg Oncol. 2020 Jun;27(6):1956–67.

139. Higbee RG, Byers AM, Dhir V, Drake D, Fahlenkamp HG, Gangur J, et al. An Immunologic Model for Rapid Vaccine Assessment — A Clinical Trial in a Test Tube. Altern Lab Anim. 2009 Sep;37(1_suppl):19–27.

140. Mazzaglia C, Munir H, Lei IM, Gerigk M, Huang YYS, Shields JD. Modeling Structural Elements and Functional Responses to Lymphatic-Delivered Cues in a Murine Lymph Node on a Chip. Adv Healthc Mater. 2024 Jul;13(18):2303720.

141. Cooper LJ, Heppell JP, Clough GF, Ganapathisubramani B, Roose T. An Image-Based Model of Fluid Flow Through Lymph Nodes. Bull Math Biol. 2016 Jan;78(1):52–71.

142. Luciani A, Itti E, Rahmouni A, Meignan M, Clement O. Lymph node imaging: Basic principles. Eur J Radiol. 2006 Jun;58(3):338–44.

143. Kwon S, Sevick-Muraca EM. Noninvasive Quantitative Imaging of Lymph Function in Mice. Lymphat Res Biol. 2007 Dec;5(4):219–32.

144. Harrell MI, Iritani BM, Ruddell A. Tumor-Induced Sentinel Lymph Node Lymphangiogenesis and Increased Lymph Flow Precede Melanoma Metastasis. Am J Pathol. 2007 Feb;170(2):774–86.

145. Srinivasan S, Vannberg FO, Dixon JB. Lymphatic transport of exosomes as a rapid route of information dissemination to the lymph node. Sci Rep. 2016 Apr 18;6(1):24436.

146. Zhou Q, Wood R, Schwarz EM, Wang Y, Xing L. Near-infrared lymphatic imaging demonstrates the dynamics of lymph flow and lymphangiogenesis during the acute versus chronic phases of arthritis in mice. Arthritis Rheum. 2010 Jul;62(7):1881–9.

147. Meijer EFJ, Jeong HS, Pereira ER, Ruggieri TA, Blatter C, Vakoc BJ, et al. Murine chronic lymph node window for longitudinal intravital lymph node imaging. Nat Protoc. 2017 Aug;12(8):1513–20.

148. Browse NL, Doig RL, Sizeland D. The resistance of a lymph node to lymph flow. Br J Surg. 2005 Dec 7;71(3):192–6.

149. Neeland MR, Meeusen ENT, De Veer MJ. Afferent lymphatic cannulation as a model system to study innate immune responses to infection and vaccination. Vet Immunol Immunopathol. 2014 Mar;158(1–2):86–97.

150. Ozulumba T, Montalbine AN, Ortiz-Cárdenas JE, Pompano RR. New tools for immunologists: models of lymph node function from cells to tissues. Front Immunol. 2023 May 10;14:1183286.

151. O'Melia MJ, Lund AW, Thomas SN. The Biophysics of Lymphatic Transport: Engineering Tools and Immunological Consequences. iScience. 2019 Dec;22:28–43.

152. Dietrich T, Bock F, Yuen D, Hos D, Bachmann BO, Zahn G, et al. Cutting Edge: Lymphatic Vessels, Not Blood Vessels, Primarily Mediate Immune Rejections After Transplantation. J Immunol. 2010 Jan 15;184(2):535–9.

153. Alitalo K. The lymphatic vasculature in disease. Nat Med. 2011 Nov;17(11):1371–80.

154. Paget S. The distribution of secondary growths in cancer of the breast. The Lancet. 1889;133(3421):571–3.

155. Jatoi I, Hilsenbeck SG, Clark GM, Osborne CK. Significance of Axillary Lymph Node Metastasis in Primary Breast Cancer. J Clin Oncol. 1999 Aug;17(8):2334–2334.

156. Kawada K, Taketo MM. Significance and Mechanism of Lymph Node Metastasis in Cancer Progression. Cancer Res. 2011 Feb 15;71(4):1214–8.

157. Jana S, Muscarella RA, Jones D. The Multifaceted Effects of Breast Cancer on Tumor-Draining Lymph Nodes. Am J Pathol. 2021 Aug;191(8):1353–63.

158. Luker KE, Luker GD. Functions of CXCL12 and CXCR4 in breast cancer. Cancer Lett. 2006 Jul;238(1):30–41.

159. Wu W, Qian L, Chen X, Ding B. Prognostic significance of CXCL12, CXCR4, and CXCR7 in patients with breast cancer. Int J Clin Exp Pathol. 2015;8(10):13217–24.

160. Zielińska KA, Katanaev VL. The Signaling Duo CXCL12 and CXCR4: Chemokine Fuel for Breast Cancer Tumorigenesis. Cancers. 2020 Oct 21;12(10):3071.

161. Shieh AC, Swartz MA. Regulation of tumor invasion by interstitial fluid flow. Phys Biol. 2011 Feb 1;8(1):015012.

162. Munson J, Shieh A. Interstitial fluid flow in cancer: implications for disease progression and treatment. Cancer Manag Res. 2014 Aug;317.

163. Shields JD, Fleury ME, Yong C, Tomei AA, Randolph GJ, Swartz MA. Autologous Chemotaxis as a Mechanism of Tumor Cell Homing to Lymphatics via Interstitial Flow and Autocrine CCR7 Signaling. Cancer Cell. 2007 Jun;11(6):526–38.

164. Haessler U, Teo JCM, Foretay D, Renaud P, Swartz MA. Migration dynamics of breast cancer cells in a tunable 3D interstitial flow chamber. Integr Biol. 2012 Apr 1;4(4):401–9.

165. Roberts LM, Perez MJ, Balogh KN, Mingledorff G, Cross JV, Munson JM. Myeloid Derived Suppressor Cells Migrate in Response to Flow and Lymphatic Endothelial Cell Interaction in the Breast Tumor Microenvironment. Cancers. 2022 Jun 18;14(12):3008.

166. Beeghly GF, Thomas C, Yuan JX, Harris AR, Munson JM. Designing Patient-Driven, Tissue-Engineered Models of Primary and Metastatic Breast Cancer. Bioengineering. 2022 Jan 18;9(2):44.

167. Aspelund A, Antila S, Proulx ST, Karlsen TV, Karaman S, Detmar M, et al. A dural lymphatic vascular system that drains brain interstitial fluid and macromolecules. J Exp Med. 2015 Jun 29;212(7):991–9.

168. Louveau A, Smirnov I, Keyes TJ, Eccles JD, Rouhani SJ, Peske JD, et al. Structural and functional features of central nervous system lymphatic vessels. Nature. 2015 Jul 16;523(7560):337–41.

169. Antila S, Karaman S, Nurmi H, Airavaara M, Voutilainen MH, Mathivet T, et al. Development and plasticity of meningeal lymphatic vessels. J Exp Med. 2017 Dec 4;214(12):3645–67.

170. Da Mesquita S, Louveau A, Vaccari A, Smirnov I, Cornelison RC, Kingsmore KM, et al. Functional aspects of meningeal lymphatics in ageing and Alzheimer's disease. Nature. 2018 Aug;560(7717):185–91.

171. Bolte AC, Dutta AB, Hurt ME, Smirnov I, Kovacs MA, McKee CA, et al. Meningeal lymphatic dysfunction exacerbates traumatic brain injury pathogenesis. Nat Commun. 2020 Dec;11(1):4524.

172. Hu X, Deng Q, Ma L, Li Q, Chen Y, Liao Y, et al. Meningeal lymphatic vessels regulate brain tumor drainage and immunity. Cell Res. 2020 Mar;30(3):229–43.

173. Graham MS, Mellinghoff IK. Meningeal lymphatics prime tumor immunity in glioblastoma. Cancer Cell. 2021 Mar;39(3):304–6.

174. Zhou C, Ma L, Xu H, Huo Y, Luo J. Meningeal lymphatics regulate radiotherapy efficacy through modulating anti-tumor immunity. Cell Res. 2022 Jun;32(6):543–54.

175. Rostami R, Mittal S, Rostami P, Tavassoli F, Jabbari B. Brain metastasis in breast cancer: a comprehensive literature review. J Neurooncol. 2016 May;127(3):407–14.

176. Scott BJ, Oberheim-Bush NA, Kesari S. Leptomeningeal metastasis in breast cancer - a systematic review. Oncotarget. 2016 Jan 26;7(4):3740–7.

177. Punt J. Adaptive Immunity. In: Cancer Immunotherapy [Internet]. Elsevier; 2013 [cited 2024 Jun 10]. p. 41–53. Available from: https://linkinghub.elsevier.com/retrieve/pii/B978012394296800004X

178. Ng CP, Swartz MA. Fibroblast alignment under interstitial fluid flow using a novel 3-D tissue culture model. Am J Physiol-Heart Circ Physiol. 2003 May 1;284(5):H1771–7.

179. Ng CP, Swartz MA. Mechanisms of Interstitial Flow-Induced Remodeling of Fibroblast–Collagen Cultures. Ann Biomed Eng. 2006 Mar;34(3):446–54.

180. Ng C, Hinz B, Swartz M. Contribution of Interstitial Fluid Flow to Fibroblast Alignment and Differentiation. Wound Repair Regen [Internet]. 2005 Jan [cited 2024 Jun 10];13(1). Available from: https://onlinelibrary.wiley.com/doi/10.1111/j.1067-1927.2005.130117x.x

181. Ng CP, Hinz B, Swartz MA. Interstitial fluid flow induces myofibroblast differentiation and collagen alignment in vitro. J Cell Sci. 2005 Oct 15;118(20):4731–9.

182. Saito N, Adachi H, Tanaka H, Nakata S, Kawada N, Oofusa K, et al. Interstitial fluid flow-induced growth potential and hyaluronan synthesis of fibroblasts in a fibroblast-populated stretched collagen gel culture. Biochim Biophys Acta BBA - Gen Subj. 2017 Sep;1861(9):2261–73.

183. Shi ZD, Ji XY, Qazi H, Tarbell JM. Interstitial flow promotes vascular fibroblast, myofibroblast, and smooth muscle cell motility in 3-D collagen I via upregulation of MMP-1. Am J Physiol-Heart Circ Physiol. 2009 Oct;297(4):H1225–34.

184. Garanich JS, Mathura RA, Shi ZD, Tarbell JM. Effects of fluid shear stress on adventitial fibroblast migration: implications for flow-mediated mechanisms of arterialization and intimal hyperplasia. Am J Physiol-Heart Circ Physiol. 2007 Jun;292(6):H3128–35.

185. Wiedenmann CJ, Gottwald C, Zeqiri K, Frömmichen J, Bungert E, Gläser M, et al. Slow Interstitial Fluid Flow Activates TGF-β Signaling and Drives Fibrotic Responses in Human Tenon Fibroblasts. Cells. 2023 Sep 4;12(17):2205.

186. Galie PA, Russell MW, Westfall MV, Stegemann JP. Interstitial fluid flow and cyclic strain differentially regulate cardiac fibroblast activation via AT1R and TGF-β1. Exp Cell Res. 2012 Jan;318(1):75–84.

187. Miteva DO, Rutkowski JM, Dixon JB, Kilarski W, Shields JD, Swartz MA. Transmural Flow Modulates Cell and Fluid Transport Functions of Lymphatic Endothelium. Circ Res. 2010 Mar 19;106(5):920–31.

188. Valignat MP, Theodoly O, Gucciardi A, Hogg N, Lellouch AC. T Lymphocytes Orient against the Direction of Fluid Flow during LFA-1-Mediated Migration. Biophys J. 2013 Jan;104(2):322–31.

189. Chittur KK, Mcintire LV, Rich RR. Shear Stress Effects on Human T Cell Function. Biotechnol Prog. 1988 Jun;4(2):89–96.

190. Birmingham KG, O'Melia MJ, Bordy S, Reyes Aguilar D, El-Reyas B, Lesinski G, et al. Lymph Node Subcapsular Sinus Microenvironment-On-A-Chip Modeling Shear Flow Relevant to Lymphatic Metastasis and Immune Cell Homing. iScience. 2020 Nov;23(11):101751.

191. Kwee BJ, Akue A, Sung KE. On-chip human lymph node stromal network for evaluating dendritic cell and T-cell trafficking [Internet]. 2023 [cited 2024 Jul 30]. Available from: http://biorxiv.org/lookup/doi/10.1101/2023.03.21.533042

192. Munson JM, Bellamkonda RV, Swartz MA. Interstitial Flow in a 3D Microenvironment Increases Glioma Invasion by a CXCR4-Dependent Mechanism. Cancer Res. 2013 Mar 1;73(5):1536–46.

193. Kingsmore KM, Logsdon DK, Floyd DH, Peirce SM, Purow BW, Munson JM. Interstitial flow differentially increases patient-derived glioblastoma stem cell invasion *via* CXCR4, CXCL12, and CD44-mediated mechanisms. Integr Biol. 2016 Dec 5;8(12):1246–60.

194. Harris AR, Esparza S, Azimi MS, Cornelison R, Azar FN, Llaneza DC, et al. Platinum Chemotherapy Induces Lymphangiogenesis in Cancerous and Healthy Tissues That Can be Prevented With Adjuvant Anti-VEGFR3 Therapy. Front Oncol. 2022 Mar 17;12:801764.

195. Kingsmore KM, Vaccari A, Abler D, Cui SX, Epstein FH, Rockne RC, et al. MRI analysis to map interstitial flow in the brain tumor microenvironment. APL Bioeng. 2018 Sep;2(3):031905.

196. McGuire JA, Monclova JL, Coariti ACS, Stine CA, Toussaint KC, Munson JM, et al. Tear propagation in vaginal tissue under inflation. Acta Biomater. 2021 Jun;127:193–204.

197. Schindelin J, Arganda-Carreras I, Frise E, Kaynig V, Longair M, Pietzsch T, et al. Fiji: an open-source platform for biological-image analysis. Nat Methods. 2012 Jul;9(7):676–82.

198. Fernandez-Botran R, Yan J, Justus DE. BINDING OF INTERFERON γ BY GLYCOSAMINOGLYCANS: A STRATEGY FOR LOCALIZATION AND/OR INHIBITION OF ITS ACTIVITY. Cytokine. 1999 May;11(5):313–25.

199. Ozulumba T, Zatorski JM, Arneja A, Hammel JH, Braciale TJ, Luckey CJ, et al. Mitigating reactive oxygen species production and increasing gel porosity improves lymphocyte motility and fibroblast spreading in photocrosslinked gelatin-thiol hydrogels [Internet]. 2024 [cited 2024 Jul 29]. Available from: http://biorxiv.org/lookup/doi/10.1101/2024.01.14.574282

200. Krummel MF, Bartumeus F, Gérard A. T cell migration, search strategies and mechanisms. Nat Rev Immunol. 2016 Mar;16(3):193–201.

201. Katakai T, Kinashi T. Microenvironmental Control of High-Speed Interstitial T Cell Migration in the Lymph Node. Front Immunol [Internet]. 2016 May 13 [cited 2024 Jul 29];7. Available from: http://journal.frontiersin.org/Article/10.3389/fimmu.2016.00194/abstract

202. Miller MJ, Wei SH, Parker I, Cahalan MD. Two-Photon Imaging of Lymphocyte Motility and Antigen Response in Intact Lymph Node. Science. 2002 Jun 7;296(5574):1869–73.

203. Stine CA, Munson JM. Convection-Enhanced Delivery: Connection to and Impact of Interstitial Fluid Flow. Front Oncol. 2019 Oct 2;9:966.

204. Kataru RP, Baik JE, Park HJ, Wiser I, Rehal S, Shin JY, et al. Regulation of Immune Function by the Lymphatic System in Lymphedema. Front Immunol. 2019 Mar 18;10:470.

205. Katakai T, Hara T, Sugai M, Gonda H, Shimizu A. Lymph Node Fibroblastic Reticular Cells Construct the Stromal Reticulum via Contact with Lymphocytes. J Exp Med. 2004 Sep 20;200(6):783–95.

206. Siegert S, Luther SA. Positive and negative regulation of T cell responses by fibroblastic reticular cells within paracortical regions of lymph nodes. Front Immunol [Internet]. 2012 [cited 2024 Aug 23];3. Available from: http://journal.frontiersin.org/article/10.3389/fimmu.2012.00285/abstract

207. Lukacs-Kornek V, Malhotra D, Fletcher AL, Acton SE, Elpek KG, Tayalia P, et al. Regulated release of nitric oxide by nonhematopoietic stroma controls expansion of the activated T cell pool in lymph nodes. Nat Immunol. 2011 Nov;12(11):1096–104.

208. Nicolas-Boluda A, Vaquero J, Vimeux L, Guilbert T, Barrin S, Kantari-Mimoun C, et al. Tumor stiffening reversion through collagen crosslinking inhibition improves T cell migration and anti-PD-1 treatment. eLife. 2021 Jun 9;10:e58688.

209. Sadjadi Z, Zhao R, Hoth M, Qu B, Rieger H. Migration of Cytotoxic T Lymphocytes in 3D Collagen Matrices. Biophys J. 2020 Dec;119(11):2141–52.

210. Majedi FS, Hasani-Sadrabadi MM, Thauland TJ, Li S, Bouchard LS, Butte MJ. T-cell activation is modulated by the 3D mechanical microenvironment. Biomaterials. 2020 Sep;252:120058.

211. Martinez VG, Pankova V, Krasny L, Singh T, Makris S, White IJ, et al. Fibroblastic Reticular Cells Control Conduit Matrix Deposition during Lymph Node Expansion. Cell Rep. 2019 Nov;29(9):2810-2822.e5.

212. Pruitt HC, Lewis D, Ciccaglione M, Connor S, Smith Q, Hickey JW, et al. Collagen fiber structure guides 3D motility of cytotoxic T lymphocytes. Matrix Biol. 2020 Jan;85–86:147–59.

213. Tabdanov ED, Rodríguez-Merced NJ, Cartagena-Rivera AX, Puram VV, Callaway MK, Ensminger EA, et al. Engineering T cells to enhance 3D migration through structurally and mechanically complex tumor microenvironments. Nat Commun. 2021 May 14;12(1):2815.

214. Fernandes NRJ, Reilly NS, Schrock DC, Hocking DC, Oakes PW, Fowell DJ. CD4+ T Cell Interstitial Migration Controlled by Fibronectin in the Inflamed Skin. Front Immunol. 2020 Jul 24;11:1501.

215. Pruitt HC, Guan Y, Liu H, Carey AE, Brennen WN, Lu J, et al. Collagen VI deposition mediates stromal T cell trapping through inhibition of T cell motility in the prostate tumor microenvironment. Matrix Biol. 2023 Aug;121:90–104.

216. Dasoveanu DC, Park HJ, Ly CL, Shipman WD, Chyou S, Kumar V, et al. Lymph node stromal CCL2 limits antibody responses. Sci Immunol. 2020 Mar 13;5(45):eaaw0693.

217. Basic M, Peppermüller PP, Bolsega S, Bleich A, Bornemann M, Bode U, et al. Lymph Node Stromal Cells From Different Draining Areas Distinctly Regulate the Development of Chronic Intestinal Inflammation. Front Immunol. 2021 Feb 16;11:549473.

218. Taub DD, Proost P, Murphy WJ, Anver M, Longo DL, Van Damme J, et al. Monocyte chemotactic protein-1 (MCP-1), -2, and -3 are chemotactic for human T lymphocytes. J Clin Invest. 1995 Mar 1;95(3):1370–6.

219. Loetscher P, Seitz M, Lewis IC, Baggiolini M, Moser B. Monocyte chemotactic proteins MCP-1, MCP-2, and MCP-3 are major attractants for human $CD4^+$ and $CD8^+$ T lymphocytes. FASEB J. 1994 Oct;8(13):1055–60.

220. Flaishon L, Hart G, Zelman E, Moussion C, Grabovsky V, Lapidot Tal G, et al. Anti-inflammatory effects of an inflammatory chemokine: CCL2 inhibits lymphocyte homing by modulation of CCL21-triggered integrin-mediated adhesions. Blood. 2008 Dec 15;112(13):5016–25.

221. Tedla N, Wang HW, McNeil HP, Di Girolamo N, Hampartzoumian T, Wakefield D, et al. Regulation of T Lymphocyte Trafficking into Lymph Nodes During an Immune Response by the Chemokines Macrophage Inflammatory Protein (MIP)-1α and MIP-1β. J Immunol. 1998 Nov 15;161(10):5663–72.

222. Valença-Pereira F, Fang Q, Marié IJ, Giddings EL, Fortner KA, Yang R, et al. IL-6 enhances CD4 cell motility by sustaining mitochondrial Ca^{2+} through the noncanonical STAT3 pathway. Proc Natl Acad Sci. 2021 Sep 14;118(37):e2103444118.

223. Leal IS, Flórido M, Andersen P, Appelberg R. Interleukin-6 regulates the phenotype of the immune response to a tuberculosis subunit vaccine. Immunology. 2001 Jul;103(3):375–81.

224. Wee JLK, Greenwood DLV, Han X, Scheerlinck JPY. Inflammatory cytokines IL-6 and TNF-α regulate lymphocyte trafficking through the local lymph node. Vet Immunol Immunopathol. 2011 Nov;144(1–2):95–103.

225. Taub DD, Anver M, Oppenheim JJ, Longo DL, Murphy WJ. T lymphocyte recruitment by interleukin-8 (IL-8). IL-8-induced degranulation of neutrophils releases potent chemoattractants for human T lymphocytes both in vitro and in vivo. J Clin Invest. 1996 Apr 15;97(8):1931–41.

226. Wang JM, Xu L, Murphy WJ, Taub DD, Chertov O. IL-8-Induced T-Lymphocyte Migration: Direct as Well as Indirect Mechanisms. Methods. 1996 Aug;10(1):135–44.

227. Munk R, Ghosh P, Ghosh MC, Saito T, Xu M, Carter A, et al. Involvement of mTOR in CXCL12 Mediated T Cell Signaling and Migration. Unutmaz D, editor. PLoS ONE. 2011 Sep 12;6(9):e24667.

228. Zhang T, Somasundaram R, Berking C, Caputo L, Van Belle P, Elder DE, et al. Preferential involvement of CX chemokine receptor 4 and CX chemokine ligand 12 in T-Cell migration toward melanoma cells. Cancer Biol Ther. 2006 Oct 11;5(10):1304–12.

229. Ghosh MC, Collins GD, Vandanmagsar B, Patel K, Brill M, Carter A, et al. Activation of Wnt5A signaling is required for CXC chemokine ligand 12–mediated T-cell migration. Blood. 2009 Aug 13;114(7):1366–73.

230. Rosen PP, Saigo PE, Braun DW, Weathers E, Fracchia AA, Kinne DW. Axillary Micro- and Macrometastases in Breast Cancer: Prognostic Significance of Tumor Size. Ann Surg. 1981 Nov;194(5):585–91.

231. Weaver DL, Ashikaga T, Krag DN, Skelly JM, Anderson SJ, Harlow SP, et al. Effect of Occult Metastases on Survival in Node-Negative Breast Cancer. N Engl J Med. 2011 Feb 3;364(5):412–21.

232. De Boer M, Van Deurzen CHM, Van Dijck JAAM, Borm GF, Van Diest PJ, Adang EMM, et al. Micrometastases or Isolated Tumor Cells and the Outcome of Breast Cancer. N Engl J Med. 2009 Aug 13;361(7):653–63.

233. Naidoo K, Pinder SE. Micro- and macro-metastasis in the axillary lymph node: A review. Surg J R Coll Surg Edinb Irel. 2017 Apr;15(2):76–82.

234. Balla A, Weaver DL. Pathologic Evaluation of Lymph Nodes in Breast Cancer. Surg Pathol Clin. 2022 Mar;15(1):15–27.

235. Paduch R. The role of lymphangiogenesis and angiogenesis in tumor metastasis. Cell Oncol Dordr Neth. 2016 Oct;39(5):397–410.

236. Greenlee JD, King MR. Engineered fluidic systems to understand lymphatic cancer metastasis. Biomicrofluidics. 2020 Jan 1;14(1):011502.

237. Hoshida T, Isaka N, Hagendoorn J, Di Tomaso E, Chen YL, Pytowski B, et al. Imaging Steps of Lymphatic Metastasis Reveals That Vascular Endothelial Growth Factor-C Increases Metastasis by Increasing Delivery of Cancer Cells to Lymph Nodes: Therapeutic Implications. Cancer Res. 2006 Aug 15;66(16):8065–75.

238. Daniele A, Zito AF, Giannelli G, Divella R, Asselti M, Mazzocca A, et al. Expression of metalloproteinases MMP-2 and MMP-9 in sentinel lymph node and serum of patients with metastatic and non-metastatic breast cancer. Anticancer Res. 2010 Sep;30(9):3521–7.

239. Rizwan A, Bulte C, Kalaichelvan A, Cheng M, Krishnamachary B, Bhujwalla ZM, et al. Metastatic breast cancer cells in lymph nodes increase nodal collagen density. Sci Rep. 2015 Sep 22;5(1):10002.

240. Martinez VG, Pankova V, Krasny L, Singh T, Makris S, White IJ, et al. Fibroblastic Reticular Cells Control Conduit Matrix Deposition during Lymph Node Expansion. Cell Rep. 2019 Nov;29(9):2810-2822.e5.

241. Vega F, Coombes KR, Thomazy VA, Patel K, Lang W, Jones D. Tissue-Specific Function of Lymph Node Fibroblastic Reticulum Cells. Pathobiology. 2006;73(2):71–81.

242. Pelon F, Bourachot B, Kieffer Y, Magagna I, Mermet-Meillon F, Bonnet I, et al. Cancer-associated fibroblast heterogeneity in axillary lymph nodes drives metastases in breast cancer through complementary mechanisms. Nat Commun. 2020 Jan 21;11(1):404.

243. Itou RA, Uyama N, Hirota S, Kawada N, Wu S, Miyashita S, et al. Immunohistochemical characterization of cancer-associated fibroblasts at the primary sites and in the metastatic lymph nodes of human intrahepatic cholangiocarcinoma. Hum Pathol. 2019 Jan;83:77–89.

244. Zhou J, Wang XH, Zhao YX, Chen C, Xu XY, Sun Q, et al. Cancer-Associated Fibroblasts Correlate with Tumor-Associated Macrophages Infiltration and Lymphatic Metastasis in Triple Negative Breast Cancer Patients. J Cancer. 2018;9(24):4635–41.

245. Naxerova K, Reiter JG, Brachtel E, Lennerz JK, Van De Wetering M, Rowan A, et al. Origins of lymphatic and distant metastases in human colorectal cancer. Science. 2017 Jul 7;357(6346):55–60.

246. Barry P, Vatsiou A, Spiteri I, Nichol D, Cresswell GD, Acar A, et al. The Spatiotemporal Evolution of Lymph Node Spread in Early Breast Cancer. Clin Cancer Res. 2018 Oct 1;24(19):4763–70.

247. Mathe A, Wong-Brown M, Morten B, Forbes JF, Braye SG, Avery-Kiejda KA, et al. Novel genes associated with lymph node metastasis in triple negative breast cancer. Sci Rep. 2015 Nov 5;5(1):15832.

248. Chatterjee G, Pai T, Hardiman T, Avery-Kiejda K, Scott RJ, Spencer J, et al. Molecular patterns of cancer colonisation in lymph nodes of breast cancer patients. Breast Cancer Res. 2018 Dec;20(1):143.

249. Urrutia G, Laurito S, Marzese DM, Gago F, Orozco J, Tello O, et al. Epigenetic variations in breast cancer progression to lymph node metastasis. Clin Exp Metastasis. 2015 Feb;32(2):99–110.

250. To B, Isaac D, Andrechek ER. Studying Lymphatic Metastasis in Breast Cancer: Current Models, Strategies, and Clinical Perspectives. J Mammary Gland Biol Neoplasia. 2020 Sep;25(3):191–203.

251. Püspöki Z, Storath M, Sage D, Unser M. Transforms and Operators for Directional Bioimage Analysis: A Survey. In: De Vos WH, Munck S, Timmermans JP, editors. Focus on Bio-Image Informatics [Internet]. Cham: Springer International Publishing; 2016 [cited 2024 Aug 25]. p. 69–93. (Advances in Anatomy, Embryology and Cell Biology; vol. 219). Available from: http://link.springer.com/10.1007/978-3-319-28549-8_3

252. Rezakhaniha R, Agianniotis A, Schrauwen JTC, Griffa A, Sage D, Bouten CVC, et al. Experimental investigation of collagen waviness and orientation in the arterial adventitia using confocal laser scanning microscopy. Biomech Model Mechanobiol. 2012 Mar;11(3–4):461–73.

253. Jiang Y, Wang B, Li JK, Li SY, Niu RL, Fu NQ, et al. Collagen fiber features and COL1A1: are they associated with elastic parameters in breast lesions, and can COL1A1 predict axillary lymph node metastasis? BMC Cancer. 2022 Sep 21;22(1):1004.

254. Kakkad SM, Solaiyappan M, Argani P, Sukumar S, Jacobs LK, Leibfritz D, et al. Collagen I fiber density increases in lymph node positive breast cancers: pilot study. J Biomed Opt. 2012 Nov 1;17(11):116017.

255. Piperigkou Z, Karamanos NK. Estrogen receptor-mediated targeting of the extracellular matrix network in cancer. Semin Cancer Biol. 2020 May;62:116–24.

256. Hansen RK, Bissell MJ. Tissue architecture and breast cancer: the role of extracellular matrix and steroid hormones. Endocr Relat Cancer. 2000 Jun;7(2):95–113.

257. Cakala-Jakimowicz M, Kolodziej-Wojnar P, Puzianowska-Kuznicka M. Aging-Related Cellular, Structural and Functional Changes in the Lymph Nodes: A Significant Component of Immunosenescence? An Overview. Cells. 2021 Nov 12;10(11):3148.

258. Hielscher AC, Qiu C, Gerecht S. Breast cancer cell-derived matrix supports vascular morphogenesis. Am J Physiol-Cell Physiol. 2012 Apr 15;302(8):C1243–56.

259. Pisano M, Triacca V, Barbee KA, Swartz MA. An in vitro model of the tumor–lymphatic microenvironment with simultaneous transendothelial and luminal flows reveals mechanisms of flow enhanced invasion. Integr Biol. 2015;7(5):525–33.

260. Ghajar CM, Chen X, Harris JW, Suresh V, Hughes CCW, Jeon NL, et al. The Effect of Matrix Density on the Regulation of 3-D Capillary Morphogenesis. Biophys J. 2008 Mar;94(5):1930–41.

261. Guarnieri D, Battista S, Borzacchiello A, Mayol L, De Rosa E, Keene DR, et al. Effects of fibronectin and laminin on structural, mechanical and transport properties of 3D collageneous network. J Mater Sci Mater Med. 2007 Feb;18(2):245–53.

262. Netti PA, Berk DA, Swartz MA, Grodzinsky AJ, Jain RK. Role of Extracellular Matrix Assembly in Interstitial Transport in Solid Tumors1. Cancer Res. 2000 May 1;60(9):2497–503.

263. Roberts LM, Hammel JH, Azar F, Feng TY (Alkaid), Cunningham JJ, Rutkowski M, et al. Demonstration of chemotherapeutic mediated lymphatic changes in meningeal lymphatics in vitro, ex vivo, and in vivo [Internet]. Bioengineering; 2024 Jan [cited 2024 Jan 31]. Available from: http://biorxiv.org/lookup/doi/10.1101/2024.01.06.574460

264. Kanamori M, Kipnis J. Meningeal lymphatics “drain” brain tumors. Cell Res. 2020 Mar;30(3):191–2.

265. Harris AR, Esparza S, Azimi MS, Cornelison R, Azar FN, Llaneza DC, et al. Platinum Chemotherapy Induces Lymphangiogenesis in Cancerous and Healthy Tissues That Can be Prevented With Adjuvant Anti-VEGFR3 Therapy. Front Oncol. 2022 Mar 17;12:801764.

266. DeSisto J, O’Rourke R, Jones HE, Pawlikowski B, Malek AD, Bonney S, et al. Single-Cell Transcriptomic Analyses of the Developing Meninges Reveal Meningeal Fibroblast Diversity and Function. Dev Cell. 2020 Jul;54(1):43-59.e4.

267. Xu H, Wang N, Cao W, Huang L, Zhou J, Sheng L. Influence of various medium environment to in vitro human T cell culture. Vitro Cell Dev Biol - Anim. 2018 Sep;54(8):559–66.

268. Du X, Klaschik K, Mallmann P, Isachenko E, Rahimi G, Zhao Y, et al. An Experimental Model of Breast Cancer Cells: Informative Protocol for *In Vitro* Culture. Anticancer Res. 2018 Nov;38(11):6237–45.

269. Sato K, Kondo M, Sakuta K, Hosoi A, Noji S, Sugiura M, et al. Impact of culture medium on the expansion of T cells for immunotherapy. Cytotherapy. 2009;11(7):936–46.

270. Rauniyar K, Jha SK, Jeltsch M. Biology of Vascular Endothelial Growth Factor C in the Morphogenesis of Lymphatic Vessels. Front Bioeng Biotechnol. 2018 Feb 12;6:7.

271. Lee SJ, Park C, Lee JY, Kim S, Kwon PJ, Kim W, et al. Generation of pure lymphatic endothelial cells from human pluripotent stem cells and their therapeutic effects on wound repair. Sci Rep. 2015 Jun 12;5(1):11019.

272. Marino D, Angehrn Y, Klein S, Riccardi S, Baenziger-Tobler N, Otto VI, et al. Activation of the epidermal growth factor receptor promotes lymphangiogenesis in the skin. J Dermatol Sci. 2013 Sep;71(3):184–94.

273. Phadke L, Lau DHW, Aghaizu ND, Ibarra S, Navarron CM, Granat L, et al. A primary rodent triculture model to investigate the role of glia-neuron crosstalk in regulation of neuronal activity. Front Aging Neurosci. 2022 Dec 1;14:1056067.

274. Cornelison RC, Yuan JX, Tate KM, Petrosky A, Beeghly GF, Bloomfield M, et al. A patient-designed tissue-engineered model of the infiltrative glioblastoma microenvironment. Npj Precis Oncol. 2022 Jul 29;6(1):54.

275. Sousa GFD, Wlodarczyk SR, Monteiro G. Carboplatin: molecular mechanisms of action associated with chemoresistance. Braz J Pharm Sci. 2014 Dec;50(4):693–701.

276. Herbst RS, Khuri FR. Mode of action of docetaxel – a basis for combination with novel anticancer agents. Cancer Treat Rev. 2003 Oct;29(5):407–15.

277. Hernández-Vargas H, Palacios J, Moreno-Bueno G. Telling Cells How to Die: Docetaxel Therapy in Cancer Cell Lines. Cell Cycle. 2007 Apr;6(7):780–3.

278. Am W, Je B, H P, C L, Jy S, Rp K, et al. Docetaxel causes lymphatic endothelial cell apoptosis and impairs lymphatic function and gene expression in vitro. J Transl Sci [Internet]. 2021 [cited 2024 Aug 2];7(2). Available from: https://www.oatext.com/docetaxel-causes-lymphatic-endothelial-cell-apoptosis-and-impairs-lymphatic-function-and-gene-expression-in-vitro.php

279. Park SI, Jeon WH, Jeung HJ, Kim GC, Kim DK, Sim YJ. Clinical Features of Docetaxel Chemotherapy-Related Lymphedema. Lymphat Res Biol. 2014 Sep;12(3):197–202.

280. Akita S, Nakamura R, Yamamoto N, Tokumoto H, Ishigaki T, Yamaji Y, et al. Early Detection of Lymphatic Disorder and Treatment for Lymphedema following Breast Cancer. Plast Reconstr Surg. 2016 Aug;138(2):192e–202e.

281. Béhar A, Pujade-Lauraine E, Maurel A, Brun MD, Lagrue G, Feuilhade De Chauvin F, et al. The pathophysiological mechanism of fluid retention in advanced cancer patients treated with docetaxel, but not receiving corticosteroid comedication. Br J Clin Pharmacol. 1997 Jun;43(6):653–8.

282. Worley DR, Hansen RJ, Wittenburg LA, Chubb LS, Gustafson DL. Docetaxel Accumulates in Lymphatic Circulation Following Subcutaneous Delivery Compared to Intravenous Delivery in Rats. Anticancer Res. 2016 Oct 12;36(10):5071–8.

283. Bernatz S, Ilina EI, Devraj K, Harter PN, Mueller K, Kleber S, et al. Impact of Docetaxel on blood-brain barrier function and formation of breast cancer brain metastases. J Exp Clin Cancer Res. 2019 Dec;38(1):434.

284. McNeer JL, Schmiegelow K. Management of CNS Disease in Pediatric Acute Lymphoblastic Leukemia. Curr Hematol Malig Rep. 2022 Feb;17(1):1–14.

285. Jonart LM, Ebadi M, Basile P, Johnson K, Makori J, Gordon PM. Disrupting the leukemia niche in the central nervous system attenuates leukemia chemoresistance. Haematologica. 2020 Aug;105(8):2130–40.

286. Cao J, Donell B, Deaver DR, Lawrence MB, Dong C. In VitroSide-View Imaging Technique and Analysis of Human T-Leukemic Cell Adhesion to ICAM-1 in Shear Flow. Microvasc Res. 1998 Mar;55(2):124–37.

287. Tsuda H, Nishimura H, Sawada T, Takatsuki K. The roles of lymph node stromal cells in proliferation of lymphoid leukaemia cells. Br J Cancer. 1990 Mar;61(3):362–4.

288. Mittal AK, Chaturvedi NK, Rai KJ, Gilling-Cutucache CE, Nordgren TM, Moragues M, et al. Chronic Lymphocytic Leukemia Cells in a Lymph Node Microenvironment Depict Molecular Signature Associated with an Aggressive Disease. Mol Med. 2014 Jan;20(1):290–301.

289. Herndon TM, Chen SS, Saba NS, Valdez J, Emson C, Gatmaitan M, et al. Direct in vivo evidence for increased proliferation of CLL cells in lymph nodes compared to bone marrow and peripheral blood. Leukemia. 2017 Jun;31(6):1340–7.

290. Bhojwani D, Pui CH. Relapsed childhood acute lymphoblastic leukaemia. Lancet Oncol. 2013 May;14(6):e205–17.

291. Meadows AT, Evans AE. Effects of chemotherapy on the central nervous system—A study of parenteral methotrexate in long-term survivors of leukemia and lymphoma in childhood. Cancer. 1976 Feb;37(S2):1079–85.

292. Shuper A, Stark B, Kornreich L, Cohen IJ, Aviner S, Steinmetz A, et al. Methotrexate Treatment Protocols and the Central Nervous System: Significant Cure With Significant Neurotoxicity. J Child Neurol. 2000 Sep;15(9):573–80.

293. Baker WJ, Royer GL, Weiss RB. Cytarabine and neurologic toxicity. J Clin Oncol. 1991 Apr;9(4):679–93.

294. Chan ESL, Cronstein BN. Methotrexate—how does it really work? Nat Rev Rheumatol. 2010 Mar;6(3):175–8.

295. Jang JH, Jeong SH, Lee YB. Preparation and In Vitro/In Vivo Characterization of Polymeric Nanoparticles Containing Methotrexate to Improve Lymphatic Delivery. Int J Mol Sci. 2019 Jul 5;20(13):3312.

296. Kim CK, Han JH. Lymphatic delivery and pharmacokinetics of methotrexate after intramuscular injection of differently charged liposome-entrapped methotrexate to rats. J Microencapsul. 1995 Jan;12(4):437–46.

297. Lenk L, Alsadeq A, Schewe DM. Involvement of the central nervous system in acute lymphoblastic leukemia: opinions on molecular mechanisms and clinical implications based on recent data. Cancer Metastasis Rev. 2020 Mar;39(1):173–87.

298. Shattock AJ, Johnson HC, Sim SY, Carter A, Lambach P, Hutubessy RCW, et al. Contribution of vaccination to improved survival and health: modelling 50 years of the Expanded Programme on Immunization. The Lancet. 2024 May;403(10441):2307–16.

299. Henderson DA. The eradication of smallpox – An overview of the past, present, and future. Vaccine. 2011 Dec;29:D7–9.

300. Yao W, Li Y, Ding G. Interstitial Fluid Flow: The Mechanical Environment of Cells and Foundation of Meridians. Evid Based Complement Alternat Med. 2012;2012:1–9.

301. Serrano JC, Gillrie MR, Li R, Ishamuddin SH, Moeendarbary E, Kamm RD. Microfluidic-Based Reconstitution of Functional Lymphatic Microvasculature: Elucidating the Role of Lymphatics in Health and Disease. Adv Sci. 2024 Feb;11(5):2302903.

302. Abdreshov SN, Demchenko GA, Gorchakov VN, Yeshmukhanbet AN, Yessenova MA. LYMPH FLOW AND CELLULAR COMPOSITION, RHEOLOGICAL PROPERTIES OF LYMPH AND BLOOD IN ANIMALS WITH EXPERIMENTAL PERITONITIS. Ser Biol Med. 2021 Dec 10;4(346):5–13.

303. Adair TH, Moffatt DS, Paulsen AW, Guyton AC. Quantitation of changes in lymph protein concentration during lymph node transit. Am J Physiol-Heart Circ Physiol. 1982 Sep 1;243(3):H351–9.

304. Bates DO, Levick JR, Mortimer PS. Starling pressures in the human arm and their alteration in postmastectomy oedema. J Physiol. 1994 Jun;477(2):355–63.

305. Semaeva E, Tenstad O, Skavland J, Enger M, Iversen PO, Gjertsen BT, et al. Access to the Spleen Microenvironment through Lymph Shows Local Cytokine Production, Increased Cell Flux, and Altered Signaling of Immune Cells during Lipopolysaccharide-Induced Acute Inflammation. J Immunol. 2010 Apr 15;184(8):4547–56.

306. Nathanson SD, Mahan M. Sentinel Lymph Node Pressure in Breast Cancer. Ann Surg Oncol. 2011 Dec;18(13):3791–6.

307. Miura Y, Mikada M, Ouchi T, Horie S, Takeda K, Yamaki T, et al. Early diagnosis of lymph node metastasis: Importance of intranodal pressures. Cancer Sci. 2016 Mar;107(3):224–32.

308. Swartz MA, Lund AW. Lymphatic and interstitial flow in the tumour microenvironment: linking mechanobiology with immunity. Nat Rev Cancer. 2012 Mar;12(3):210–9.

309. Ayuso JM, Gong MM, Skala MC, Harari PM, Beebe DJ. Human Tumor-Lymphatic Microfluidic Model Reveals Differential Conditioning of Lymphatic Vessels by Breast Cancer Cells. Adv Healthc Mater. 2020 Feb;9(3):1900925.

310. Pond C. In vivo evidence for the involvement of the adipose tissue surrounding lymph nodes in immune responses. Immunol Lett. 1998 Oct;63(3):159–67.

311. Pond CM, Mattacks CA. The source of fatty acids incorporated into proliferating lymphoid cells in immune-stimulated lymph nodes. Br J Nutr. 2003 Mar;89(3):375–82.

312. Cheong LY, Wang B, Wang Q, Jin L, Kwok KHM, Wu X, et al. Fibroblastic reticular cells in lymph node potentiate white adipose tissue beiging through neuro-immune crosstalk in male mice. Nat Commun. 2023 Mar 3;14(1):1213.

313. Weitman ES, Aschen SZ, Farias-Eisner G, Albano N, Cuzzone DA, Ghanta S, et al. Obesity Impairs Lymphatic Fluid Transport and Dendritic Cell Migration to Lymph Nodes. Allen IC, editor. PLoS ONE. 2013 Aug 12;8(8):e70703.

314. Kim CS, Lee SC, Kim YM, Kim BS, Choi HS, Kawada T, et al. Visceral Fat Accumulation Induced by a High-fat Diet Causes the Atrophy of Mesenteric Lymph Nodes in Obese Mice. Obesity. 2008 Jun;16(6):1261–9.

315. Balaban S, Shearer RF, Lee LS, Van Geldermalsen M, Schreuder M, Shtein HC, et al. Adipocyte lipolysis links obesity to breast cancer growth: adipocyte-derived fatty acids drive breast cancer cell proliferation and migration. Cancer Metab. 2017 Dec;5(1):1.

316. Lee Isla Crake R, Phillips E, Kleffmann T, Currie MJ. Co-culture With Human Breast Adipocytes Differentially Regulates Protein Abundance in Breast Cancer Cells. Cancer Genomics - Proteomics. 2019;16(5):319–32.

317. Nickel A, Blücher C, Kadri OA, Schwagarus N, Müller S, Schaab M, et al. Adipocytes induce distinct gene expression profiles in mammary tumor cells and enhance inflammatory signaling in invasive breast cancer cells. Sci Rep. 2018 Jun 21;8(1):9482.

318. Bougaret L, Delort L, Billard H, Le Huede C, Boby C, De La Foye A, et al. Adipocyte/breast cancer cell crosstalk in obesity interferes with the anti-proliferative efficacy of tamoxifen. Migliaccio A, editor. PLOS ONE. 2018 Feb 1;13(2):e0191571.

319. Nottegar A, Veronese N, Senthil M, Roumen RM, Stubbs B, Choi AH, et al. Extra-nodal extension of sentinel lymph node metastasis is a marker of poor prognosis in breast cancer patients: A systematic review and an exploratory meta-analysis. Eur J Surg Oncol EJSO. 2016 Jul;42(7):919–25.

320. Ma X, Yang X, Yang W, Shui R. Prognostic value of extranodal extension in axillary lymph node-positive breast cancer. Sci Rep. 2021 May 5;11(1):9534.

321. Felcher CM, Bogni ES, Kordon EC. IL-6 Cytokine Family: A Putative Target for Breast Cancer Prevention and Treatment. Int J Mol Sci. 2022 Feb 5;23(3):1809.

322. Salgado R, Junius S, Benoy I, Van Dam P, Vermeulen P, Van Marck E, et al. Circulating interleukin-6 predicts survival in patients with metastatic breast cancer. Int J Cancer. 2003 Feb 20;103(5):642–6.

323. Kozłowski L, Zakrzewska I, Tokajuk P, Wojtukiewicz MZ. Concentration of interleukin-6 (IL-6), interleukin-8 (IL-8) and interleukin-10 (IL-10) in blood serum of breast cancer patients. Rocz Akad Med W Bialymstoku 1995. 2003;48:82–4.

324. Van De Velde M, Ebroin M, Durré T, Joiret M, Gillot L, Blacher S, et al. Tumor exposed-lymphatic endothelial cells promote primary tumor growth via IL6. Cancer Lett. 2021 Jan;497:154–64.

325. Cho HY, Choi JH, Kim KJ, Shin M, Choi JW. Microfluidic System to Analyze the Effects of Interleukin 6 on Lymphatic Breast Cancer Metastasis. Front Bioeng Biotechnol. 2021 Feb 15;8:611802.

326. Studebaker AW, Storci G, Werbeck JL, Sansone P, Sasser AK, Tavolari S, et al. Fibroblasts Isolated from Common Sites of Breast Cancer Metastasis Enhance Cancer Cell Growth Rates and Invasiveness in an Interleukin-6–Dependent Manner. Cancer Res. 2008 Nov 1;68(21):9087–95.

327. Walter M, Liang S, Ghosh S, Hornsby PJ, Li R. Interleukin 6 secreted from adipose stromal cells promotes migration and invasion of breast cancer cells. Oncogene. 2009 Jul 30;28(30):2745–55.

328. Hoene M, Weigert C. The role of interleukin-6 in insulin resistance, body fat distribution and energy balance. Obes Rev. 2008 Jan;9(1):20–9.

329. Shah AD, Bouchard MJ, Shieh AC. Interstitial Fluid Flow Increases Hepatocellular Carcinoma Cell Invasion through CXCR4/CXCL12 and MEK/ERK Signaling. Avila MA, editor. PLOS ONE. 2015 Nov 11;10(11):e0142337.

330. Tchafa AM, Ta M, Reginato MJ, Shieh AC. EMT Transition Alters Interstitial Fluid Flow–Induced Signaling in *ERBB2* -Positive Breast Cancer Cells. Mol Cancer Res. 2015 Apr 1;13(4):755–64.

331. Scimone ML, Felbinger TW, Mazo IB, Stein JV, Von Andrian UH, Weninger W. CXCL12 Mediates CCR7-independent Homing of Central Memory Cells, But Not Naive T Cells, in Peripheral Lymph Nodes. J Exp Med. 2004 Apr 19;199(8):1113–20.

332. Blades MC, Manzo A, Ingegnoli F, Taylor PR, Panayi GS, Irjala H, et al. Stromal Cell-Derived Factor 1 (CXCL12) Induces Human Cell Migration into Human Lymph Nodes Transplanted into SCID Mice. J Immunol. 2002 May 1;168(9):4308–17.

333. Rogic A, Pant I, Grumolato L, Fernandez-Rodriguez R, Edwards A, Das S, et al. High endogenous CCL2 expression promotes the aggressive phenotype of human inflammatory breast cancer. Nat Commun. 2021 Nov 25;12(1):6889.

334. Kitamura T, Qian BZ, Soong D, Cassetta L, Noy R, Sugano G, et al. CCL2-induced chemokine cascade promotes breast cancer metastasis by enhancing retention of metastasis-associated macrophages. J Exp Med. 2015 Jun 29;212(7):1043–59.

335. Tsuyada A, Chow A, Wu J, Somlo G, Chu P, Loera S, et al. CCL2 Mediates Cross-talk between Cancer Cells and Stromal Fibroblasts That Regulates Breast Cancer Stem Cells. Cancer Res. 2012 Jun 1;72(11):2768–79.

336. Fang WB, Jokar I, Zou A, Lambert D, Dendukuri P, Cheng N. CCL2/CCR2 Chemokine Signaling Coordinates Survival and Motility of Breast Cancer Cells through Smad3 Protein- and p42/44 Mitogen-activated Protein Kinase (MAPK)-dependent Mechanisms. J Biol Chem. 2012 Oct;287(43):36593–608.

337. Ksiazkiewicz M, Gottfried E, Kreutz M, Mack M, Hofstaedter F, Kunz-Schughart LA. Importance of CCL2-CCR2A/2B signaling for monocyte migration into spheroids of breast cancer-derived fibroblasts. Immunobiology. 2010 Sep;215(9–10):737–47.

338. Waugh DJJ, Wilson C. The Interleukin-8 Pathway in Cancer. Clin Cancer Res. 2008 Nov 1;14(21):6735–41.

339. Liu Q, Li A, Tian Y, Wu JD, Liu Y, Li T, et al. The CXCL8-CXCR1/2 pathways in cancer. Cytokine Growth Factor Rev. 2016 Oct;31:61–71.

340. Regier MC, Maccoux LJ, Weinberger EM, Regehr KJ, Berry SM, Beebe DJ, et al. Transitions from mono- to co- to tri-culture uniquely affect gene expression in breast cancer, stromal, and immune compartments. Biomed Microdevices. 2016 Aug;18(4):70.

341. Shao L, Yu Q, Xia R, Zhang J, Gu S, Yu D, et al. B7-H3 on breast cancer cell MCF7 inhibits IFN-γ release from tumour-infiltrating T cells. Pathol - Res Pract. 2021 Aug;224:153461.

342. Saraiva DP, Matias AT, Braga S, Jacinto A, Cabral MG. Establishment of a 3D Co-culture With MDA-MB-231 Breast Cancer Cell Line and Patient-Derived Immune Cells for Application in the Development of Immunotherapies. Front Oncol. 2020 Aug 27;10:1543.

343. Strömvall K, Sundkvist K, Ljungberg B, Halin Bergström S, Bergh A. Reduced number of CD169 $^{+}$ macrophages in pre-metastatic regional lymph nodes is associated with subsequent metastatic disease in an animal model and with poor outcome in prostate cancer patients. The Prostate. 2017 Nov;77(15):1468–77.

344. Tacconi C, Commerford CD, Dieterich LC, Schwager S, He Y, Ikenberg K, et al. CD169+ lymph node macrophages have protective functions in mouse breast cancer metastasis. Cell Rep. 2021 Apr;35(2):108993.

345. AL-Ghadban S, Cromer W, Allen M, Ussery C, Badowski M, Harris D, et al. Dilated Blood and Lymphatic Microvessels, Angiogenesis, Increased Macrophages, and Adipocyte Hypertrophy in Lipedema Thigh Skin and Fat Tissue. J Obes. 2019 Mar 3;2019:1–10.

346. Kruppa P, Gohlke S, Łapiński K, Garcia-Carrizo F, Soultoukis GA, Infanger M, et al. Lipedema stage affects adipocyte hypertrophy, subcutaneous adipose tissue inflammation and interstitial fibrosis. Front Immunol. 2023 Jul 28;14:1223264.

347. Wolf S, Rannikko JH, Virtakoivu R, Cinelli P, Felmerer G, Burger A, et al. A distinct M2 macrophage infiltrate and transcriptomic profile decisively influence adipocyte differentiation in lipedema. Front Immunol. 2022 Dec 20;13:1004609.

348. Kovalchuk A, Kolb B. Chemo brain: From discerning mechanisms to lifting the brain fog—An aging connection. Cell Cycle. 2017 Jul 18;16(14):1345–9.

349. Brown T, McElroy T, Simmons P, Walters H, Ntagwabira F, Wang J, et al. Cognitive impairment resulting from treatment with docetaxel, doxorubicin, and cyclophosphamide. Brain Res. 2021 Jun;1760:147397.

350. Fardell JE, Vardy J, Johnston IN. The short and long term effects of docetaxel chemotherapy on rodent object recognition and spatial reference memory. Life Sci. 2013 Oct;93(17):596–604.

351. Maloveska M, Danko J, Petrovova E, Kresakova L, Vdoviakova K, Michalicova A, et al. Dynamics of Evans blue clearance from cerebrospinal fluid into meningeal lymphatic vessels and deep cervical lymph nodes. Neurol Res. 2018 May 4;40(5):372–80.

352. Radjavi A, Smirnov I, Derecki N, Kipnis J. Dynamics of the meningeal CD4+ T-cell repertoire are defined by the cervical lymph nodes and facilitate cognitive task performance in mice. Mol Psychiatry. 2014 May;19(5):531–2.

353. Wang L, Zhang Y, Zhao Y, Marshall C, Wu T, Xiao M. Deep cervical lymph node ligation aggravates AD-like pathology of APP/PS1 mice. Brain Pathol. 2019 Mar;29(2):176–92.

354. Liu Z, Huang Y, Wang X, Li JY, Zhang C, Yang Y, et al. The cervical lymph node contributes to peripheral inflammation related to Parkinson's disease. J Neuroinflammation. 2023 Apr 10;20(1):93.

355. Li X, Qi L, Yang D, Hao S, Zhang F, Zhu X, et al. Meningeal lymphatic vessels mediate neurotropic viral drainage from the central nervous system. Nat Neurosci. 2022 May;25(5):577–87.

356. Henderson AR, Ilan IS, Lee E. A bioengineered lymphatic vessel model for studying lymphatic endothelial cell-cell junction and barrier function. Microcirculation [Internet]. 2021 Oct 4 [cited 2021 Nov 12]; Available from: https://onlinelibrary.wiley.com/doi/10.1111/micc.12730

357. Kim M, Choi S, Choi DH, Ahn J, Lee D, Song E, et al. An advanced 3D lymphatic system for assaying human cutaneous lymphangiogenesis in a microfluidic platform. NPG Asia Mater. 2024 Feb 2;16(1):7.

358. Frenkel N, Poghosyan S, Alarcón CR, García SB, Queiroz K, Van Den Bent L, et al. Long-Lived Human Lymphatic Endothelial Cells to Study Lymphatic Biology and Lymphatic Vessel/Tumor Coculture in a 3D Microfluidic Model. ACS Biomater Sci Eng. 2021 Jul 12;7(7):3030–42.

359. Fathi P, Holland G, Pan D, Esch MB. Lymphatic Vessel on a Chip with Capability for Exposure to Cyclic Fluidic Flow. ACS Appl Bio Mater. 2020 Oct 19;3(10):6697–707.

360. Lee HG, Cho MJ, Choi JM. Bystander CD4+ T cells: crossroads between innate and adaptive immunity. Exp Mol Med. 2020 Aug;52(8):1255–63.

361. Tantalo DG, Oliver AJ, von Scheidt B, Harrison AJ, Mueller SN, Kershaw MH, et al. Understanding T cell phenotype for the design of effective chimeric antigen receptor T cell therapies. J Immunother Cancer. 2021 May;9(5):e002555.

362. Baptista AP, Roozendaal R, Reijmers RM, Koning JJ, Unger WW, Greuter M, et al. Lymph node stromal cells constrain immunity via MHC class II self-antigen presentation. eLife. 2014 Nov 19;3:e04433.

363. Nadafi R, Gago De Graça C, Keuning ED, Koning JJ, De Kivit S, Konijn T, et al. Lymph Node Stromal Cells Generate Antigen-Specific Regulatory T Cells and Control Autoreactive T and B Cell Responses. Cell Rep. 2020 Mar;30(12):4110-4123.e4.

364. Ledford H. Translational research: 4 ways to fix the clinical trial. Nature. 2011 Sep 28;477(7366):526–8.

365. Kershaw EE, Flier JS. Adipose Tissue as an Endocrine Organ. J Clin Endocrinol Metab. 2004 Jun;89(6):2548–56.

366. Yilmaz M, Hotamisligil GS. Damned If You Do, Damned If You Don’t: The Conundrum of Adipose Tissue Vascularization. Cell Metab. 2013 Jan;17(1):7–9.

367. Dewhirst MW, Secomb TW. Transport of drugs from blood vessels to tumour tissue. Nat Rev Cancer. 2017 Dec;17(12):738–50.

368. Stenkula KG, Erlanson-Albertsson C. Adipose cell size: importance in health and disease. Am J Physiol-Regul Integr Comp Physiol. 2018 Aug 1;315(2):R284–95.

369. Wiedner M, Aghajanzadeh D, Richter DF. Differential diagnoses and treatment of lipedema. Plast Aesthetic Res [Internet]. 2020 Mar 6 [cited 2024 Jun 18];2020. Available from: https://www.oaepublish.com/articles/2347-9264.2019.51

370. Van La Parra RFD, Deconinck C, Pirson G, Servaes M, Fosseprez Ph. Lipedema: What we don't know. J Plast Reconstr Aesthet Surg. 2023 Sep;84:302–12.

371. Poojari A, Dev K, Rabiee A. Lipedema: Insights into Morphology, Pathophysiology, and Challenges. Biomedicines. 2022 Nov 30;10(12):3081.

372. Buck DW, Herbst KL. Lipedema: A Relatively Common Disease with Extremely Common Misconceptions. Plast Reconstr Surg - Glob Open. 2016 Sep;4(9):e1043.

373. Felmerer G, Stylianaki A, Hägerling R, Wang A, Ströbel P, Hollmén M, et al. Adipose Tissue Hypertrophy, An Aberrant Biochemical Profile and Distinct Gene Expression in Lipedema. J Surg Res. 2020 Sep;253:294–303.

374. Forner-Cordero I, Oliván-Sasot P, Ruiz-Llorca C, Muñoz-Langa J. Lymphoscintigraphic findings in patients with lipedema. Rev Esp Med Nucl E Imagen Mol Engl Ed. 2018 Nov;37(6):341–8.

375. Crescenzi R, Donahue PMC, Garza M, Patel NJ, Lee C, Guerreso K, et al. Subcutaneous Adipose Tissue Edema in Lipedema Revealed by Noninvasive 3T MR Lymphangiography. J Magn Reson Imaging. 2023 Feb;57(2):598–608.

376. Lohrmann C, Foeldi E, Langer M. MR imaging of the lymphatic system in patients with lipedema and lipo-lymphedema. Microvasc Res. 2009 May;77(3):335–9.

377. Crescenzi R, Marton A, Donahue PMC, Mahany HB, Lants SK, Wang P, et al. Tissue Sodium Content is Elevated in the Skin and Subcutaneous Adipose Tissue in Women with Lipedema. Obesity. 2018 Feb;26(2):310–7.

378. Gould DJ, El-Sabawi B, Goel P, Badash I, Colletti P, Patel KM. Uncovering Lymphatic Transport Abnormalities in Patients with Primary Lipedema. J Reconstr Microsurg. 2020 Feb;36(02):136–41.

379. Rasmussen JC, Aldrich MB, Fife CE, Herbst KL, Sevick-Muraca EM. Lymphatic function and anatomy in early stages of lipedema. Obesity. 2022 Jul;30(7):1391–400.

380. Zaleska MT, Olszewski WL, Krzesniak NE. Lower Limb Lipedema–Superficial Lymph Flow, Skin Water Concentration, Skin and Subcutaneous Tissue Elasticity. Lymphat Res Biol. 2023 Feb 1;21(1):60–9.

381. Nielsen NB, Højbjerre L, Sonne MP, Alibegovic AC, Vaag A, Dela F, et al. Interstitial concentrations of adipokines in subcutaneous abdominal and femoral adipose tissue. Regul Pept. 2009 Jun;155(1–3):39–45.

382. Schaupp L, Ellmerer M, Brunner GA, Wutte A, Sendlhofer G, Trajanoski Z, et al. Direct access to interstitial fluid in adipose tissue in humans by use of open-flow microperfusion. Am J Physiol-Endocrinol Metab. 1999 Feb 1;276(2):E401–8.

383. Bauer AT, Von Lukowicz D, Lossagk K, Hopfner U, Kirsch M, Moog P, et al. Adipose Stem Cells from Lipedema and Control Adipose Tissue Respond Differently to Adipogenic Stimulation In Vitro. Plast Reconstr Surg. 2019 Sep;144(3):623–32.

384. Al-Ghadban S, Diaz ZT, Singer HJ, Mert KB, Bunnell BA. Increase in Leptin and PPAR-γ Gene Expression in Lipedema Adipocytes Differentiated in vitro from Adipose-Derived Stem Cells. Cells. 2020 Feb 12;9(2):430.

385. Al-Ghadban S, Pursell IA, Diaz ZT, Herbst KL, Bunnell BA. 3D Spheroids Derived from Human Lipedema ASCs Demonstrated Similar Adipogenic Differentiation Potential and ECM Remodeling to Non-Lipedema ASCs In Vitro. Int J Mol Sci. 2020 Nov 7;21(21):8350.

386. Ernst AM, Steiner M, Kainz V, Tempfer H, Spitzer G, Plank T, et al. Lipedema: The Use of Cultured Adipocytes for Identification of Diagnostic Markers. Plast Reconstr Surg. 2023 Nov;152(5):1036–46.

387. Al-Ghadban S, Walczak SG, Isern SU, Martin EC, Herbst KL, Bunnell BA. Enhanced Angiogenesis in HUVECs Preconditioned with Media from Adipocytes Differentiated from Lipedema Adipose Stem Cells In Vitro. Int J Mol Sci. 2023 Sep 1;24(17):13572.

388. Al-Ghadban S, Isern SU, Herbst KL, Bunnell BA. The Expression of Adipogenic Marker Is Significantly Increased in Estrogen-Treated Lipedema Adipocytes Differentiated from Adipose Stem Cells In Vitro. Biomedicines. 2024 May 9;12(5):1042.

389. Hammel JH, Bellas E. Endothelial cell crosstalk improves browning but hinders white adipocyte maturation in 3D engineered adipose tissue. Integr Biol. 2020 Apr 20;12(4):81–9.

390. Anvari G, Bellas E. Hypoxia induces stress fiber formation in adipocytes in the early stage of obesity. Sci Rep. 2021 Dec;11(1):21473.

391. Di Caprio N, Bellas E. Collagen Stiffness and Architecture Regulate Fibrotic Gene Expression in Engineered Adipose Tissue. Adv Biosyst. 2020 Jun;4(6):1900286.

392. Baptista LS, Silva KR, Jobeili L, Guillot L, Sigaudo-Roussel D. Unraveling White Adipose Tissue Heterogeneity and Obesity by Adipose Stem/Stromal Cell Biology and 3D Culture Models. Cells. 2023 Jun 8;12(12):1583.

393. Muller S, Ader I, Creff J, Leménager H, Achard P, Casteilla L, et al. Human adipose stromal-vascular fraction self-organizes to form vascularized adipose tissue in 3D cultures. Sci Rep. 2019 May 10;9(1):7250.

394. Kang JH, Gimble JM, Kaplan DL. *In Vitro* 3D Model for Human Vascularized Adipose Tissue. Tissue Eng Part A. 2009 Aug;15(8):2227–36.

395. Parkhurst MR, Saltzman WM. Quantification of human neutrophil motility in three-dimensional collagen gels. Effect of collagen concentration. Biophys J. 1992 Feb;61(2):306–15.

396. Kruppa P, Georgiou I, Biermann N, Prantl L, Klein-Weigel P, Ghods M. Lipedema—Pathogenesis, Diagnosis, and Treatment Options. Dtsch Ärztebl Int [Internet]. 2020 Jun 1 [cited 2024 Aug 22]; Available from: https://www.aerzteblatt.de/10.3238/arztebl.2020.0396

397. Autoren FD, Ghods M. In Reply. Dtsch Ärztebl Int [Internet]. 2021 Jan 22 [cited 2024 Aug 22]; Available from: https://www.aerzteblatt.de/10.3238/arztebl.m2021.0060

398. Herpertz U. The Prevalence Was Probably Overestimated. Dtsch Ärztebl Int [Internet]. 2021 Jan 22 [cited 2024 Aug 22]; Available from: https://www.aerzteblatt.de/10.3238/arztebl.m2021.0059

399. Chang E, Varghese M, Singer K. Gender and Sex Differences in Adipose Tissue. Curr Diab Rep. 2018 Sep;18(9):69.

400. Fuente-Martín E, Argente-Arizón P, Ros P, Argente J, Chowen JA. Sex differences in adipose tissue: It is not only a question of quantity and distribution. Adipocyte. 2013 Jul 24;2(3):128–34.

401. Gavin KM, Bessesen DH. Sex Differences in Adipose Tissue Function. Endocrinol Metab Clin North Am. 2020 Jun;49(2):215–28.

402. Karastergiou K, Smith SR, Greenberg AS, Fried SK. Sex differences in human adipose tissues – the biology of pear shape. Biol Sex Differ. 2012 Dec;3(1):13.

403. Moreira-Pais A, Ferreira R, Neves JS, Vitorino R, Moreira-Gonçalves D, Nogueira-Ferreira R. Sex differences on adipose tissue remodeling: from molecular mechanisms to therapeutic interventions. J Mol Med. 2020 Apr;98(4):483–93.

404. Zhang Y, Zitsman JL, Hou J, Fennoy I, Guo K, Feinberg J, et al. Fat cell size and adipokine expression in relation to gender, depot, and metabolic risk factors in morbidly obese adolescents. Obesity. 2014 Mar;22(3):691–7.

405. Ramis JM, Salinas R, García-Sanz JM, Moreiro J, Proenza AM, Lladó I. Depot- and Gender-related Differences in the Lipolytic Pathway of Adipose Tissue from Severely Obese Patients. Cell Physiol Biochem. 2006;17(3–4):173–80.

406. Sjöström L, Smith U, Krotkiewski M, Björntorp P. Cellularity in different regions of adipose tissue in young men and women. Metabolism. 1972 Dec;21(12):1143–53.

407. McLaughlin T, Lamendola C, Coghlan N, Liu TC, Lerner K, Sherman A, et al. Subcutaneous adipose cell size and distribution: Relationship to insulin resistance and body fat. Obesity. 2014 Mar;22(3):673–80.

408. Mundi MS, Karpyak MV, Koutsari C, Votruba SB, O'Brien PC, Jensen MD. Body Fat Distribution, Adipocyte Size, and Metabolic Characteristics of Nondiabetic Adults. J Clin Endocrinol Metab. 2010 Jan;95(1):67–73.

409. Nickelson KJ, Stromsdorfer KL, Pickering RT, Liu TW, Ortinau LC, Keating AF, et al. A Comparison of Inflammatory and Oxidative Stress Markers in Adipose Tissue from Weight-Matched Obese Male and Female Mice. Exp Diabetes Res. 2012;2012:1–8.

410. Garciaescobar E, Soriguer F, Garciaserrano S, Gomezzumaquero J, Morcillo S, Haro J, et al. Dietary oleic acid and adipocyte lipolytic activity in culture☆. J Nutr Biochem. 2008 Nov;19(11):727–31.

411. Karacor K, Cam M. Effects of oleic acid. Med Sci Discov. 2015 Jan 15;2(1):125.

412. Mårin P, Rebuffé-Scrive M, Björntorp P. Uptake of triglyceride fatty acids in adipose tissue *in vivo* in man. Eur J Clin Invest. 1990 Apr;20(2Part1):158–65.

413. Murru E, Manca C, Carta G, Banni S. Impact of Dietary Palmitic Acid on Lipid Metabolism. Front Nutr. 2022 Mar 23;9:861664.

414. Iggman D, Ärnlöv J, Vessby B, Cederholm T, Sjögren P, Risérus U. Adipose tissue fatty acids and insulin sensitivity in elderly men. Diabetologia. 2010 May;53(5):850–7.

415. Korbecki J, Bajdak-Rusinek K. The effect of palmitic acid on inflammatory response in macrophages: an overview of molecular mechanisms. Inflamm Res. 2019 Nov;68(11):915–32.

416. Saraswathi V, Kumar N, Gopal T, Bhatt S, Ai W, Ma C, et al. Lauric Acid versus Palmitic Acid: Effects on Adipose Tissue Inflammation, Insulin Resistance, and Non-Alcoholic Fatty Liver Disease in Obesity. Biology. 2020 Oct 22;9(11):346.

417. Laine PS, Schwartz EA, Wang Y, Zhang WY, Karnik SK, Musi N, et al. Palmitic acid induces IP-10 expression in human macrophages via NF-κB activation. Biochem Biophys Res Commun. 2007 Jun;358(1):150–5.

418. Blade SP, Falkowski DJ, Bachand SN, Pagano SJ, Chin L. Mechanobiology of Adipocytes. Biology. 2024 Jun 13;13(6):434.

419. Pellegrinelli V, Heuvingh J, Du Roure O, Rouault C, Devulder A, Klein C, et al. Human adipocyte function is impacted by mechanical cues. J Pathol. 2014 Jun;233(2):183–95.

420. Lecoutre S, Lambert M, Drygalski K, Dugail I, Maqdasy S, Hautefeuille M, et al. Importance of the Microenvironment and Mechanosensing in Adipose Tissue Biology. Cells. 2022 Jul 27;11(15):2310.

421. Rendon CJ, Flood E, Thompson JM, Chirivi M, Watts SW, Contreras GA. PIEZO1 mechanoreceptor activation reduces adipogenesis in perivascular adipose tissue preadipocytes. Front Endocrinol. 2022 Aug 31;13:995499.